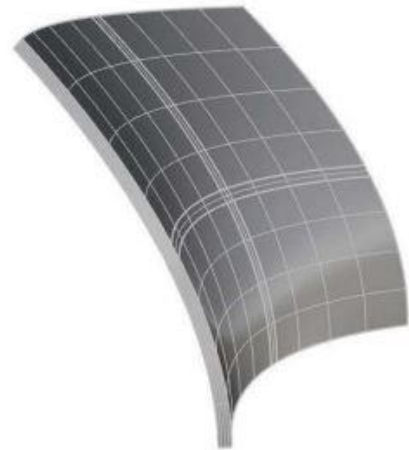
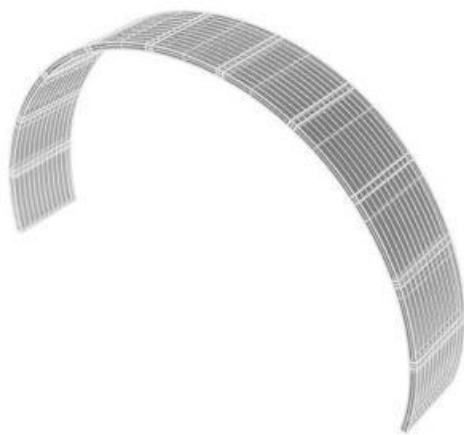
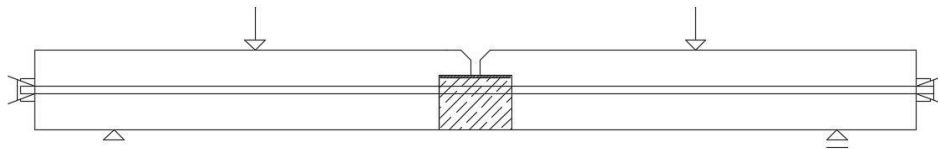


# Master's Thesis

Panteleimon Vrachas

## Post-tensioned concrete produced with the Flexible Mould



Developing the Flexible Mould. Aiming at structurally efficient concrete shapes

# Master's Thesis

## Post-tensioned concrete produced with the Flexible Mould

By

Panteleimon Vrachas

in partial fulfilment of the requirements for the degree of

**Master of Science**  
in Civil Engineering

at the Delft University of Technology,  
to be defended publicly on Friday August 17, 2018

Thesis chair	Prof. Ir. R. Nijssen
Thesis supervisor	Dr. Ir. H.R. Schipper
Thesis committee	Dr. Ir. C.R. Braam
	Ir. J.M. Houben
	MSc Ir. Eigenraam

# Contents

<b>I Introduction</b>	<b>8</b>
<b>1 Introduction to the problem - Research objectives</b>	<b>8</b>
1.1 Summary	8
1.2 Introduction	8
1.3 Earlier research	10
1.4 Research project	11
1.4.1 Problem definition	11
1.4.2 Research question	11
1.4.3 Research objectives	11
1.4.4 Report outline	11
<b>II Literature review</b>	<b>13</b>
<b>2 Summary</b>	<b>13</b>
2.1 Adjustable mould concept	13
2.2 Flexible mould's development	14
2.3 "Flexible Formwork"	16
2.3.1 Actuators	16
2.3.2 Elastic layer	17
2.3.3 Mould	18
<b>3 Design parameters</b>	<b>19</b>
3.1 Summary	19
3.2 Introduction	19
3.3 Mechanics	20
3.3.1 Relations for hypars with curved edges	21
3.4 Concrete type	23
3.5 Reinforcement	24
3.5.1 Prestressing reinforcement	26
3.6 Panel segmentation	27
3.7 Connections	28
3.8 Edge profiling	30
3.9 Other geometrical aspects	30
<b>III Experimental investigation on double curved concrete elements</b>	<b>32</b>
<b>4 Summary</b>	<b>32</b>
4.1 Design of the shells geometry	32
4.1.1 Shells' coordinates	33
4.2 Laboratory tests	34
4.2.1 240mm grid test	34
4.2.2 120mm grid test	35
4.3 Results	36
4.3.1 240mm grid distance	36

4.3.2	120mm grid distance	36
4.4	Conclusions	37
4.4.1	240mm grid distance	37
4.4.2	120mm grid distance	37
4.5	Test limitations	37
4.6	Recommendations	38

## **IV Modeling straight and curved prestressed concrete beams in DIANA10.1** **39**

<b>5</b>	<b>Summary</b>	<b>39</b>
5.1	Physical problem	39
5.2	Model parameters	41
5.3	Hand calculations	42
5.4	Finite element modeling (FEM) - Initial models	43
5.4.1	Element type and mesh - 2D	43
5.4.2	Element type and mesh - 3D	44
5.4.3	Prestressing steel reinforcement	45
5.4.4	Structural interface elements	46
5.5	Linear static analysis	46
5.5.1	Introduction	46
5.6	Conclusions	46
5.6.1	Influence of tendon's position	46
5.6.2	Influence of steel plates	47
5.6.3	Influence of curved geometry input 1	48
5.6.4	Influence of curved geometry input 2	49
5.6.5	Division in two elements	50
5.6.6	Division in three elements	51
5.6.7	Including a structural interface element	52
5.6.8	Effect of the properties of the interface	52
5.6.9	Input from RHINO	53
5.6.10	Comparison between 2D and 3D models	53
5.7	Conclusions	55

## **V Four point bending test - Brittle joint** **56**

<b>6</b>	<b>Introduction</b>	<b>56</b>
6.1	Physical problem	56
6.2	Concrete material properties	57
6.3	Prestressing steel material properties	58
6.4	Loads and load combinations:	58
6.5	Code requirements	59
6.6	Hand calculations	59
6.6.1	Linear static analysis	59
6.6.2	Discrete cracking	61
6.7	Finite element modeling (FEM) - Four point bending test	63
6.7.1	Element type and mesh	63
6.7.2	Post-tensioning steel reinforcement	64

6.7.3	Structural interface element	64
6.7.4	Types of analyses:	66
6.8	Linear static analysis	67
6.8.1	Force control (F.C.)	67
6.8.2	Displacement control (D.C.)	69
6.8.3	Conclusions	70
6.8.4	Test limitations	70
6.9	Phased nonlinear static analysis	71
6.9.1	Point 0	73
6.9.2	Load step 7	74
6.9.3	Load step 14	75
6.9.4	Load step 24	76
6.9.5	Load step 25	77
6.9.6	Load step 29	78
6.9.7	Load step 45	79
6.9.8	Load step 70	81
6.9.9	Load step 116	82
6.9.10	Load step 154	83
6.9.11	Relation between curvature and load	84
6.10	Conclusions	87
6.11	General conclusion	87
<b>VI</b>	<b>Post-tensioned concrete arch structure</b>	<b>89</b>
<b>7</b>	<b>Summary</b>	<b>89</b>
7.1	Physical problem	89
7.2	Initial CAD model	90
7.3	Final CAD model	91
7.4	Finite element modeling (FEM) - Arch structure	93
7.4.1	Element types and mesh	93
7.5	Linear static analysis	93
7.5.1	Test limitations	94
7.6	Recommendations	95
<b>VII</b>	<b>Discussion &amp; Conclusions</b>	<b>96</b>
<b>8</b>	<b>Discussion</b>	<b>96</b>
<b>9</b>	<b>Conclusions</b>	<b>98</b>
<b>A</b>	<b>DIANA10.1 simple shaped models</b>	<b>99</b>
<b>B</b>	<b>Four point bending test</b>	<b>206</b>
B.1	Linear static analysis	206
B.1.1	Supports distance included	206
B.1.2	Supports distance included	209
B.2	Cracking loads	212
B.2.1	Calculations with regard to the maximum displacements	
	$u_{max}$	212

B.2.2	Calculations with regard to the displacements at start of horizontal plateau - $u = 0.6[mm]$	214
B.2.3	Point 0	215
B.2.4	Load step 7	216
B.2.5	Load step 24	217
B.2.6	Load step 25	218
B.2.7	Load step 29	219
B.2.8	Load step 45	220
B.2.9	Load step 70	221
B.2.10	Load step 116	223
B.2.11	Load step 154	224
B.2.12	Relation between curvature and load	225
<b>C</b>	<b>Post-tensioned concrete arch structure</b>	<b>226</b>
C.1	Hand calculations:	226
C.2	Linear static analysis	230
C.2.1	DIANA10.2 results	230
C.2.2	Comparison of DIANA10.2 results with hand-calculations	232
<b>References</b>		<b>233</b>

# Preface

This report presents my Master's Thesis at the faculty of Civil Engineering at Delft University of Technology. It marks the completion of my studies for the track of Structural Engineering.

The content of the current research is related to experimental investigation and structural analysis on post-tensioned concrete produced with the flexible mould. In the first part, the relation between the number of actuators and the curvature of the mould surface was qualitatively analyzed. In the second part, a structural analysis was performed in order to investigate improvements on the flexural tensile capacity of post-tensioned concrete made with the flexible mould.

I would like to thank my graduation committee: Dr. H.R. Schipper, MSc. P. Eigenraam, Dr. C.R. Braam, Prof. R. Nijssen and Dr. J.M. Houben for their guidance and time spent during this study. I would also like to thank my father for his support during this academic and life cycle. I also want to thank my friends for their support, and namely Vaggelis, Panagiotis, Tudor, Vasilis, Elli, Marina, Eutichia, Sunny, Giorgos.

Panteleimon Vrachas  
Delft, August 2018

# Abstract

Nowadays, precast technology is mainly used for the production of concrete shell elements. Computer Numerically Controlled (CNC) milling techniques is the main production method of single or double-curved concrete elements, creating astonishing shapes with high accuracy. However, these techniques are also accompanied with high costs and large material waste. Skilled carpentry or curved steel formwork are other techniques used for the production of concrete shells. An alternative to the aforementioned techniques is the “Flexible Mould” method being developed at Delft University of Technology. This method is based on mass customization of the produced panels, due to the adaptability of the formwork’s shape according to the specified geometry. The concept of the “Flexible Mould” will be used as a starting point for the current thesis.

Concrete shells are mainly used for decorative reasons such as claddings and facade elements. Their structural capacity has still to be improved so that they can be applied as load-bearing elements and avoid sub-optimal or even “bad” designs. Several researches are being conducted in order to analyze and improve the load bearing capacity of concrete shells produced with the adjustable formwork technique. Applying conventional steel reinforcement to take up possible occurring tensile stresses in concrete shells produced with the Flexible Mould, has been proved to be possible only with limited diameters due to construction requirements.

In the first part of the thesis, a research was conducted on possible improvements in the production of concrete shells with the flexible mould, so that they could be considered feasible to be applied in real life structures. Having conducted a literature review on production parameters related to the “Flexible Mould” concept, Computer Aided Design (CAD) was used as the main tool to create the digital geometry of double-curved concrete elements. Dimensional limitations imposed from the existing test set-up of the adjustable formwork at TU Delft laboratories, as well as the inherent geometry of shell elements, had to be taken into account. As a next step towards the implementation of double-curved concrete elements in real life structures, non-load-bearing laboratory tests took place. These tests were performed for illustrating reasons with sand to be the main material used instead of concrete. During these tests, a steel wire mesh diamond shaped was applied as the elastic layer of the flexible mould, being a different material in comparison with the previous studies on the flexible mould. Grid distance between the actuators was the main parameter investigated during this part of the research.

In the second part of the thesis, a study was conducted on possible improvements in the flexural tensile capacity of concrete shells via prestressing steel reinforcement. CAD design and Finite Element Modeling (FEM) were the main tools used. Due to shell’s complex geometry, the research was conducted first for simple geometrical shapes under linear static analyses. Two and three dimensional elements were investigated being modeled as plane stress elements and solids respectively. Linear or single-curved prestressed concrete elements were analyzed with regard to their deflection and stress field. The number of concrete elements as well as the influence of an intermediate element in-between them simulating a joint, was an additional investigated parameter.

Subsequently, a four-point bending that will take place at TU Delft, was

simulated with Finite Element Modeling (FEM), investigating its structural response under both linear and nonlinear static analyses. The created (FEM) comprises of two centrally prestressed concrete elements connected with a mortar joint in between them. No bond interaction between the post-tensioning steel reinforcement and the concrete is incorporated in the FE model. The type and size of the applied reinforcement is investigated in this model. The main goal of this part was to analyze the structure's response for loads exceeding the cracking load of the concrete, taking into account a brittle concrete failure at joint's location.

In the final part of the thesis, a post-tensioned arch structure segmented in a series of concrete elements and joints, was first designed with CAD software and then analyzed under a linear static analysis via FEM. Although more complex, a three-dimensional (3D) modeling was conducted, aiming at describing the three dimensional state of stress and deflection field of the arch. Based on a draft CAD model, several geometrical parameters had to be adjusted in order to meet construction requirements of the final concrete shell structure. Modeling and meshing requirements imposed from the Finite Element Analysis (FEA) software were also taken into consideration for the final shape of the arch.

The current thesis is a part of a research program that is being performed at TU Delft, aiming at developing the Flexible Mould with regard to construction and structural application of concrete shells in real life structures.

## Part I

# Introduction

## 1 Introduction to the problem - Research objectives

### 1.1 Summary

In this section, the main subject of this thesis is presented, and this is the investigation on improvements in the tensile capacity of double-curved concrete panels produced with the “Flexible Formwork” via prestressing reinforcement. Initially, the reader is introduced to free-form architecture and the relevant production techniques of precast concrete shells. An overview of the developments in the adjustable formwork is also given. Several researches were conducted with respect not only to the mechanical evolution of the flexible mould but also to the structural capacity of the shell elements produced with this concept. Subsequently, the necessity for applying reinforcement in the panels is highlighted and as an alternative way to be investigated in this thesis, will be the use of post-tensioning reinforcement. In addition, the applicability of prestressed elements in three on-going projects will be analyzed. Finally, the main outline that will be used as directive in this thesis is presented.

### 1.2 Introduction

The time domain of 1950 - 1960, is considered to be a golden era for free-form architecture. Single or double curved elements made out of different materials, such as plastic, glass, timber, steel and concrete made a leap in modern architecture, creating astonishing shapes for several structures. Concrete can be distinguished from its durability, smooth finishing, texture, color, slenderness and strength. It is also characterized by its thixotropic behavior and viscosity during the elements’ manufacturing process. Precast technology techniques are mainly used for the production of complex geometrical shapes. Excellent curing properties, less creep and shrinkage, weather independent conditions, superior finishing and minimization of construction tolerances are the most important features of precast concrete [\[Schipper 2015\]](#).

In 1960, the Italian architect Renzo Piano was the first to publish his research related to double-curved fibre reinforced plastic (FRP) elements, with the renowned pneumatic device of “Stampo Deformabile” of “Flexible Mould”. Several architects and engineers such as Heinz Isler (figure [1.1](#)) and Eduardo Torroja focused on concrete shell structures that were not only aesthetically appealing but also characterized by high strength properties.

After this flourishing period, shell architecture stagnated. Design and production of double curved elements was quite a cumbersome task for engineers. Lack of knowledge in Finite Element Method (FEM), undeveloped Computer Aided Design (CAD) and insufficient production techniques accompanied with high costs were the main causes.

Nowadays, advances in the computer technology and specifically in digital-parametric and FEM software design, resulted in an increasing interest for com-

plex shaped single- or double-curved structures. As a result, free form architecture is regaining ground in the construction industry, see figure 1.2. Double-curved panels are mostly used for architectural reasons, such as roof claddings and facade elements. These type of panels are considered to be non-load bearing. Panels of single or double curvature can also obtain a load-bearing function when designed according to the design codes with regard to their strength, stiffness, durability. However, their structural behavior is not yet adequately analyzed.

For the production of double-curved concrete panels, computer numerically controlled (CNC) milling techniques are mainly used, elsewhere skilled carpentry or curved steel formwork are required. Although these methods offer high accuracy for the end product, they result in high costs. For the first method, this can be explained by the large volume of waste that is produced and the single use of the formwork. Skilled carpentry implies labor intensive tasks, slow production process and higher costs for the curved panels. In addition, in case of using curved timber or steel formwork, conflicts arise between cost and final aesthetics of the shell structure. The more complex is the geometry of the building, the larger the number of uniquely shaped elements that have to be produced with the precast technology. In order to minimize the total cost, the aforementioned production techniques are based on optimized segmentation methods, the entitled rationalization of the structure [Schipper, 2015].

To overcome this problem and develop a more sustainable and cost effective technique with a high repetition factor, the concept of “Flexible Mould” is being researched by several scientists at Delft University of Technology. This production technique seems promising, since it can be adjusted according to the demands of the project, creating single or double curved elements, taking into advantage the benefits of precast technology. The main superior feature of this method is the reconfigurability of the mould for creating different geometries of shell elements. This may lead to smaller cost differences between different panels used for the free-form structure [Schipper, 2015]. Hence, the adjustable formwork sets an alternative to rationalization techniques used in CNC and carpentry formworks. The flexible mould concept is based on mass-customization of the produced panels due to the adaptability of the formwork’s shape according to the specified geometry. Using this type of formwork implies a great potential in industrial production of precast complex-shaped concrete panels.



Figure 1.1: Triangle cupola roofs, Highway service area Deitingen, 1968, Heinz Isler [Wikipedia]



Figure 1.2: Heydar Aliyev Cultural Center, Baku, Azerbaijan, 2013, Zaha Hadid [Wikipedia]

### 1.3 Earlier research

The “Flexible Mould” concept was studied by [Hughe and Schoofs \[2009\]](#) who constructed a prototype of an adjustable formwork. [Janssen \[2011\]](#) focused on a mechanical model to describe the elastic layer used in the “Flexible Mould” and determined experimentally the required time of deformation of concrete, to produce the double curved elements. Later on, [Schipper \[2015\]](#) studied the rheological properties of concrete elements produced with the re-configurable mould as well as several functional requirements for the design of curved concrete elements. [Eigenraam \[2013\]](#) simulated the mechanical behavior of the elastic layer with a digital parametric model and constructed a new prototype for the flexible mould.

Other relevant studies with the production of concrete shells have also taken place during the past years at TU Delft. [Roesbroeck \[2006\]](#) analyzed the construction of prefabricated concrete, optimizing the design and production process of shells. [Maten \[2011\]](#) investigated the application of Ultra High Performance Concrete in large span shell structures. [Troian \[2014\]](#) made a crack evaluation of double curved concrete elements using the flexible mould concept. [Witterholt \[2016\]](#) investigated the application of double curved concrete elements in a sphere shaped shell structure and analyzed via FEM software the connections between the precast concrete elements. [Kok \[2013\]](#) investigated reinforcement possibilities of elements produced with the adjustable formwork and made a feasibility study on their production process.

The present thesis is built upon the previous research projects and aims at investigating the structural applicability of concrete shells produced with the flexible formwork in real life structures.

## **1.4 Research project**

The content of this Master Thesis is presented in this section:

### **1.4.1 Problem definition:**

Double-curved concrete elements produced with the adjustable formwork, will be subjected to multiple loads during their construction and service life. As a result, tensile stresses may occur, which in case they exceed the tensile concrete strength, cracking is caused. Conventional steel reinforcing bars may be used up to small diameters due to the casting procedure, followed by the use of the adjustable formwork. Aiming at slender concrete structures consisted of shells, prestressing the elements with cables is regarded as an alternative reinforcement method. In case of no bond between the concrete and the applied prestressing steel reinforcement, brittle failure at joints location in between the concrete shells may also occur, assuming that the weakest spot in a precast concrete structure is the mortar joint. The final goal of this thesis is to check whether the prestressed panels, can be considered as structural members, so that their application is extended from architectural to structural. An investigation in construction parameters of double curved concrete elements produced with the flexible mould will also be a part of this thesis.

### **1.4.2 Research question**

Having defined the problem, the main research question of this master thesis are:

1. “What is the influence of prestressing on the load bearing capacity of precast concrete double curved elements?”

### **1.4.3 Research objectives**

1. To investigate and choose the most suitable from the various prestressing reinforcement possibilities of the double-curved concrete elements.
2. To focus on the computational modeling and analysis of the load bearing capacity of straight and curved elements under different load combinations.

### **1.4.4 Report outline**

#### **Part I Introduction and research**

Part I “Introduction to the problem - Research objectives” contains an introductory research on previous studied on the “Flexible Formwork”, as well as the problem definition, the research scope and the objectives to be answered on the current thesis.

#### **Part II Literature review**

The “Flexible Mould” concept that will be used in this project is presented first. Then, an introduction to the “Theory of shells” is given, the background of which will be used to attain knowledge on the internal load distribution in shell structures. Last, the “Design Parameters” includes an extensive literature review

on the design parameters such as reinforcement possibilities, connection detailing and load bearing capacity of concrete panels produced with the adjustable mould.

### **Part III Experimental investigation on double curved concrete elements**

Investigation on the constructability of four prestressed double curved concrete elements produced with the flexible mould is included in this part. Sand tests simulating the weight of concrete shells, can be used as indicative to reach this goal.

### **Part IV Introduction to Finite Element Modeling (FEM) with DIANA 10.1**

Straight or curved prestressed concrete elements will be designed using Computer Aided Design (CAD) techniques - RHINOCEROS5 (RHINO). The digital models of the concrete panels will be used as input for the design in finite element modeling (FEM) - DIANA10.1. Structural linear static analysis under the applied loads will be performed for several cases of simple geometrical elements. The computed results should be validated via hand calculations. Conclusions and recommendations will be included.

### **Part V Four point bending test - Brittle joint**

Two rectangular post-tensioned concrete elements will be subjected to a four-point bending test simulated with FEM. The two concrete elements are intersected with a mortar joint in-between them, its strength assumed to be brittle. CAD design and FEM analysis with DIANA10.2, will be the main output of this part. Linear and nonlinear static analyses will be performed. The computed numerical analyses results should be validated with hand calculations. Conclusions and recommendations will be included.

### **Part VI Post-tensioned concrete arch structure**

A post-tensioned arch structure will be designed in RHINO and input in DIANA10.2 for linear static analysis under the applied loads. Hand-calculations will be compared with the computed Finite Element Analyses (FEA) results. Conclusions and recommendations will be included.

### **Part VII Discussion**

General conclusions based on the obtained results from the numerical analysis and the laboratory tests will be included in the last part of the thesis, answering the main research question and giving recommendations for further research.

### **Part VIII Annex**

Hand calculations, finite element analyses results will be included in this part.

## Part II

# Literature review

## 2 Summary

An overview of the developments of the Flexible Formwork is presented in the current section. At first, the concept of deliberate deformation of concrete after casting is described. Then, the most important conclusions gathered from several researches on the development of the flexible mould are briefly described. Subsequently, the formwork members are presented in detail, in order to have a clearer view of the production process of precast panels. This will provide us with the necessary information when performing laboratory tests to investigate the applicability of elements produced with the adjustable formwork.

### 2.1 Adjustable mould concept

The production process with an adjustable mould implies that one single open mould can be re-used to manufacture several panels with different curvature. The concept of the design of the flexible mould is based on the notion of either deforming the semi-hardened cast concrete on top of the mould or by placing a thermoplastic material that can be softened when heated and hardened when cooled [Schipper, 2015]. However, the flexible mould can also be used in an alternative way, by first deforming it and then spraying concrete on top of it or casting concrete with a high shear yield strength. The first case will be analyzed in the current study, which refers to the deliberate deformation of concrete after casting [Hughe and Schoofs, 2009]. In particular the concrete is firstly placed on top of the mould in a horizontal position, and after the required setting time which depends on the concrete composition, the deformation of the concrete element takes place (see figure 2.1). It was proved that deforming after casting is essential to provide a smooth surface and equal thickness along the elements' lengths. Attention has to be paid on the correct time of deformation, so that the concrete can still be deformed to the desired shape and has also gained adequate strength and stiffness so that it does not flow out of the mould. Proper curing of the freshly cast concrete is also of great importance in order to avoid shrinkage strains that may result in cracking. Demoulding of the panels takes place after one day of hardening and is done mechanically by a crane.

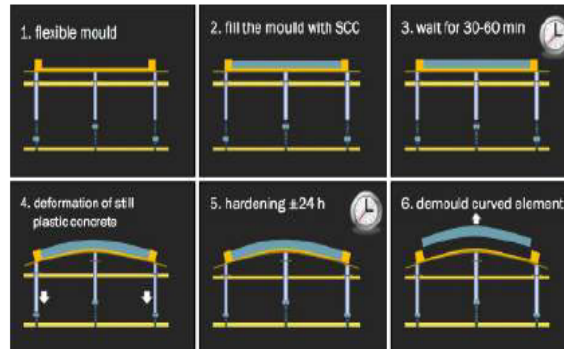


Figure 2.1: Casting procedure with the “Flexible Formwork”

## 2.2 Flexible mould’s development

It was in 1960 when Renzo Piano introduced the concept of the “Flexible Mould” or “Stampo Deformabile”. His intention was to use a master mould which would be re-configurable to produce double-curved glass-reinforced plastic facade panels for the creation of free-form pavilions. He used a scale-up model to define the shell’s geometry as input for a machine which determined the height of several points along the shell surface. These points were digitally transferred with the machine and defined the height of plungers, which were on their turn supporting a flexible mat to form the final shell’s surface. Due to lack of sufficient knowledge in the structural analysis of shell elements in that period, the idea of the adjustable mould as means of shell elements’ production was not put in practice. However, the concept of the “Stampo Deformabile” set the basis for the development of the “Flexible Formwork” used for the production of double-curved concrete elements.

Based on this innovative concept, a “Pin bed mould” was designed by Quack. It is a closed mould consisted of two square grids of pins, the entitled pin beds, placed above each other, in order to produce double curved elements with a varying thickness and curvatures. It is suitable for casting elements of very fluid concrete. The pin heights can be adjusted mechanically with the use of screw driving systems and hence a minimum distance between the pins is required for the placement of the lifting screw jacks. A flexible layer is placed on top of the bottom pin bed and on bottom of the top pin bed series, in order to form a smooth surface for the cast concrete. [Roesbroeck \[2006\]](#) conducted experimental tests on load-bearing shells using the “Pin bed mould”, and concluded that the shell’s surface is disturbed at some positions over the pin heads. In addition, the large number of pins resulted in a very expensive solution. Vulnerability issues should also be taken into consideration, since it is mentioned that one immobile pin would could cause blocking of the whole production process. Low accessibility and maintenance-repair are additional disadvantages of the “Pin bed mould”.

In order to reduce the number of pins, [Janssen \[2011\]](#) and [Schipper \[2015\]](#) designed two different alternatives for the flexible mould, the “Strip Mould” and the “Plate Mould” (see [2.2](#), [2.3](#)) for the production of double-glass fibre reinforced plastic facade elements. Both are open single-sided moulds consisting

of a rectangular grid of actuators positioned on a larger distance compared with the “Pin bed Mould”. Above the actuators, two layers of wooden strips were arranged perpendicular to each other in the first case and one wooden plate in the second case. A sealed polyether mat was placed on top of the strips / plate, forming the final shell element’s surface. [Janssen \[2011\]](#) cited in his research that since NURBS surfaces use a number of control points to represent the elements’ shape, the Strip Mould could be combined with a CAD program to obtain the digital design of the shell’s geometry in case the number of the support points of the mould is equal to the number of control points of the NURBS surfaces. It was concluded that the strips could follow the curvature of the deformed mould better than using a single wooden plate. In addition buckling of the shell’s surface was limited. However, wriggling and ponding effects above the actuators were still visible at some points of the shell surface. In addition, sealing of the polyether mat to impregnate it, resulted in a rough surface of the produced panels. The occurrence of tensile stresses at some locations above the actuators is an issue that can be addressed by tightening the actuators via strings with the bottom plate, hence introducing a counteracting compressive force.

[Hartog \[2008\]](#) studied several aspects aiming to optimization of the design and production of precast shell elements. Structural analysis, grid generation techniques, panel segmentation, edge profiling and concrete composites were the main topics in her master thesis. Among her most important conclusions was that the application of Fiber Reinforced Concrete (FRC is a suitable material for the precast technology, due to its high performance.

[Hughe and Schoofs \[2009\]](#) focused on developing the production process of double-curved concrete panels. Based on the principle of first casting the wet concrete in a horizontal position and second deforming the mould after the required setting time, it was stated that the optimum deformation time is highly interlinked with the type of concrete used. Both [Hartog \[2008\]](#) and [Hughe and Schoofs \[2009\]](#) in their research, found that the magnitude of concrete strains developing during the mould deformation depends mostly on the thickness and curvature of the shells elements.

[Maten \[2011\]](#) investigated the use of Ultra High Performance Concrete (UHPC) in large span thin shell structures. He conducted a structural analysis on spherical shells and concluded that it is an advantageous material for increasing the compression and tensile strength as well the ductility of thin curved concrete panels.

[Schipper \[2015\]](#) studied several aspects concerning the development of the flexible mould. Different prototypes for the production of single- and double-curved elements were analyzed and compared, aiming at the optimization of the production of precast concrete shells. A parametric research on the relation between numerous concrete mixtures and the imposed forced deformation by the flexible formwork is another topic analyzed in depth. In addition, he investigated the application of different reinforcement set-ups that could be efficiently used in the production of precast concrete shell panels.

[Eigenraam \[2013\]](#) constructed a new prototype of the “Strip” mould. An improved version of the elastic surface and a more accurate actuator mechanism was developed. In addition to the new experimental set-up of the flexible mould namely the “Kine-Mould” a digital parametric design was conducted in order to simulate the mechanical response of the elastic layer.

[Kok 2013] researched the application of textile glass reinforcement in double-curved concrete cladding panels. After laboratory tests, It was concluded that textile reinforced concrete showed an increase in both tensile and flexural strength compared with unreinforced concrete shells. However, the use of textile reinforcement was found to be insufficient to provide the elements with adequate tensile strength and hence it should be combined with other types of reinforcement.

[Troian 2014] studied the relation between the deformation imposed by the flexible mould and the response of concrete in a microscopic level. After testing several concrete panels produced with the flexible mould, sizes and distribution of cracks as a result of the deformation of the mould were quantified.

[Witterholt 2016] investigated the application of double-curved precast concrete elements using the “Flexible Formwork” as an alternative method for constructing an already built sphere-shaped shell structure. In his findings, it was proved that the use of precast technology is feasible but more expensive than the use of laminated wood beams and steel roof panels as in the already existing construction.

## 2.3 “Flexible Formwork”

The mechanical behavior of the “Flexible mould” is governed by the following three components, see figures [Strip mould components](#), [Strip mould cross-section](#)

1. the actuators
2. the elastic layer
3. mould or “interpolating” layer

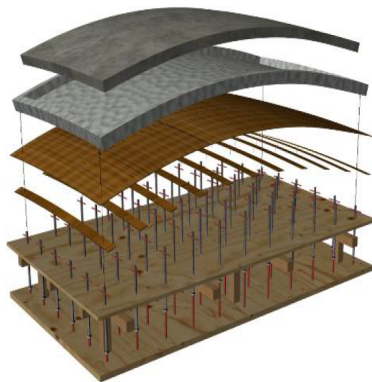


Figure 2.2: Strip mould components



Figure 2.3: Strip mould cross-section

### 2.3.1 Actuators

The actuators refer to threaded studs bolted to hollow steel tubes. The threaded studs are screwed to a wooden base plate and their fixity with the base plate

is tight but not rigid so that jamming will not take place [Eigenraam, 2013] in order to take the horizontal displacements that may occur after the concrete deformation. The bolts guarantee a certain height for the hollow steel tubes, specified by the end-user of the adjustable formwork. The height of the actuators can be determined manually or mechanically in an automated process using Computer Aided Manufacturing (CAM) techniques. The hollow steel tubes are connected to the elastic layer, and by their set height they function together with the threaded studs as support points for the elastic layer. The connection between the actuators and the elastic layer must allow rotation between them. The rectangular grid-distance of the actuators is also defined by the user, in accordance with the stiffness of the elastic layer. A contradictory aspect accompanies the number of actuators and a balanced optimization process must be determined prior to the production process so that efficiency is guaranteed. A larger number of actuators would limit the vertical deflections of the elastic layer and result in obtaining stronger curvatures and more complex shapes for the produced elements. Doubling the actuators spacing would result in increasing the deflection due to the concrete load by a factor  $2^4$  [Schipper, 2015]. However, it would increase the final cost of the end product, since the increased number of steel supports implies more steel used and a more laborious task for the user of the flexible mould. In addition, a higher risk of blocking the production process in case one actuator is damaged, increases the vulnerability of the flexible formwork and thus the final cost of the production process.

### 2.3.2 Elastic layer

The main function of the elastic layer is to approximate with the highest degree of accuracy the deformed concrete surface. Different materials, and shapes have been investigated so that the flexible layer would describe best the deformed concrete surface. Initially, [Janssen, 2011] and [Schipper, 2015] compared the mechanical behavior of a wooden strip plate model and a single wooden plate model with the first to approximate better the deformed shape of the surface. In addition, [Eigenraam, 2013] developed and studied a digital parametric model based on non-uniform rational basis spline (NURBS) surface to approximate the mechanical response of the elastic layer of the flexible mould.

Several materials have been applied to form the elastic surface on top of which the mould will be placed. [Roesbroeck, 2006] used a thermoplastic foil and a thin rubber layer to create the elastic surface. A time consuming process which required careful handling when heating the surface at high temperatures was the main disadvantage of this option. [Hughe and Schoofs, 2009] used a synthetic rubber as an intermediate layer. Aiming to a stiffer surface in order to take up the buckling stresses occurring with the use rubber surface, thin plywood panels single- or double-placed crossing each other, were also used by [Schipper, 2015] and [Janssen, 2011]. These types of elastic surface configurations are entitled as the “Plate” and “Strip” mould respectively. The “Plate” mould was proved to be unreliable for the production of double-curved concrete surfaces with small radii, since buckling occurred at the edges of the plate. In order to facilitate the production of curved surfaces with non-zero Gaussian curvature, the “Strip” mould was also investigated. Placing two layers of plywood strips perpendicular to each other, proved to be efficient for taking not only the out-of-plane bending (B) but also the in-plane stretching (S) stresses, that occur in

non-developable surfaces. Buckling effects were also minimized but inaccuracies were still present, since the strips were leaving their footprint visible in the in the surface of the final product. In addition, it is cited that sliding and tilting of the strips may result in additional inaccuracies in the production process.

The elastic layer that is used for the current research is a steel wire mesh diamond shaped, able to undertake the in-plane shear deformations that occur after the concrete deformation of the non-developable double-curved concrete surface. It is expected that a smoother final surface without the “strip footprint” effect will be made possible. To avoid ponding and wriggling effects on the concrete surface attention has to be paid on the bending stiffness of the elastic layer. Doubling the thickness of the elastic layer would result in a decrease in deflections by a factor  $2^3$  [Schipper, 2015]. A balanced design for the elastic layer, taking into account both the required low stiffness for creating small radii and buckling effects between the actuators must be done by the user prior to the production [Schipper, 2015]. If it is too high, the actuators will not be in contact with the elastic layer and additional weights must be added or pulling and tightening the elastic layer to the supports, in order to compensate for the occurring tensile forces. If the bending stiffness is too low, then ponding and waving effects will take place, creating an undesirable concrete surface of the precast panels.

### 2.3.3 Mould

The mould refers to the components that will form the shape and size of the double curved concrete elements [Kok, 2013]. Initially, the mould is supported by a horizontally leveled wooden plate in order to carry the self-weight of the freshly cast concrete. After the chosen waiting time (30-60 min for a self-compacting concrete mixture according to experimental research of [Kok, 2013], the plate is lowered and the mould together with the elastic layer beneath it, will rest on the predefined actuator heights. Flexibility must govern the mechanical behavior of the mould, so that the desired shape and size of the curved panels is achieved. Adjustments in the edges must be possible after casting the concrete and hence that the elements fit together. By doing so, the elements’ segmentation is beneficially accommodated. Since, the “Flexible Mould” is an open formwork, five components will be used to form the elements, namely the bottom horizontal face and the four vertical edges. The bottom horizontal layer should follow the curvature of the elastic layer and for that reason, a silicone sheet will be placed on top of the elastic layer so that the concrete is cast without filling-destroying the diamond shape voids of the wire mesh. The edges will acquire their required flexibility with the use of polyurethane foams [Janssen, 2011]. In order to protect the edges from the cast concrete to fill in their pores after it is cast, the foam edges will be impregnated with silicone.

## 3 Design parameters

### 3.1 Summary

In order to consider shells as load-bearing elements, their design must be done in a clear distinct way than it would be done in case of architectural shells. This section gives an overview of the design parameters necessary for the investigation on improvements in structural capacity of precast double-curved concrete panels. At first, a brief introduction to the “Theory of Shells” is presented in order to obtain knowledge on their internal stress distribution due to applied loads. Subsequently, important aspects highly correlated with the structural behavior of shells are analyzed. Selecting the appropriate concrete type for the production of panels with the flexible mould is of prime importance for the current structural design. High Performance Concrete (HPC) with high compressive yield strength and self-consolidating properties was proved to be suitable for shells produced with the adjustable formwork and thus will be used in this case. The necessity to apply reinforcement in the shell elements is noted in previous studies, and as an alternative way of reinforcing them, prestressing will be applied. Connections must be designed according to specific requirements concerning strength and stiffness, in order to guarantee structural integrity between the shell elements. Last, a panel segmentation type and the profile of edges are determined in order to achieve minimum force flow distribution along the element edges and comply with functional requirements.

### 3.2 Introduction

Several shell projects are already designed and constructed using precast concrete panels. A distinction between load-bearing or “structural” shells and non-load bearing or “architectural” shells must be made, since different design considerations must be applied in each case respectively. In particular, “architectural” shells are mainly used as roof or cladding elements for structures, improving not only their aesthetics but also their thermal and sound insulation properties. These non-load bearing elements are designed to carry their self-weight only, see figure 3.1. The temperature, wind or snow loads are transferred via a supporting structure to the main load-bearing structure, which may be a steel truss or frame. The second category of precast curved concrete panels comprises of shell elements that their design is based not only on their self-weight but also on the other load configurations aforementioned for the architectural shells, see figure 3.2. In order to be considered as structural elements, they should provide the structure with adequate strength and stiffness while their connections between them must cooperate structurally. The structural analysis of the double curved concrete elements produced with the re-configurable mould can be divided in two stages, namely the hardening and hardened stage respectively. This research will focus on the design and applicability of load-bearing double curved concrete panels produced with the “Flexible Formwork”.



Figure 3.1: Architectural shells, Heydar Aliyev Center, Baku, Azerbaijan



Figure 3.2: Structural shells, Millau Tollgate, Aveyron, France

### 3.3 Mechanics

Free-form architecture has led to the completion of architectural masterpieces, enabling the architect to integrate their personality with the structure. Ingenious architectural and engineering skills must be combined in order to materialize a complex shaped structure. Special attention must be paid in the design of shell structures in order to avoid sub-optimal designs, modified according “geometrical disturbances”. A characteristic example is the Arnhem central station. A column-free structural design on a small footprint was initially planned to be built as a shell structure but was finally modified to a concrete structure hardly approximating a shell’s structural behavior. Edge disturbances may give rise to bending moments which makes the design of a shell structure complicated.

Shells’ behavior is characterized by their property to carry loads by developing in-plane membrane forces. Also called “form resistant structures” since they obtain their strength through their shape, developing mostly in-plane stresses. Their geometry is described by the curved shape of the middle surface and the thickness of the shell. Shell surfaces can be classified according to the Gaussian curvature  $k_g = k_1 \times k_2$ , (with  $k_1, k_2$  : principal curvatures) in:

1. synclastic ( $k_g > 0$ ) or undeveloped surface
2. single curved ( $k_g = 0$ ) or developed surface
3. anticlastic ( $k_g < 0$ ) or undeveloped surface

Discriminating the surfaces in developed and undeveloped implies their difference in their structural behavior. Surfaces that cannot be developed, so they cannot deform to plain form of their middle surface, without stretching or cutting, require more external energy than the developed surfaces. Hence, undeveloped surfaces are in general more stronger and stable than the developed shells [Hoefakker, 2014](#).

In case of an idealized behavior of a shell structure, no bending moments occur, a situation which is described by the “membrane theory of shells”. However, in case of edge disturbances, bending moments develop in these regions

to compensate for the shortcomings of the “membrane theory” in these zones. Edge disturbances may be considered the following cases [Hoefakker, 2014]:

1. A boundary condition where the occurring reaction force and bending moment from the support is not aligned with the shell member in case of a hinged support and a clamped support respectively.
2. At the position of concentrated loads acting on the shell structure
3. A change in geometry between the shell members.

The “bending theory of shells” describes the shell behavior in these disturbed regions. The size of the edge disturbances is specified by their “influence length”, which is considered to be small in comparison with the “undisturbed length”, where normal forces govern the shell’s behavior.

The flexural capacity of double-curved concrete panels can be improved by applying ribs on the meridional shell surface in order to transfer the occurring transverse bending loads [Maten, 2011]. In regions where membrane forces develop, and compression forces cause instability of the shell structure, a provisional measure may be the use of ring stiffeners in the circumferential direction of the shell in order to increase the linear critical buckling load in the plane acting in the plane of the ring [Maten, 2011].

The shells that will be studied in this master thesis, will be consisted of anticlastic surfaces and specifically hyperbolic paraboloids (hyppars), consisted of curved edges. According to [Hoefakker, 2014], an analytical description of their shell surface is given by the following formula  $z = \frac{1}{2 \times r_1} \times x^2 - \frac{1}{2 \times r_2} \times y^2$ , where  $r_1, r_2$ : principal radii of curvature, see figure 3.3. The stresses acting on a curved shell are depicted in figure 3.4



Figure 3.3: Hyppar surface

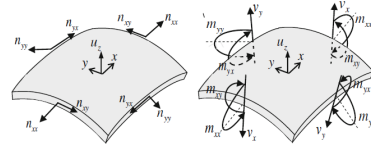


Figure 3.4: Hyppar stresses

### 3.3.1 Relations for hyppars with curved edges

The following formulas are based on the theory of shells ([Hoefakker, 2014]).

**Kinematics:** The relation between the strains ( $\varepsilon$ ) and displacements ( $u$ ) is:

$$\begin{bmatrix} \varepsilon_{xx} \\ \varepsilon_{yy} \\ \gamma_{xy} \\ k_{xx} \\ k_{yy} \\ \rho_{xy} \end{bmatrix} = \begin{bmatrix} \frac{\partial}{\partial x} & 0 & -k_x \\ 0 & \frac{\partial}{\partial y} & -k_y \\ \frac{\partial}{\partial y} & \frac{\partial}{\partial x} & -2k_{xy} \\ 0 & 0 & -\frac{\partial^2}{\partial x^2} \\ 0 & 0 & -\frac{\partial^2}{\partial y^2} \\ 0 & 0 & -2\frac{\partial^2}{\partial x \partial y} \end{bmatrix} = \begin{bmatrix} u_x \\ u_y \\ u_z \end{bmatrix}$$

with  $k_{xy} = 0$

**Constitutive:** The relation between the stresses ( $\mathbf{n}$ ) and the strains ( $\boldsymbol{\varepsilon}$ ) is:

$$\begin{bmatrix} n_{xx} \\ n_{yy} \\ n_{xy} \\ m_{xx} \\ m_{yy} \\ m_{xy} \end{bmatrix} = \begin{bmatrix} D_m & vD_m & 0 & 0 & 0 & 0 \\ vD_m & D_m & 0 & 0 & 0 & 0 \\ 0 & 0 & D_m(\frac{1-v}{2}) & 0 & 0 & 0 \\ 0 & 0 & 0 & D_b & vD_b & 0 \\ 0 & 0 & 0 & vD_b & D_b & 0 \\ 0 & 0 & 0 & 0 & 0 & D_b(\frac{1-v}{2}) \end{bmatrix} = \begin{bmatrix} \varepsilon_{xx} \\ \varepsilon_{yy} \\ \gamma_{xy} \\ m_{xx} \\ m_{yy} \\ \rho_{xy} \end{bmatrix}$$

where,  $D_m = \frac{E \times t}{1-v^2}$  : membrane rigidity and  $D_b = \frac{E \times t^3}{12 \times (1-v^2)}$ : flexural rigidity

**Equilibrium:** The relation between the stresses ( $\mathbf{n}$ ) and forces ( $\mathbf{p}$ ) is:

$$\begin{bmatrix} n_{xx} \\ n_{yy} \\ n_{xy} \\ m_{xx} \\ m_{yy} \\ m_{xy} \end{bmatrix} = \begin{bmatrix} -\frac{\partial}{\partial x} & 0 & -\frac{\partial}{\partial y} & 0 & 0 & 0 \\ 0 & -\frac{\partial}{\partial y} & -\frac{\partial}{\partial x} & 0 & 0 & 0 \\ -k_x & -k_y & -2k_{xy} & -\frac{\partial^2}{\partial x^2} & -\frac{\partial^2}{\partial y^2} & -2\frac{\partial^2}{\partial x \partial y} \end{bmatrix} = \begin{bmatrix} p_x \\ p_y \\ p_z \end{bmatrix}$$

where,  $k_x = \frac{\partial^2 z}{\partial x^2}$ ,  $k_y = \frac{\partial^2 z}{\partial y^2}$  and  $k_{xy} = \frac{\partial^2 z}{\partial x \partial y} = 0$

**In-plane-state in case of one displacement:** Introducing the Airy stress function  $\Phi$  so that:

$$n_{xx} = \frac{\partial^2 \Phi}{\partial y^2}, n_{yy} = \frac{\partial^2 \Phi}{\partial x^2}, n_{xy} = \frac{\partial^2 \Phi}{\partial x \partial y}$$

the fourth order differential equation describing the in-plane-state is derived:

$$\frac{\partial^4 \Phi}{\partial x^4} + 2 \times \frac{\partial^4 \Phi}{\partial x^2 \partial y^2} + \frac{\partial^4 \Phi}{\partial y^4} + D_m \times (1-v^2) \times (k_x \times \frac{\partial^2 u_z}{\partial y^2} - 2 \times k_{xy} \times \frac{\partial^2 u_z}{\partial x \partial y} + k_y \times \frac{\partial^2 u_z}{\partial x^2})$$

**Out-of-plane state in case of one displacement:** A second fourth order differential equation describing the out-of-plane state is derived:

$$-k_x \times \frac{\partial^2 \Phi}{\partial y^2} + 2 \times k_{xy} \times \frac{\partial^2 \Phi}{\partial x \partial y} - k_y \times \frac{\partial^2 \Phi}{\partial x^2} + D_b \times (\frac{\partial^4 u_z}{\partial x^4} + 2 \frac{\partial^4 u_z}{\partial x^2 \partial y^2} + \frac{\partial^4 u_z}{\partial y^4}) = 0$$

**Coupled state in case of one displacement:** The two fourth order differential equations describing the in-plane and out-of-plane state behavior of the shell are coupled for the unknowns  $\Phi$  and  $u_z$ . Introducing the differential operator  $\Gamma = k_x \times \frac{\partial^2}{\partial y^2} - 2 \times k_{xy} \times \frac{\partial^2}{\partial x \partial y} + k_y \times \frac{\partial^2}{\partial x^2}$  and the Laplacian operator  $\Delta = \frac{\partial^2}{\partial x^2} + \frac{\partial^2}{\partial y^2}$ , an eight order differential equation is obtained:

$$D_b \times \Delta \times \Delta \times \Delta \times \Delta \times u_z + D_m \times (1-v^2) \times \Gamma^2 \times u_z = \Delta \times \Delta \times p_z$$

The inhomogenous solution to the above equation is equal to the membrane solution. The homogeneous solution describes the edge disturbance-bending behavior of the shell.

### 3.4 Concrete type

The type of concrete is an important parameter that is correlated not only with the production of curved concrete elements with the “Flexible Formwork” but also influences the force distribution and finally the load bearing resistance of the elements. Generally, a robust concrete mixture satisfying ease of casting and good quality with regard to the final strength, stiffness and durability is of prime importance. In the case of producing concrete elements with the flexible mould concept, certain factors have to be taken into consideration in the design and composition of the concrete mixture. In particular, the applied concrete must have the required workability to be plastic when cast on the mould. It must also be characterized by a quick increase of strength so that it follows the curvature of the deformed mould surface without being cast out or accompanied with tensile cracks. In addition, mechanical compaction and vibration of the concrete is better to be avoided when using the flexible mould method (Schipper 2015, Hughe and Schoofs 2009). It is noted that a self-compacting concrete with thixotropic properties would be suitable for the adjustable formwork in order to comply with the aforementioned requirements (Schipper 2015). The final concrete elements must be characterized by homogeneous filling of the mould, a smooth and even top surface. No segregation is allowed to take place. In case of using a concrete mixture that is not self-leveling, ease of finishing must be guaranteed.

Normal strength concrete (NSC) types are not considered a really good option for use in case of application of prestressing steel reinforcement. Normal strength concrete is more prone to corrosion than high strength concrete. Since creep and relaxation losses are considered to be larger in case of normal strength concrete, it is mandatory to use high strength concrete in case of use of prestressing steel reinforcement.

In this research, High Performance Concrete (HPC) with high self-compacting properties will be used as the construction material of the double curved concrete panels. Ease of placement, compaction without segregation, early age strength and improved durability are the most important advantages of this type of concrete mixtures. HPC is mostly used in infrastructure projects, such as tunnels, bridges and high-rise buildings. Due to lower water cement ratios (0.2 – 0.45) HPC usually have higher compressive strength ( $> 40[MPa]$ ) than NSC. However, NSC can be considered as HPC when designed accordingly. In this thesis, HPC with high compression strength will be used.

Several reasons lie in for this material choice as reinforcement in this research. Roesbroeck 2006, Hartog 2008, Hughe and Schoofs 2009 note that high performance fibre reinforced concrete is a suitable material for precast shell elements. An extensive study based on the use of UHPC on large span spherical shells was conducted by Maten 2011, and a high potential as a structural material for precast concrete shells is proved. Its denser and less porous structure, in combination with the increased ductility due to the use of fibers, can result in more durable and slender structures in comparison with normally reinforced concrete (NRC) structures. This would also diminish the total weight of the structure, and the initial higher cost of UHPC may prove to be financially beneficial when compared to NRC. In addition, due to the short diffusion paths at hydration, pozzolanic reactions and other physical-chemical reactions, UHPC gains strength and high performance very rapidly (Maten 2011). Another ben-

eficial factor for using UHPC is its outstanding properties with respect to its compressive as well as tensile strength and ductility when combined with fibers. When UHPC is applied without the use of fibers, the material shows brittle behavior and limited toughness and tensile capacity, so the addition of fibers is required [Maten, 2011]. Additional aspects must be taken into account when designing with HPC in comparison with a design in NSC. Except from the higher initial cost, due to the low water cement ratio in HSC, autogenous shrinkage can develop in the hardening stage, followed by cracking if not designed properly. According to [Hughe and Schoofs, 2009] a lower water-cement ratio results in larger crack widths, depths and number of cracks. Wetting the elements' concrete surface or covering it with a cellophane foil immediately after casting the concrete, is expected to keep the concrete wet during the hardening process. A clear disadvantage when using UHPC is the non or limited existence of specific guidelines and design codes, which makes its use as structural material more complicated than using NRC. Comparing pros and cons of HPC fibre-reinforced (HPFRC), the advantages outmatch the disadvantages. Therefore, it is considered as a highly suitable material for the conducted research, and thus will be used as the main material for the production of the precast concrete panels. [Schipper, 2015] and [Hughe and Schoofs, 2009] investigated experimentally the mechanical behavior of two different mixtures made of HSC. It was proved that both mixtures can be successfully applied in order to create concrete shells with the flexible mould method. [Schipper, 2015]'s concrete mixtures resulted in shorter processing time due to a lower dosage of plasticizers in comparison with [Hughe and Schoofs, 2009] concrete composition, achieving a better control of the casting production. Therefore, the concrete mixture proposed by [Schipper, 2015] with a 28-day compressive strength of 89.3[MPa] will be an independent parameter to be used in the current thesis.

### 3.5 Reinforcement

The production of double-curved concrete shells with the adjustable mould, may result in tensile forces during the deformation of the concrete panels. The applied curvature will result in bending moments, and flexural tensile stresses may cause cracking of the concrete if the design tensile concrete strength is exceeded. In particular, deforming the elements from a horizontal shape to single- or double-curved, implies a change in Gaussian curvature. Single-curved surfaces such as cylindrical or spherical shapes are accompanied by out-of-plane bending (B) effects, while double-curved surfaces show also in-plane stretching (S) effects. According to [Schipper, 2015], tensile and compressive stresses may occur due to the bending effects during the deformation of the mould. This stage refers to the hardening stage, and is influenced by additional parameters such as the rheological and self-healing properties of the concrete as well as the time of deformation after casting the water. In the hardening stage, when the concrete is cast, plastic shrinkage may result in tensile stresses at the edges of the panels, which in their turn may result in cracking. In addition, several load combinations coming from the self-weight of the panels, uniformly distributed loads such as wind or snow may result in the development of tensile stresses in the panels, which may cause cracking of the concrete.

Several studies have been carried out with regard to the load bearing capacity of double-curved concrete elements using different reinforcement config-

urations. Traditional steel reinforcement could be used up to a rather small and limited diameter, thus a desired increase in the tensile capacity of the concrete panel is also limited. A bigger diameter that would result in a higher flexural and tensile design strength for the concrete elements cannot be used in the case of the double-curved concrete due to its higher bending stiffness, which would not allow steel bars to smoothly follow the curvature of the adjustable mould. [Janssen \[2011\]](#) studied the load bearing capacity concrete shells by using small diameter galvanized steel rods as reinforcement, and a limited increase in the load bearing capacity of the concrete elements was observed. It is also reported that traditionally reinforcing elements of high concrete strength results in a small rebar spacing, even in the case of using the minimum allowed reinforcement ratio to avoid brittle failure of the structure. The application of a very dense rebar spacing may result in improper filling of the mould [\[Schipper 2015\]](#). Therefore, it was suggested that other reinforcement methods shall be investigated. [Kok \[2013\]](#) researched and proved the feasibility of application of textile reinforcement in concrete shell elements to be used for cladding purposes in free-form buildings. [Maten \[2011\]](#) investigated the mechanical behavior of shells with positive Gaussian curvature, applying UHPC combined with fibers and proved that the buckling capacity is governing over compressive and tensile strength for the shells' load bearing resistance. However, for the dome structure that he analyzed, application of a prestressed ring at the structure's connection with the foundation was required, in order to take up the occurring thrust forces. In another study, [Witterholt \[2016\]](#) recommends the need for applying post-tension cables at the foundation of the shells structure in order to take up the large thrust forces.

For the current project, the application of fibre or textile reinforcement in combination with prestressing reinforcement will be used to reinforce the double-curved concrete panels. A reason behind this choice is the low-bending stiffness of textiles and the discontinuity of fibers, that could easily follow the curvature of the deformed mould. Single glass or polyvinyl-alcohol (PVA) fibres will be placed autonomously or in a mesh structure by stitching.

The application of fibre or textile reinforcement will have impact on several aspects related to the produced shell elements and an investigation must be carried out in order to choose the best reinforcing in the current thesis. An efficient amount of fibres are expected to enhance the ductility and reduce the plastic shrinkage of concrete. In addition, the production of Fiber Reinforced Concrete (FRC) is easier than the production of Textile Reinforced Concrete (TRC). However, their contribution to improving the tensile and flexural strength of concrete depends on the fibre orientation [Kok \[2013\]](#). In the first case, the fibers are placed randomly in the elements whereas in the second case TRC is placed in the direction of principal stresses, by either a lamination procedure or by clamping the textile reinforcement at the mould edges. [Hartog \[2008\]](#) mentions in her research that the use of fibers cannot provide the same tensile strength as would the use of traditional steel reinforcement, but at least reduce the amount of reinforcement needed. Furthermore, it is noted that TRC results in better surface qualities, since the textile fibers are not visible at the concrete surface, whereas the single ones are. Concerning cost efficiency, the application of fibres is considered cheaper than using textiles, since in the first case the placement in the concrete mixture is easier. Attention has to be paid to the positioning of the yarns in the cross-section. It is noted that deforming the panels may result

in a change of yarns' initial position [Kok, 2013]. These inaccuracies may have impact on the flexural strength of the shell elements. Furthermore, the addition of fibres into a concrete mixture results in a decrease of its workability and a maximum reinforcement ratio is allowed in order to comply with the selected production technique using the "Flexible Formwork".

### 3.5.1 Prestressing reinforcement

The application of prestressing reinforcement as an alternative way of reinforcing the double curved concrete panels produced with the adjustable formwork will be investigated in this research. Bendable shapes such as shell elements can be reinforced via post-tensioning so that more slender structures are achieved. In this way, large spans with a reduced height can be constructed, which causes a reduction of the self-weight, the forces acting on the foundation and finally the total cost. The aim is to check the possibilities for improvement of the tensile and flexural capacity of double-curved concrete elements during their service life. "Prestressing the concrete panels, will introduce compressive forces in the concrete and tensile ones in the applied prestressing steel reinforcement. By superposition of the stresses caused by the prestressing loads, the self-weight and static loads, tensile stresses at the top side of the elements are to be minimized. In order to prevent the occurrence of cracks, the occurring tensile stresses should not exceed the design tensile strength of the concrete. Compression stresses must also be limited" [J.C. Walraven, 2015]. It is also expected that prestressing the panels will introduce compression in the joints, adding the required strength and stiffness to ensure the structural integrity of the structure. In addition, the segmental design of prestressing reinforcement of a concrete shell structure requires special attention, and cannot be done in the same way as with usual prestressing techniques of rather single elements monolithically connected. The segmental connection of thin shells is done step wise.

#### Methods of prestressing

Methods of prestressing the elements can also be varied. Fully prestressing them requires that no cracks are acceptable in the Serviceability Limit State (SLS). If limited prestressing is applied, cracks are allowed to occur in SLS but then must be limited. Thus, crack width limitations are needed to be estimated too. In case of partially prestressed concrete, both reinforcing and prestressing steel is used and this may lead to a more economical solution. Since fibers are going to be used in combination with post-tension cables, the partially prestressing method will be investigated in this research.

In relevance to the methods of prestressing the elements the following ones are used nowadays:

1. Prestressing with post-tensioned steel, with bond
2. Prestressing with post-tensioned steel, without bond
3. Prestressing with pre-tensioned steel

Prestressing with pre-tensioned steel, implies the application of straight or kinked strands or wires. In this master thesis, post-tensioned steel will be used.

This is due to constructability requirements of the double curved concrete elements, hence curved tendons-cables are applied. It is expected that bonded elements will have a higher load bearing resistance than the unbonded tendons, since the concrete fails in compression before yielding of the prestressing steel (J.C. Walraven (2015)). However, in case of use of unbonded tendons, a limited concrete cover is required due to their good protection against corrosion. The advantageous result of using unbonded tendons would be a smaller thickness of the double-curved concrete elements.

Taking into account the aforementioned, prestressing with unbonded post-tensioning steel will be the method of prestressing in the current case study.

### 3.6 Panel segmentation

Panelization is the technique used to segment a surface into elements (Janssen, 2011). The structural division of concrete's surface into segments is a critical aspect for the precast concrete shells, since different fields are highly interwoven with the selected panel segmentation. The dimensions of the curved concrete elements are defined by production and transport limitations. In particular, production and erection of precast concrete elements has to be done in the least labor intensive and fastest way. This can be achieved by minimizing the number of connections, which is obviously influenced by the chosen segmentation method. Furthermore, optimizing the panel pattern so that form follows force will improve the structural efficiency of the connections of concrete shells.

There are two basic grid types, namely the structured and the unstructured grid. In the first type, the grid nodes are determined based on a general mathematical rule. This type of grid is more suitable for simple geometries. In the second type, the connections of the grids differs from point to point and no analytical rule defines the position of the grid nodes. This type of grids is usually preferred for complex shapes of structures. There are also other types of grids, the entitled "hybrid" or "composite" grids, which combine both the structured and unstructured grids, so that an irregular geometry of the structure can be segmented in a more efficient way.

(Rippman and Block (2013) analyzed the influence of panel segmentation on force-flow distribution along the shell elements. Two cases were analyzed (figures: 3.5, 3.6):

1. A horizontal hexagonal pattern,
2. A 90 degree rotation of an hexagonal pattern

In order to follow the aforementioned principle that form follows force and to align the forces with the faces of a pattern an hexagonal pattern is rotated under 90 degrees and compared with a horizontal hexagonal pattern. In particular in the second case, a brick pattern is mapped over a shell surface after several iterations of dynamic relaxation. Combined with Finite Element Modeling (FEM), pattern lines related with a specific vector are rotated around an angle of 90 degrees. Several geometrical alterations are repeated until the maximum alignment of the elements with the force flow is achieved. It was expected that between a 90 degree rotation pattern and an hexagonal pattern, the distribution of force would be better when the hexagonal pattern is rotated under an angle of 90 degrees, since in this case the faces of the brick would be aligned

with the force flow . However, it was proved after FEM analysis, that the force distribution was far better in the first case of the horizontal hexagonal pattern.

Therefore, the horizontal hexagonal pattern will be used for the structural division of the double curved surfaces in the current project aiming to minimize the forces acting on the segmented shells. By doing so, the separation lines are aligned perpendicular to the force flow, hence preventing or minimizing the development of shear forces in the connections [Luitse, 2016].

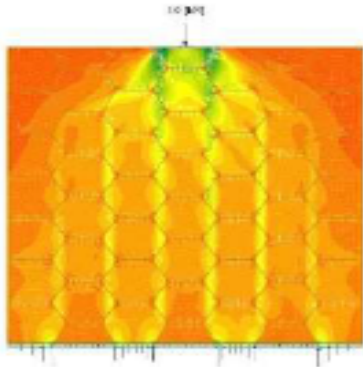


Figure 3.5: Force flow - Horizontal hexagonal pattern

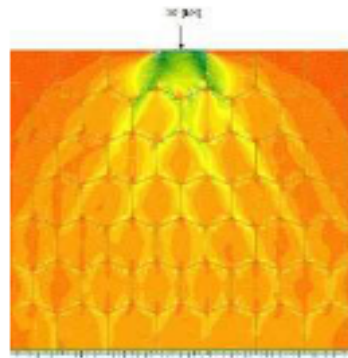


Figure 3.6: Force flow - Rotated hexagonal pattern

### 3.7 Connections

In prefabricated concrete structures the strength, stiffness and location of the connections are of utmost important for the structural design. Joint locations or areas close to joints are considered to be the weakest points within a prefabricated concrete shell structure. Therefore, the place and type of connections have to be know prior i in order to perform a sound structural analysis and ensure the structural integrity of the designed shell. Several joint configurations are used nowadays, the most important of which are the following:

1. the wet connection
2. the bolted connection
3. the post-tensioned connection
4. the welded connection
5. the glued connection
6. the fiber connection

The type of the connection to be used, differs for each individual shell structure. Not only the geometry of the structure but also the type of concrete are crucial factors that must be considered for a proper joint design. When using the precast technology the most suitable connection types are the wet connection, the bolted connection and the post-tensioned connection. [Hartog, 2008]

investigated the influence of a wet, a bolted and a glued connection on the force transfer in a shell structure. [Witterholt 2016](#) studied the relation between the stiffness of a monolithic connection with the occurring buckling loads and displacements of a shell structure. [Maten 2011](#) also compared the different types of connections that can be used for precast concrete shells. In his research, notes that the prestressing connection via local or continuous post-tensioning seems to have high potential in combination with UHPC in case there are high requirements for tensile strength. [Janssen 2011](#) also refers to the need for prestressing connections with post-tensioning cables and bolts in order to achieve structural cooperation between the concrete panels. It is cited that the influence of the connections to the load-bearing capacity of the concrete shells has to be investigated.

In this thesis the post-tensioned connection with cables will be investigated. The application of prestress in the connection, means applying tension in the cables and compression in the joints. This type of configuration is expected to make the joints cooperate structurally with each other and also provide them with the required liquid tightness. The joints will be modeled and designed in FEM so that a structural analysis is to be performed, the results of which will be evaluated in order to check the structural joint capacities. The connections between the elements will be fixed and hence they will be subjected to normal, shear, bending and torsion. It is expected that the normal forces will be governing for this type of connection.

There are two types of post-tensioned connections, the design of which was researched by [Maten 2011](#). The first type is the continuous post-tensioned connection, in which the tendons are put into continuous ducts passing through different hardened concrete elements and then fixed at the anchors. This type of connection is characterized by its strength and durability however the elements may need to be thickened so that the ducts fit. The second type of connection is the local post-tensioned connection, in which the tendons are placed through ducts that are close to the edges of the shell elements. The advantage of this type is the easy and fast assembly procedure in comparison with the first type. However, the element thickness must be increased near the edges where the ducts pass through, resulting in a varying thickness of the shell elements. It is also stated that in case of higher strength demands, the use of the continuous post-tensioned connection is preferred than the local post-tensioned connection [Maten, 2011](#).

Taking into account that the open “Flexible Formwork” production of double-curved concrete elements with a varying thickness is more laborious, a modification of the mould with a closed one, may be an option to tackle this issue. However, this research will focus on production of concrete elements with the open mould configuration. Taking into account the aforementioned, the option of continuous post-tensioning will be used in this research for connecting the concrete shell elements together, see [3.7](#)

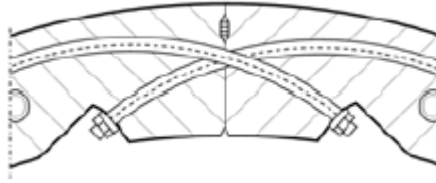


Figure 3.7: Continuous post-tensioning connection - [Maten \[2011\]](#)

### 3.8 Edge profiling

The angles between the elements are interlinked with the chosen segmentation method and the used formwork type. [Hartog \[2008\]](#) conducted a detailed analysis of different edge profiles in concrete shells. Minimum and maximum values of angles in- and out-of-plane of the elements are defined by transport requirements. It is cited that sharper angles between the elements make them more susceptible to damages during transportation and a minimum angle of 45 degrees must be guaranteed. A 90 degree angle in the element's cross-section and between the elements in their plane is considered to be the best choice for protecting the concrete shells from damage during transportation.

The formation of the in-plane angles is defined by the chosen hexagonal pattern mentioned above. For the out of plane angles, so the angles in the cross-section, different ways are proposed. The perpendicular slicing method will be used in this thesis, which implies that the cross-section edges are formed under an angle of 90 degrees to the surface of the element. In this way, the produced shell elements are less fragile and the least laborious way of production with the adjustable formwork is achieved.

### 3.9 Other geometrical aspects

As already mentioned, the element size and shape are depending on several parameters such as the chosen production method and transportation requirements. In this research, the maximum length and width of the segmented panels is determined by the available flexible formwork. The  $1.0 \times 1.0$  m mould surface will set a maximum surface for the produced shell elements of  $0.8 \times 0.8$  m, taking into account the dimensions of the foam edges. It is noted that the size of the elements influences the maximum slope of the flexible mould. The larger the element the larger the curvature that can be achieved for each panel [\[Schipper, 2015\]](#). Up till now, elements of  $0.8 \times 0.4$  m have been successfully produced with the adjustable formwork. In this research, the produced panels will have a prismatic square shape of  $0.8 \times 0.8$  m.

Regarding the radii of curvature, it is noted that they are inversely proportional to the resulting bending moments. It was experimentally proved that an increased curvature resulted in a bigger number of cracks for a certain element thickness [\[Troian, 2014\]](#). The maximum radius of curvature produced with the flexible mould is 1.5m. Concerning the thickness of the elements, it is highly interlinked with the reciprocal of the selected radius of curvature and both influence the crack pattern that may occur. Assuming a constant slope of the strain across the panels' cross-section, it was proved that increasing the thick-

ness of the panels resulted in a linear increase of strains for slopes smaller than 30 degrees (Schipper [2015], Hughe and Schoofs [2009]). In addition, an increase in the elements' thickness will possibly result in an increase of the occurring bending moments during the deformation of the mould. A higher reinforcement percentage will also be needed in this case. Therefore, it is interesting to vary the thickness of the panels according to the selected curvature of the mould, and investigate its influence on the capacity of the produced elements. In this research the shells' element thickness will be set to be equal to values ranging between 50–55 mm as a choice of the author.

A successful production of shells using the adjustable formwork implies that the produced elements will have the initial intended shape and size. Deviations must be kept to the smallest possible value. In order to check the accuracy of the production method, Quack refers to laser measurement techniques.

## Part III

# Experimental investigation on double curved concrete elements

## 4 Summary

In order to check the constructability and applicability of post-tensioned double-curved concrete elements via the flexible mould on the three ongoing projects in India and Kuwait, an experimental investigation took place at the TU-Delft laboratories in February 2017. Steel wire mesh was used as interpolating layer between the concrete and the actuators. Four concrete shells prestressed with post-tensioning steel were to be constructed using the flexible formwork. Sand tests simulating the weight of a designed concrete shell, were performed aiming at finding the influence of the number of actuators as well as the stiffness of the newly applied flexible layer on its resulting deflections.

### 4.1 Design of the shells geometry

The design of the shells' geometry was done in Rhinoceros 5. An initial surface that would include the four concrete shells, was modeled by four non uniform rational B-splines (NURBS). In order to obtain a strong curvature of the elements that could be created with the flexible mould, a minimum radius of curvature of 1m was prescribed for the designed surface, with the smallest radius of curvature to be found 1.125m. The length of the edge curves should be restricted to the maximum length allowed to be produced with the flexible mould. Hence, after taking into account the dimensions of the flexible foam edges, the maximum  $1.0 \times 1.0$ m surface of the mould resulted in approximately  $0.8 \times 0.8$ m elements with a thickness of 50mm. The shell thickness was selected based on previous experimental data for double-curved concrete elements produced with the flexible formwork. Having defined the geometry of the surface, it was split vertically and horizontally in 4 elements. Subsequently the 4 surfaces were used to create the respective four shell elements. The edge curves that form the base of the shell structure are horizontal, while the edge curves that are between the top and bottom shells, are formed perpendicular to the shells' surface. The in-plane angles between the surface edge curves and the out-of-plane angles of the shells' cross section are approximately 90 degrees, fulfilling the angle limitation between 45 and 135 degrees, see figure [4.1](#).

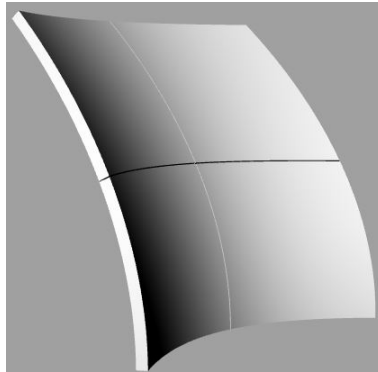


Figure 4.1: Double curved concrete elements geometry - RHINO

#### 4.1.1 Shells' coordinates

Prior to casting the concrete elements on the flexible mould, the coordinates of the surface to be cast on the mould, must be obtained. In order to do so, using Grasshopper, a plug-in tool for RHINO, two different models based on the grid distance between the actuators were created. Hence, two rectangular patterns were analyzed, with the spacings between the actuators set at 240 mm and at 120 mm respectively. Firstly, the elements were rotated from vertical to horizontal position, with the surface to be cast being the bottom surface of the rotated shell. Secondly, bounding boxes with a minimum volume were created so as to contain each of the four horizontally placed double-curved elements. The four bounding boxes are used as an additional check of the maximum length dimensions of the shells on the XY plane, as well as a way to symmetrically place the shells in a horizontal position with regard to the grid pattern of the actuators.

Initially, the distance between the actuators was set at 240 mm. This choice was made according to the available set up of the adjustable formwork at the TU Delft laboratory. A rectangular grid pattern was created in Grasshopper, simulating the 5x5 actuators of the physical model. The x,y coordinates of the actuators were calculated based on a reference point in Rhino determined by the user. Thereafter, the bottom surfaces of the double-curved elements were extended to such a length, that the area of the rectangular pattern of the actuators would be smaller than the area of the extended surfaces. Subsequently, the z coordinates of the surface to be cast on the mould were defined as the intersection of the projected lines from the grid pattern to the extended shell's inner surface, see figures, [4.2](#), [4.3](#), [4.4](#).



height was fixed to the calculated Grasshopper height, using nuts. It must be noted that the actuators were set a “bit” loose at their connections with the bottom wooden mould surface, so as to allow their rotation and hence being able to take up the imposed shear deformation after applying the elements’ self-weight. A steel wire diamond shaped mesh acting as the elastic layer, was placed and “fixed” on top of the actuators, also allowing rotation between the wire mesh and the actuators in order to take up the imposed shear deformations from the applied shell’s self-weight. Thereafter, a silicone sheet forming the bottom surface of the mould, was placed on top of the steel wire mesh, aiming at producing a smooth bottom shell surface following the curvature of the elastic layer beneath it. Two strips of polyurethane foams were stuck on top of the silicone layer, in order to form the four edges of the double curved element. Subsequently, the sand test was performed by pouring the required amount of sand to simulate the concrete shell element that would be cast in another step, see figures [4.5](#),[4.6](#).



Figure 4.5: Sand test on 240mm grid distance



Figure 4.6: Deflection of the elastic layer on 240mm grid distance

#### 4.2.2 120mm grid test

The distance between the actuators decreased to half in comparison with the previous experiment and a 120[mm]grid spacing was investigated. This was this only parameter changed, see figures [4.7](#) [4.8](#).



Figure 4.7: Sand test on 120mm grid distance



Figure 4.8: Deflection of the elastic layer on 120mm grid distance

### **4.3 Results**

Qualitative results were obtained from both experimental set ups.

#### **4.3.1 240mm grid distance**

1. The steel wire mesh did not follow the desired-designed shape of the elements but wriggling and ponding effects were observed along its surface.
2. Several actuators were not in contact with the elastic layer as they should, while others were acting high compression forces on the elastic layer leading to punching shear effects on its surface.

#### **4.3.2 120mm grid distance**

1. The steel wire mesh did follow the desired curvature of the CAD designed shell elements. The surface of the elastic layer seemed to comply and resemble with the CAD designed shell surface.
2. Wriggling and ponding effects were minimized.
3. All actuators were in contact with the steel wire mesh. A considerable reduction in magnitude of the compressive forces acting from the actuators to the elastic layer was observed in this case.

## **4.4 Conclusions**

### **4.4.1 240mm grid distance**

1. The aim for flexibility based on a “large” actuator distance, resulted in large deformations of the flexible layer.
2. The imposed strong curvature in combination with the material stiffness of the elastic layer and the available number of actuators, is considered to be the underlying cause for the occurring high buckling forces.

### **4.4.2 120mm grid distance**

1. Doubling the number of actuators and decreasing the grid distance, implied higher costs and increased labour time in comparison with the first experimental set up.
2. The increase of the number of actuators acting as support points for the elastic layer, can be recognized as an effective way to reduce the vertical deflections of the steel wire mesh and achieve to a satisfying degree, the required shape of the CAD designed shell surface.

## **4.5 Test limitations**

Having obtained the x,y coordinates of the four shell elements from Grasshopper and Rhino, they were printed on an A4 size paper. This paper would be used as an image to be digitally magnified and projected from a beamer to the mould surface, in order to define the exact position of the four edges of the shell elements. The positioning of the beamer at the required altitude above the mould surface was not an easy task, but in the end, it was doable. However the magnified digital image projected on the mould, was not as accurate as intended. This aspect was very important for the process of casting concrete as a next step for the laboratory tests. Having not managed to find the way to overcome the problem of the exact position of the edges for the double curved elements and taking into account lack of time and experience, it was decided not to proceed with the creation of the four shell elements as planned.

## 4.6 Recommendations

1. Instead of increasing the number of actuators, thus decreasing the grid distance between them, a different type of the steel wire mesh could be used as the elastic layer for the adjustable formwork. Aiming for the creation of strong radii of curvature of 1m for the shell elements, could be also done with an increased stiffness of the steel wire mesh. Therefore the number of actuators required to achieve the desired shell surface could be minimized. A cost and quality trade-off between the new type of the elastic layer and the minimum number of actuators required to form the shells' surface, could result in the most effective choice for optimization of the flexible layer.
2. A different process to project the CAD designed elements on the mould surface has to be found in order to produce accurately the intended shape of the shell elements. A way to overcome this issue could be the use of a different beamer that could project without distortions the shells' geometry on the horizontal surface of the mould.

## Part IV

# Modeling straight and curved prestressed concrete beams in DIANA10.1

## 5 Summary

This chapter presents an introduction to Finite Element Analysis (FEA) via DIANA 10.1. Although the geometry of concrete shells is considered to be rather complex, an initial Finite Element Modeling (FEM) of two dimensional elements (2D) of simpler geometrical shapes, was considered to be the first step in this stage. As a next step, taking into account aspects concerning 2D elements, the models geometry will be expanded to three dimensional (3D). In addition, the influence of a joint in between two elements as well as of the cross-section shape on the deflections and stress field, will also be analyzed under linear structural analyses of single-curved geometrical shapes.

### 5.1 Physical problem

A simply supported concrete beam (figure 5.1), the material and geometrical properties of which are presented in tables 5.1 5.2, is loaded by the concrete-self weight  $q_{sw}$ , a uniformly downward distributed  $q_{UDL} = 1000 \text{ N/m}$  applied at beam's top side and a downward point load  $P_{Point} = 1000 \text{ N}$  acting at midspan of the elements' top side (or at quarter lengths of the beam), with the loading sequence shown in table 5.5. One prestressing steel reinforcing bar (see table 5.3) fully bonded to the concrete, will be tensioned with a force  $P = 1000 \text{ N}$  from the anchors located at both beam's ends. The values of the applied loads are a random choice of the author. A linear static analysis was performed with DIANA10.1 for all the investigated cases.

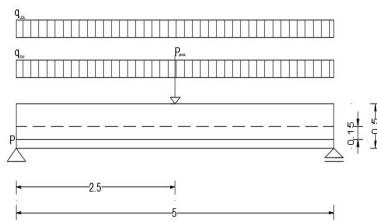


Figure 5.1: Loads and boundary conditions - Case 7 - DIANA 10.1

Length [m]	5
Height h [m]	0.5
Width b [m]	0.5
Concrete cross-section area $A_c [m^2]$	0.25
Second moment of area $I_c [m^4]$	5.208e-3
Elastic section modulus $W_c [m^3]$	0.02083

Table 5.1: Concrete element geometrical properties - Simple shape models

Concrete type	C45/55
Concrete Young's modulus of elasticity $E_c [N/m^2]$	36e+09
Concrete specific weight $\rho_c [KN/m^3]$	24
Concrete material factor $\gamma_c$	1.5
Poisson's ratio $\nu$	0.2

Table 5.2: Concrete material properties - Simple shape models

Prestressing steel type	Y1860C
Prestressing steel modulus of elasticity $E_P [MPa]$	205000
Prestressing steel material factor $\gamma_s$	1.1
Characteristic tensile strength $f_{pk} [MPa]$	1860
Area of prestressing steel $[m^2]$	10e-04

Table 5.3: Prestressing steel material and geometrical properties - Simple shape models

Steel plate modulus of elasticity $E_S [MPa]$	210000
Steel material factor $\gamma_s$	1.15
Characteristic tensile strength $f_{yk} [MPa]$	500
Steel plate length $l_{pl} [m]$	0.1
Steel plate height $h_{pl} [m]$	0.02
Steel specific weight $\rho_s [KN/m^3]$	7.85
Steel plate cross-section area $A_{s,pl} [m^2]$	2e-03
Poisson's ration $\nu$	0.3

Table 5.4: - Simple shape models

LC1	Concrete self weight	SW
LC2	Uniformly distributed load	QUDL
LC3	Point load	$P_{Point}$
LC4	Prestressing steel forces	P
LC5	Total	SW+ QUDL+ $P_{Point}$ + P

Table 5.5: Load combinations - Simple shape models

## 5.2 Model parameters

First, the geometry of the models was designed in DIANA10.1, see [A](#). Two dimensional rectangular models (Cases 1-6) were created. The influence of prestressing steel reinforcement on the deflection and stress field was analyzed and compared with the case of an unreinforced concrete beam. The tendon profile was an investigated parameter, therefore two cases of tendon profiles were selected. First, a straight tendon profile is anchored either at the centroidal axis (c.a) of the beam or at a distance  $e_p = 0.15$  m below the c.a. Subsequently, a curved tendon profile anchored at c.a with a drupe  $f = e_p = 0.15$  m was investigated. The way of modeling the prestressing loads was also a variable parameter. The prestressing loads were applied either by two compression forces acting on the concrete elements' sides without including the physical and geometrical properties of the tendon, or by applied stresses on the prestressing steel defined by its material and geometrical data, when pre-processing the model in DIANA10.1 For the aforementioned models (Cases 1-6), hand calculations were performed with regard to the midspan element stresses at top and bottom fiber level of the beam element in order to validate the FEA results.

As an additional model, Case 7 includes a refined way of modeling concentrated loads in a rectangular shaped concrete element. In this case, at the positions of concentrated loading, i.e. at supports, anchors and downward forces location at element's top side, steel plates were added in order to spread the local loads over a certain area of the steel plates before acting on the concrete element. Furthermore, an extra model was created in Case 14 analogous to Case 1, but with two downward point loads acting at quarter lengths  $\frac{l}{4} = 1.25$  m on the elements' top side, as a step towards modeling a 4-point bending test.

The influence of curvature of the concrete element's top and bottom side on the deflection and stress field was the new input parameter to be investigated in the linear static analyses performed. Two types of concrete elements were created for this purpose. As a first type, curved top and bottom sides with a curvature of  $\kappa = 0.032 \text{ m}^{-1}$  were now forming the top and bottom faces of the concrete elements (Cases 8-10), while the side edges were designed vertical as in the previous models. The second type was similar to the first type, having curved top and bottom sides, but the angles between the side edges with the top and bottom ones were now set to be forming right angles. All these models were set up to include the material and geometrical properties of the prestressing steel reinforcement anchored either at beam's centroidal axis (c.a) or at an eccentric position  $e_p = 0.15$  m from the c.a. In all these cases (8-13), the prestressing steel followed the same curvature with the concrete elements' top and bottom sides.

For further analyses, Cases 15-20 were created in order to investigate the influence of the number of concrete elements on the deflection and stress field. In particular, the previously single shaped concrete element geometries were divided in two parts, each having a length equal to half of the single ones. The tendon profiles were not split as was done with the concrete elements, and continuous prestressing was applied in these cases too. In the following models (Cases 21-26), the initial models consisting of rectangular or curved element shapes were split in two larger in length elements representing the concrete elements, and in one smaller element, simulating a 1cm joint in between them. The three elements are monolithically connected to each other and assumed to

have the same material properties.

The next parameter investigated in the models (Case 27-37) was the inclusion of a structural interface at the sides of the smaller element, the geometry of which was created previously (Cases 21-26). In particular, the 1 cm joint between the larger concrete elements was not connected rigidly to them, but with an interface element, specifying the relation between the normal and tangential tractions relative to normal and tangential relative displacements. This relation is specified by the elastic and the tangential stiffness modulus. Two types of interface stiffnesses were investigated. In Cases 27-32, a value of elastic stiffness  $k_n = 36 \times 10^{11} N/m^3$  and a decreased value of shear stiffness modulus  $k_t = 18 \times 10^{11} N/m^3$  were applied. In Cases 33-37, an increased value for both normal  $k_n = 36 \times 10^{14} N/m^3$  and shear stiffness modulus  $k_t = 36 \times 10^{14} N/m^3$  was applied. The interface stiffness properties were defined by the prescribed-suggested values in DIANA10.1 manual. Varying the stiffness of the interface is aiming at simulating a joint having different stiffness from its neighboring concrete elements.

Having obtained the results from linear static analyses for these models (Cases 1-37), a next step was the creation of the elements' geometry with a CAD software - RHINOCEROS 5 and subsequently imported in DIANA10.1 environment (Cases 38 to 52). The aim for this investigation was to verify if the imported CAD geometries in DIANA10.1 would produce the same structural analysis results as with the cases that their geometry was set-up in DIANA10.1. Three dimensional models (3D) were also created (Cases 41-52) for gaining insight in the more complex solid elements and their occurring three spread of internal loads.

### 5.3 Hand calculations

The deflection of a beam element under a uniformly distributed load  $q$  and a point load  $P$  applied in the middle of the top face of the beam, was calculated via the following formulas:

$$\delta_{uni} = \frac{5}{384} \times \frac{q \times l^4}{E \times I} \quad (5.1)$$

$$\delta_{point} = \frac{P \times l^3}{48 \times E \times I} \quad (5.2)$$

The total midspan deflection is calculated as the sum of the displacements occurring from the applied loads according to:

$$\delta_{tot} = \delta_{SW} + \delta_{UDL} + \delta_{Point} + \delta_P \quad (5.3)$$

The bending moments of a beam elements due to a uniformly distributed load and a point load applied in the middle of its top face, were calculated via the following formulas:

$$M_{uni} = \frac{q \times l^2}{8} \quad (5.4)$$

$$M_{Point} = \frac{P \times l}{4} \quad (5.5)$$

The absolute values of the resulting stresses at top and bottom fiber of the beam element are calculated as:

$$\sigma_c^{load} = \frac{M}{w_c}$$

Based on the engineering model [J.C. Walraven \[2015\]](#), in case of a curved tendon profile, i.e assuming a constant curvature pressure  $q_p$  along the tendon, a bending moment occurs equal to:

$$M_{q_p} = \frac{q_p \times l^2}{8} \quad (5.6)$$

Assuming a parabolic tendon profile, the curvature pressure is equal to:

$$q_p = \frac{P}{R} = \frac{8 \times P \times f}{l^2} \quad (5.7)$$

Where f: drape of tendon, R: radius of curvature

Hence, the resulting bending moment due to curvature pressure is:

$$M_{q_p} = P \times f \quad (5.8)$$

Eccentricity  $e_p$  of the linear tendon profile was set to be equal to the drape f of the curved tendon for ease of verification:  $e_p = f$

Assuming a parabolic tendon profile, the curvature of the curved tendon is calculated as:

$$k = \frac{1}{R} = \frac{1}{\frac{l^2}{8 \times f}} \quad (5.9)$$

The hand calculations are presented in Annex [A](#)

## 5.4 Finite element modeling (FEM) - Initial models

The models were created by two dimensional (2D) plane stress elements, or literally speaking as  $(2 + \frac{1}{2})D$  elements and three dimensional (3D) solid elements. The 2D elements were modeled in a flat plane (here denoted as XY) including their width of their cross section in their out-of-plane direction (Z).

### 5.4.1 Element type and mesh - 2D

Between a plane strain and a plane stress model, based on the finite and limited length of the investigated beam, a plane stress is chosen for the current modeling of the concrete elements. According to DIANA10.1 manual, an eight node quadrilateral isoparametric plane stress element, namely the CQ16M (figures [5.2](#), [5.3](#)) based on quadratic interpolation and Gauss integration scheme, will be used in this type of analysis. A default 2 x 2 or alternatively a 3 x 3 integration scheme is the basis for this type of elements. Quadratic interpolation was selected instead of linear, so that a more refined analysis will be performed in terms of the deflection and stress field components.

A regular plane stress element must fulfill the following requirements:

1. the coordinates of the element nodes must be in one flat plane

2. the thickness - width must be small in relation to the dimensions in the plane of the element
3. loading must act in the plane of the element
4. the stress components perpendicular to the face are zero;  $\sigma_{zz} = 0$
5. no bending out-of-plane of the structure can be applied

The strain  $\epsilon_{xx}$  varies linearly in x direction and quadratically in y direction, while  $\epsilon_{yy}$  varies linearly in y direction and quadratically in x direction. The shear strain varies quadratically in both x and y directions.

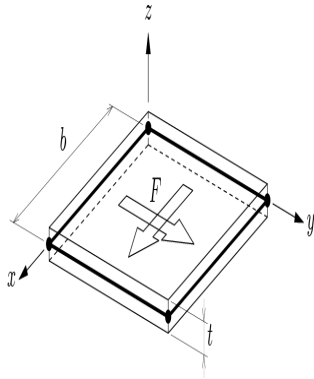


Figure 5.2: Plane stress element

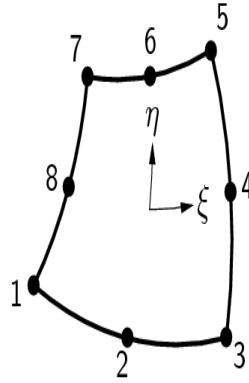


Figure 5.3: Element CQ16M - concrete element

According to [Hendriks \[2016\]](#) the mesh element size is limited to a maximum value in order to obtain a smooth transition of stresses from one element to the other and avoid “snap-back” behavior in the stress - strain relationship:

$$\max(\text{element}; \text{size}) \leq \min\left(\frac{l}{50}, \frac{b}{6}\right) \quad (5.10)$$

The minimum element size is determined by the increasing calculation time and cost while decreasing the element size. For the current analysis, a mesh element size of  $0.05[m]$  was chosen, so that a series of 10 elements are formed over the height of the elements.

#### 5.4.2 Element type and mesh - 3D

Solid elements were used for modeling the three dimensional elements (3D). According to DIANA10.1 manual, these elements may produce inaccurate results and should be applied only when other elements are unsuitable. With the aim at analyzing the three dimensional spread of forces within a structure taking into account the geometry of an arch structure consisted of shell elements as a next step in this thesis, three dimensional modeling (3D) was the final choice. Two types of solids were used for modeling the concrete, namely the CHX60 20-node brick element (figure [5.4](#)) and the CTP45 15-node wedge element (figure [5.5](#)).

- For the CHX60 brick element the strain  $\epsilon_{xx}$  and stress  $\sigma_{xx}$  vary linearly in x direction and quadratically in y and z direction. The strain  $\epsilon_{yy}$  and stress  $\sigma_{yy}$  vary linearly in y direction and quadratically in x and z direction. The strain  $\epsilon_{zz}$  and stress  $\sigma_{zz}$  vary linearly in z direction and quadratically in y and z direction. A  $3 \times 3$  integration scheme was selected by default.
- For the CTP45 wedge element, the strains and stresses vary linearly in x, y and z direction. A four-point integration scheme was selected in  $\xi$  and  $\eta$  direction by default. A 2-point integration scheme was applied for the  $\zeta$  direction.

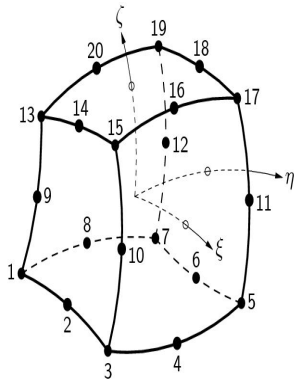


Figure 5.4: Solid element - Brick CHX60

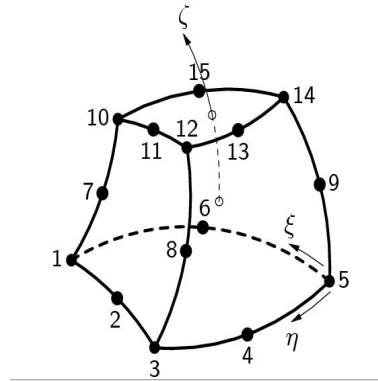


Figure 5.5: Solid element - Wedge CTP45

### 5.4.3 Prestressing steel reinforcement

Embedded steel reinforcement fully bonded to the mother elements was used in the models with inputted material and geometrical properties of the prestressing steel. According to DIANA10.1 manual, embedding reinforcement in concrete, implies perfect bond between steel and concrete and the steel strains in the reinforcement in that case, are computed from the displacement field of the mother concrete elements.

For the input of location of the reinforcing steel, DIANA10.1 divides the total length of the reinforcement in particles and computes the resulting steel stresses and strains along its length. The position of the particles in the model are defined by location points, see figures [5.6](#) [5.7](#).

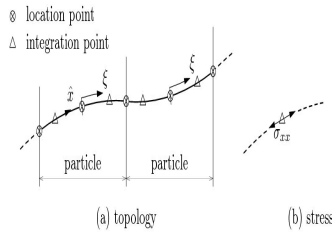


Figure 5.6: Steel reinforcement location input

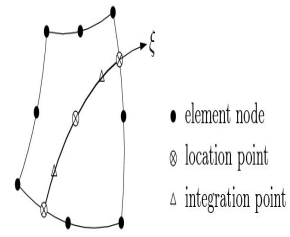


Figure 5.7: Steel reinforcement in plane stress element

#### 5.4.4 Structural interface elements

According to DIANA 10.1 manual, “the structural interface elements describe the interface behavior in terms of relation between the normal and shear tractions and the normal and shear relative displacements across the interface. One of the typical applications for structural interface elements are joints”. The following suggested rules from DIANA10.1 were applied for the interface stiffnesses in Cases 27-32:

1. Normal stiffness modulus:  $k_n = \frac{E}{l_{fr}} = 36 \times 10^{11} N/m^2/m$
2. Shear stiffness modulus:  $k_s = k_t = \frac{E}{2 \times l_{fr}} = 18 \times 10^{11} N/m^2/m$

For Cases 33-37 with an increased stiffness in both normal and shear direction, the stiffness moduli are calculated as:

1. Normal stiffness modulus:  $k_n = \frac{E_c \times 1000}{l_{cont.element}} = 36 \times 10^{14} N/m^2/m$
2. Shear stiffness modulus:  $k_s = k_t \approx k_n = 36 \times 10^{14} N/m^2/m$

## 5.5 Linear static analysis

### 5.5.1 Introduction

In the subsections below some results will be highlighted as being representative of the performed analyses. The influence of the model parameters defined in [5.2](#) on the deflection and stress field will be the main output of the current investigation.

## 5.6 Conclusions

### 5.6.1 Influence of tendon's position

Inputting the tendon at an eccentricity 0.15 m below the centroidal axis results in a decrease of the element's deflections compared with the case of centrally prestressed concrete model. Cases 3 and 5 are presented in figures [5.8](#) and [5.9](#) respectively. The beneficial influence of eccentric prestressing on the element's deflection is proved when comparing figures [5.10](#) with [5.11](#) and [5.12](#) and [5.13](#).



Figure 5.8: Loads and boundary conditions - Case 3



Figure 5.9: Loads and boundary conditions - Case 5

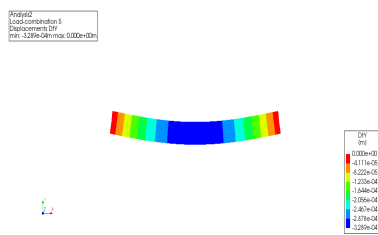


Figure 5.10: Deflection DtY - Case 3

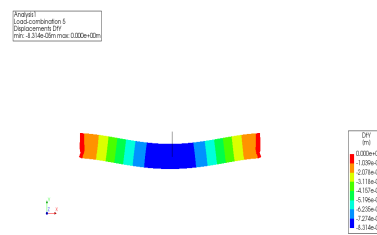


Figure 5.11: Deflection DtY - Case 5

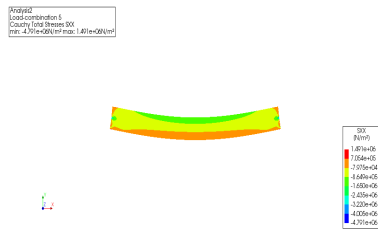


Figure 5.12: Element stresses SXX - LC5 - Case 3

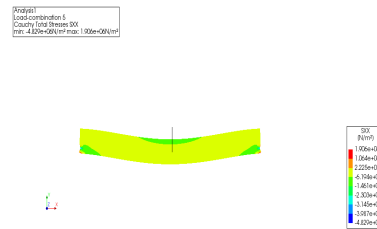


Figure 5.13: Element stresses SXX - LC5 - Case 5

### 5.6.2 Influence of steel plates

Stress concentrations at positions of concentrated loads, could be reduced by inserting steel plates  $0.02 \times 0.1$  m, see figures [5.14](#), [5.16](#) and [A](#) Case 4 and 7 respectively. In fact, introducing steel plates at the location of concentrated loads, results in a smooth introduction of compressive stresses and a reduction in the total stresses of at top fiber level at midspan, see tables [A.8](#), [A.14](#) and figures [5.15](#) and [5.17](#). Another solution, could be the substitution of the applied concentrated loads with distributed ones over a distance (for example  $0.1 \times 0.1m$ ) near the load application.

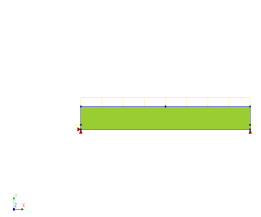


Figure 5.14: Element stresses SXX  
- LC5 - Case 4

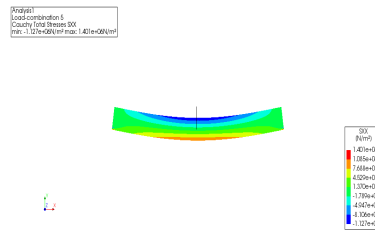


Figure 5.15: Element stresses - LC5  
- Case 4

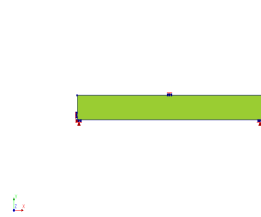


Figure 5.16: Element stresses SXX  
- LC5 - Case 7

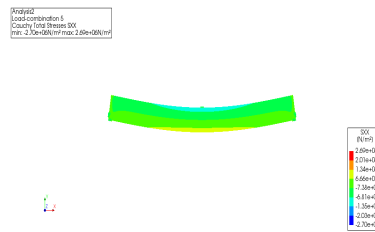


Figure 5.17: Element stresses - LC5  
- Case 7

### 5.6.3 Influence of curved geometry input 1

Applying a curvature at both top and bottom sides of the beam, resulted in an increase of the element's deflection at mid-span in comparison with the straight elements. For instance, the curved geometrical model of Case 9 (figures [5.20](#), [5.21](#)) has a larger midspan deflection compared with the deflection of the straight geometrical model of Case 3 (figures [5.18](#), [5.19](#)).

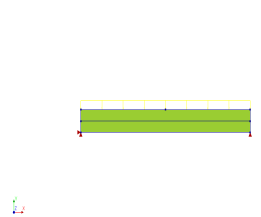


Figure 5.18: Loads and boundary  
conditions - Case 3

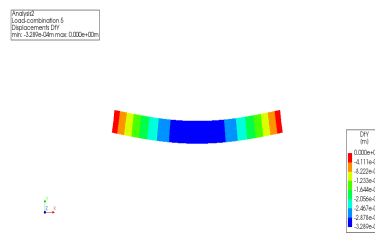


Figure 5.19: Deflection DtY - Case  
3



Figure 5.20: Loads and boundary conditions - Case 9 - input 1

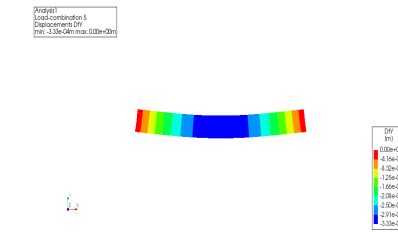


Figure 5.21: Deflection DtY - Case 9 - input 1

Inputting a curvature at top and bottom sides of the models resulted in approximately the same values or for some case in an increase of concrete stresses at midspan, compared with the straight models (figures 5.23 and 5.25).



Figure 5.22: Loads and boundary conditions - Case 3

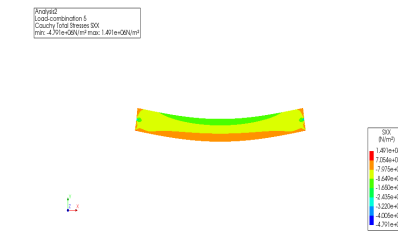


Figure 5.23: Element stresses SXX - LC5 - Case 3



Figure 5.24: Loads and boundary conditions - Case 9 - input 1

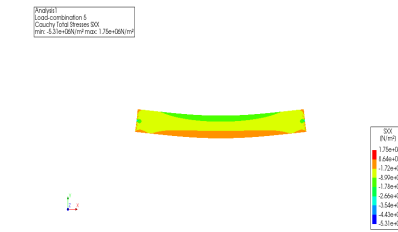


Figure 5.25: Element stresses SXX - LC5 - Case 9 - input 1

#### 5.6.4 Influence of curved geometry input 2

Creating right angles between the element edges resulted in a decrease of midspan deflection relative to the curved models without the right angles (figure 5.27, figure 5.21). However, it appeared that larger deflections occurred for the input 2 models in comparison with the straight elements (figures 5.27, 5.19).

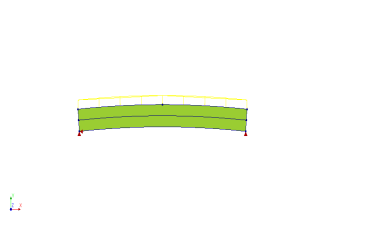


Figure 5.26: Loads and boundary conditions - Case 12 - input 2

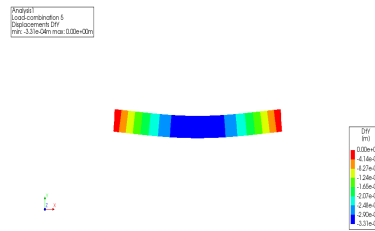


Figure 5.27: Deflection DtY - Case 12 - input 2

No improvement in the stress distribution was achieved by the right angles (input 2) models in comparison with the straight geometrical models, see figures [5.23](#) and [5.29](#).

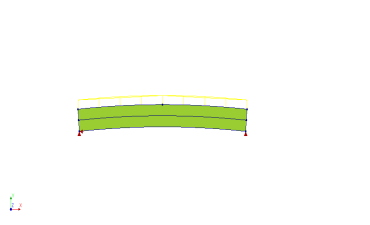


Figure 5.28: Loads and boundary conditions - Case 12 - input 2

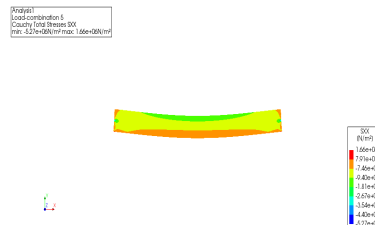


Figure 5.29: Element stresses SXX - LC5 - Case 12 - input 2

### 5.6.5 Division in two elements

Splitting the single geometrical shapes in two elements with a continuous tendon over the elements length, resulted in the same values of deflections and stresses, compared with the values found for the single undivided geometrical shapes. Cases 3 and 15 are representative of this result. The stress distribution of the concrete cross-section under the total load combination is presented in figures [5.31](#) and [5.33](#).

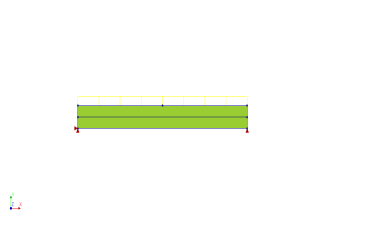


Figure 5.30: Loads and boundary conditions - Case 3



Figure 5.31: Concrete stresses SXX at midspan - Case 3

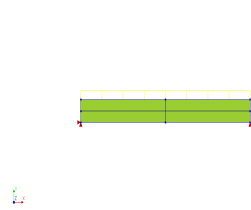


Figure 5.32: Loads and boundary conditions - Case 15

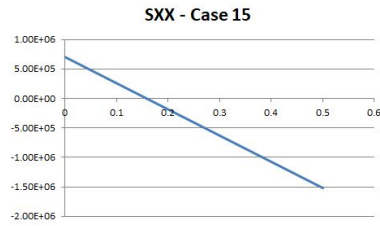


Figure 5.33: Concrete stresses SXX at midspan - Case 15

### 5.6.6 Division in three elements

Having split the initial concrete elements in three parts, two of which were larger in length than a middle element in order to simulate a joint, resulted in the same values with regard to the deflection field, compared to the undivided models. Concerning the comparison of stresses between the initial single and the divided in three elements models, as a general conclusion it can be said that the midspan concrete stresses are found to be similar. Cases 15 and 21 are representative of this result, see figures [5.34](#), [5.35](#), [5.36](#), [5.37](#), [5.38](#), [5.39](#).

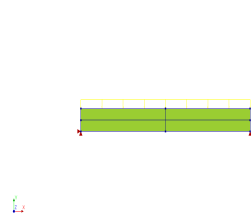


Figure 5.34: Loads and boundary conditions - Case 15

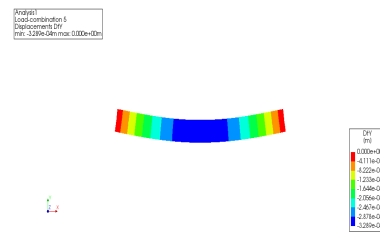


Figure 5.35: Deflection DtY - Case 15

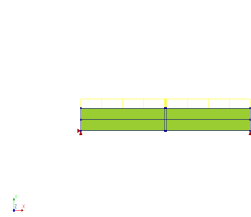


Figure 5.36: Loads and boundary conditions - Case 21

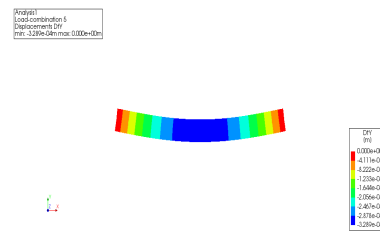


Figure 5.37: Deflection DtY - Case 21



Figure 5.38: Concrete stresses at midspan - Case 15

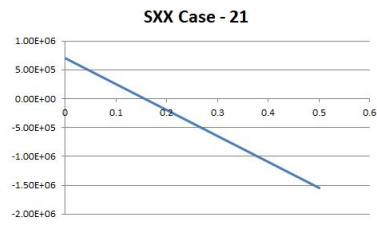


Figure 5.39: Concrete stresses at midspan - Case 21

### 5.6.7 Including a structural interface element

Inputting a structural interface with linear elastic material properties at the connection of the joint with its surrounding concrete elements, defining its stiffness moduli according to DIANA Guidelines, resulted in an increase of midspan deflections compared with the not including an interface. Cases 23 (rigid) and 29 (interface stiffness) are presented below in figures 5.40, 5.41 in order to illustrate this result.

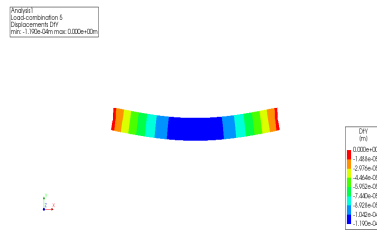


Figure 5.40: Element deflection DtY - LC5 - Case 23

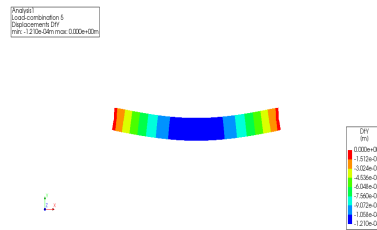


Figure 5.41: Element deflection DtY - LC5 - Case 29

### 5.6.8 Effect of the properties of the interface

Increasing the normal and shear stiffness moduli of the interface at joint's location resulted in a decrease of midspan deflection, in comparison with the models having lower normal and shear stiffness moduli. This result is illustrated in Cases 27 (lower stiffness) and 33 (increased stiffness), see figures 5.40, 5.41

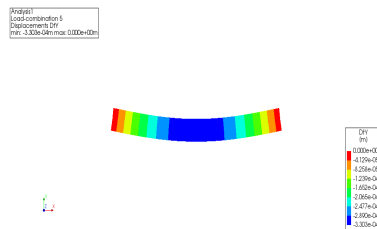


Figure 5.42: Element deflection DtY - LC5 - Case 27

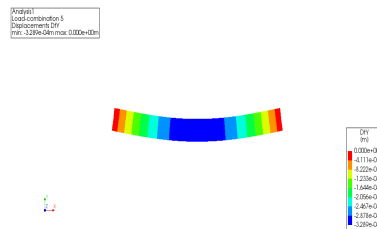


Figure 5.43: Element deflection DtY - LC5 - Case 33

### 5.6.9 Input from RHINO

It was proved that designing the element's geometry in RHINOCEROS5 and using it as an input file to DIANA for the creating of the elements geometry, produced the same results with the model's whose geometry was pre-processed exclusively in the DIANA environment.

### 5.6.10 Comparison between 2D and 3D models

The deflections of the 2D models were found to be similar with the ones found in 3D models in most cases of single elements, see figures [5.44](#), [5.45](#), [5.46](#), [5.47](#).

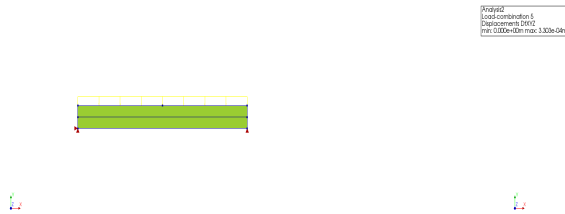


Figure 5.44: Loads and boundary conditions - Case 3

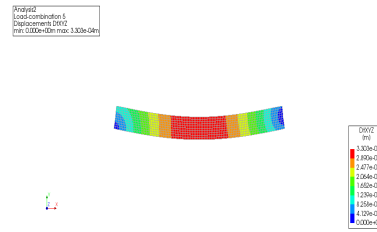


Figure 5.45: Element deflection DtXYZ - LC5 - Case 3

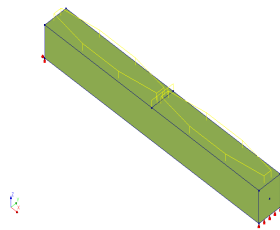


Figure 5.46: Loads and boundary conditions - Case 42

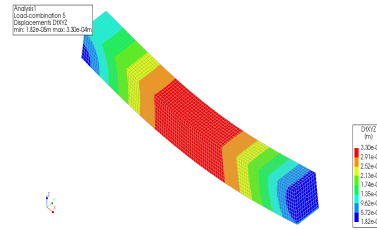


Figure 5.47: Element deflection DtXYZ - LC5 - Case 42

The stress distribution depends on both the geometry and position of the tendon and big variances occur between modeling in 2D and 3D. There are still cases like 3 and 42 that verify the equal stress distribution between the 2D and 3D models, see figures [5.48](#), [5.49](#), [5.50](#), [5.51](#).

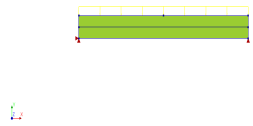


Figure 5.48: Loads and boundary conditions - Case 3

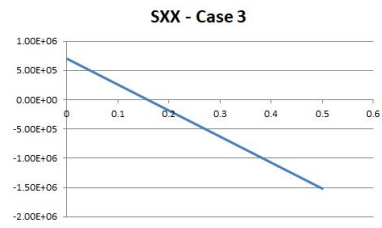


Figure 5.49: Element stresses SXX - LC5 - Case 3

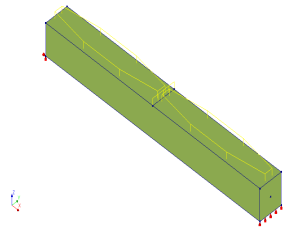


Figure 5.50: Loads and boundary conditions - Case 42

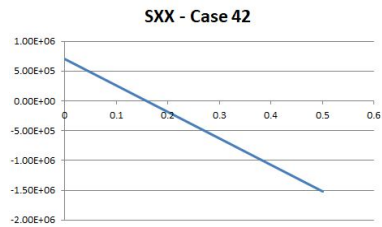


Figure 5.51: Element stresses SXX - LC5 - Case 42

## 5.7 Conclusions

1. The tendon's position over the element's height was proved via F.E.A. to be important for the resulted stress distribution. However, although the eccentric tendon profile resulted in lower stresses compared with the centrally prestressed elements, central tends will be used in the next chapters due to the limited height of the investigated concrete elements.
2. The application of steel plates at the concentrated loads location resulted in a reduction of concrete compressive stresses. It could be used if such a case was found in the following part of this study.
3. Creating curved elements resulted in larger deflections and stresses compared with the straight models. The influence of the curved elements cross-section on the deflection and stress field is to be considered in the next parts. Creating right angles between the curved element edges had a beneficial impact and this concept will be used for the formation of the precast arch structure.
4. Division of the initial geometry in two or three elements proved that has no effect on the deflection and stress distribution compared with the single geometrical elements.
5. Increasing the interface stiffness of an interface element resulted in a decrease of the elements deflection at midspan. Modeling an interface element with linear elastic properties can be used to simulate joints with different material properties from the surrounding concrete. This approach will set the basis for the creation of a discrete cracking interface in a four point bending test in the next chapter.
6. Inputting RHINO models in DIANA10.2 did not show considerable deviations in the results compared with the models having their geometry exclusively defined in DIANA10.2. Therefore the more complex geometry of the arch structure will be formed in RHINO.
7. Comparison between the 2D and 3D models showed similar values for the elements deflection at midspan. Stress deviations were found concerning the stress distribution between the 2D and 3D models. However, same stresses were found between the 2D and 3D model for the case of centrally prestressed concrete element. This will be taken into account in modeling the centrally prestressed concrete structure in the next part of this study.

## Part V

# Four point bending test - Brittle joint

## 6 Introduction

A four point bending test on two linear centrally prestressed concrete elements is modeled via Finite Element Analysis (FEM). Considering joints as the “weakest” spot in precast concrete structures, the influence of a brittle in strength joint on the structural capacity of the two concrete elements under a displacement control test is analyzed. Firstly, two linear static analyses are performed without interface properties in order to get insight and verification of the FEM results by hand calculations. Subsequently, a new phased nonlinear analysis was carried out including a discrete cracking interface element, assuming that the joint in between the precast concrete elements is expected to fail first under the applied loading.

### 6.1 Physical problem

Two concrete elements having a total length of  $l_{tot} = 613$  mm will be subjected to a four point bending test at the TU Delft laboratories. The cross section of the elements is  $200 \times 55$  mm, see table [6.1](#). The elements are connected with a cement mortar joint having a length  $l_{mj} = 50$  mm, as well as with post-tensioning steel reinforcement anchored at the outer edges of the elements' centroidal axis. First the elements are cast and then prestressing steel forces are applied on the two anchorages. No bond between concrete and steel is assumed in this experiment. A plastic duct containing the continuous tendon, will be covered with grease after the application of prestress. Two downward point loads will be applied at quarter lengths  $a = 153.25$  mm on the elements top side. The joint in between the elements will be modeled with brittle strength and cracking is assumed to start at zero concrete tensile strength. The structural requirement to be fulfilled when prestressing the two elements, is the occurrence of zero tensile stresses in the bottom fiber of the concrete elements after the application of all loads. Varying the tendon diameter and the prestressing steel forces, the main task is to investigate the structure's response for the applied concentrated loads on the top side of the elements. The test is simulated with FE analysis using DIANA10.2, see figure [6.1](#).

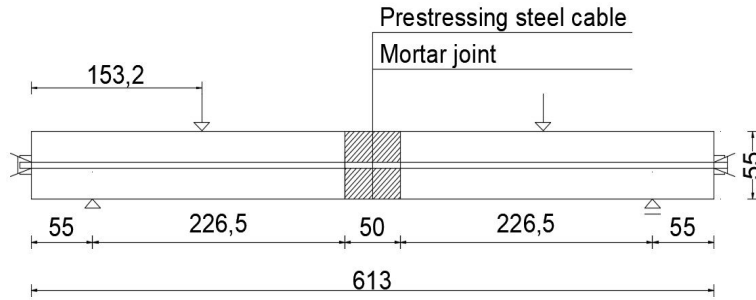


Figure 6.1: Loads and boundary conditions

Concrete elements' geometrical properties	
Total elements length $l_{tot}$ (mm)	613
Element height $h$ (mm)	55
Element width $b$ (mm)	200
Supports distance from outer ends $a$ (mm)	55
Cross section area $A_c$ (mm <sup>2</sup> )	11000
Elastic section modulus $W_c$ (mm <sup>3</sup> )	100833.33
Moment of inertia $I_c$ (mm <sup>4</sup> )	2772916.67
Mortar joint length $l_{mj}$ (mm)	50

Table 6.1: Concrete elements geometrical data

## 6.2 Concrete material properties

High strength concrete C80/95 was assigned to the two precast concrete members, see table 6.2. The reason behind this choice lies in the previous experimental results with regard to its suitability for use in the adjustable formwork. Note that a zero mean concrete tensile strength is set for this experiment, instead of  $f_{ctm} = 4.8$  MPa given by "Eurocode 2 - NEN-EN 1992", European committees for standardization, assuming that the concrete elements will not have concrete tensile strength. Cracking is expected to occur at positive tensile stresses. Poisson's ratio was set to a constant value neglecting the influence of cracking due to creep and shrinkage.

Concrete type	C80/95
Concrete Young's modulus of elasticity $E_c$ [MPa]	42000
Mean tensile concrete strength $f_{ctm}$ [MPa]	0
Design compressive strength $f_{cd}$ [MPa]	53.33
Concrete specific weight $\rho_c$ [KN/m <sup>3</sup> ]	25
Concrete material factor $\gamma_c$	1.5
Poisson's ratio $\nu$	0.2

Table 6.2: Concrete material properties

### 6.3 Prestressing steel material properties

Prestressing steel cables type Y1860 (S3,S7,S7G) constructed from 3 to 7 wires were used in this model, see table 6.3. A single cable will be anchored at the outer edges of the two concrete elements' centroidal axis. The applied value of characteristic tensile strength  $f_{pk} = 1860$  MPa for all the investigated post-tensioning cables, is a choice of the author for ease of calculations, and based on the fact that it is the maximum steel quality that can be used in such cases. Note that some types of cables can or should have a different characteristic tensile strength, ranging from 700 MPa to 2160 MPa. The diameter of the prestressing steel was a varying parameter to be investigated. No bond between steel and concrete was assumed. Friction and wedge set losses that may occur during tensioning were not considered. Unintended rotations during tensioning of the prestressing steel are neglected, setting the wobble factor equal to zero. Time dependent losses due to creep, shrinkage and relaxation are also disregarded in the current study, resulting in constant prestressing steel force at time  $t_0$  and  $t_\infty$ :

$$P_{m0} = P_{m\infty} \quad (6.1)$$

Prestressing steel type	Y1860C
Prestressing steel modulus of elasticity $E_P$ [MPa]	195000
Prestressing steel material factor $\gamma_s$	1.1
Characteristic tensile strength $f_{pk}$ [MPa]	1860

Table 6.3: Prestressing steel material properties

### 6.4 Loads and load combinations:

The loads that were applied in the following sequence - load combinations ( $LC_{i=1,\dots,4}$ ) are presented in table 6.4. Note that although post-tensioning implies that first concrete is cast and then prestressing is applied at the anchorages, in this case the loads are applied vice versa. The reason for this choice lies in the way the post-tensioning load is modeled in DIANA10.2. The point loads were applied either as forces or as displacements for both the linear and the phased nonlinear static analyses. Having assumed the values of the applied prestressing steel forces, the values of the point loads that would cause cracking of the concrete elements were calculated and set as a third load case for this experiment. Note that concrete's self-weight could have been omitted in the calculations due to the geometry of the current test set-up. However, it was decided to be included in the model.

LC1	Prestressing steel forces	P
LC2	Concrete self weight	SW
LC3	Point loads	F; u
LC4	Total	$P + SW + F; u$

Table 6.4: Load combinations - DIANA10.2

## 6.5 Code requirements

The following equations are taken from EN992-1-1 cl. 5.10.2.2:

The maximum prestressing steel stress during tensioning is calculated as:

$$\sigma_{p,max} = \min(0.8 \times f_{pk}, 0.9 \times f_{p0.1k}) = 1488 \text{ MPa}$$

The maximum prestressing steel stress after tensioning is calculated as:

$$\sigma_{p,m0} = \min(0.75 \times f_{pk}, 0.85 \times f_{p0.1k}) = 1395 \text{ MPa}$$

Where,

$$f_{p0.1k} = 0.9 \times f_{pk} = 1674 \text{ MPa} \quad (6.2)$$

The design tensile strength of the prestressing steel is calculated as:

$$f_{pd} = \frac{0.9 \times f_{pk}}{\gamma_s} = 1522 \text{ MPa} \quad (6.3)$$

The maximum prestressing steel stress is calculated as:

$$\sigma_{p,max} = \frac{f_{pk}}{\gamma_s} = 1691 \text{ MPa} \quad (6.4)$$

The concrete compressive stresses caused by prestressing should be limited to:

$$\sigma_{c,alwd} \leq 0.6 \times f_{ck} = 48 \text{ MPa} \quad (6.5)$$

## 6.6 Hand calculations

### 6.6.1 Linear static analysis

Two cases with regard to the location of the supports were analyzed in this part. In the first case it was assumed that the supports are located at the elements outer edges, while in the second case the 55[mm] distance between the supports and the edges was included.

Based on the maximum allowed prestressing steel stress after tensioning, and the cross-section area of the selected prestressing steel type, the values of the applied prestressing steel forces for the respective steel cable diameters  $d_i$ , are calculated as:

$$P_i = \sigma_{p,m0} \times S_{n,i} \quad (6.6)$$

The prestressing steel forces  $P_i$  for the chosen type of prestressing steel cables, were the values used to simulate the prestressing steel loads acting on both anchorages in the DIANA10.2 model. Based on meeting the requirement of zero concrete tensile stresses at bottom fiber, the maximum point loads  $F_i$  to be applied on the elements top side were calculated. Assuming that the concrete elements will have zero concrete tensile strength, the point loads  $F_i$  are actually the cracking loads  $F_{cr}$  in this case.

$$\sigma_{c,tot}^{bot} = -\frac{P_i}{A_c} + \frac{\left(\frac{q_{sw} \times l^2}{8} + \frac{F_i \times l}{4}\right)}{W_c} \leq 0 \quad (6.7)$$

$$F_i \leq \frac{4 \times W_c}{l} \times \left( -\frac{q_{sw} \times l^2}{8 W_c} + \frac{P}{A_c} \right) \quad (6.8)$$

$$F_i = F_{cr} \quad (6.9)$$

The values obtained from equation [6.8](#) are used to calculate the concentrated loads  $F$  acting on the elements top side at the force control method in linear static analysis. The displacement of the beam elements is calculated in relevance to the applied loads according to equations [6.10](#), [6.13](#), [6.14](#), [6.15](#). Note that the distance between the supports and the elements outer edges is neglected in the linear static analysis. For the non linear analysis the 55 mm distance of the supports from the concrete specimens outer ends is included in the models, see [B.1.1](#) and [B.1.2](#).

1. The midspan deflection of concrete due to the centroidal prestressing loads is:

$$\delta_P = 0 \text{ mm} \quad (6.10)$$

2. The midspan deflection of concrete due to self-weight is:

$$\delta_G = \frac{5}{384} \times \frac{q_{sw} \times l^4}{E_c \times I_c} \quad (6.11)$$

where,

$$q_G = A_c \times \gamma_c \quad (6.12)$$

3. The midspan deflection of concrete due to point loads:

$$\delta_{F_i; x=\frac{l}{4}} = \frac{F_i \times l^3}{24 \times E_c \times I_c} \quad (6.13)$$

$$\delta_{F_i; x=\frac{l}{2}} = \frac{11 \times F_i \times l^3}{384 \times E_c \times I_c} \quad (6.14)$$

The vertical downward deflections to be applied at quarter lengths  $a = \frac{l}{4}$  on top of the beam for the displacement control linear static analysis model, are calculated as:

$$u_{i; x=a} = \frac{F_i \times a^2}{6 \times E_c \times I_c} \times (3 \times l - 4 \times a) \quad (6.15)$$

Note, that the equations describing the deflections are based on single beam elements loaded by uniformly distributed load and symmetrical concentrated loads at quarter lengths. These equations were used assuming that the two different concrete elements are monolithically connected with each other, hence neglecting the mortar joint in between them.

The values of the applied loads and load combinations relevant to the applied prestressing steel type are presented in table [B.1](#) for the model without the supports-edge distance and in [B.6](#) for the model with the supports-edge distance. The occurring midspan concrete stresses at top and bottom fiber level due to the applied cracking loads, are presented in tables [B.4](#) and in [B.7](#) for both models.

According to tables [B.8](#) and [B.9](#) no concrete crushing failure is expected and no yielding of the prestressing steel reinforcement is expected for the applied loads.

### 6.6.2 Discrete cracking

The 55[mm] distance between the supports and the element edges was taken into consideration in this part. For loads exceeding the cracking load it was assumed that a single crack will occur at the location of the joint in-between the elements at midspan, see figure 6.2. As a result of the discrete cracking at midspan, the two concrete elements next to the crack are rotated by an angle  $\vartheta$ , assuming that they are rigid bodies.

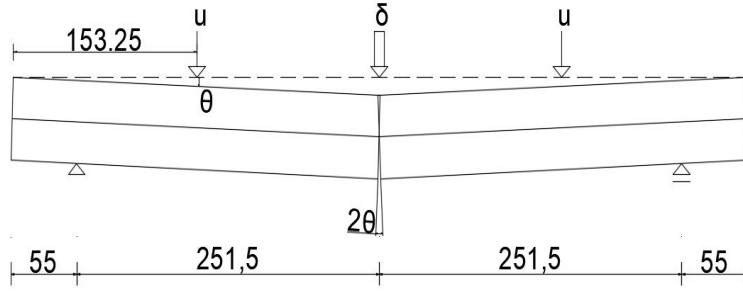


Figure 6.2: Rigid bodies rotation - single crack at midspan at displacements  $u$

The embedded prestressing steel cable will follow the rotation of the surrounding concrete elements by an angle  $\vartheta$  as well. Tendon elongation  $\Delta l_p$  is expected to occur at the location of the crack, resulting in an increase of the prestressing steel  $\Delta \varepsilon_p$  of the unbonded prestressing steel reinforcement. Therefore, an increase of the prestressing steel stress  $\Delta \sigma_p$  and force  $\Delta P$  will take place for loads exceeding the cracking load of the concrete elements. The left hand-side rigid body rotation with the applied forces is shown in figure 6.3. The midspan concrete cross-section forces for loads exceeding the cracking load are depicted in figure 6.4.

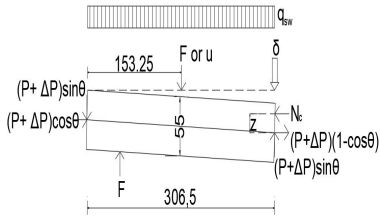


Figure 6.3: Left hand-side rigid body rotation

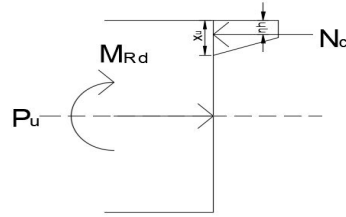


Figure 6.4: Midspan cross-section forces at  $u$

The relation between the angle of rotation  $\vartheta$  and the applied displacements  $u$  at is calculated as:

$$\theta = \frac{u}{\frac{l}{4} - a} = \frac{u}{98.25} \text{ rad} \quad (6.16)$$

Assuming that the concrete compressive force  $N_c$  is applied at top fiber level

as presented in figure [6.3](#), the lever arm  $z$  is getting its maximum value, i.e.

$$z = \frac{h}{2} = 27.5 \text{ mm} \quad (6.17)$$

Note that the actual position of the concrete compressive force  $N_c$  is below the top fiber level, compare with figure [6.4](#). This simplification will result in an upper bound value for the applied loads  $F$  or  $u$ .

Based on the increase of the tendon length  $\Delta l_p$  at the location of the crack, the increase of the prestressing steel strain  $\Delta \varepsilon_p$  over the full tendon length  $l_p$  is calculated as:

$$\Delta \varepsilon_p = \frac{\Delta l_p}{l_p} = \frac{2 \times \theta \times z}{l_p} = \frac{2 \times \frac{u}{98.25} \times z}{l_p} = 9.132 \times 10^{-4} \times u \quad (6.18)$$

The total prestressing steel strain  $\varepsilon_{p,tot,u}$  under the applied displacements  $u$  is calculated as:

$$\varepsilon_{p,tot,u} = \varepsilon_{p,m\infty} + \Delta \varepsilon_p \quad (6.19)$$

The corresponding increase in the prestressing steel force  $\Delta P$  per cable diameter, can then be formulated as:

$$\Delta P_i = \Delta \sigma_p \times S_{ni} \quad (6.20)$$

where,  $S_{ni}$ : Area of prestressing steel

The subscript  $i$  used in equation [6.20](#) refers to the investigated cable size.

The total prestressing steel force after cracking, per cable diameter, is calculated as:

$$P_{u,i} = P_i + \Delta P_i \quad (6.21)$$

Taking the horizontal equilibrium of forces of the left-hand side rigid body presented in figure [6.3](#), it is proved that the concrete compressive force is equal to the total prestressing load:

$$N_c = P_u \quad (6.22)$$

Taking the moment equilibrium of forces results in the following relation between the applied loads:

$$F \times \left(\frac{l}{4} - a\right) + \frac{q_{sw} \times l^2}{8} - \frac{q_{sw} \times a \times l}{2} = P_u \times \frac{h}{2} \quad (6.23)$$

Therefore the point load  $F_i$  to be resisted per cable diameter after cracking, under the applied displacements can be calculated as:

$$F_i = \frac{1}{\left(\frac{l}{4} - a\right)} \times \left\{ P_{u,i} \times \frac{h}{2} - \left( \frac{q_{sw} \times l^2}{8} - \frac{q_{sw} \times a \times l}{2} \right) \right\} \quad (6.24)$$

Note that the concrete self-weight component could have been omitted in the above calculation due to its small contribution to the bending moment. However, it is chosen to be included in the models as well as the hand-calculations.

The concrete compressive force  $N_c$  acting at hinge location is calculated as:

$$N_c = \frac{1}{2} \times b \times x_{u,i} \times f_{cd} \quad (6.25)$$

Taking the horizontal equilibrium of forces in the cross-section (figure [6.4](#)), the compression zone height for the applied  $u$  displacements, is then calculated as:

$$x_{u,i} = \frac{P_{u,i}}{0.5 \times b \times f_{cd}} = \frac{P_i + \Delta P}{0.5 \times b \times f_{cd}} \quad (6.26)$$

As an indicative result for the performed calculations for the applied loads, the smallest prestressing steel cable diameter with nominal area of prestressing steel  $S_{n,5.2} = 13.6 \text{ mm}^2$  is presented in [B.2](#). The performed calculations with regard to the 5.2[mm] prestressing steel cable diameter are presented analytically in the Appendix. Having run the nonlinear static analysis under  $u = 1 \text{ mm}$  displacements, a load - deflection (F - u) diagram was obtained. It is found that a horizontal plateau occurs at approximately 0.6 mm displacement.

In order to analyze this outcome, emphasis was given at the start of the horizontal plateau, hence at  $u = 0.6 \text{ mm}$  and at the displacement values  $u_{max}$  where the prestressing steel reaches its maximum stress value  $\sigma_{p,max}$ . Hand calculations concerning these points of attention can be found in the Appendix, [B.2.2](#) and [B.2.1](#).

## 6.7 Finite element modeling (FEM) - Four point bending test

Between a one-dimensional (1D) element that would not describe accurately the stress distribution for the current physical problem of the four point bending test, and a three dimensional element (3D) that would result in more complicated analysis and larger computation time, it was decided to model the structure as two dimensional (2D), or literally speaking as  $(2 + \frac{1}{2})D$ . Note that the 55 mm distance between the supports and the element edges was initially neglected in the FE model as well as the in the calculations, forming a simplified geometrical model. However, as a next step towards a more refined model, this distance was included in both linear and nonlinear analyses. The physical 50 mm length of the joint in between the elements (figure [6.1](#)) was considered in the model by applying a free length at the interface location when pre-processing the FEM, although in figure [6.9](#) it is shown that the concrete elements were modeled to be in direct contact with each other.

### 6.7.1 Element type and mesh

Between a plane strain and a plane stress model, based on the finite and limited length of the test specimens, a plane stress is chosen for the current modeling of the concrete elements. According to DIANA10.2 manual, an eight node quadrilateral isoparametric plane stress element namely the CQ16M, based on quadratic interpolation and Gauss integration scheme will be used in this type of analysis. Quadratic interpolation was selected for the case considered for more refined analysis results. A mesh element size of 5.5 mm was chosen, so that a series of ten elements are formed over the height of the elements. This value complies with the maximum mesh element given by equation [5.10](#), according to [Hendriks \[2016\]](#).

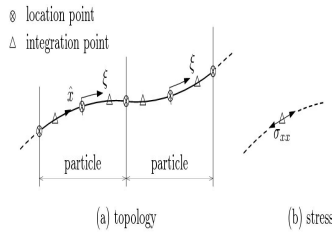


Figure 6.5: Steel reinforcement location input

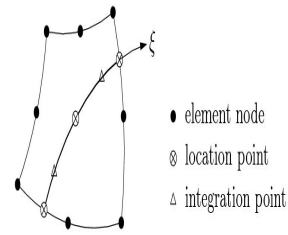


Figure 6.6: Steel reinforcement in plane stress element

### 6.7.2 Post-tensioning steel reinforcement

It was decided not to grout the duct after tensioning in this specific test set-up. Therefore, embedded steel reinforcement not bonded to the mother elements was used in this model. By modeling a no-bond interaction between concrete and prestressing steel reinforcement, means that the the steel cables do not contribute to the stiffness of the concrete. The steel strains and stresses do not change during concrete's deformation according to DIANA10.2 manual.

For the input of location of the reinforcing steel, DIANA divides the total length of the reinforcement in particles and computes the resulting steel stresses and strains along its length. The position of the particles in the model are defined by location points, see figures 6.5,6.6. The post tensioning load is applied as an external load in the model and is based on the Coulomb friction model, according to DIANA10.2 manual. Although applied externally, the prestressing load turns into internal, being fully embedded to the surrounding concrete elements and the not bonded internal tendon can be simulated. Immediate losses due to anchor retention length, friction and local irregularities denoted by the wobble factor can be set as parameters in this models. However, their values are set to zero for ease of simplicity. Time dependent losses are not included in this model too. The number of anchors can also be set by the user. One anchor per element outer side was set for the current FEM.

### 6.7.3 Structural interface element

A structural 2D line interface was defined on the inner faces of the two elements, considered as connected, due to the fact that the interface is in between two continuum elements, see DIANA10.2 manual. According to it, the structural interface elements describe the interface behavior in terms of a relation between the normal and shear stresses, denoted as "tractions"  $t$ , and and the displacements  $u_e$ . For two dimensional line interface that was used in the current research, the variables of tractions and relative displacements are defined as:

$$u_e = \begin{Bmatrix} u_x \\ u_y \end{Bmatrix} \Delta u = \begin{Bmatrix} \Delta u_{sx} \\ \Delta u_{ny} \end{Bmatrix} t = \begin{Bmatrix} t_{sx} \\ t_{ny} \end{Bmatrix} \quad (6.27)$$

The constitutive law that describes discrete cracking in DIANA, relates the tractions as a nonlinear function of the total relative displacements, the crack width  $\Delta u_n$  and the crack slip  $dt$ :

$$\begin{cases} t_n = f_n(\Delta u_n) \\ t_t = f_t(dt) \end{cases} \quad (6.28)$$

where,

$t_n$ : traction normal to the interface

$t_t$ : traction tangential to the interface

Discrete cracking is specified as initiation of a tension softening criterion governing the normal traction  $t_n$ , and a shear criterion governing the shear slip  $t_t$ . For the tension softening criterion (denoted as Mode I), brittle cracking was chosen to simulate the physical problem of full reduction of the strength of the mortar joint, after the strength criterion has been violated, see figure 6.7

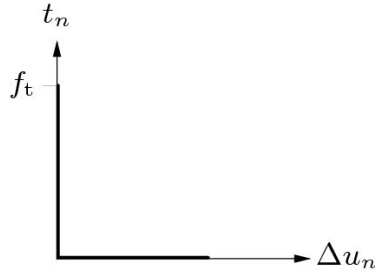


Figure 6.7: Brittle softening criterion

In general, the shear traction  $t_t$  is reduced after cracking (Mode II) according to:

$$f_t = \begin{cases} k_t \times dt & , \text{if } \Delta u_n < \frac{f_t}{k_n} \\ \beta \times k_t \times dt & , \text{if } \Delta u_n \geq \frac{f_t}{k_n} \end{cases} \quad (6.29)$$

Zero shear traction was selected for the model according to Hendriks [2016].

Based on the assumption that the mortar joint in between the adjacent concrete elements does not add stiffness to them, and under the applied loads cracking will occur at the joint location, a zero value for the tensile strength should be applied. However, in order to avoid numerical errors in the structural analysis, a value close to zero was set for the tensile strength:

$$f_t = 0.01[N/m^2] \quad (6.30)$$

The normal and shear interface stiffness were determined according to DIANA10.2 Guidelines:

$$K_n = \frac{E}{l_e} \quad (6.31)$$

$$K_t = \frac{K_n}{100} \quad (6.32)$$

where  $E$  is the modulus of elasticity of the elements surrounding the interface, hence taken equal to the modulus of elasticity of concrete  $E_c$ , and  $l_e$  is the average element size in the mesh defined previously. An assumption was made of zero shear traction and stiffness after cracking used by default in DIANA10.2. Note that no concrete crushing criterion was incorporated in the FEM.

The following parameters [6.5](#) were used to set up the structural interface:

Structural interface type	Discrete cracking
Normal stiffness modulus-y $K_n[N/m^2/m]$	7.636e12
Shear stiffness modulus-x $K_t[N/m^2/m]$	7.636e10
Tensile strength $[N/m^2]$	0.01
Mode-I tension softening criterion	Brittle
Mode II-shear criterion for crack development	Zero shear traction

Table 6.5: Structural interface parameters

#### 6.7.4 Types of analyses:

Two different types of analyses were performed in this research, namely a linear and a phased nonlinear static. The first type of analysis took place in order to assess the response of the investigated elements under the 4-point bending test in the linear elastic range. The second type was carried out in phases in order to investigate the elements response for loads exceeding the cracking load of concrete. Note that the term nonlinear analysis is used, although it is not a “fully” nonlinear analysis. Including a discrete cracking interface element was the only non-linearity in the physical properties of the model and the term nonlinear analysis also refers to the set type of analysis in DIANA10.2. In order to include the addition of vertical support reactions under the applied concentrating loads at elements top face, the nonlinear analysis was done in sequential stages, denoted as phased.

The phased analysis was set to consist of three stages. In the first phase, the prestressing loads (P) were applied in one step. In the second phase the concrete self-weight (S.W) was added to the applied prestressing loads. The self-weight of concrete was also applied at once using one increment in the second phase. The point loads (u) were set to be acting in a third phase and were added to the previously set loads of prestressing and concrete’s self-weight.

Displacement control method was chosen, considering it more suitable to model the “snap-through” behavior of concrete while softening, compared with the force control method. The applied vertical displacements acting on the elements top side, were applied in 50 increments of a 0.0020 size, 40 increments of 0.005 size and 70 increments of 0.01 size. Using different step sizes to model the vertical displacements at the elements top side, a better insight of the analysis results can be obtained at the instant of cracking and further on. The applied displacement values at quarter lengths of the concrete elements top side were set to be  $u = 1$  mm by initial choice of the author.

As an iterative procedure to reach equilibrium between the internal and external force vector, the regular Newton-Raphson method with 10 iterations per increment was selected. Therefore, the stiffness matrix relating the internal forces to incremental displacements is updated in every iteration within an increment, see figure [6.8](#). A smaller number of iterations could be used, as was proved by the results converging with regard to the specified norms, after 0 iterations. This is due to the nearly linear behavior resulting in convergence at the first prediction of the load increment. The convergence norms used for the nonlinear analysis were force and displacement, both set at a value of 0.01.

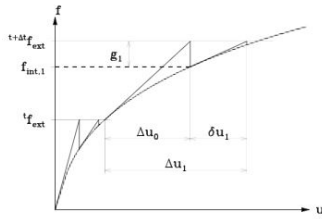


Figure 6.8: Loads and boundary conditions - DIANA manual

## 6.8 Linear static analysis

The two precast concrete elements are assumed to be monolithically connected and the influence of joint stiffness in between them is neglected in this stage of analysis. Based on fulfilling the requirement of zero concrete stresses at bottom fiber level, the cracking values of point loads  $F$  or  $u$  are calculated via equations 6.8 and 6.15, and their values are applied in the the finite element (F.E.) linear static analysis for a force and a displacement control test respectively. In order to limit the range of calculations, it was decided to select one specific prestressing steel cable, namely the Y1860S3 with characteristic diameter of 5.2[mm] and area of prestressing steel 13.6 mm<sup>2</sup>.

### 6.8.1 Force control (F.C.)

Two downward point loads with a value  $F = 1050.52$  N equal to the cracking load of the concrete, calculated according to equation 6.8, are acting at quarter lengths of the elements' top side (figure Loads and boundary conditions).

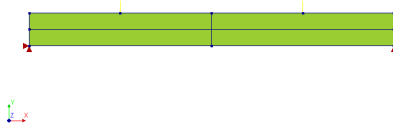


Figure 6.9: Loads and boundary conditions

Note that equation (7) is based on the assumption of a zero concrete tensile strength at the moment of cracking:

$$\sigma_{cr} = f_{ctm} = 0 \text{ MPa}$$

A pinned support on the left edge and a roller support on the right edge of the element, form the boundary conditions, see figure 6.9. Central prestressing steel forces  $P_{5.2} = 18972$  N, calculated according to equation 6.6 (see table B.1), are acting on both anchorages of the element. Self-weight of the concrete elements is included. The following results with regard to concrete stresses

SXX are obtained for the linear static analysis performed with DIANA10.2, see figures 68,68,68,68,68,68,69,69. A comparison between the FEA values of midspan concrete stresses with the predicted values from hand calculations are shown in Annex - four-point bending test, table B.4

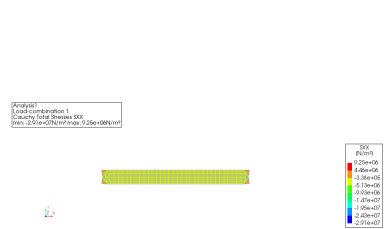


Figure 6.10: Prestressing load (P) concrete stresses SXX - F.C.

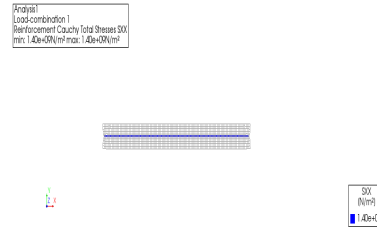


Figure 6.11: Reinforcement stresses SXX due to P- F.C.

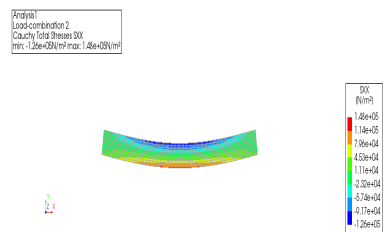


Figure 6.12: Self weight (SW) concrete stresses SXX - F.C.

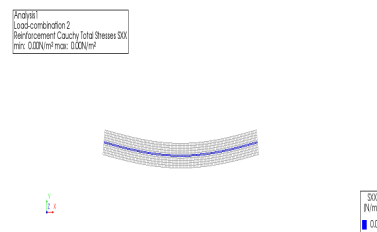


Figure 6.13: Reinforcement stresses SXX due to SW - F.C.

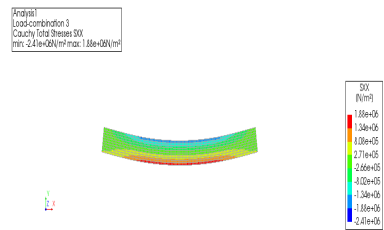


Figure 6.14: Point load (F) concrete stresses SXX - F.C.

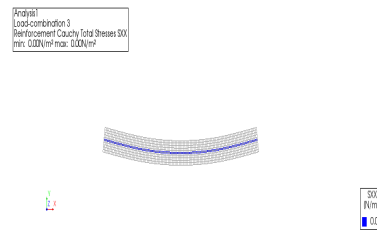


Figure 6.15: Reinforcement stresses SXX due to F- F.C.

Analysis  
Load-combination 4  
Cauchy Total Stresses SXX  
min: -2.91e+07N/m² max: 2.25e+08N/m²



Figure 6.16: Total concrete stresses (P+SW+F) SXX - F.C.

Analysis  
Load-combination 4  
Midspan Element Cauchy Total Stresses SXX  
min: 1.43e+08N/m² max: 1.43e+08N/m²



Figure 6.17: Midspan element concrete stresses SXX due to P+SW+F - F.C.

### 6.8.2 Displacement control (D.C.)

According to DIANA10.2 manual, in order to apply a vertical displacement on an element, the corresponding degree of freedom (DOF) at loads' location, hence the vertical, must be restrained. The vertical translations, is the only load case for this displacement control model and cannot be combined with the other loads of prestressing and self weight. However, superimposing the results from the displacement control model to the ones from the force control method, the total internal loads and displacements can be calculated. In particular, when the displacement control model with the imposed vertical translations as a single and only load, is combined with the force control model including the prestressing and self-weight loads only, the total internal loads can be found.

Two downward vertical displacements  $u_{5,2} = 0.045$  mm are applied at quarter lengths of the element's top side. This value is in the range found from the hand calculations estimated deflection  $u$  and the DIANA10.2 DtY deflection, and selected so that the reaction force at loads location would approximate the calculated cracking load of the elements, see equations [6.8](#) [6.9](#). In particular, by applying  $u_{5,2} = 0.045$  mm, the reaction forces at loads location after running a linear static analysis in DIANA10.2, are equal to  $FbY_{5,2} = 1050.28$  N which is almost the same with the hand-calculated cracking load. The hand-calculated point loads, concrete stresses, prestressing steel stresses and deflections are verified by the FEA results, see tables [B.2](#), [B.3](#). The concrete stresses SXX due to the applied downward vertical displacements  $u$  (displacement control) are found to be identical with the occurring ones due to the vertical concentrated loads  $F$  (force control), and thus not presented again.

### 6.8.3 Conclusions

1. The DIANA10.2 result values of the internal stresses SXX and deflections DtY are verified by the hand calculations.
2. The predicted via hand calculations values of the concentrated forces (force control) and the vertical displacements (displacement control) that would cause cracking of the elements, are considered very small. The cause is the assumed zero tensile strength of concrete at the moment of cracking.
3. The internal element stresses SXX are found to be zero at midspan bottom fiber level for the total load combination, verifying the initial model assumption for prestressing taking up the tensile loading. At top fiber level, the requirement with regard to maximum concrete compressive stresses due to prestressing is also fulfilled. In addition no concrete crushing failure is expected due to the applied loads.
4. At the locations of the anchorages and the applied point loads, concentration of compressive stresses occurs. These are the locations where highest compressive stresses are found in the whole test set-up, the magnitude of which is in the range of the allowed concrete compressive stresses during and after tensioning.
5. The prestressing steel force is constant along the elements' length due to the assumption of zero instantaneous and time dependent losses in the prestressing steel.
6. The prestressing steel is proved to be in the linear elastic stage as expected.
7. The no bond interaction between concrete and the prestressing steel reinforcement is proved via the linear static analyses, since no increase in the prestressing steel steel stress occurs after the application of concrete self-weight and the applied concentrated loads at top side of the elements.

### 6.8.4 Test limitations

Constant prestressing steel forces were applied on the two anchorages of the post-tensioning steel. Instantaneous dependent losses caused by wedge-set and unintended rotations during tensioning, were input with zero values during pre-processing the post-tensioning load in DIANA10.2. The reason that lies in this choice is the fact that based on this way of modeling the prestressing loads were set-up in DIANA10.2. Even when several non-zero values were applied either for anchor retention lengths or for wobble factor, the results of the post-tensioning steel forces applied were the same as if it were the case without any losses considered. It seems that the non-zero values for the instantaneous losses cannot be incorporated in DIANA10.2, assuming that the way of modeling the physical problem is correct. It must be noted that the length of the specimen is small and therefore, instantaneous time dependent losses are also expected to be small.

## 6.9 Phased nonlinear static analysis

The  $a = 55$  mm distance between the supports and the concrete elements outer edges was included in the FEM and the hand calculations, see figure [6.18](#)

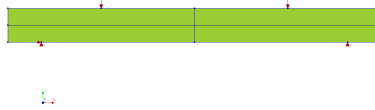


Figure 6.18: Loads and boundary conditions - Supports at 55 mm from elements edges

In case two concentrated loads acting on the elements' top side are causing tensile stresses in the element, cracking of concrete is expected to occur. The mean concrete tensile strength is neglected and set to zero ( $f_{ctm} = 0$  MPa) by choice of the author. Based on the assumption that the “weakest part” of the structure is the mortar joint in-between the elements, this would also be the location of a crack. Assuming that the formation of a crack in a joint is localized at the spot where it was initiated and no other cracks are formed in the elements, a discrete cracking interface of brittle strength was set up at joint's connection with the surrounding concrete elements.

A phased nonlinear static analysis based on displacement control, was carried out, in order to investigate the response of the concrete elements under the four point bending test for loads larger than the cracking load. Note that the term nonlinear refers to the input of nonlinear material properties for the discrete cracking interface as well as the set type of analysis in DIANA10.2. In particular, first  $u = 1$  mm displacements were set to be acting at quarter lengths on the elements' top side. Based on the applied prestressing steel forces determined by the cross-section area of the steel and the maximum allowed prestressing steel stress after tensioning, a load - deflection (F-u) diagram per cable diameter was the main output of this analysis, see figure [6.19](#). Note that the load F in the F-u diagram corresponds to the vertical reaction force FBY set at the location of the applied displacements u when pre-processing the FEM.

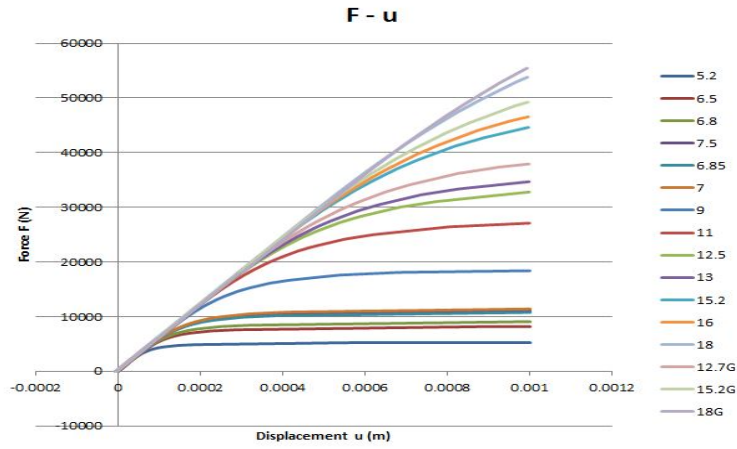


Figure 6.19: Load deflection diagram -  $\Phi_i - u = 1 \text{ mm}$

The minimum prestressing steel cable diameter  $\Phi_P = 5.2 \text{ mm}$  was analyzed. The resulting F - u diagram of the investigated prestressing steel cable, shows an increase of the force for increasing values of the applied displacements up to a value 0.56 mm, see figure 6.20. This result would be expected in case of either concrete or prestressing steel failure. However as it is proved in the Appendix this is not the case for the current model (see B.2.2 and B.2.1).

In order to explain the horizontal plateau in the F-u diagram of figure 6.20, a new nonlinear static analysis was carried out with  $u = 0.6 \text{ mm}$  as applied loads (figure 6.21). The diagram was discretized in ten different points, denoted by the the number of load step set in the nonlinear analysis and the corresponding value of the reaction force, i.e. Load Step (FBY). Note that point 0 refers to Load step 2, where the concrete self-weight is added to the prestressing steel loads. Hand calculations were performed in order to explain the FEA resulted diagram (Appendix B.2).

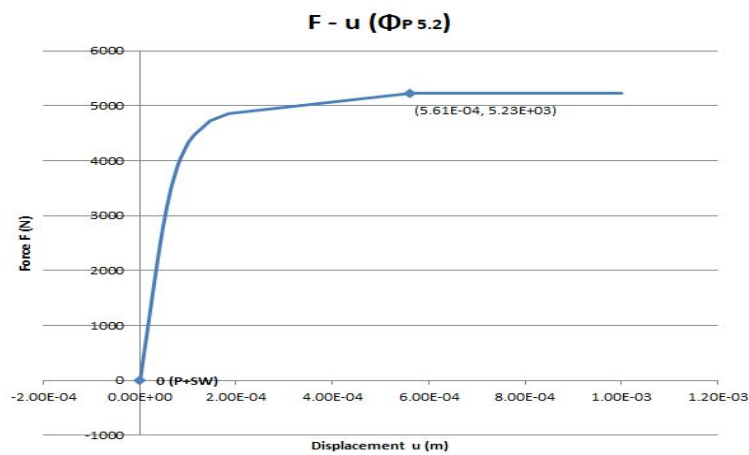


Figure 6.20: Load deflection diagram -  $\Phi_{5.2} - u = 1 \text{ mm}$

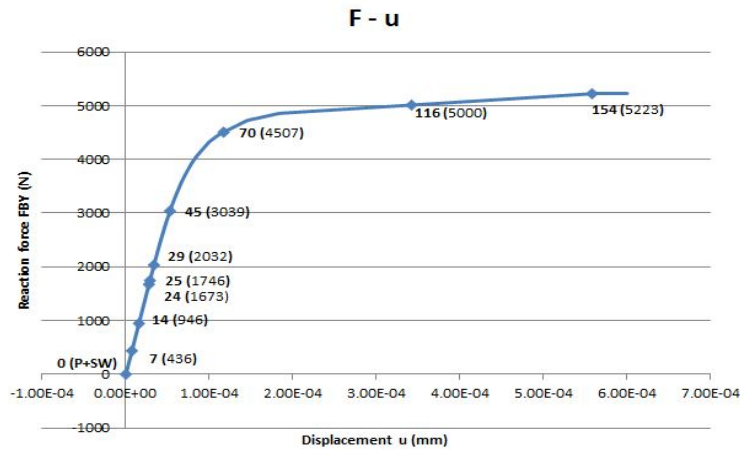


Figure 6.21: Load deflection diagram -  $\Phi 5.2 - u = 0.6 \text{ mm} / 0.6$

### 6.9.1 Point 0

The concrete self-weight (SW) is superimposed to the post-tensioning loads (P) applied at both anchors of the elements outer edges. As it can be seen from figures 6.22 and 6.23 the concrete cross-section at midspan is under compression. The reinforcement strains (EXX) remain constant after the application of concrete's self-weight due to the no bond-interaction between concrete and the prestressing steel reinforcement. The interface normal tractions (STNy) show that the two elements are in full contact with each other, see figure 6.25. The hand-calculated results are verified with the FEA results, see Annex, B.2.3.

The deflection of the reinforcement follows concrete's displacement, see figure 6.24. The beam elements together with the reinforcement deflect downwards due to the concrete self weight and a slight curvature is present over the elements length (figure 6.23).

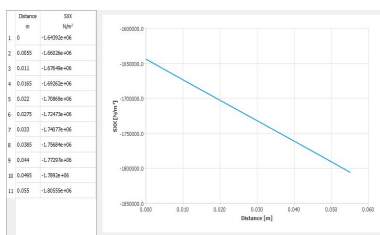


Figure 6.22: Midspan concrete stresses SXX - Point 0

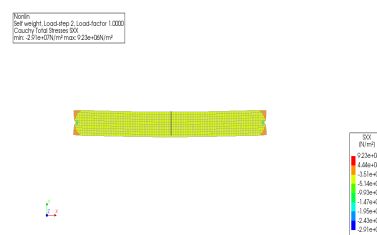


Figure 6.23: Concrete stresses SXX - Point 0

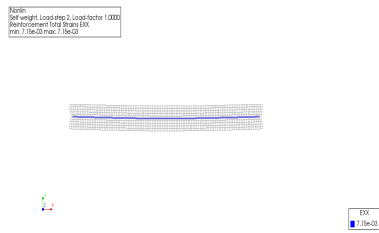


Figure 6.24: Reinforcement strains EXX - Point 0

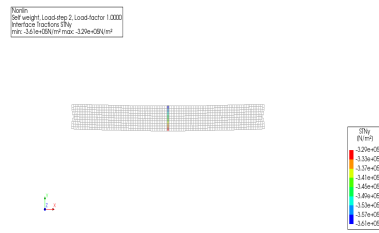


Figure 6.25: Interface normal stresses STNy; Point 0

### 6.9.2 Load step 7

In addition to the previously applied loads of prestressing (P) and self-weight (SW), the displacements  $u$  are acting at the elements top side. The value of the imposed deflections for this step is:

$$u = 7.82E - 06 \text{ m}$$

Reaction forces (FBY) are now present at the locations of the applied displacements :

$$FBY = 436 \text{ N}$$

The concrete cross-section is under compression over its full height, however the stresses (SXX) decrease at bottom and increase at top fiber level due to the applied  $u$  displacements, compared with the previous load step, see figures 6.26 and 6.27. The difference in concrete stresses between the previous load step and the current one is found to be 19%. As it can be seen from 6.29 the two concrete elements are in full contact with each other. The prestressing steel reinforcement (EXX) strains remain constant over the full tendon length after the application of the additional displacement. The downward deflection of the tendon follows the deflection of the surrounding concrete (figure 6.28).

An increase of the elements' downward displacement occurs as a result of the increase of the imposed  $u$  displacements at the elements top side. A smooth upward curvature is present over the elements length (figure 6.27).

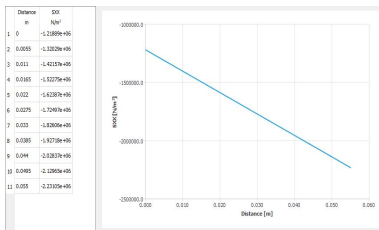


Figure 6.26: Midspan concrete stresses SXX - L.S. 14

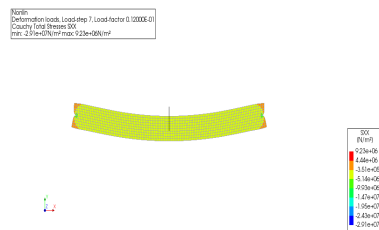


Figure 6.27: Concrete stresses SXX - L.S. 14

Name: Deflection load, Load step 7, Load factor 0.10000E+01  
 Deflection load, Load step 7, Load factor 0.10000E+01  
 min: -1.66e-05 max: 1.66e-05

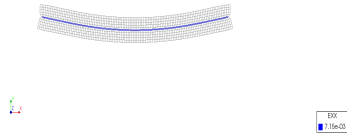


Figure 6.28: Reinforcement strains EXX - L.S. 14

Name: Deflection load, Load step 7, Load factor 0.10000E+01  
 Interface factors FBy  
 min: -4.68e-03 max: 2.44e-03 N/m²

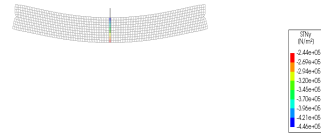


Figure 6.29: Interface normal stresses STNy; L.S. 14

### 6.9.3 Load step 14

The two downward displacements  $u$  at the elements top side increase in magnitude to a value:

$$u = 1.62E - 05 \text{ m}$$

The reaction forces (FBY) at the locations of the applied displacements are increased to:

$$FBY = 946 \text{ N}$$

The concrete cross-section at midspan is under compression over its full height, see figure 6.30. Likewise with the previous load step, the concrete stresses (SXX) increase at top (18%), and decrease at bottom fiber level (figure 6.31). In figure 6.33 it is shown that the two concrete elements are in full contact with each other. The prestressing steel reinforcement (EXX) strains remain constant over the full tendon length after the application of the additional displacement. The downward deflection of the tendon follows the deflection of the surrounding concrete (figure 6.32).

The elements' downward displacement increases as a result of the increased values of displacements at the elements top side. An increased upward curvature following a smooth shape is present over the elements length (figure 6.31).

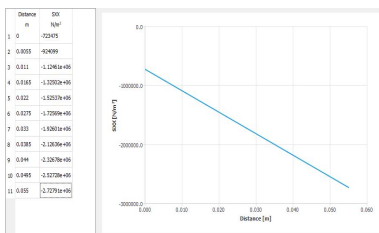


Figure 6.30: Midspan concrete stresses SXX - L.S. 14

Name: Deflection load, Load step 14, Load factor 0.20000E+01  
 Concrete Stress SXX  
 min: -2.91e-03 max: 2.22e-03 N/m²



Figure 6.31: Concrete stresses SXX - L.S. 14

Name: Deformation load, Load step 14, Load factor 0.26000E+01  
 Reinforcement strain EXX  
 min: 1.06E-03  
 max: 1.96E-03

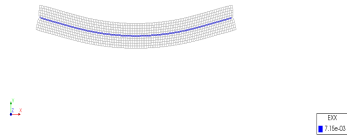


Figure 6.32: Reinforcement strains EXX - L.S. 14

Name: Deformation load, Load step 14, Load factor 0.26000E+01  
 Interface normal stress STNy  
 min: -1.45E+09(N/m²)  
 max: 1.45E+09(N/m²)

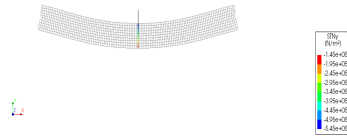


Figure 6.33: Interface normal stresses STNy; L.S. 14

### 6.9.4 Load step 24

This step refers to the load before cracking. The two downward displacements  $u$  at the elements top side increase in magnitude to a value:

$$u = 2.82E - 05 \text{ m}$$

The reaction forces (FBY) at the locations of the applied displacements are increased to:

$$FBY = 1673 \text{ N}$$

Analogous to the previous load step, the concrete cross-section at midspan is under compression over its full height, see figure 6.34. The concrete compression zone height at midspan is:

$$x_u = 55 \text{ mm}$$

The concrete stresses (SXX) linearly increased at top (21%), and decrease at bottom fiber level, compared with the previous load step (figure 6.35). In figure 6.37 it is shown that the two concrete elements are in full contact with each other. The prestressing steel reinforcement (EXX) strains remain constant over the full tendon length after the application of the additional displacement. The downward deflection of the tendon follows the deflection of the surrounding concrete (figure 6.36).

The elements' downward displacement increases as a result of the increased applied loads at the elements top side. A smooth upward curvature is present over the elements length (figure 6.35).

The curvature of the midspan concrete cross-section can be related to the increase in concrete strains over the compression zone height  $x_u$  with the following relation:

$$k = \frac{\Delta\epsilon}{x_u} = 1.485E - 03 \text{ m}^{-1}$$

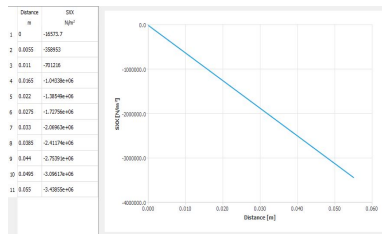


Figure 6.34: Midspan concrete stresses SXX - L.S. 24

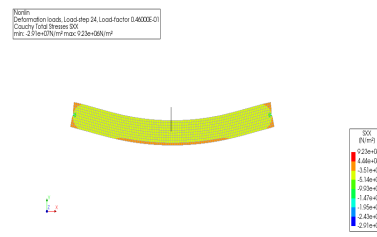


Figure 6.35: Concrete stresses SXX - L.S. 24

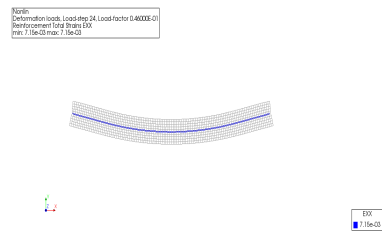


Figure 6.36: Reinforcement strains EXX - L.S. 24

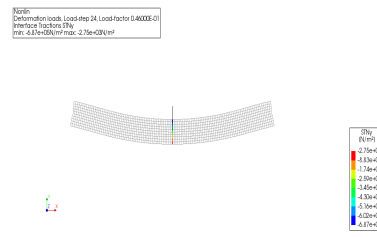


Figure 6.37: Interface normal stresses STNy; L.S. 24

### 6.9.5 Load step 25

This step refers to the load after cracking. The two downward displacements  $u$  at the elements top side increase in magnitude to a value:

$$u = 2.94E - 05 \text{ m}$$

The reaction forces ( $F_{BY}$ ) at the locations of the applied displacements are increased to:

$$F_{BY} = 1746 \text{ N}$$

The concrete compression zone height at midspan is considered to be:

$$x_u \simeq 55 \text{ mm}$$

Since tensile stresses resulting from the bending moment at the bottom fiber, start to surpass the initially present compressive stresses caused by post-tensioning, cracking initiates and the stresses drop to zero at the location of the crack, see figure 6.38. The concrete stresses increased at top by 1.7%, compared with the previous load step (figure 6.39). In figure 6.41 it is shown that the two concrete elements are starting to open at the joint's location bottom side. However the crack is still not visible due to the small value of the tensile stresses. Although cracking occurs, the prestressing steel reinforcement (EXX) strains appear to remain constant over the full tendon length after the application of the additional displacement. The downward deflection of the tendon follows the deflection of the surrounding concrete (figure 6.40).

The elements' downward displacement increases as a result of the increased applied loads at the elements top side. A smooth upward curvature is present over the elements length [6.39](#).

The curvature of the midspan concrete cross-section increases to:

$$k = \frac{\Delta\varepsilon}{x_u} = 1.515E - 03 \text{ m}^{-1}$$

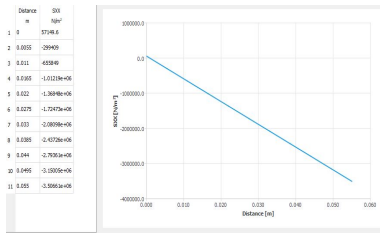


Figure 6.38: Midspan concrete stresses SXX - L.S. 25

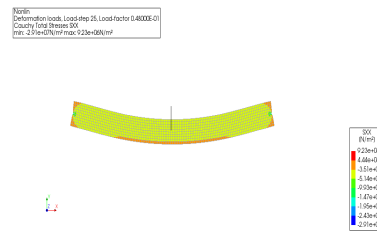


Figure 6.39: Concrete stresses SXX - L.S. 25

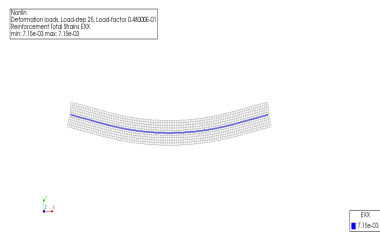


Figure 6.40: Reinforcement strains EXX - L.S. 25

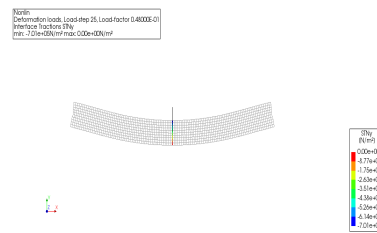


Figure 6.41: Interface normal stresses STNy; L.S. 25

### 6.9.6 Load step 29

A further increase of the two downward displacements  $u$  takes place at the elements top side to:

$$u = 3.42E - 05 \text{ m}$$

The reaction forces (FBY) at the locations of the applied displacements are increased to:

$$FBY = 2032 \text{ N}$$

Due to the increased cracking loads, the tensile zone is increased and the concrete compression zone height at midspan is found to be:

$$x_u \simeq 50 \text{ mm}$$

The tensile strength is now exceeded over a larger height at the bottom, leading to zero stresses for these fibers, see figure [6.42](#). A larger increase in concrete stresses (8%) occurs at top fiber level at this load step, compared

with the previous load step (figure 6.43). The crack at midspan is still not visible for the current displacement loads (figure 6.45). Although cracking took place, no increase in the prestressing steel reinforcement (EXX) strains is found. They remain constant over the full tendon length after the application of the additional displacement load. The downward deflection of the tendon follows the deflection of the surrounding concrete (figure 6.44).

The elements' downward displacement increases as a result of the increased applied loads at the elements top side. A smooth upward curvature is present over the elements length, see figure 6.43.

The curvature of the midspan concrete cross-section increases to:

$$k = \frac{\Delta\varepsilon}{x_u} = 1.810E - 03 \text{ m}^{-1}$$

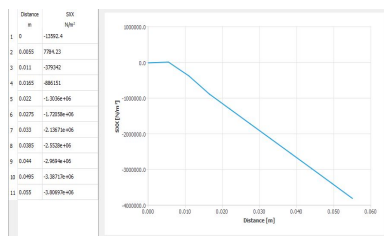


Figure 6.42: Midspan concrete stresses SXX - L.S. 29

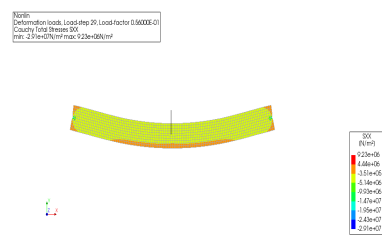


Figure 6.43: Concrete stresses SXX - L.S. 29

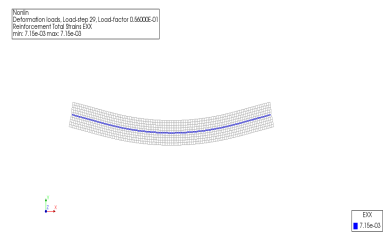


Figure 6.44: Reinforcement strains EXX - L.S. 29

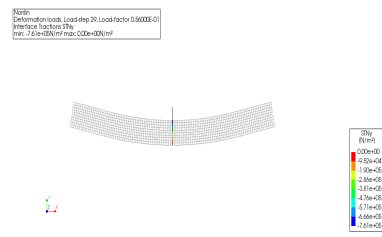


Figure 6.45: Interface normal stresses STNy; L.S. 29

### 6.9.7 Load step 45

A further increase of the two downward displacements  $u$  takes place at the elements top side to:

$$u = 5.34E - 05 \text{ m}$$

The reaction forces (FBY) at the locations of the applied displacements are increased to:

$$FBY = 3038N$$

Due to the increased cracking loads, the tensile zone is further increased and the concrete compression zone height at midspan is found to be:

$$x_u \simeq 33 \text{ mm}$$

Since the concrete tensile strength is exceeded, zero stresses are now visible over an increased part of the cross-section. Concrete tensile stresses (SXX) are present over the increased height of the tensile zone at midspan cross-section, see figure 6.46. An even larger increase in concrete stresses (30.9%) occurs at top fiber level at this load step, compared with the previous load step (figure 6.47). The crack at midspan is still not visible for the current displacement loads (figure 6.49). No increase in the prestressing steel reinforcement (EXX) strains is found. They remain constant over the full tendon length after the application of the additional displacement load. The downward deflection of the tendon follows the deflection of the surrounding concrete (figure 6.48).

As it can be seen from figure 6.35, the curvature of the concrete elements appears to be slightly decreased over their length.

The curvature of the midspan concrete cross-section increases to:

$$k = \frac{\Delta\varepsilon}{x_u} = 3.968E - 03 \text{ m}^{-1}$$

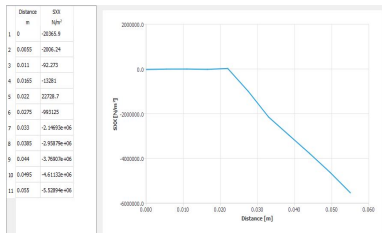


Figure 6.46: Midspan concrete stresses SXX - L.S. 45

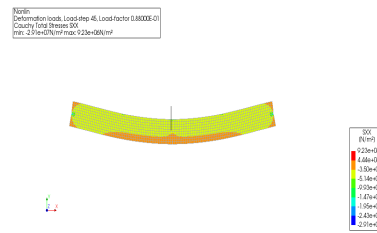


Figure 6.47: Concrete stresses SXX - L.S. 45

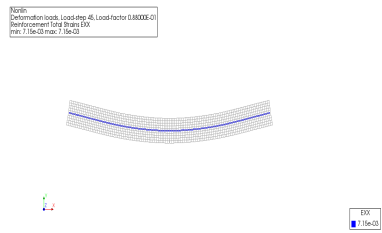


Figure 6.48: Reinforcement strains EXX - L.S. 45

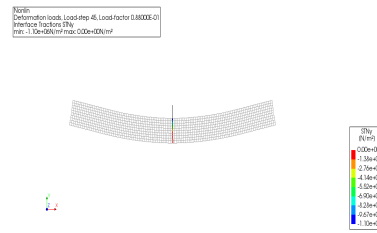


Figure 6.49: Interface normal stresses STNy; L.S. 45

### 6.9.8 Load step 70

A further increase of the two downward displacements  $u$  takes place at the elements top side to:

$$u = 1.18E - 04 \text{ m}$$

The reaction forces (FBY) at the locations of the applied displacements are increased to:

$$FBY = 4508 \text{ N}$$

Due to the increased cracking loads, the tensile zone is further increased and the concrete compression zone height at midspan is found to be:

$$x_u \simeq 12 \text{ mm}$$

Zero stresses (SXX) are present over most of the midspan cross-section's height as seen in figure 6.50. An even larger increase in concrete stresses (68%) occurs at top fiber level at this load step, compared with the previous load step at top fiber level (figure 6.51). The crack at midspan is clearly visible for the current displacement loads (figure 6.53). No increase in the prestressing steel reinforcement (EXX) strains is found. They remain constant over the full tendon length after the application of the additional displacement load. The downward deflection of the tendon follows the deflection of the surrounding concrete (figure 6.52).

The elements' downward displacement increases as a result of the increased applied loads at the elements top side. It appears that the elements curvature due to the applied loads has now substantially decreased over the elements length.

An even larger increase in curvature of the midspan concrete cross-section occurs:

$$k = \frac{\Delta\varepsilon}{x_u} = 3.433E - 02 \text{ m}^{-1}$$

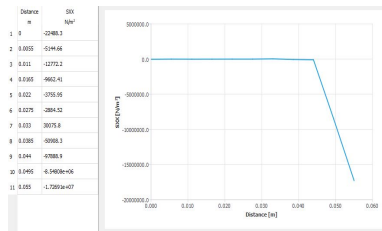


Figure 6.50: Midspan concrete stresses SXX - L.S. 70

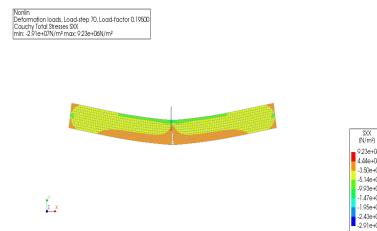


Figure 6.51: Element displacements SXX - L.S. 70

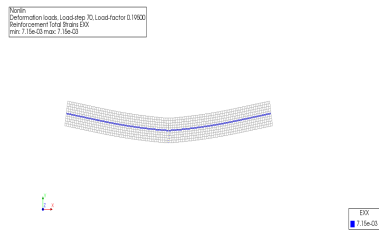


Figure 6.52: Reinforcement strains EXX - L.S. 70

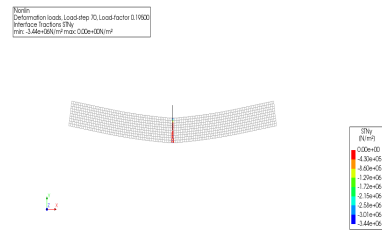


Figure 6.53: Interface normal stresses STNy; L.S. 70

### 6.9.9 Load step 116

A further increase of the two downward displacements  $u$  takes place at the elements top side to:

$$u = 3.31E - 04 \text{ m}$$

The reaction forces (FBY) at the locations of the applied displacements are increased to:

$$FBY = 5000 \text{ N}$$

Due to the increased cracking loads, the tensile zone is further increased and the concrete compression zone height at midspan is found to be:

$$x_u \simeq 5 \text{ mm}$$

The concrete stress distribution of the two concrete elements is shown in [6.54](#). An increase in concrete stresses (64%) occurs at top fiber level at this load step, compared with the previous load step (figure [6.55](#)). The crack at midspan is further increased (figure [6.57](#)). The prestressing steel reinforcement strains (EXX) remain constant over the full tendon length after the application of the additional displacement load. The downward deflection of the tendon follows the deflection of the surrounding concrete (figure [6.56](#)).

The elements' downward displacement increases as a result of the increased applied loads at the elements top side. However, the elements curvature has decreased to such an extent that the elements appear to be straight.

The curvature of the midspan concrete cross-section largely increases to:

$$k = \frac{\Delta \varepsilon}{x_u} = 2.319E - 01 \text{ m}^{-1}$$

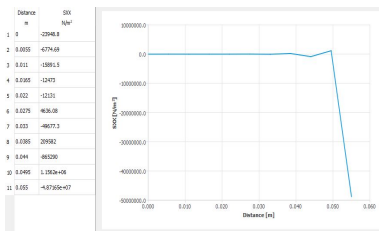


Figure 6.54: Midspan concrete stresses SXX - L.S. 116

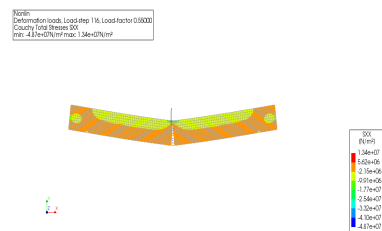


Figure 6.55: Concrete stresses SXX - L.S. 116

Name:   
 Deformation load, Load step 116, Load factor 0.58000   
 Reinforcement strain EXX   
 min.: 1.0e+001 max.: 1.5e+02

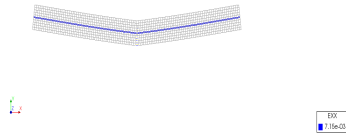


Figure 6.56: Reinforcement strains EXX - L.S. 116

Name:   
 Deformation load, Load step 116, Load factor 0.58000   
 Interface normal stress STNy   
 min.: -1.5e+001 max.: 0.0e+000 [N/m²]

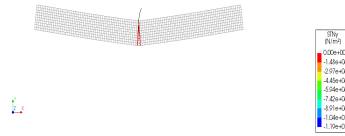


Figure 6.57: Interface normal stresses STNy; L.S. 116

### 6.9.10 Load step 154

A further increase of the two downward displacements  $u$  takes place at the elements top side to:

$$u = 5.59E - 04 \text{ m}$$

The reaction forces (FBY) at the locations of the applied displacements are increased to:

$$FBY = 5223 \text{ N}$$

Due to the increased cracking loads, the tensile zone is further increased and the concrete compression zone height at midspan has reached its minimum value in the present calculation:

$$x_u \simeq 4 \text{ mm}$$

The concrete stress distribution of the two concrete elements is shown in figure 6.58. An increase in concrete stresses 32.73% occurs at top fiber level at this load step, compared with the previous load step (figure 6.59). The crack at midspan is further increased (figure 6.61). No concrete compressive failure is proved, see figure 6.62. Due to small integration issues (mesh element size of 5.5 mm), irregularities are visible in the stress (SXX) and strain (EXX) diagrams. There were considered to be of minor importance and are expected to disappear after refinement of the mesh. The prestressing steel reinforcement strains (EXX) remain constant over the full tendon length after the application of the additional displacement load, although the beam is loaded by a large cracking load. The downward deflection of the tendon follows the deflection of the surrounding concrete (figure 6.60).

The elements' downward displacement increases as a result of the increased applied loads at the elements top side. However, the elements curvature has decreased to such an extent that the elements appear to be straight.

The curvature of the midspan concrete cross-section largely increases to:

$$k = \frac{\Delta \varepsilon}{x_u} = 4.310E - 01 \text{ m}^{-1}$$

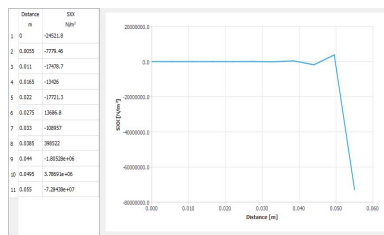


Figure 6.58: Midspan concrete stresses SXX - L.S. 154

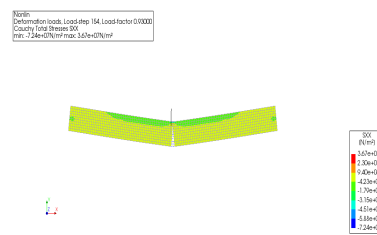


Figure 6.59: Concrete stresses SXX - L.S. 154

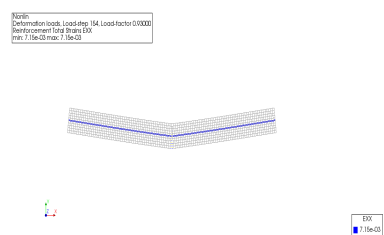


Figure 6.60: Reinforcement strains EXX - L.S. 154

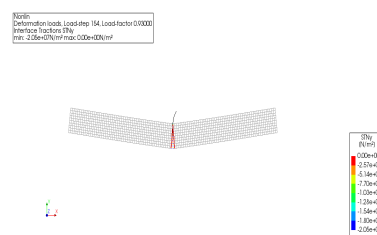


Figure 6.61: Interface normal stresses STNy; L.S. 154

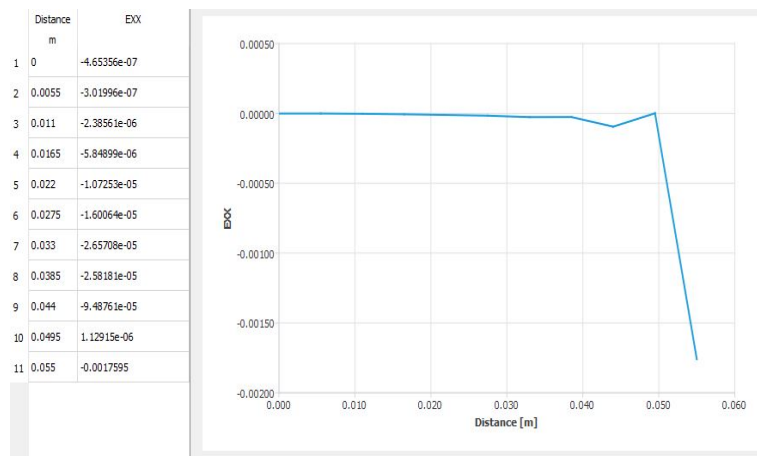


Figure 6.62: Midspan concrete strains EXX -L.S.154

### 6.9.11 Relation between curvature and load

Focusing on the start of horizontal plateau of figure 6.20, an explanation that can be given for the unexpected shape of diagram is based on the change of stiffness during the incremental loading. A load curvature (F-k) diagram was obtained for the midspan concrete cross-section for six of the ten investigated load steps (see figure 6.63 and table B.13). It is found that the curvature of the

midspan concrete cross-section increases linearly up to load step 24 and above, to a value of approximately 2800 N. After reaching that point, the curvature increases non-linearly with increasing loads. The increase in curvature is still limited with increasing loads up to 4000 N. From that point, a huge increase of curvature of the midspan cross-section occurs with the increasing loads, see load step 70 and beyond, in figure 6.63.

As it is shown in the images of the deflected concrete elements, their curvature changes differently during the imposed displacement loads along their length (figure 6.23, 6.35, 6.43, 6.46, 6.51, 6.55, 6.59). In particular, it was found that the elements' curvature was increasing under the applied displacements up to load step 70. A smooth upward curvature was present over the total length of the concrete elements. However, increasing the displacements to load steps 116 and 154 resulted in a huge or complete decrease of the elements curvature. At these points the elements shape is straight. It seems that the deflection scheme of the concrete elements resembles a kinematic mechanism with a "plastic" hinge at midspan, although no concrete or reinforcement failure is found, see figures 6.64, 6.65.

It seems that before reaching a 4000 N force, the elements curvature increases with an increase of curvature of the midspan cross-section. For loads larger than this value, the curvature of the elements decreases substantially while the curvature of the midspan cross-section increases dramatically, see table B.13 and figure 6.63. The combination of the decreasing curvature of the two elements with the increasing curvature at joint's location can be considered as the cause of the "change" in the beams deflection scheme into a kinematic mechanism referring to plastic failure, although no concrete or reinforcement failure is proved to occur.

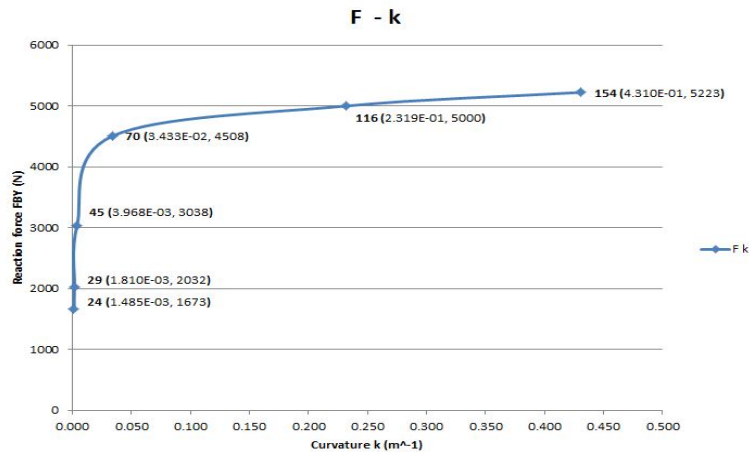


Figure 6.63: Load curvature diagram -  $\Phi 5.2 - u = 0.6[mm]$

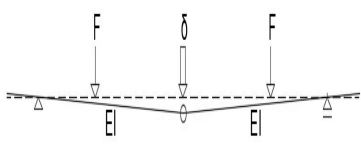


Figure 6.64: Element deflection scheme before 4000 [N]

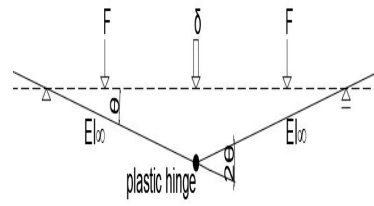


Figure 6.65: Element deflection scheme after 4000 [N]

## 6.10 Conclusions

1. For the investigated size of the prestressing steel reinforcement of  $\Phi 5.2$ , an increase in the reaction forces at the vertical displacements' location was observed, followed by a horizontal plateau occurring at quarter length displacements  $u = 0.6$  mm in the load deflection diagram presented in figure 6.20. This result was not expected since it was proved via hand-calculations and FE analysis results that no failure of concrete or reinforcement took place under this load. Note that no concrete crushing failure criterion was set in the model and the only non-linearity that was input in the model was the discrete cracking interface model at joint's location. The reason that lies in the initiation of the horizontal plateau may be explained by the relation between the change of curvature of the two concrete elements and the change of curvature of the joint element in-between them, while increasing the applied displacement loads at the element's top side. It was proved that after reaching a certain load ( $\simeq 4$  KN), the surrounding concrete elements appear as having an infinite stiffness compared to the stiffness of the the joint element in between them. From that load and increasing its value further on, the deflection scheme of the model resembles a kinematic mechanism with a plastic hinge at midspan. This mechanism can be considered as the cause of the horizontal plateau in the load deflection diagram in figure 6.20.
2. Although the internal bending moment was verified versus the externally applied loads, the resulting displacements in DIANA cannot be trusted. The rigid body motion with a "straightening" of the two concrete elements under the applied loads of the FE model, resulted in large values of concrete compressive forces compared with the hand-calculated results.
3. The main function of the post-tensioning steel reinforcement was to connect the concrete elements. It was proved that a certain decrease of flexural tensile stresses under the applied loads can be achieved taking into account that anchors were set at the elements centroidal axis.
4. The deflection of the reinforcement seems to follow the deflection of the surrounding concrete elements. After concrete cracking the tendon remains horizontal in the crack and two kinks are formed on the prestressing steel reinforcement. Although an increase in the prestressing steel reinforcement is expected, the FEM does not show an increase in the prestressing steel loads after cracking.
5. The structural interface input at the connection of the concrete elements with the joint in-between, resulted in the expected localized cracking at midspan after reaching the concrete cracking load. It was proved that an increase in the crack width and a reduction of the compression zone height occurs by further increasing the cracking load.

## 6.11 General conclusion

The connection of two concrete elements with unbonded post-tensioning steel reinforcement in order to improve their flexural strength is indeed a measure that can be taken. However, due to the slender height of the investigated concrete

elements, the prestressing steel was anchored at the elements centroidal axis. Therefore the additional value for the test specimens tensile capacity, is only caused via compression and not through bending, as it would have been done in cases of eccentric prestressing steel reinforcement. It must be noted that shell structures are form-resistant and their structural response is not the same with the investigated straight elements of this research.

## Part VI

# Post-tensioned concrete arch structure

## 7 Summary

As a step towards the implementation of structural double curved concrete elements in real life structures, a post-tensioned arch consisting of eleven precast concrete elements, was investigated under a linear static analysis. Hand calculations were also performed in order to verify the FEM analysis results. The main goals were first to combine CAD and FEM software for the more complex curved geometry of an arch, and subsequently to analyze its structural response under the applied loads.

### 7.1 Physical problem

A post-tensioned arch structure consisting of eleven curved precast concrete elements is going to be produced via the flexible mould, the CAD and FEM design of the arch had to be investigated. The arch structure is assumed to have clamped connections with an assumed stiff soil. Similarly to the four point bending test, high strength concrete C80/95 will be used in the current model, see table [6.2](#). The connections between the elements are formed by cement mortar joints and two continuous post-tensioned steel cables, anchored at the two edges of the structure. The type of prestressing steel to be used is cables consisting of 3-wire strands of type Y1860S3 and a diameter  $\Phi = 6.8$  mm. The prestressing steel cables are positioned at a distance from the element edge, equal to one sixth of the element width ( $x = 166.67$  mm), table [7.1](#). No bond between concrete and steel is taken into account in this model. Instantaneous losses from wedge set, friction or unintended rotations during tensioning are set to zero. Time dependent losses from shrinkage, creep and relaxation are not taken into account in the current analysis, as was the case of the four-point bending test. The prestressing steel cables are loaded by  $P = 10$  KN at the position of the four anchorages. The loads applied at the structure are the concrete self-weight and the prestressing steel forces. After having designed the final shape and size of the arch structure in RHINO, a linear static analysis will be performed in DIANA10.2 to analyze its response under the applied loads.

Prestressing steel type	Y1860S3
Number of cables n	2
Distance from edge x [mm]	166.67
Diameter $\Phi$ [mm]	6.8
Cross -section area $S_n$ [mm <sup>2</sup> ]	23.4
Prestressing steel modulus of elasticity $E_P$ [MPa]	195000
Prestressing steel material factor $\gamma_s$	1.1
Characteristic tensile strength $f_{pk}$ [MPa]	1860

Table 7.1: Prestressing steel - Arch structure

## 7.2 Initial CAD model

An initial RHINO model including the arch geometry was provided, as a guidance for the creation of its final geometry, see figure 7.1. The eleven concrete elements are double-curved with a decreasing arc width from bottom to crown. The two bottom dark colored elements have a maximum width of  $b_{max} = 712.38$  mm, while the two top green colored elements have the minimum arc width of  $b_{min} = 421.94$  mm. The arc length of the different elements is defined by a radial segmentation technique, and has an approximately constant value of  $l_{el} = 620$  mm. This model denoted as the “Initial CAD Model” for the sake of simplicity, has a drupe  $f = 2378$  mm and a span  $L = 4031$  mm. The arc surface constructed by NURBS curves, has a minimum radius of curvature is in the range of [927.87 mm, 1132.67 mm]. The joints in between the elements had still to designed, the thickness of which had to be defined by the author. In the given the geometry of the “Initial CAD Model” the joint thickness was  $t = 12$  mm.

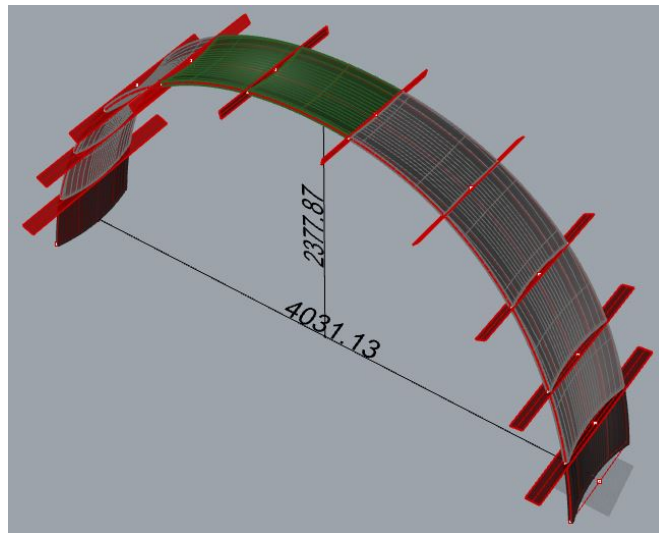


Figure 7.1: Initial model”arch geometry- varying element size

### 7.3 Final CAD model

For the design of the arc structure, it was required to determine the thickness of the joints. The indicative value of joint thickness  $t = 12\text{ mm}$  given in the “Initial CAD model” was considered small, and therefore an increased value of  $t_j = 55\text{ mm}$  was incorporated in the model, taking into account minimum concrete cover and construction requirements for placing the steel cables as well as the  $t_{et} = 50\text{ mm}$  joint thickness used for the previous model of the 4-point bending test. Radial segmentation technique was also used for this model resulting in an arc length per element of  $l_{el} = 570\text{ mm}$ , see figure 7.2. Based on the design of the “Initial model” a FEM was created. The DIANA10.2 model was pre-processed, forming the clamped connections of the arc with the soil, see figure 7.3. Having applied the self-weight of the concrete and the post-tensioning loads, when running the linear static analysis, geometrical errors occurred while meshing the elements. In particular, sharp angles between the element edges less than 10 degrees or larger than 170 degrees were indicated as a warning from DIANA10.2. Therefore, the analysis results could not be considered reliable unless geometrical modifications were made.

Several options were investigated in RHINO, in order to solve the problem of “sharp angles” between the element edges and are listed below:

1. The surfaces of the solids were rebuilt based on a degree of  $U = V = 3$ , generating a grid with higher density in comparison with the default values. A small deviation from the geometry of the final model was to be expected. However, after importing the new rebuilt model in DIANA10.2, the problem of the sharp edges was not solved.
2. Decreasing the curvature of the arch by using a smaller drapage did not result in the desired outcome of “smooth edges” that can be meshed in DIANA10.2.
3. Segmenting the arc structure in a small number of elements did not have a positive result in the formation of the edges.
4. Creating the arc surface based on the geometrically defined curve of a half circle, produced the desired outcome of “smooth edges” required for meshing in DIANA10.2. The final surface of the arch was also rebuilt and re-trimmed as described above with a degree of  $U=V=3$ . This case is denoted as the “Final model”, However, a quite different geometry was obtained with comparison to the “Initial model”, since the arc structure in the “Final model” was consisting of curved elements having constant dimensions:  $l_{el} = 593.6\text{ mm}$  and  $b_{el} = 700\text{ mm}$ , see figure 7.4, and table 7.2. Note that the dimensions shown in this figure, correspond to the center line of the arc surface.

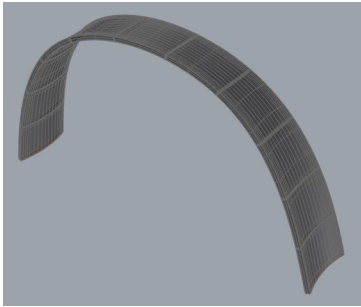


Figure 7.2: Arch structure geometry - RHINO

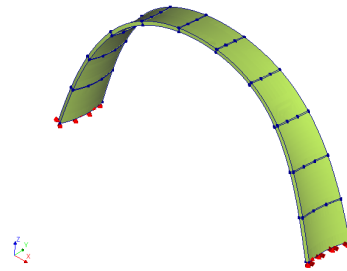


Figure 7.3: Arch structure geometry and boundary conditions- DIANA10.2

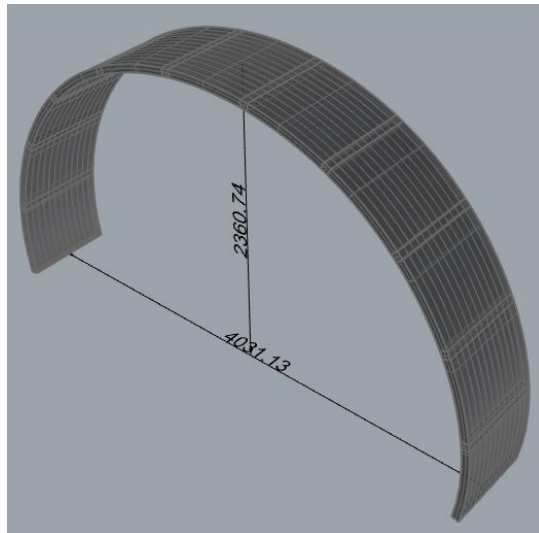


Figure 7.4: "Final model" arch geometry- constant element size

Arch radius at center line $R_C[mm]$	2015.56
Drape $f [mm]$	2360.74
Thickness $t [mm]$	55
Arch length at center line $l_{ot}[mm]$	7079.62
Concrete cross-section area $A_c [mm^2]$	348263.77
First moment of area $I_C [mm^4]$	7.07e11
Number of elements $n_{el}$	11
Element length $l_{el}[mm]$	593.60
Element width $b_{el} [mm]$	700
Number of joints	10
Joint thickness $t_j[mm]$	55

Table 7.2: Arch geometrical properties

## 7.4 Finite element modeling (FEM) - Arch structure

Three dimensional (3D) modeling was selected for the investigated arch structure. Although considered as a more complicated type of analysis, producing large number of equations in comparison with two dimensional (2D), aiming at a three dimensional spread of forces. This was the initial choice made by the author.

### 7.4.1 Element types and mesh

Solid elements were used for modeling of the arch. According to DIANA10.2 manual, these elements may produce inaccurate results and should be applied only when other elements are unsuitable. However, since the RHINO model was imported as a solid structure in the DIANA10.2 interface and was the first decision of the author to proceed with 3D modeling and solid elements, this was also the final choice. Two types of solids were used for modeling the concrete, namely the CHX60 20-node brick element (figure 5.4) and the CTP45 15-node wedge element (figure 5.5).

An eight node quadrilateral isoparametric plane stress element namely the CQ16M, based on quadratic interpolation and Gauss integration scheme were used in this type of analysis. Quadratic interpolation was selected instead of linear, so that a more refined analysis will be performed in terms of the deflection and the stress field components. The mesh element size was selected to be 50 mm creating 14 elements along the arc width, taking into account the maximum allowed element size (Hendriks, 2016).

## 7.5 Linear static analysis

The FEM model of the arch structure depicting its boundary conditions, is presented in figure 7.5 and 7.6. As indicative of FEA results for the current model, the concrete stresses due to self-weight are presented in figures 7.7, 7.8.

The hand calculations were based on the total strain energy approach in order to calculate the internal loads, see figure 7.9. Since there was poor agreement between the DIANA results and the hand-calculations, and within the available time, no clarity was obtained which of the two calculations was wrong. This needs to be further investigated by future follow-up research.



Figure 7.5: Arch structure geometry and boundary conditions- DIANA10.2

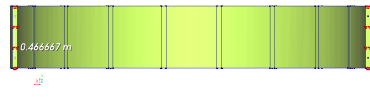


Figure 7.6: Arch structure bottom view- distance between anchors- DIANA10.2

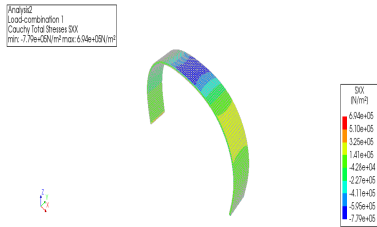


Figure 7.7: Concrete element stress distribution SXX due to self-weight SW - DIANA10.2

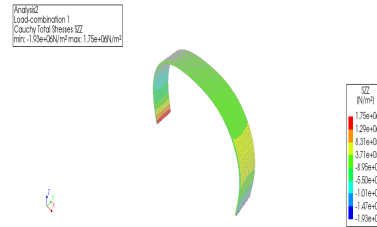


Figure 7.8: Concrete element stress distribution SZZ due to self-weight SW - DIANA10.2

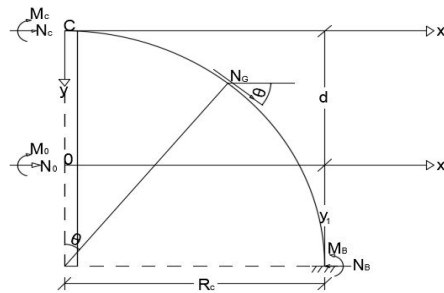


Figure 7.9: Arch internal loads and boundary conditions - Hand calculations scheme

### 7.5.1 Test limitations

1. The post-tensioning load could not be accompanied with a wedge set for this Finite Element Model and hence chosen to be neglected in the considered analysis. The reason for this choice is that warnings occurred when running the structural analysis, and a uniform stress reduction along the prestressing steel would occur.

- Concerning design limitations, the initial arch design could not be successfully meshed in DIANA10.2. Warnings occurred during the linear static analysis, indicating sharp angles between the element edges being smaller of  $10^\circ$  or larger than  $170^\circ$ .

## 7.6 Recommendations

Some recommendations that can be made for further research are:

- Modeling the arch structure with a two dimensional elements may be an alternative way in meshing the concrete elements that could provide more insight in the structural response of the arch structure.
- Using a different FEA program that could incorporate every geometrical three dimensional shape may be a way to address the problem of meshing the initial double-curved arch geometry.
- Improving the model with regard to the location of the anchors is essential for the validity of the model. Figures [7.10](#), [7.11](#), [7.12](#) show a alternative way to prestress the concrete arch structure.

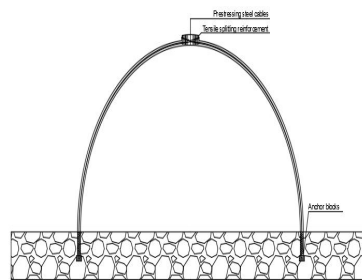


Figure 7.10: Arch structure with abutment and anchor blocks at the foundation

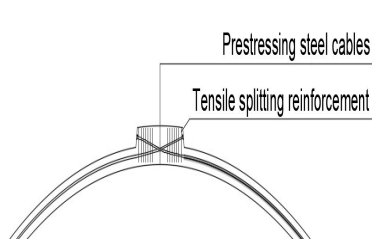


Figure 7.11: Abutment side view

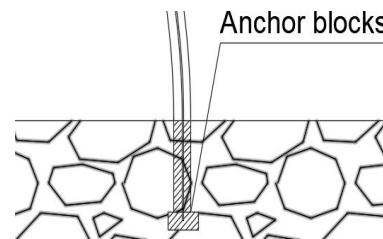


Figure 7.12: Anchor block at soil

## Part VII

# Discussion & Conclusions

## 8 Discussion

This chapter is a recapitulation of the research done in the previous parts, by analyzing aspects and conclusions made, with regard to the main research scope of the thesis. Critical viewpoints and observations that occurred during the current study are included. The sequence followed in writing the previous chapter is also used for developing the current one.

In the beginning, a literature review was done in order to gain knowledge from previous researches related to the “Flexible Mould” concept. Insights related to the development of the adjustable formwork and its constituents were considered to be essential for the experimental investigation on the applicability of double-curved concrete produced with the adjustable formwork on real life structures. The literature review also comprised of a number of studies relevant to structural analyses of shell elements, setting the basis for the current investigation on possible improvements in the tensile capacity of double-curved concrete elements via post-tensioning steel reinforcement.

Having obtained the knowledge about the production of concrete shells with the adjustable formwork, four double-curved concrete elements were CAD designed in RHINO. Their shape and size complied with the limitations imposed from the available test set-up of the flexible formwork at TU Delft. Thereafter, laboratory tests did follow, first using sand as the main material to simulate concrete’s self-weight of the designed shell elements. The main reason behind this choice was the lower cost of sand in comparison with casting concrete, as well as the lack of experience of the author with the flexible mould. In addition the complexity of edge profiling with the adjustable formwork, was still an issue to be solved prior to casting the designed concrete shells on the flexible mould. In particular, the method of projecting the designed concrete shells’ coordinates with a beamer on the horizontal surface of the mould, proved to be a difficult process which resulted in distortion of the element’s coordinates. Therefore no accurate formation of the edges was possible and concrete tests did not take place. However, the sand tests resulted in certain qualitative conclusions with regard to the relation of the deflection of the used steel wire mesh and the number of actuators used. In particular, it was proved that the increase of the number of actuators acting as support points on the elastic layer, could produce the desired-designed curvature of the elements surface without wriggling and ponding effects.

The next parts of the thesis refer to the investigation on improvements in the flexural tensile capacity of straight and curved concrete elements via post-tensioning steel reinforcement. Computer Aided Design and Finite Element Modeling were the main tools used in this part. Prior to modeling the more complex geometry of an arch structure consisting, an intermediate step was included in the research, where “simple” shaped two- and three-dimensional concrete elements were analyzed under the applied loads in a linear static analysis. Several parameters were investigated, such as the way of modeling the prestressing steel forces in the FE model, the division of single elements in

two or three smaller in length parts, the use of a structural interface with linear elastic properties at a joint, as well as the influence of the formed element edges on their deflection and stress field. Concerning the way of modeling the prestressing steel forces, it was proved that applying the prestressing loads as two compressive point loads acting on the anchorages locations was not giving the same analysis results with regard to the deflection of the beam in comparison with a beam model where the tendon's geometrical and physical properties were input. The choice for no bond or bond interaction between prestressing steel and concrete could not be incorporated in this part. It was also concluded that FEM modeling of the prestressing steel's geometry relative to the curved profile of the surrounding concrete elements, may be considered an advanced approach for a more detailed structural analysis. Therefore the second way of modeling the prestressing load may be considered a more refined method for the shell elements' geometries. Concerning the linear elastic material properties of a structural interface set on a joint element, it was proved that an increase in the stiffness moduli resulted in a decrease of the midspan deflections of the concrete.

As a further step towards the development of the Flexible Mould, considering joints as the "weakest" spot in precast concrete structures, the influence of joint stiffness in brittle failure of the surrounding concrete elements was studied in the next part of the thesis. In particular, a four point bending test on two centrally prestressed concrete elements, being connected with a mortar joint in-between them, was the next two-dimensional finite element model to be investigated. First, linear static analysis were conducted in order to gain insight of the occurring displacement and stress fields due to the applied loads. The structure was expected to fail on zero concrete tensile strength and cracking loads were applied on the elements' top side. The post-tensioning steel reinforcement was designed in order to take up the occurring tensile stresses from the applied loads. Having verified the linear static analysis results with hand calculations, a phased nonlinear static analysis was conducted in order to model the material non-linearity of a joint in between the two precast concrete elements. Due to the assumption that cracking would start and localize at the spot of zero concrete tensile strength, a discrete cracking model was created. The nonlinear static analysis results were verified. However, they are not considered to be describing the problem thoroughly. In particular, the resulted force deflection ( $F-\delta$ ) diagram at the concentrated loads' location from the 4-point bending test, showed an increase of the forces even after cracking at midspan. A smeared cracking model based on the change of material properties of the whole structure and not only at the joint location could be a point of investigation for further research.

The final part of this thesis was focused on a linear static analysis of a post-tensioned arch structure segmented in a series of single curved concrete elements. The initial goal was to model a double-curved concrete arch under its self-weight and applied post-tensioning loads. However, inputting the arch geometry from RHINO to DIANA10.2 resulted in sharp edges between the concrete elements and warnings occurred. Therefore, simplifying the initial arch geometry in single-curved was considered essential for the process of the research. The final design of the arch was made according to the conclusions drawn in the previous parts. Three dimensional solid elements were selected to describe the the occurring stress distribution in the finite element model. This choice was made taking into account the free-form shape of concrete shell structures and

their three dimensional spread of stresses caused by their shape. Differences in the predicted values of hand-calculations and the calculated DIANA10.2 results occurred. In addition, several points of attention are raised with regard to the anchors location as well as the prestressing steel reinforcement stresses, which seem to be opposing the basic notion that prestressing is pre-deforming. Further research with regard to these aspects is recommended for this part.

## 9 Conclusions

From the whole research the following conclusions are drawn:

1. It is essential to understand the manufacturing method of precast shell elements via the flexible mould process in order to perform correct calculations.
2. From the laboratory tests with sand loads it was concluded that increasing the number of actuators is crucial for obtaining a smooth curvature in the flexible mould surface. In addition, projection of the correct position of the element edges using a beamer is very challenging, due to the distortion of the CAD designed images when projected with a beamer on the mould's surface. The method appeared to lack accuracy with the available equipment in the present research.
3. It is possible to transfer 3D geometry from RHINO to DIANA, but geometrical limitations are imposed in DIANA and specific types of solid elements can be chosen.
4. The finite element modeling with DIANA of unbonded post-tensioning steel in combination with discrete cracking interface elements between the surrounding concrete elements is challenging and error-prone. The hand calculations proved to be indispensable in making mistakes in the models or produce unreliable analysis results.
5. Good agreement was found between hand calculations and DIANA results with regard to the internal and external bending moment at midspan in the 2D beam models. The calculation of the deflections, showing a plateau at an unexpectedly low load level, raises doubts around the way unbonded tendons are taken into account in the interface element. This remains to be investigated by future researchers.

## A DIANA10.1 simple shaped models

The geometry of the models was designed in DIANA10.1 and subsequently linear static analyses were performed for all cases.

### Case 1 - Unreinforced concrete beam

**Loads:** The beam will be subjected to its self-weight (SW), a uniformly distributed load  $q_{UDL} = 1000[N/m]$  and a point load  $P_{mid} = 1000[N]$ , both acting on its top face. The middle of the top face will be the position of the point load. A load combination of all the applied loads (LC4) will also be included in this case ( $SW + q_{UDL} + P_{mid}$ ), see [A.1](#).

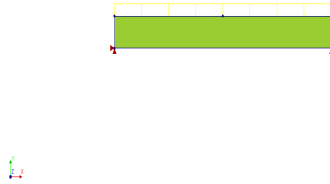


Figure A.1: Boundary and loading conditions

**Outputs:** The deflection (DtY) and the Cauchy stresses (SXX) will be the investigated results of this analysis.

**Deflection (DtY)** The deflection of the beam under the total load combination (LC4) is shown in [A.2](#). In [A.1](#), the midspan deflection values (DtY -  $\delta$ ) based on FEM and hand-calculations (H.C) for each load, are shown. It is proved that the total displacement is equal to the sum of the deflections caused by the individual components and that the maximum deflection occurs at midspan. The calculated deflections are found approximately the same with the ones calculated via DIANA 10.1, thus, it can be concluded that the deflections are verified.

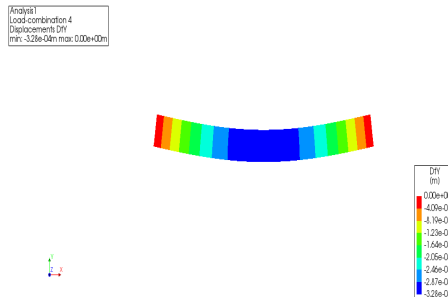


Figure A.2: Element deflection DtY - LC4

$\delta$ [m]	F.E.M. <sub>1</sub>	H.C. <sub>1</sub>	$\frac{H.C._1}{F.E.M._1}$ (%)	$\frac{H.C._1 - F.E.M._1}{H.C._1}$ (%)
$\delta_{SW}$	+2.714E-04	+2.713E-04	100	0.04
$\delta_{UDL}$	+4.604E-05	+4.340E-05	94	5.73
$\delta_{Point}$	+1.473E-05	+1.389E-05	94	5.70
$\delta_{tot}$	+3.321E-04	+3.290E-04	99	0.93

Table A.1: Midspan element deflection per load

**Cauchy stresses SXX** The bending stresses SXX of the beam under the total load combination (LC4) are shown in (A.3). In table (A.2), the FEM and H.C values of stresses at top and bottom fiber level according to the respective load are shown. A linear stress distribution based on the Euler's Bernoulli beam theory, over the height of beam's cross - section is proved, with the highest stress occurring at midspan of the beam for all loads. At top fiber level, the total (LC5) stresses differ by 1.8% and by 4.5 % at bottom fiber level. Since the calculated stresses are found approximately the same ( $< 5\%$ ) with the ones derived with DIANA 10.1, it can be concluded that the stresses are verified.

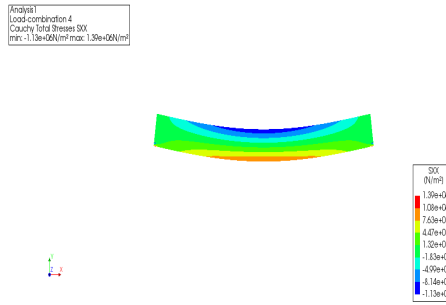


Figure A.3: Element stresses SXX - LC4

Top	SXX [N/m <sup>2</sup> ]	F.E.M. <sub>1</sub>	H.C. <sub>1</sub>	$\frac{H.C._1}{F.E.M._1}$ (%)	$\frac{H.C._1 - F.E.M._1}{H.C._1}$ (%)
	SXX <sub>SW</sub>	-8.850E+05	-9.37E+05	106	5.9
	SXX <sub>UDL</sub>	-1.500E+05	-1.50E+05	100	0.00
	SXX <sub>Point</sub>	-9.410E+04	-6.00E+04	64	36.2
	SXX <sub>tot</sub>	-1.130E+06	-1.15E+06	102	1.8
Bottom	SXX [N/m <sup>2</sup> ]	F.E.M. <sub>1</sub>	H.C	$\frac{H.C._1}{F.E.M._1}$ (%)	$\frac{H.C._1 - F.E.M._1}{H.C._1}$ (%)
	SXX <sub>SW</sub>	+8.850E+05	+9.37E+05	106	5.9
	SXX <sub>UDL</sub>	+1.500E+05	+1.50E+05	100	0.00
	SXX <sub>Point</sub>	+5.900E+04	+6.00E+04	102	1.7
	SXX <sub>tot</sub>	+1.100E+06	+1.15E+06	104	4.5

Table A.2: Midspan element stresses SXX

## Case 2 - Prestressed concrete beam - anchorages at the centroidal axis

**Loads:** Central prestressing will be applied at both ends of a simply supported beam. A linear tendon will be anchored at the supports at the position of

beam's centroidal axis. All loads from case one will be applied in addition to the prestressing force  $P = 1000[N]$ , applied as concentrating concrete compressive loads at both anchorages, see figure (A.4).



Figure A.4: Boundary and loading conditions

**Outputs:** The deflection (DtY) and the Cauchy stresses (SXX) will be the investigated results of this analysis.

**Deflection (DtY)** As it was expected no deflection due to central prestressing (LC4) occurred  $\delta_P = 3.193e - 7[m]$ . The total displacement (LC5) at midspan of the beam is almost equal to the value resulted from Case 1 ( $\delta_{tot} = 3.321e - 4$ ) where no tendon was input see figure (A.5). In table (A.3), the resulted values of deflection per load are shown.

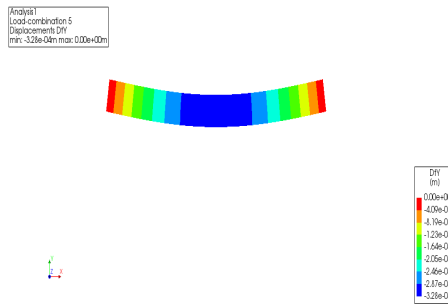


Figure A.5: Element deflection DtY - LC5

$\delta$ [m]	F.E.M. <sub>2</sub>	F.E.M. <sub>1</sub>
$\delta_{SW}$	+2.714E-04	+2.714E-04
$\delta_{UDL}$	+4.604E-05	+4.604E-05
$\delta_{Point}$	+1.473E-05	+1.473E-05
$\delta_P$	-3.193E-07	-
$\delta_{tot}$	+3.32E-04	+3.321E-04

Table A.3: Midspan element deflection per load

**Cauchy stresses SXX** The midspan stresses of the beam under the total load combination (LC5) are shown in figure (A.6). Table (A.4) shows the values of midspan stresses for each applied load. Similar to Case 1, the highest stresses appear at midspan of the beam for all loads. The prestressing force at both ends of the centroidal axis of the concrete beam, introduces a compressive stress:  $\sigma_c^P = -\frac{P}{A_c} = -4e3[N/m^2]$ . Thus, the total stresses according to case 1 will have to be superimposed to the stress introduced by the prestressing loads. Therefore, the hand calculated values from Case 2 are identical to the ones from Case 1, with the additional term of concrete stress due to the two compressive forces at both element edges. Comparing the predicted values of midspan stresses with the F.E.M. ones found in Case 1, it was proved that the differences at top and bottom fiber level are 1.47% and 4.76%, hence assumed as verified. Comparing the F.E.M. stress results found in Case 2, it was shown that at top fiber level the stresses increased by 0.35%, while at bottom fiber level they decreased by 0.82% relative to the stresses found in case 1, see table (A.4)

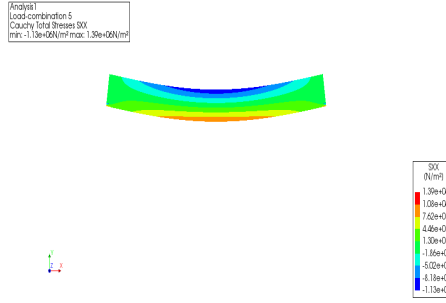


Figure A.6: Element stresses SXX - LC5

Top	SXX	H.C. <sub>2</sub>	FEM. <sub>2</sub> [N/m <sup>2</sup> ]	FEM. <sub>1</sub> [N/m <sup>2</sup> ]	$\frac{FEM_2 - FEM_1}{FEM_2}$ (%)
	SXX <sub>SW</sub>	-9.37E+05	-8.852E+05	-8.850E+05	0.02
	SXX <sub>UDL</sub>	-1.50E+05	-1.504E+05	-1.500E+05	0.27
	SXX <sub>Point</sub>	-6.00E+04	-9.411E+04	-9.410E+04	0.01
	SXX <sub>P</sub>	-4.00E+03	-4.00E+03	-	100
	SXX <sub>tot</sub>	-1.151E+06	-1.134E+06	-1.130E+06	0.35
Bottom	SXX	H.C. <sub>2</sub>	FEM. <sub>2</sub> [N/m <sup>2</sup> ]	FEM. <sub>1</sub> [N/m <sup>2</sup> ]	$\frac{FEM_2 - FEM_1}{FEM_2}$ (%)
	SXX <sub>SW</sub>	+9.37E+05	+8.852E+05	+8.850E+05	0.02
	SXX <sub>UDL</sub>	+1.50E+05	+1.504E+05	+1.500E+05	0.27
	SXX <sub>Point</sub>	+6.00E+04	+5.893E+04	+5.900E+04	0.12
	SXX <sub>P</sub>	-4.00E+03	-4.000E+03	-	100
	SXX <sub>tot</sub>	+1.143E+06	+1.091E+06	+1.100E+06	0.82

Table A.4: Midspan element stresses SXX

### Case 3 - Prestressed concrete beam - tendon at centroidal axis

An alternative to the previous model, will be the input of prestressing steel reinforcement at the centroidal axis. In this way, the interaction of concrete and steel through bond will be taken into account, see figure (A.7). Instead

of applying concrete compressive forces at the element edges as in Case 2, a prestressing steel stress was applied as a load to the linear tendon profile:  $\sigma_P = \frac{P}{A_P} = \frac{10^3}{10^{-4}} = 10e7 [N/m^2]$ .

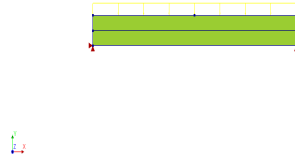


Figure A.7: Boundary and loading conditions

**Outputs:** The deflection (DtY) and the Cauchy stresses (SXX) will be the investigated results of this analysis.

**Deflection (DtY)** The difference in midspan deflections due to the total load combination (LC5) between Case 2 and Case 3 is very small (0.91%) and thus considered to be the same (see table A.5). Note that the difference in midspan deflection for the applied prestressing loads (LC4) is found to be large (54.52%).

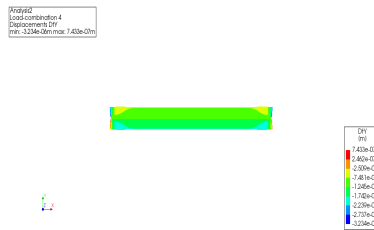


Figure A.8: Element deflection DtY - LC4

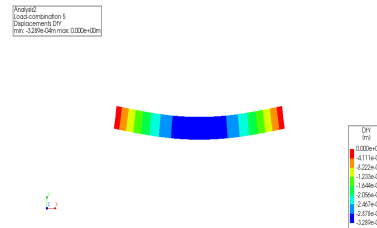


Figure A.9: Element deflection DtY - LC5

$\delta$ [m]	F.E.M. <sub>3</sub>	F.E.M. <sub>2</sub> (m)	$\frac{F.E.M._3}{F.E.M._2}$ (%)	$\frac{FEM._3 - FEM._2}{FEM._3}$ (%)
$\delta_{SW}$	+2.68E-04	+2.714E-04	99	1.27
$\delta_{UDL}$	+4.54E-05	+4.604E-05	99	1.41
$\delta_{Point}$	+1.46E-05	+1.473E-05	99	0.89
$\delta_P$	-7.02E-07	-3.193E-07	220	54.52
$\delta_{tot}$	+3.29E-04	+3.320E-04	99	0.91

Table A.5: Midspan element deflection per load

**Cauchy stresses SXX** The stresses of the beam under the total load combination (LC5) are shown in the figure (A.10). The midspan concrete stresses per applied load are shown in table (A.6). Similar to case one, the highest stresses appear at midspan of the beam for all loads. Comparing this case with the case without the tendon's physical and geometrical characteristics in the model (Case 2), it appears that in Case 3, at top fiber level, the stresses increase by 25.44%, while at bottom fiber level, the stresses decrease by 55.10%. Note also, that although it would be expected that the midspan element stresses due to prestressing loads (LC4) to be similar in values, this was not the case. There is a large difference of 98.98% in element stresses SXX for LC4 between Case 2 and Case 3. It seems that although the applied prestressing steel stress ( $10e7 \frac{N}{m^2}$ ) is proved to occur in the reinforcement stress SXX results (figure A.11), the concrete element stresses SXX for LC4 at midspan are not validated, see table A.6

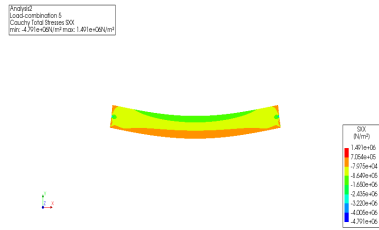


Figure A.10: Element stresses SXX - LC5

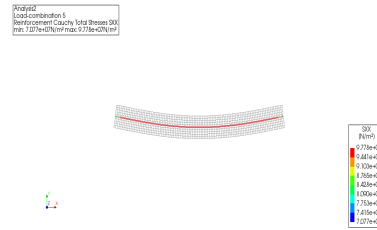


Figure A.11: Prestressing steel stresses SXX - LC5

#### Case 4 - Prestressed concrete beam - anchorages at a distance of 0.15[m] below the centroidal axis

**Loads:** Eccentric prestressing will be applied at both ends of a simply supported beam, at a distance of 0.15[m] from the centroidal axis. The tendon will be of straight linear profile in this case. All loads from case one will be applied in addition to concrete compressive prestressing forces  $P = 1000[N]$  acting on both anchorages, see figure (A.12). In this case, the tendon will be omitted and only the resultant compressive forces at both beam ends will be applied on the concrete.

Top	SXX [N/m <sup>2</sup> ]	F.E.M. <sub>3</sub>	F.E.M. <sub>2</sub>	$\frac{FEM.3 - FEM.2}{FEM.3} (\%)$
	SXX <sub>SW</sub>	-8.852E+05	-8.850E+05	0.00
	SXX <sub>UDL</sub>	-1.504E+05	-1.504E+05	0.00
	SXX <sub>Point</sub>	-9.411E+04	-9.411E+04	0.00
	SXX <sub>P</sub>	-3.911E+05	-4.000E+03	98.98
	SXX <sub>tot</sub>	-1.521E+06	-1.130E+06	25.44
Bottom	SXX [N/m <sup>2</sup> ]	F.E.M. <sub>3</sub>	F.E.M. <sub>2</sub>	$\frac{FEM.3 - FEM.2}{FEM.3} (\%)$
	SXX <sub>SW</sub>	+8.852E+05	+8.850E+05	0.00
	SXX <sub>UDL</sub>	+1.504E+05	+1.500E+05	0.00
	SXX <sub>Point</sub>	+5.893E+04	+5.900E+04	0.00
	SXX <sub>P</sub>	-3.911E+05	-4.000E+03	98.98
	SXX <sub>tot</sub>	+7.034E+05	+1.100E+06	55.10

Table A.6: Midspan element stresses SXX

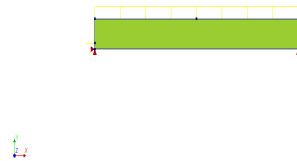


Figure A.12: Boundary and loading conditions

Outputs:

The deflection (DtY) and the Cauchy stresses (SXX) will be the investigated results of this analysis.

**Deflection (DtY)** As it was expected the total deflection of the beam (LC5) is reduced in comparison with Case 1 by 2.59%, due to the influence of prestressing force's resultant in the deflection field, see figures (A.13), (A.14). A downward curvature of the deflection line due to the total load combinations is found. The midspan deflection values per load are shown in table (A.7).

Analysis  
Load combination 4  
Displacement (DtY)  
min: 2.636e-06m max: 2.406e-05m

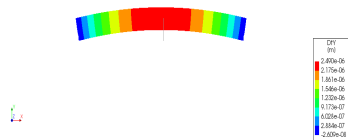


Figure A.13: Element deflection DtY - LC4

Analysis  
Load combination 5  
Displacement (DtY)  
min: -3.216e-06m max: 0.000e+00m

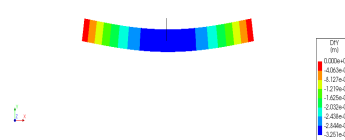


Figure A.14: Element deflection DtY - LC5

$\delta$ [m]	F.E.M. <sub>4</sub>	F.E.M. <sub>1</sub>	$\frac{F.E.M._4}{F.E.M._1}$ (%)	$\frac{FEM_4 - FEM_1}{FEM_4}$ (%)
$\delta_{SW}$	+2.66E-04	+2.71E-04	98	1.95
$\delta_{UDL}$	+4.52E-05	+4.60E-05	98	1.79
$\delta_{Point}$	+1.44E-05	+1.47E-05	98	2.29
$\delta_P$	-2.49E-06	0	-	-
$\delta_{tot}$	+3.24E-04	+3.32E-04	97	2.59

Table A.7: Midspan element deflection per load

**Cauchy stresses SXX** The concrete stresses SXX at midspan are presented in figure [A.15](#). The prestressing stresses and the total stresses of the beam are shown in figures [\(A.16\)](#), [\(A.17\)](#) correspondingly. In table [\(A.8\)](#), the values of midspan stresses according to the respective load are shown. Analogous to Case 1, the highest stresses appear at midspan of the beam for all loads. Due to the introduction of eccentric prestressing forces at the anchorages, the resultant bending moment causes tension at the top part of the beam, and thus the total element stress is reduced compared to Case 1 by 0.27% at top fiber and by 1.57% at bottom fiber level with regard to the FEM results. Note that due to the concentrated load introduction from prestressing at the two anchorages, high compressive forces may arise which in case they exceed the concrete compressive strength  $f_{cd}$ , crushing of the concrete may occur. One provision that could be taken in that case is to use steel plates at the interface between concrete and the concentrated load that is applied on the structure. Hence, a uniform distribution of the concentrated load would occur.

Concerning the predicted values of midspan stresses it must be noted that due to the eccentricity of the prestressing loads at the supports relative to beam's centroidal axis, bending moments occur, and the resulting stresses should be superimposed to the stresses found in Case 2 (central prestressing). In particular, the bending stresses due to the eccentric loading will be calculated as:  $\sigma_{c,eccent} = \frac{P \times e_p}{W_{c,top}} = 7.2e3 [N/m^2]$

According to hand calculations, the influence of eccentric prestressing results in a decrease of stresses at both fibers of the beam, in comparison with case 1 (0.9%) at both fiber levels. Since the calculated results (H.C<sub>4</sub>) are similar to the ones derived via DIANA10.1 in case 4 (F.E.M.<sub>4</sub>), it can be concluded that the stresses are verified, see table [A.8](#).

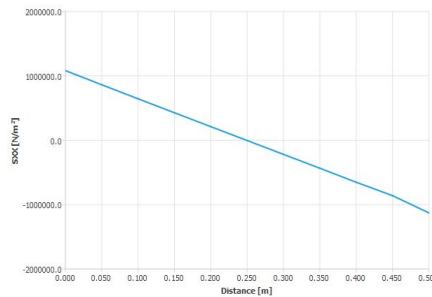


Figure A.15: Midspan element stresses SXX - LC5

Program: loadconcentration 4  
 Cauchy (2nd Stress) SXX  
 min: -2.24e+08 [N/m<sup>2</sup>]  
 max: 2.24e+08 [N/m<sup>2</sup>]

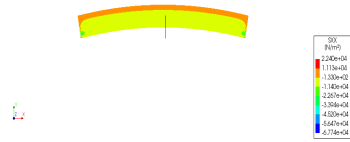


Figure A.16: Element stresses SXX  
 - LC4

Program: loadconcentration 5  
 Cauchy (2nd Stress) SXX  
 min: -1.12e+08 [N/m<sup>2</sup>]  
 max: 1.12e+08 [N/m<sup>2</sup>]

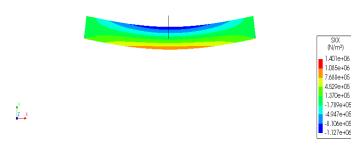


Figure A.17: Element stresses SXX  
 - LC5

Top	SXX [N/m <sup>2</sup> ]	H.C. <sub>4</sub>	F.E.M. <sub>4</sub>	F.E.M. <sub>1</sub>	$\frac{F.E.M._4}{F.E.M._1}$ (%)	$\frac{F.E.M._4 - F.E.M._1}{F.E.M._4}$ (%)
	SXX <sub>SW</sub>	-9.37E+05	-8.852E+05	-8.850E+05	100	0.02
	SXX <sub>UDL</sub>	-1.50E+05	-1.504E+05	-1.500E+05	100	0.27
	SXX <sub>Point</sub>	-6.00E+04	-9.411E+04	-9.410E+04	100	0.01
	SXX <sub>P</sub>	+3.20E+03	+3.200E+03	-	-	-
	SXX <sub>tot</sub>	-1.14E+06	-1.127E+06	-1.130e6	100	0.27
Bottom	SXX [N/m <sup>2</sup> ]	H.C. <sub>4</sub>	F.E.M. <sub>4</sub>	F.E.M. <sub>1</sub>	$\frac{F.E.M._4}{F.E.M._1}$ (%)	$\frac{F.E.M._4 - F.E.M._1}{F.E.M._4}$ (%)
	SXX <sub>SW</sub>	+9.37E+05	+8.852E+05	+8.850E+05	100	0.02
	SXX <sub>UDL</sub>	+1.50E+05	+1.504E+05	+1.500E+05	100	0.27
	SXX <sub>Point</sub>	+6.00E+04	+5.893E+04	+5.900E+04	100	0.12
	SXX <sub>P</sub>	-11.20E+03	-1.120E+04	-	-	-
	SXX <sub>tot</sub>	+1.14E+06	+1.083E+06	+1.100E+06	98	1.57

Table A.8: Midspan element stresses SXX

**Case 5 - Prestressed concrete beam - anchorages at a distance of 0.15[m] below the centroidal axis, tendon model**

Eccentric prestressing is applied at both ends of a simply supported beam, at a distance of 0.15[m] below the centroidal axis. Tendon is of linear straight profile in this case too. All loads from Case 1 will be applied in addition to the prestressing force  $P = 1000[N]$  at both anchorages, see figure [A.18](#)



Figure A.18: Boundary and loading conditions

**Outputs:** Deflection (DtY) and Cauchy stresses (SXX) will be the investigated results of this analysis.

**Deflection (DtY)** As it was expected the total deflection of the beam will be smaller comparing with Case 1 (unreinforced single beam) by 0.803%, due to the influence of prestressing force's resultant in deflection field, see figures A.19, A.20 and table A.9. The beam shows an upward curvature at midspan and a downward curvature at the supports with regard to its deflection for the total load combination (LC5). This results is not expected and seems like the result that would be anticipated in case of a clamped beam at both ends. The total deflection at midspan is decreased by 74.36% when comparing with the deflection in Case 1. Comparing the deflection under the total load combination between Case 5 and Case 4 (eccentric tendon - no steel in), it is found that the deflection in the first model is reduced by 74.31%. It must be noted that the shape of the element's deflection due to the total load combination is not expected and cannot be compared with the shape of the deflection found in Case 4. In particular, in Case 5, near the element edges a downward curvature is observed, whereas at midspan an upward curvature is governing.

Figure A.19: Element deflection DtY - LC4

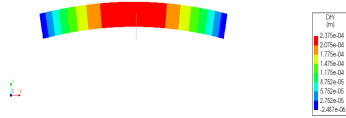


Figure A.19: Element deflection DtY - LC4

Figure A.20: Element deflection DtY - LC5

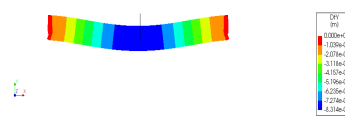


Figure A.20: Element deflection DtY - LC5

$\delta$ [m]	F.E.M. <sub>5</sub>	F.E.M. <sub>4</sub>	$\frac{F.E.M._5}{F.E.M._4}$ (%)
$\delta_{SW}$	+2.62E-04	+2.66E-04	98
$\delta_{UDL}$	+4.44E-05	+4.52E-05	98
$\delta_{Point}$	+1.42E-05	+1.44E-05	99
$\delta_P$	-2.38E-04	-2.49E-06	9546
$\delta_{tot}$	+8.31E-05	+3.24E-04	26

Table A.9: Midspan element deflection per load

**Cauchy stresses SXX** The stresses of concrete and reinforcement under the total load combination (LC5) are shown in figures A.22, A.23. In table A.10 the values of concrete stresses at midspan per applied load are shown. Similar to case 1, the highest stresses appear at midspan of the beam for all loads. Due to eccentricity of the prestressing loads relative to the element's centroidal axis, tensile stresses occur at the top fiber of the beam (LC4). A noticeable difference between Case 4 and 5, is that in the last case the whole midspan cross-section is governed by compressive stresses, contrary to Case 4, where tensile stresses

appear at bottom fiber level for the total load combination (LC5), see figure [A.21](#). It must also be noted that although the prestressing load causes different element stresses at top and bottom fiber level compared with case 4, where no input of the tendon profile was set up in the model, see table [A.7](#).

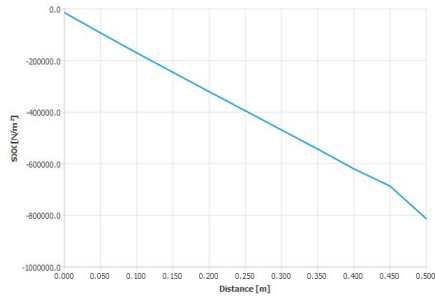


Figure A.21: Midspan element stresses SXX - LC5

Project1  
Loadcombination 5  
Reinforcement Cauchy, total stress SXX  
min: 7.286e+07, max: 9.92e+07 [N/m²]

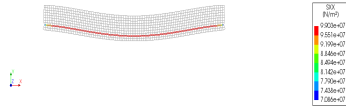


Figure A.22: Prestressing steel stresses SXX - LC5

Project1  
Loadcombination 5  
Cauchy total stress SXX  
min: -4.82e+05, max: 1.92e+06 [N/m²]

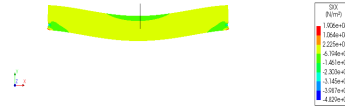


Figure A.23: Element stresses SXX - LC5

Top	SXX [N/m <sup>2</sup> ]	F.E.M. <sub>5</sub>	F.E.M. <sub>4</sub>	F.E.M. <sub>3</sub>	$\frac{F.E.M._5}{F.E.M._4}$ (%)	$\frac{F.E.M._5}{F.E.M._3}$ (%)
	SXX <sub>SW</sub>	-8.76E+05	-8.852E+05	-8.852E+05	99	99
	SXX <sub>UDL</sub>	-1.49E+05	-1.504E+05	-1.504E+05	99	99
	SXX <sub>Point</sub>	-9.35E+04	-9.411E+04	-9.411E+04	99	99
	SXX <sub>P</sub>	+3.06E+05	+3.200E+03	-3.911E+05	9545	sign change
	SXX <sub>tot</sub>	-8.13E+05	-1.127E+06	-1.521E+06	72	53
Bottom	SXX [N/m <sup>2</sup> ]	F.E.M. <sub>5</sub>	F.E.M. <sub>4</sub>	F.E.M. <sub>3</sub>	$\frac{F.E.M._5}{F.E.M._4}$ (%)	$\frac{F.E.M._5}{F.E.M._3}$ (%)
	SXX <sub>SW</sub>	+8.53E+05	+8.852E+05	+8.852E+05	96	96
	SXX <sub>UDL</sub>	+1.45E+05	+1.504E+05	+1.504E+05	96	96
	SXX <sub>Point</sub>	+5.68E+04	+5.893E+04	+5.893E+04	96	96
	SXX <sub>P</sub>	-1.07E+06	-1.120E+04	-3.911E+05	9545	273
	SXX <sub>tot</sub>	-1.45E+04	+1.083E+06	+7.034E+05	sign change	sign change

Table A.10: Midspan element stresses SXX

### Case 6 - Prestressed concrete beam - anchorages at the centroidal axis, curved tendon

A curved tendon profile will be modeled in this case. The tendon will have a drupe equal to 0.15[m] at mid-span and will be anchored at the centroidal axis at the supports, see fig A.24. The drupe [f] is equal in size with the tendon's eccentricity ( $e_p=0.15$ [m]) at the supports in Case 4.

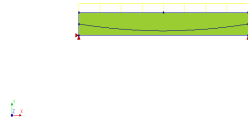


Figure A.24: Boundary and loading conditions

**Outputs:** Deflection (DtY) and Cauchy stresses (SXX) will be the investigated results of this analysis.

**Deflection (DtY)** Although it would be expected that the deflections due to the total load combination (LC5) between Case 5 and 6 would be of the same magnitude, it is found that they are larger by 30.18% in comparison with Case 5 of linear eccentric tendon, (figures A.25, A.26, table A.11).

Figure A.25: Element deflection DtXYZ - LC4



Figure A.25: Element deflection DtXYZ - LC4

Figure A.26: Element deflection DtXYZ - LC5

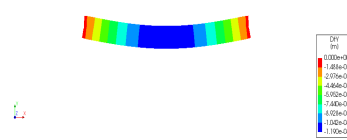


Figure A.26: Element deflection DtXYZ - LC5

$\delta$ [m]	F.E.M. <sub>6</sub>	F.E.M. <sub>5</sub>	$\frac{F.E.M._6}{F.E.M._5}$ (%)	$\frac{FEM_6 - FEM_5}{FEM_5}$ (%)
$\delta_{SW}$	+2.63E-04	+2.62E-04	100	0.42
$\delta_{UDL}$	+4.46E-05	+4.44E-05	100	0.43
$\delta_{Point}$	+1.43E-05	+1.42E-05	100	0.35
$\delta_P$	-2.03E-04	-2.38E-04	85	17.05
$\delta_{tot}$	+1.19E-04	+8.31E-05	143	30.18

Table A.11: Midspan element deflection per load

**Cauchy stresses SXX** The prestressing steel as well as the concrete stresses of the beam under the total load combination (LC5) are shown in figures A.27 and A.28 respectively. The values of midspan stresses according to the respective load are shown in table A.12. The prestressing steel stresses appear to be constant after a distance from the anchors. The midspan stress values per load are found to be the same between Cases 5 and 6 as expected.

Analysis  
Load combination 5  
Reference element Cauchy total (Prestrs) (SXX)  
min: 8.58e+05 N/m² max: 9.54e+05 N/m²

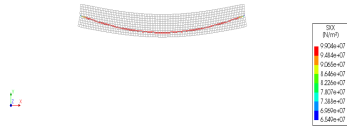


Figure A.27: Prestressing steel stresses SXX - LC5

Analysis  
Load combination 5  
Cauchy total (Prestrs) (SXX)  
min: -4.53e+05 N/m² max: 1.44e+06 N/m²



Figure A.28: Element stresses SXX - LC5

Top	SXX [N/m <sup>2</sup> ]	F.E.M. <sub>6</sub>	F.E.M. <sub>5</sub>	$\frac{FEM_6}{FEM_5}$ (%)
	SXX <sub>SW</sub>	-8.76E+05	-8.76E+05	100
	SXX <sub>UDL</sub>	-1.49E+05	-1.49E+05	100
	SXX <sub>Point</sub>	-9.35E+04	-9.35E+04	100
	SXX <sub>P</sub>	+3.08E+05	+3.06E+05	101
	SXX <sub>tot</sub>	-8.11E+05	-8.13E+05	100
Top	SXX [N/m <sup>2</sup> ]	F.E.M. <sub>6</sub>	F.E.M. <sub>5</sub>	$\frac{FEM_6}{FEM_5}$ (%)
	SXX <sub>SW</sub>	+8.53E+05	+8.53E+05	100
	SXX <sub>UDL</sub>	+1.45E+05	+1.45E+05	100
	SXX <sub>Point</sub>	5.68E+04	+5.68E+04	100
	SXX <sub>P</sub>	-1.07E+06	-1.07E+06	100
	SXX <sub>tot</sub>	-1.58E+04	-1.45E+04	109

Table A.12: Midspan element stresses SXX

**Case 7 - Prestressed concrete beam - linear eccentric tendon at  $e_p = 0.15[m]$ , steel plates**

This case will be similar to Case 4 with an assumed linear tendon profile set at a distance of  $0.15m$  from the centroidal axis (without including the physical and geometrical tendon's properties), creating a more refined model in the first case. In particular, 5 steel plates of  $a0.02m \times 0.1m$  cross-section, will be positioned respectively at the location of concentrated forces, i.e at mid-span top face, supports and anchors, see fig A.29. The interface between the steel plates and the concrete will be modeled such that the initial deformation of a mesh element ( $l_{element} = 0.05[m]$ ) is negligible relative to the deformation of an adjacent mesh element. This implies that the following rules should apply:

1. Elastic stiffness modulus  $K_n = \frac{E_s \times 1000}{l_{element}} = 4.1e15[N/m^3]$
2. Shear stiffness modulus  $K_s = \frac{E_s}{l_{element} \times 1000} = 4.1e9[N/m^3]$

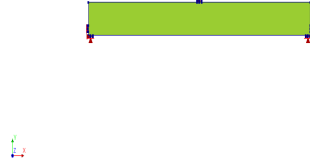


Figure A.29: Boundary and loading conditions

**Outputs:** Deflection (DtY) and Cauchy stresses (SXX) will be the investigated results of this analysis.

**Deflection (DtY)** The deflection due to the total load combination (LC5) is found to be smaller than in Case 4 by 9.73%, see figure [A.30](#) and table [A.13](#)

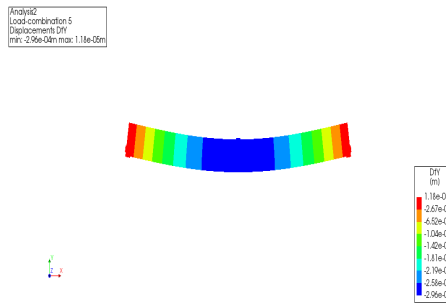


Figure A.30: Element deflection DtY - LC5

$\delta$ [m]	F.E.M. <sub>7</sub>	F.E.M. <sub>4</sub>	$\frac{F.E.M._7}{F.E.M._4}$ (%)	$\frac{FEM._7 - FEM._4}{FEM._7}$ (%)
$\delta_{SW}$	+2.43E-04	+2.66E-04	91	9.55
$\delta_{UDL}$	+4.11E-05	+4.52E-05	91	10.05
$\delta_{Point}$	+1.35E-05	+1.44E-05	94	6.67
$\delta_P$	-2.40E-06	-2.49E-06	96	3.67
$\delta_{tot}$	+2.95E-04	+3.24E-04	91	9.73

Table A.13: Midspan element deflection per load

**Cauchy stresses SXX** The resulting stresses in this case are found to be a bit smaller at top fiber level by 5.33% and by 4.13% at bottom fiber level than in Case 4 (figure [A.31](#), table [A.14](#)). No concentration of forces is introduced at the anchors location in Case 5. Therefore, it can be concluded that the steel plates application at the locations of concentrated loads can be considered as an effective measure to reduce the compressive stresses at these locations.

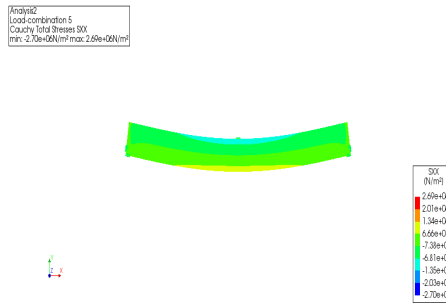


Figure A.31: Element stresses SXX - LC5

Top	SXX [N/m <sup>2</sup> ]	F.E.M. <sub>7</sub>	F.E.M. <sub>4</sub>	$\frac{FEM_7}{FEM_4}$ (%)
	SXX <sub>SW</sub>	-8.54E+05	-8.85E+05	101
	SXX <sub>UDL</sub>	-1.45E+05	-1.50E+05	100
	SXX <sub>Point</sub>	-7.99E+04	-9.41E+04	85
	SXX <sub>P</sub>	+3.24E+03	+3.20E+03	101
	SXX <sub>tot</sub>	-1.07E+06	-1.13E+06	95
Bottom	SXX [N/m <sup>2</sup> ]	F.E.M. <sub>7</sub>	F.E.M. <sub>4</sub>	$\frac{FEM_7}{FEM_4}$ (%)
	SXX <sub>SW</sub>	+8.60E+05	+8.85E+05	97
	SXX <sub>UDL</sub>	+1.44E+05	+1.50E+05	96
	SXX <sub>Point</sub>	+5.77E+04	+5.89E+04	98
	SXX <sub>P</sub>	-1.12E+04	-1.12E+04	100
	SXX <sub>tot</sub>	+1.04E+06	+1.08E+06	96

Table A.14: Midspan element stresses SXX

### Case 8 - Unreinforced concrete beam - curved top and bottom sides

In this case, the geometry of the model's cross section is modified, by introducing a curvature of  $k = \frac{1}{R} = \frac{1}{\frac{12}{8 \times f}} = 0.032[m^{-1}]$  at both top and bottom sides of the element ( $f = 0.10$ ). The element edges are set vertical, see figure [A.32](#).

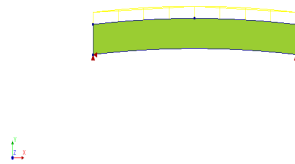


Figure A.32: Boundary and loading conditions

**Outputs:** Deflection (DtY) and Cauchy stresses (SXX) will be the investigated results of this analysis.

**Deflection (DtY)** The deflection of the beam under the total load combination (LC4) is shown in figure A.33. The values of deflections according to the respective load are shown in table A.15. The midspan deflections in this case, are found to be similar to those found in Case 1 (linear geometry). However, the deflections in this specific model decrease by 1.25%.

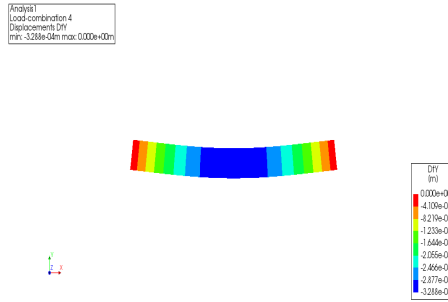


Figure A.33: Element deflection DtY - LC4

$\delta$ [m]	F.E.M. <sub>8</sub>	F.E.M. <sub>1</sub>	$\frac{F.E.M._8}{F.E.M._1}$ (%)
$\delta_{SW}$	+2.68E-04	+2.71E-04	99
$\delta_{UDL}$	+4.55E-05	+4.60E-05	99
$\delta_{Point}$	+1.46E-05	+1.47E-05	99
$\delta_{tot}$	+3.28E-04	+3.32E-04	99

Table A.15: Midspan element deflection per load

**Cauchy stresses SXX** The bending stresses of the beam under the total load combination (LC5) are shown in figure A.34. In table A.16, the midspan concrete stresses per load at top and bottom fiber level are depicted. It appears that the stresses in this case are found similar to Case 1 (straight element). In this case it is proved that the stresses decrease at top fiber level by 0.53% and are the same at bottom fiber level. Since the differences are small, it may be concluded that the curved geometry of the element does not have great impact on the stress field.

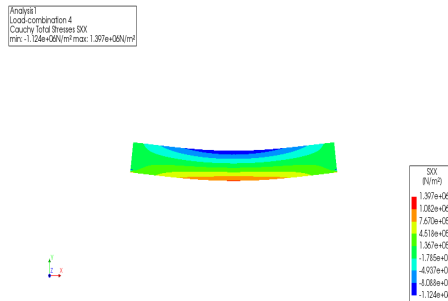


Figure A.34: Element stresses SXX - LC4

Top	SXX [N/m <sup>2</sup> ]	F.E.M. <sub>8</sub>	F.E.M. <sub>1</sub>	$\frac{FEM_{.8}}{FEM_{.1}}$ (%)
	SXX <sub>SW</sub>	-8.81E+05	-8.85E+05	99
	SXX <sub>UDL</sub>	-1.50E+05	-1.50E+05	100
	SXX <sub>Point</sub>	-9.38E+04	-9.41E+04	100
	SXX <sub>tot</sub>	-1.12E+06	-1.13E+06	99
Bottom	SXX [N/m <sup>2</sup> ]	F.E.M. <sub>8</sub>	F.E.M. <sub>1</sub>	$\frac{FEM_{.8}}{FEM_{.1}}$ (%)
	SXX <sub>SW</sub>	+8.90E+05	+8.85E+05	101
	SXX <sub>UDL</sub>	+1.51E+05	+1.50E+05	101
	SXX <sub>Point</sub>	+5.92E+04	+5.90E+04	100
	SXX <sub>tot</sub>	+1.10E+06	+1.10E+06	100

Table A.16: Midspan element stresses SXX

### Case 9 - Prestressed concrete beam - curved tendon at centroidal axis - curved top and bottom sides

An alternative to the previous model, will be the input of prestressing steel reinforcement at the centroidal axis. The curvature of the tendon will be equal to the curvature of the beam, see figure [A.35](#).

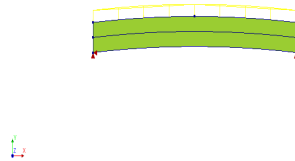


Figure A.35: Boundary and loading conditions

**Outputs:** Deflection (DtY) and Cauchy stresses (SXX) will be the investigated results of this analysis.

**Deflection (DtY)** The total midspan displacement (LC5) at mid-span of the beam is increased by 1.20% in comparison with the value resulted from Case 3 (linear geometry), see figure [A.36](#) and table [A.17](#). Note that the deflection caused by the prestressing steel load (LC4) in Case 9 is increased by 79.53% relative to the one found in Case 3.

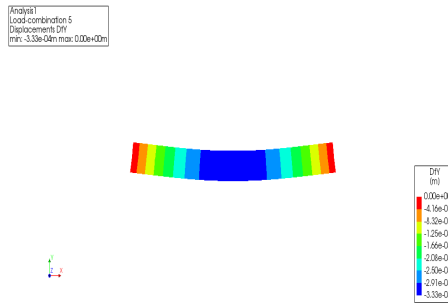


Figure A.36: Element deflection DtY - LC5

$\delta$ [m]	F.E.M. <sub>9</sub>	F.E.M. <sub>3</sub>	$\frac{FEM_9 - FEM_3}{FEM_9}$ (%)
$\delta_{SW}$	+2.69E-04	+2.68E-04	0.37
$\delta_{UDL}$	+4.56E-05	+4.54E-05	0.44
$\delta_{Point}$	+1.46E-05	+1.46E-05	0.00
$\delta_P$	-3.43E-06	-7.02E-07	79.53
$\delta_{tot}$	+3.33E-04	+3.29E-04	1.20

Table A.17: Midspan element deflection per load

**Cauchy stresses SXX** The bending stresses of the beam under the total load combination (LC5) are shown in figure [A.37](#). In table [A.18](#), the values of midspan concrete stresses according to the respective load are shown. Comparing this case with the model of linear geometry (Case 3), it appears that the curved geometry resulted in similar midspan stress values, see table [A.14](#).

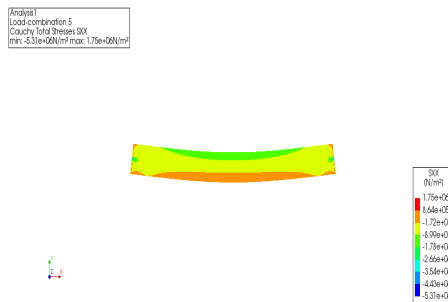


Figure A.37: Element total stresses SXX - LC5

Top	SXX [N/m <sup>2</sup> ]	F.E.M. <sub>9</sub>	F.E.M. <sub>3</sub>	$\frac{FEM_7}{FEM_4}$ (%)
	SXX <sub>SW</sub>	-8.80E+05	-8.85E+05	99
	SXX <sub>UDL</sub>	-1.50E+05	-1.50E+05	100
	SXX <sub>Point</sub>	-9.38E+04	-9.41E+04	100
	SXX <sub>P</sub>	-3.91E+05	-3.91E+05	100
	SXX <sub>tot</sub>	-1.52E+06	-1.52E+06	100
Bottom	SXX [N/m <sup>2</sup> ]	F.E.M. <sub>9</sub>	F.E.M. <sub>3</sub>	$\frac{FEM_7}{FEM_4}$ (%)
	SXX <sub>SW</sub>	+8.90E+05	+8.85E+05	101
	SXX <sub>UDL</sub>	+1.51E+05	+1.50E+05	100
	SXX <sub>Point</sub>	+5.92E+04	+5.893E+04	100
	SXX <sub>P</sub>	-3.91E+05	-3.91E+05	100
	SXX <sub>tot</sub>	+7.10E+05	+7.03E+05	101

Table A.18: Midspan element stresses SXX

**Case 10 - Prestressed concrete beam - curved tendon at eccentricity  $e_p=0.15$ [m] - curved top and bottom sides**

Case's 8 geometry is modified by introducing a curved tendon at an eccentricity of 0.15[m] below the centroidal axis of the beam, see figure [A.38](#). The curvature of the tendon is equal to the curvature of the beam.

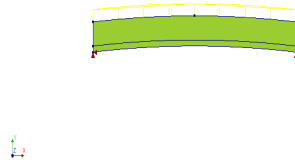


Figure A.38: Boundary and loading conditions

**Outputs:** Deflection (DtY) and Cauchy stresses (SXX) will be the investigated results of this analysis.

**Deflection (DtY)** The total displacement (LC5) in this case is larger by 2.75% in comparison with Case 5 (straight linear element), see table [A.19](#). The shape of the element deflection is similar in both cases, i.e. the deflection shows a downward curvature near the supports and an upward curvature near the midspan, which is considered as an unexpected result, see figures [A.20](#) and [A.39](#). In particular, an upward curvature would be anticipated for the deflection line of the whole concrete element due to the total load combination (LC5).

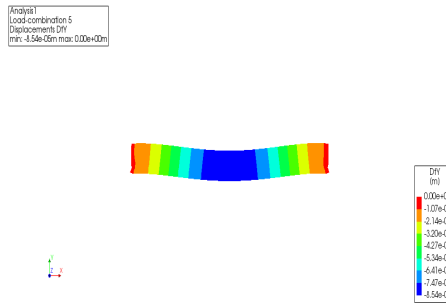


Figure A.39: Element deflection DtY - LC5

$\delta$ [m]	F.E.M. <sub>10</sub>	F.E.M. <sub>5</sub>	$\frac{FEM_{10} - FEM_5}{FEM_{10}}$ (%)
$\delta_{SW}$	+2.63E-04	+2.62E-04	0.38
$\delta_{UDL}$	4.46E-05	+4.44E-05	0.45
$\delta_{Point}$	+1.43E-05	+1.42E-05	0.28
$\delta_P$	-2.37E-04	-2.38E-04	0.42
$\delta_{tot}$	+8.54E-05	+8.31E-05	2.75

Table A.19: Midspan element deflection per load

### Cauchy stresses SXX

The total stresses of the beam (LC5) are shown in figure [A.40](#). In table [A.20](#), the values of midspan concrete stresses per load are shown. The total element stresses resulted in Case 10, show that the mid-span cross section is under compression at both top and bottom fiber level. Comparing this case with the case of linear geometry (Case 5), it appears that the curved geometry resulted in a decrease of stresses by 0.20% and 13.83% at top and bottom fiber level correspondingly. It can be concluded that the curvature at top and bottom sides of the beam, will have a positive influence on the stress field deflections at bottom fiber level, in comparison with the corresponding model of straight linear geometry.

Analysis  
 Load-combination 5  
 Cauchy Total Stresses SXX  
 min: -5.25e+06 N/m<sup>2</sup> max: 1.97e+06 N/m<sup>2</sup>



Figure A.40: Element total stresses SXX - LC5

Top	SXX [N/m <sup>2</sup> ]	F.E.M. <sub>10</sub>	F.E.M. <sub>5</sub>	$\frac{FEM_{10}}{FEM_5}$ (%)
	SXX <sub>SW</sub>	-8.72E+05	-8.76E+05	0.52
	SXX <sub>UDL</sub>	-1.48E+05	-1.49E+05	0.47
	SXX <sub>Point</sub>	-9.32E+04	-9.35E+04	0.32
	SXX <sub>P</sub>	3.02E+05	3.06E+05	1.29
	SXX <sub>tot</sub>	-8.11E+05	-8.13E+05	0.20
Bottom	SXX [N/m <sup>2</sup> ]	F.E.M. <sub>10</sub>	F.E.M. <sub>5</sub>	$\frac{FEM_{10}}{FEM_5}$ (%)
	SXX <sub>SW</sub>	+8.58E+05	+8.53E+05	0.54
	SXX <sub>UDL</sub>	+1.46E+05	+1.45E+05	0.62
	SXX <sub>Point</sub>	+5.71E+04	+5.68E+04	0.53
	SXX <sub>P</sub>	-1.07E+06	-1.07E+06	0.37
	SXX <sub>tot</sub>	-1.27E+04	-1.45E+04	13.83

Table A.20: Midspan element stresses SXX

### Case 11- Unreinforced concrete beam - curved top and bottom sides - right angles

The same model used in Case 8 will be used, modifying the vertical side edges to inclined ones. Right angles will be formed between the horizontal and vertical sides of the element, see figure [A.41](#).

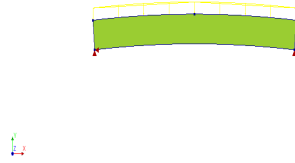


Figure A.41: Boundary and loading conditions

**Outputs:** Deflection (DtY) and Cauchy stresses (SXX) will be the investigated results of this analysis.

**Deflection (DtY)** The maximum midspan deflections found in this case, are similar to those found in Case 8 (curved element - vertical side edges), see figure A.42 and table A.21. Since they are found smaller than in Case 8 it can be also concluded that they are smaller than the midspan deflections in Case 1 of straight element. Therefore, the addition of right angles between the element edges is proved to have a beneficial impact on the deflection values at midspan.

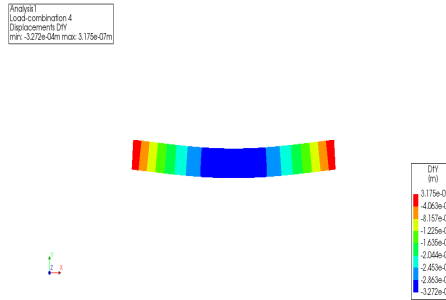


Figure A.42: Element deflection DtY - LC4

$\delta$ [m]	F.E.M. <sub>11</sub>	F.E.M. <sub>8</sub>	$\frac{FEM_{11}}{FEM_{8}}$ (%)
$\delta_{SW}$	+2.67E-04	+2.68E-04	100
$\delta_{UDL}$	+4.53E-05	+4.55E-05	99
$\delta_{Point}$	+1.44E-05	+1.46E-05	99
$\delta_{tot}$	+3.26E-04	+3.28E-04	99

Table A.21: Midspan element deflection per load

### Cauchy stresses SXX

The stresses of the beam under the total load combination (LC4) are shown in figure A.43. The values of midspan stresses according to the respective load are shown in table A.22. Comparing the element stresses of this case with those found in Case 8 (curved element - vertical side edges), it appears that the total

stresses have similar values, see table A.18. Since it was proved that Case 1 of straight geometry has the same concrete stresses at midspan with Case 8, it can be concluded that the addition of right angles does not improve the stress distribution in this case.

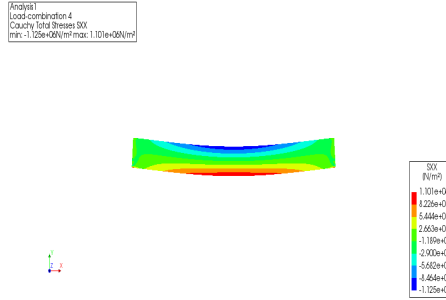


Figure A.43: Element total stresses SXX - LC4

Top	SXX [N/m <sup>2</sup> ]	F.E.M. <sub>11</sub>	F.E.M. <sub>8</sub>	$\frac{FEM_{11}}{FEM_8}$ (%)
	SXX <sub>SW</sub>	-8.81E+05	-8.81E+05	100
	SXX <sub>UDL</sub>	-1.50E+05	-1.50E+05	100
	SXX <sub>Point</sub>	-9.39E+04	-9.38E+04	100
	SXX <sub>tot</sub>	-1.13E+06	-1.12E+06	100
Bottom	SXX [N/m <sup>2</sup> ]	F.E.M. <sub>11</sub>	F.E.M. <sub>8</sub>	$\frac{FEM_{11}}{FEM_8}$ (%)
	SXX <sub>SW</sub>	+8.90E+05	+8.90E+05	100
	SXX <sub>UDL</sub>	+1.51E+05	+1.51E+05	100
	SXX <sub>Point</sub>	+5.92E+04	+5.92E+04	100
	SXX <sub>tot</sub>	+1.10E+06	+1.10E+06	100

Table A.22: Midspan element stresses SXX

### Case 12 - Prestressed concrete beam - curved tendon at centroidal axis - curved top and bottom sides, right angles

The position of the prestressing steel reinforcement is set at the centroidal axis. The curvature of the tendon will be equal to the curvature of the beam, see figure A.44.

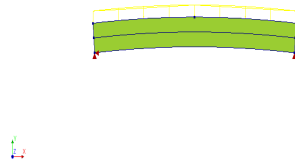


Figure A.44: Boundary and loading conditions

**Outputs:** Deflection (DtY) and Cauchy stresses (SXX) will be the investigated results of this analysis.

**Deflection (DtY)** The total displacement (LC5) at mid-span of the beam is similar with the deflection value resulted from Case 11. Although they should have been the same, a slight increase of 1.51% is shown in Case 12, see figure and table. Comparing Case 12 and 9 (vertical side edges), it is proved that the total displacement (LC5) is similar in both cases since they differ by 0.6%, with Case 12 to have a reduced value, see figure [A.45](#) and table [A.23](#).

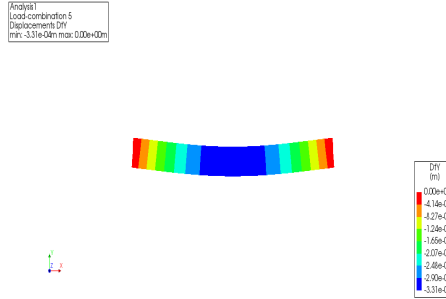


Figure A.45: Element deflection DtY - LC5

$\delta$ [m]	F.E.M. <sub>12</sub>	F.E.M. <sub>11</sub>	F.E.M. <sub>9</sub>	$\frac{FEM_{12}}{FEM_{11}}$ (%)	$\frac{FEM_{12}}{FEM_9}$ (%)
$\delta_{SW}$	+2.67E-04	+2.62E-04	+2.69E-04	100	99
$\delta_{UDL}$	+4.54E-05	+4.53E-05	+4.56E-05	100	99
$\delta_{Point}$	+1.45E-05	+1.44E-05	+1.46E-05	101	100
$\delta_P$	-3.18E-06	-	-3.43E-06	-	93
$\delta_{tot}$	+3.31E-04	+3.26E-04	+3.33E-04	101	99

Table A.23: Midspan element deflection per load

**Cauchy stresses SXX** The maximum midspan stresses of the beam under the total load combination (LC5) are shown in figure [A.46](#). In table [A.24](#), the values of stresses according to the respective load are shown. It is proved that the total stresses at mid-span in this case, are smaller by 0.33% at top, and larger by 0.93% at bottom fiber level, than those in Case3 (straight linear geometry).

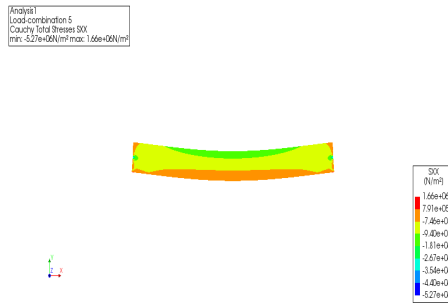


Figure A.46: Element total stresses SXX - LC5

Top	SXX [N/m <sup>2</sup> ]	F.E.M. <sub>12</sub>	F.E.M. <sub>3</sub>	$\frac{FEM_{12}}{FEM_{3}}$ (%)	$\frac{FEM_{12} - FEM_{3}}{FEM_{3}}$ (%)
	SXX <sub>SW</sub>	-8.81E+05	-8.85E+05	100	0.49
	SXX <sub>UDL</sub>	-1.50E+05	-1.50E+05	99	0.53
	SXX <sub>Point</sub>	-9.39E+04	-9.41E+04	100	0.21
	SXX <sub>P</sub>	-3.91E+05	-3.91E+05	100	0.08
	SXX <sub>tot</sub>	-1.52E+06	-1.52E+06	100	0.33
Bottom	SXX [N/m <sup>2</sup> ]	F.E.M. <sub>12</sub>	F.E.M. <sub>3</sub>	$\frac{FEM_{12}}{FEM_{3}}$ (%)	$\frac{FEM_{12} - FEM_{3}}{FEM_{3}}$ (%)
	SXX <sub>SW</sub>	8.90E+05	8.85E+05	101	0.57
	SXX <sub>UDL</sub>	1.51E+05	1.50E+05	101	0.53
	SXX <sub>Point</sub>	5.92E+04	5.89E+04	101	0.52
	SXX <sub>P</sub>	-3.91E+05	-3.91E+05	100	0.08
	SXX <sub>tot</sub>	7.10E+05	7.03E+05	101	0.93

Table A.24: Midspan element stresses SXX

**Case 13 - Prestressed concrete beam - curved tendon at eccentricity  $e_p=0.15$ [m] - curved top and bottom sides, right angles**

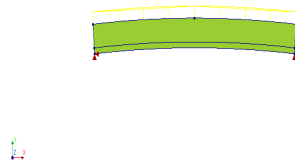


Figure A.47: Boundary and loading conditions

**Outputs:** Deflection (DtY) and Cauchy stresses (SXX) will be the investigated results of this analysis.

**Deflection (DtY)** Likewise with case 10 (vertical side edges), in Case 13, the deflection shows a downward curvature near the supports and an upward

curvature near the mid-span, a result that was not anticipated. At midspan, the total deflection is found smaller by 0.68% compared with the deflection found in Case 10 with the vertical side edges, see figure [A.48](#) and table [A.25](#).

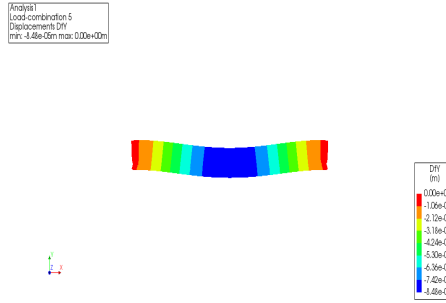


Figure A.48: Element deflection DtY - LC5

$\delta$ [m]	F.E.M. <sub>13</sub>	F.E.M. <sub>10</sub>	$\frac{FEM_{13}}{FEM_{10}}$ (%)	$\frac{FEM_{13}-FEM_{10}}{FEM_{10}}$ (%)
$\delta_{SW}$	+2.61E-04	+2.63E-04	100	0.46
$\delta_{UDL}$	+4.43E-05	+4.46E-05	99	0.52
$\delta_{Point}$	+1.42E-05	+1.43E-05	100	0.35
$\delta_P$	-2.36E-04	-2.37E-04	100	0.42
$\delta_{tot}$	+8.49E-05	+8.54E-05	99	0.68

Table A.25: Midspan element deflection per load

**Cauchy stresses SXX** The stresses of the beam under the total load combination (LC5) are shown in figure [A.49](#). In table [A.26](#), the values of midspan stresses per load are shown. The total stresses (LC5) resulted in Case 13, show that the midspan cross-section is under compression. The stresses in this case are found to be approximately the same at top fiber level, while at bottom fiber level they are decreased by 2.58% in comparison with Case 10. This result can be considered beneficial with regard to the element midspan element stresses. Comparing this case with the case with the case of linear geometry case (Case 5), it appears that the total stresses are approximately the same at top fiber level. However, the curved geometry combined with right angles between the element sides (Case 13), resulted in a decrease of stresses by 16.76% at bottom fiber level, considered as a beneficial influence of the applied curvature in Case13. Note though that the validity of FEM result in Case 13 may have to be reconsidered.

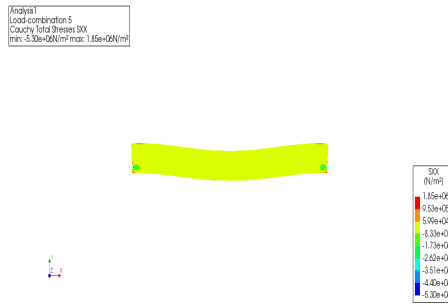


Figure A.49: Element total stresses SXX - LC5

Top	SXX [N/m <sup>2</sup> ]	F.E.M. <sub>13</sub>	F.E.M. <sub>10</sub>	F.E.M. <sub>5</sub>	$\frac{FEM_{13}}{FEM_{10}}$ (%)	$\frac{FEM_{13}}{FEM_5}$ (%)
	SXX <sub>SW</sub>	-8.72E+05	-8.72E+05	-8.76E+05	100	100
	SXX <sub>UDL</sub>	-1.48E+05	-1.48E+05	-1.49E+05	99	100
	SXX <sub>Point</sub>	-9.33E+04	-9.32E+04	-9.35E+04	100	100
	SXX <sub>P</sub>	3.02E+05	3.02E+05	+3.06E+05	100	99
	SXX <sub>tot</sub>	-8.12E+05	-8.11E+05	-8.13E+05	100	100
Bottom	SXX [N/m <sup>2</sup> ]	F.E.M. <sub>13</sub>	F.E.M. <sub>10</sub>	F.E.M. <sub>5</sub>	$\frac{FEM_{13}}{FEM_{10}}$ (%)	$\frac{FEM_{13}}{FEM_5}$ (%)
	SXX <sub>SW</sub>	8.58E+05	8.58E+05	+8.53E+05	100	101
	SXX <sub>UDL</sub>	1.46E+05	1.46E+05	+1.45E+05	100	101
	SXX <sub>Point</sub>	5.71E+04	5.71E+04	+5.68E+04	100	101
	SXX <sub>P</sub>	-1.07E+06	-1.07E+06	-1.07E+06	100	100
	SXX <sub>tot</sub>	-1.24E+04	-1.27E+04	-1.45E+04	97	86

Table A.26: Midspan element stresses SXX

#### Case 14 - Prestressed concrete beam - tendon at centroidal axis - 4-point bending test

**Loads:** Case's 3 geometry will be used in this case. Two point loads  $Point = 1000[N]$  at  $\frac{l}{4} = 1.25[m]$  from the supports will be applied in Case 14, instead of one point load at midspan (figure [A.50](#)).

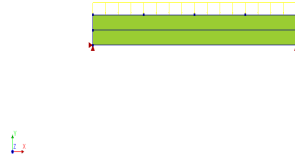


Figure A.50: Boundary and loading conditions

**Outputs:** The deflection (DtY) and the Cauchy stresses (SXX) will be the investigated results of this analysis.

**Deflection (DtY)** The total deflection of the beam under the loads is shown in (A.50). The values of deflections at mid-span according to the respective load are shown in table (A.27). It is proved that the total displacement is equal to the sum of the deflections caused by the individual components and that the maximum deflection occurs at midspan. The total deflection of the beam is increased by 1.56% compared with Case 3 (3-point bending).

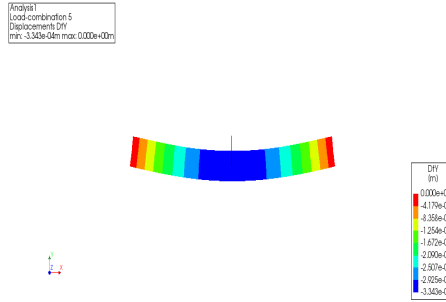


Figure A.51: Element deflection DtY - LC5

$\delta$ [m]	F.E.M. <sub>14</sub>	F.E.M. <sub>3</sub>	$\frac{FEM_{14}}{FEM_{3}}$ (%)	$\frac{FEM_{13} - FEM_{10}}{FEM_{10}}$ (%)
$\delta_{SW}$	2.68E-04	2.68E-04	100	0.11
$\delta_{UDL}$	4.54E-05	4.54E-05	100	0.02
$\delta_{Point}$	1.99E-05	1.46E-05	136	26.63
$\delta_P$	7.02E-07	7.02E-07	100	0.00
$\delta_{tot}$	3.34E-04	3.29E-04	102	1.56

Table A.27: Midspan element deflection per load

**Cauchy stresses SXX** The bending stresses of the beam under the load combination are shown in (A.52). The element stresses (SXX) caused by the total load combination at midspan are shown in figure (A.53). In table (A.28), the values of stresses at top and bottom fiber level according to the respective load are shown. A linear stress distribution based on the Euler's Bernoulli beam theory, over the height of beam's cross - section is proved. Comparing Cases 3 (3-point bending) and 14 (4-point bending), it is found that the total midspan stresses decrease by 2% at top fiber level, while they differ by 0.10% at bottom fiber level.

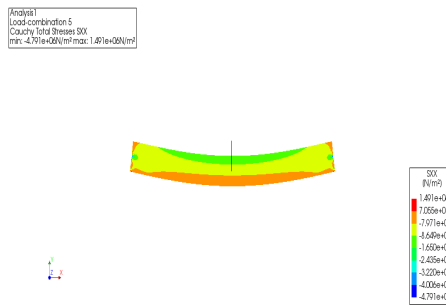


Figure A.52: Element total stresses SXX - LC5

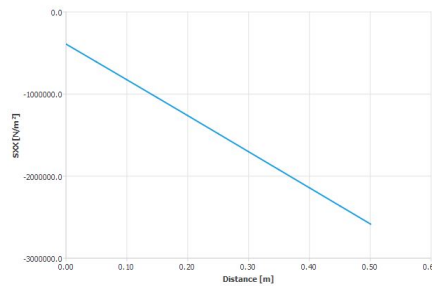


Figure A.53: Element stresses SXX at midspan cross section - LC5

Top	SXX [N/m <sup>2</sup> ]	F.E.M. <sub>14</sub>	F.E.M. <sub>3</sub>	$\frac{FEM_{14}}{FEM_{3}}$ (%)
	SXX <sub>SW</sub>	-8.85E+05	-8.85E+05	100
	SXX <sub>UDL</sub>	-1.50E+05	-1.50E+05	100
	SXX <sub>Point</sub>	-6.00E+04	-9.41E+04	64
	SXX <sub>P</sub>	-3.91E+05	-3.91E+05	100
	SXX <sub>tot</sub>	-1.49E+06	-1.52E+06	100
Bottom	SXX [N/m <sup>2</sup> ]	F.E.M. <sub>14</sub>	F.E.M. <sub>3</sub>	$\frac{FEM_{14}}{FEM_{3}}$ (%)
	SXX <sub>SW</sub>	8.85E+05	8.85E+05	100
	SXX <sub>UDL</sub>	1.50E+05	1.50E+05	100
	SXX <sub>Point</sub>	6.00E+04	5.89E+04	102
	SXX <sub>P</sub>	-3.91E+05	-3.91E+05	100
	SXX <sub>tot</sub>	7.04E+05	7.03E+05	100

Table A.28: Midspan element stresses SXX

### Case 15 - Prestressed concrete beam - tendon at centroidal axis - rigid connection

An alternative to Case 3, will be the division of the beam element in half, creating two beam elements with each length to be equal to  $\frac{l}{2}$ , see figure (A.54). The connection between the two beam elements is considered to be rigid.

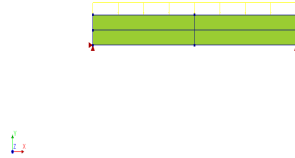


Figure A.54: Boundary and loading conditions

**Outputs:** The deflection (DtY) and the Cauchy stresses (SXX) will be the investigated results of this analysis.

**Deflection (DtY)** The total deflection in Case 15 is found to be the same with the deflection in Case 3 (central prestressing single beam), see figure A.56 and table A.29. The vertical deflection of the element due to central prestressing (LC4) should be negligible (figure A.55).

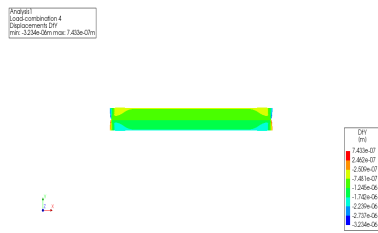


Figure A.55: Element deflection DtY - LC4

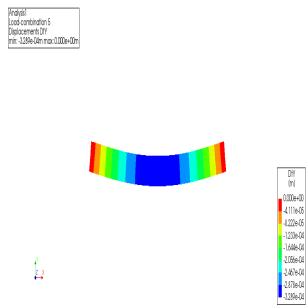


Figure A.56: Element deflection DtY - LC5

$\delta$ [m]	F.E.M. <sub>15</sub>	F.E.M. <sub>3</sub>	$\frac{FEM_{15}}{FEM_{3}}$ (%)
$\delta_{SW}$	2.68E-04	2.68E-04	100
$\delta_{UDL}$	4.54E-05	4.54E-05	100
$\delta_{Point}$	1.46E-05	1.46E-05	100
$\delta_P$	7.02E-07	7.02E-07	100
$\delta_{tot}$	3.29E-04	3.29E-04	100

Table A.29: Midspan element deflection per load

**Cauchy stresses SXX** The prestressing steel stresses (LC4) of the beam are shown in figure A.57, while in figure (A.58) the total stresses (LC5) are depicted. The midspan stress values according to the respective load are presented in table A.30. Comparing the midspan stresses between Cases 15 and 3, it is found that the stresses have identical values.

Project1  
Load combination 4  
Reinforcement Cauchy Total Stress SXX  
max: 7.02e+05 N/m<sup>2</sup> min: -7.02e+05 N/m<sup>2</sup>



Figure A.57: Prestressing steel stresses SXX - LC4

Project1  
Load combination 5  
Cauchy Total Stress SXX  
max: 4.54e+05 N/m<sup>2</sup> min: -4.54e+05 N/m<sup>2</sup>

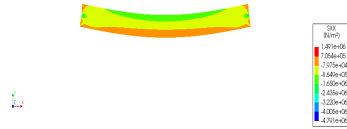


Figure A.58: Element total stresses SXX - LC5

Top	SXX [N/m <sup>2</sup> ]	F.E.M. <sub>15</sub>	F.E.M. <sub>3</sub>	$\frac{FEM_{15}}{FEM_{3}}$ (%)
SXX <sub>SW</sub>		-8.85E+05	-8.85E+05	100
SXX <sub>UDL</sub>		-1.50E+05	-1.50E+05	100
SXX <sub>Point</sub>		-9.41E+04	-9.41E+04	100
SXX <sub>P</sub>		-3.91E+05	-3.91E+05	100
SXX <sub>tot</sub>		-1.52E+06	-1.52E+06	100
Bottom	SXX [N/m <sup>2</sup> ]	F.E.M. <sub>15</sub>	F.E.M. <sub>3</sub>	$\frac{FEM_{15}}{FEM_{3}}$ (%)
SXX <sub>SW</sub>		8.85E+05	8.85E+05	100
SXX <sub>UDL</sub>		1.50E+05	1.50E+05	100
SXX <sub>Point</sub>		5.89E+04	5.89E+04	100
SXX <sub>P</sub>		-3.91E+05	-3.91E+05	100
SXX <sub>tot</sub>		7.03E+05	7.03E+05	100

Table A.30: Midspan element stresses SXX

**Case 16 - Prestressed concrete beam - anchorages at a distance  $e_p = 0.15$ [m] from the centroidal axis - two elements**

The geometry used in Case 5 is used in this model, having split the beam in two equal in length beams, see figure A.59

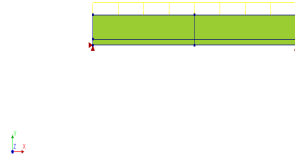


Figure A.59: Boundary and loading conditions

**Outputs:** Deflection (DtY) and Cauchy stresses (SXX) will be the investigated results of this analysis.

**Deflection (DtY)** The deflection due to the prestressing load (LC4) becomes maximum at midspan position (figure A.60). Instead of an upward curved element profile due to the total load combination (LC5), a downward curvature of the beam is present near the midspan, while an upward curvature is present near the supports of the beam (figure A.61). As aforementioned this result would be valid in a fully clamped and not a simply supported as in this model. The deflections at midspan position in Cases 16 and 5 (single beam) have the same values. The midspan element deflection values per load are shown in table A.31

Figure A.60: Element deflection DtY - LC4

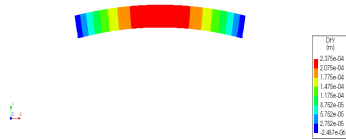


Figure A.60: Element deflection DtY - LC4

Figure A.61: Element deflection DtY - LC5

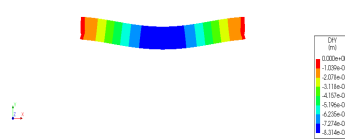


Figure A.61: Element deflection DtY - LC5

$\delta$ [m]	F.E.M. <sub>16</sub>	F.E.M. <sub>5</sub>	$\frac{FEM_{16}}{FEM_5}$ (%)
$\delta_{SW}$	2.62E-04	2.62E-04	100
$\delta_{UDL}$	4.44E-05	4.44E-05	100
$\delta_{Point}$	1.42E-05	1.42E-05	100
$\delta_P$	-2.38E-04	-2.38E-04	100
$\delta_{tot}$	8.31E-05	8.31E-05	100

Table A.31: Midspan element deflection per load

**Cauchy stresses SXX** The prestressing steel as well as the concrete stresses under the total load combination (LC5) are shown in figures A.62, A.63

correspondingly. In table [A.32](#) the values of midspan concrete stresses per load are presented. It is proved that Cases 16 and 5 (single-eccentric tendon) have the same midspan stress values.

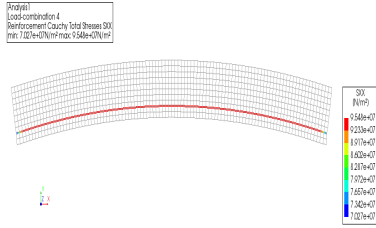


Figure A.62: Prestressing steel stresses SXX - LC4

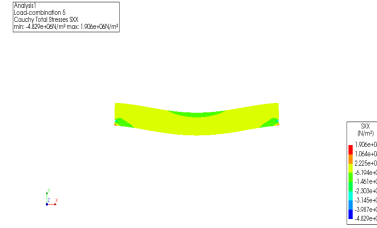


Figure A.63: Element total stresses SXX - LC5

Top	SXX [N/m <sup>2</sup> ]	F.E.M. <sub>16</sub>	F.E.M. <sub>5</sub>	$\frac{FEM_{16}}{FEM_5}$ (%)
	SXX <sub>SW</sub>	-8.76E+05	-8.76E+05	100
	SXX <sub>UDL</sub>	-1.49E+05	-1.49E+05	100
	SXX <sub>Point</sub>	-9.35E+04	-9.35E+04	100
	SXX <sub>P</sub>	+3.06E+05	+3.06E+05	100
	SXX <sub>tot</sub>	-8.13E+05	-8.13E+05	100
Bottom	SXX [N/m <sup>2</sup> ]	F.E.M. <sub>16</sub>	F.E.M. <sub>5</sub>	$\frac{FEM_{16}}{FEM_5}$ (%)
	SXX <sub>SW</sub>	+8.53E+05	+8.53E+05	100
	SXX <sub>UDL</sub>	1.45E+05	1.45E+05	100
	SXX <sub>Point</sub>	5.68E+04	5.68E+04	100
	SXX <sub>P</sub>	-1.07E+06	-1.07E+06	100
	SXX <sub>tot</sub>	-1.45E+04	-1.45E+04	100

Table A.32: Midspan element stresses SXX

### Case 17 - Prestressed concrete beam - tendon at centroidal axis - two elements

An alternative to case 6, will be the division of the beam element in half, creating two beam elements with each length to be equal to  $\frac{l}{2}$ , see figure [\(A.64\)](#).

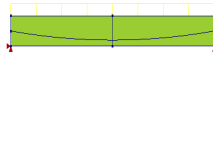


Figure A.64: Boundary and loading conditions

**Outputs:** The deflection (DtY) and the Cauchy stresses (SXX) will be the investigated results of this analysis.

**Deflection (DtY)** The midspan deflection due to the total load combination (LC5) is found to be equal with the one found in Case 6 (single beam), see table [A.33](#).

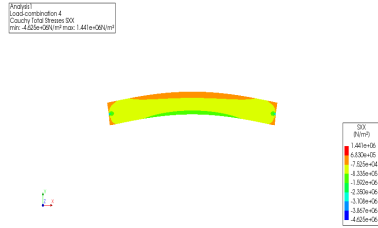


Figure A.65: Element deflection DtY - LC4

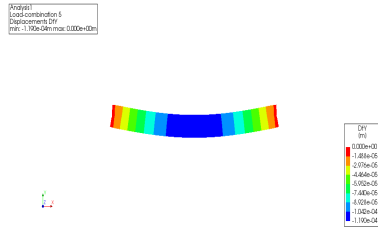


Figure A.66: Element deflection DtY - LC5

$\delta$ [m]	F.E.M. <sub>17</sub>	F.E.M. <sub>6</sub>	$\frac{FEM_{17}}{FEM_6}$ (%)
$\delta_{SW}$	2.63E-04	2.63E-04	100
$\delta_{UDL}$	4.46E-05	4.46E-05	100
$\delta_{Point}$	1.43E-05	1.43E-05	100
$\delta_P$	-2.03E-04	-2.03E-04	100
$\delta_{tot}$	1.19E-04	1.19E-04	100

Table A.33: Midspan element deflection per load - LC5

**Cauchy stresses SXX** The prestressing steel stresses of the beam due to the total load combination (LC5) are shown in figure [A.67](#) while the total concrete stresses (LC5) are depicted in figure [A.68](#). The midspan concrete stresses according to the respective load are presented in table [A.34](#). Comparing the maximum midspan stresses between Cases 17 and 6 (single element), it is found that the stresses are the same for both cases.

Project: Load-contribution 5  
 Definition: Cauchy, 1st Stress, SXX  
 min: 2.68e+07, max: 9.26e+07, unit

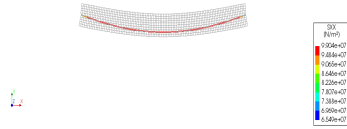


Figure A.67: Prestressing steel stresses SXX - LC5

Project: Load-contribution 5  
 Cauchy, 1st Stress, SXX  
 min: -8.16e+05, max: 1.48e+06, unit



Figure A.68: Element total stresses SXX - LC5

Top	SXX [N/m <sup>2</sup> ]	F.E.M. <sub>17</sub>	F.E.M. <sub>6</sub>	$\frac{FEM_{17}}{FEM_6}$ (%)
	SXX <sub>SW</sub>	-8.76E+05	-8.76E+05	100
	SXX <sub>UDL</sub>	-1.49E+05	-1.49E+05	100
	SXX <sub>Point</sub>	-9.35E+04	-9.35E+04	100
	SXX <sub>P</sub>	3.08E+05	3.08E+05	100
	SXX <sub>tot</sub>	-8.11E+05	-8.11E+05	100
Bottom	SXX [N/m <sup>2</sup> ]	F.E.M. <sub>17</sub>	F.E.M. <sub>6</sub>	$\frac{FEM_{17}}{FEM_6}$ (%)
	SXX <sub>SW</sub>	8.53E+05	8.53E+05	100
	SXX <sub>UDL</sub>	1.45E+05	1.45E+05	100
	SXX <sub>Point</sub>	5.68E+04	5.68E+04	100
	SXX <sub>P</sub>	-1.07E+06	-1.07E+06	100
	SXX <sub>tot</sub>	-1.58E+04	-1.58E+04	100

Table A.34: Midspan element stresses SXX

**Case 18 - Prestressed concrete beam - curved tendon at centroidal axis - curved top and bottom sides - two elements**

The geometry used in Case 9, splitting the beam in two parts of equal length rigidly connected, is incorporated in this model, see figure [A.69](#)

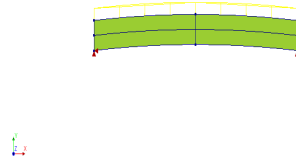


Figure A.69: Boundary and loading conditions

**Outputs:** Deflection (DtY) and Cauchy stresses (SXX) will be the investigated results of this analysis.

**Deflection (DtY)** The deflection due to central prestressing load (LC4) is shown in figure [A.70](#). The total displacement at mid-span (LC5) of the beam is found to be the same with the one found in Case 9 (single beam), see figure [A.71](#) and table [A.35](#).

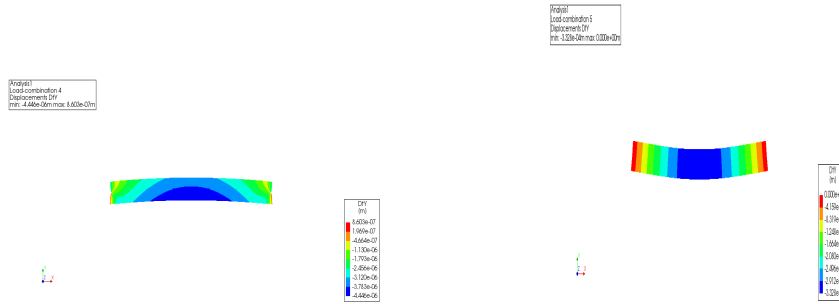


Figure A.70: Element deflection DtY - LC4

Figure A.71: Element deflection DtY - LC5

$\delta$ [m]	F.E.M. <sub>18</sub>	F.E.M. <sub>9</sub>	$\frac{FEM_{18}}{FEM_9}$ (%)
$\delta_{SW}$	2.69E-04	2.69E-04	100
$\delta_{UDL}$	4.56E-05	4.56E-05	100
$\delta_{Point}$	1.46E-05	1.46E-05	100
$\delta_P$	3.43E-06	3.43E-06	100
$\delta_{tot}$	3.33E-04	3.33E-04	100

Table A.35: Midspan element deflection per load - LC5

**Cauchy stresses SXX** The prestressing steel stresses are shown in figure [A.72](#). As expected the stresses between Case 18 and 9 (single beam) are found to be the same, see figure [A.73](#) and table [A.36](#).

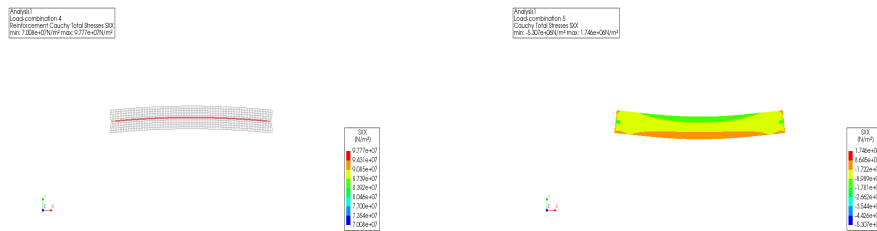


Figure A.72: Prestressing steel stresses SXX - LC4

Figure A.73: Element stresses SXX - LC5

Top	SXX [N/m <sup>2</sup> ]	F.E.M. <sub>18</sub>	F.E.M. <sub>9</sub>	$\frac{FEM_{18}}{FEM_9}$ (%)
	SXX <sub>SW</sub>	-8.81E+05	-8.80E+05	100
	SXX <sub>UDL</sub>	-1.50E+05	-1.50E+05	100
	SXX <sub>Point</sub>	-9.38E+04	-9.38E+04	100
	SXX <sub>P</sub>	-3.91E+05	-3.91E+05	100
	SXX <sub>tot</sub>	-1.52E+06	-1.52E+06	100
Bottom	SXX [N/m <sup>2</sup> ]	F.E.M. <sub>18</sub>	F.E.M. <sub>9</sub>	$\frac{FEM_{18}}{FEM_9}$ (%)
	SXX <sub>SW</sub>	+8.90E+05	+8.90E+05	100
	SXX <sub>UDL</sub>	+1.51E+05	+1.51E+05	100
	SXX <sub>Point</sub>	+5.92E+04	+5.92E+04	100
	SXX <sub>P</sub>	-3.91E+05	-3.91E+05	100
	SXX <sub>tot</sub>	+7.10E+05	+7.10E+05	100

Table A.36: Midspan element stresses SXX

**Case 19 - Prestressed concrete beam - curved tendon at eccentricity  $e_p=0.15$ [m] - curved top and bottom sides - two elements**

The geometry used in Case 10, splitting the beam in two equal in length elements is incorporated in this model, see figure [A.74](#)

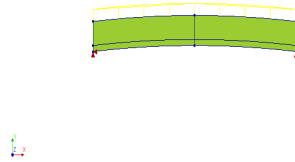


Figure A.74: Boundary and loading conditions

**Outputs:** Deflection (DtY) and Cauchy stresses (SXX) will be the investigated results of this analysis.

**Deflection (DtY)** As expected the total deflection (LC5) of the connected beams in Case 19, has the same shape and magnitude with the deflection found in Case 10 (single beam), see figure [A.75](#) and table [A.37](#). As aforementioned this deflected shape would be expected for a model with clamped supports at both ends.

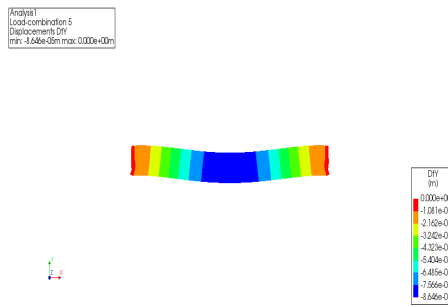


Figure A.75: Element deflection DtY - LC5

$\delta$ [m]	F.E.M. <sub>19</sub>	F.E.M. <sub>10</sub>	$\frac{FEM_{19}}{FEM_{10}}$ (%)
$\delta_{SW}$	+2.63E-04	+2.63E-04	100
$\delta_{UDL}$	+4.46E-05	+4.46E-05	100
$\delta_{Point}$	+1.43E-05	+1.43E-05	100
$\delta_P$	-2.36E-04	-2.37E-04	100
$\delta_{tot}$	+8.65E-05	+8.54E-05	101

Table A.37: Midspan element deflection per load - LC5

### Cauchy stresses SXX

The total stresses of the beam (LC5) are shown in figure [A.76](#). In table [A.38](#) the values of midspan stresses per load are shown. As expected the stresses found in Case 19 have the same values with the ones found in Case 10 (single beam).

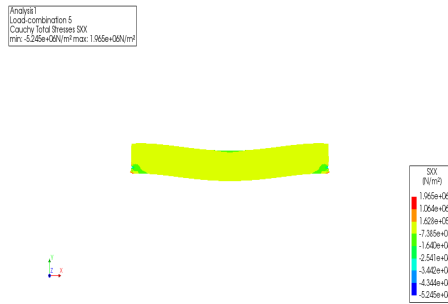


Figure A.76: Element stresses SXX - LC5

Top	SXX [N/m <sup>2</sup> ]	F.E.M. <sub>19</sub>	F.E.M. <sub>10</sub>	$\frac{FEM_{19}}{FEM_{10}}$ (%)
	SXX <sub>SW</sub>	-8.72E+05	-8.72E+05	100
	SXX <sub>UDL</sub>	-1.48E+05	-1.48E+05	100
	SXX <sub>Point</sub>	-9.32E+04	-9.32E+04	100
	SXX <sub>P</sub>	+3.02E+05	+3.02E+05	100
	SXX <sub>tot</sub>	-8.11E+05	-8.11E+05	100
Bottom	SXX [N/m <sup>2</sup> ]	F.E.M. <sub>19</sub>	F.E.M. <sub>10</sub>	$\frac{FEM_{19}}{FEM_{10}}$ (%)
	SXX <sub>SW</sub>	+8.58E+05	+8.58E+05	100
	SXX <sub>UDL</sub>	+1.46E+05	+1.46E+05	100
	SXX <sub>Point</sub>	+5.71E+04	+5.71E+04	100
	SXX <sub>P</sub>	-1.07E+06	-1.07E+06	100
	SXX <sub>tot</sub>	-1.27E+04	-1.27E+04	100

Table A.38: Midspan element stresses SXX

**Case 20 - Prestressed concrete beam - curved tendon at eccentricity  $e_p = 0.15$ [m] - curved top and bottom sides - right angles - two elements**

The geometry used in Case 13, splitting the beam in two parts of equal length, is incorporated in this model, see figure [A.77](#)

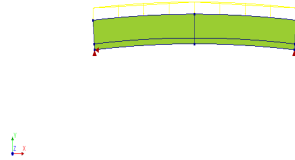


Figure A.77: Boundary and loading conditions

**Outputs:** Deflection (DtY) and Cauchy stresses (SXX) will be the investigated results of this analysis.

**Deflection (DtY)** As expected the total deflection (LC5) of the connected beams in Case 20, has the same value with the deflection found in Case 13 (single beam), see figure [A.78](#) and table [A.39](#)

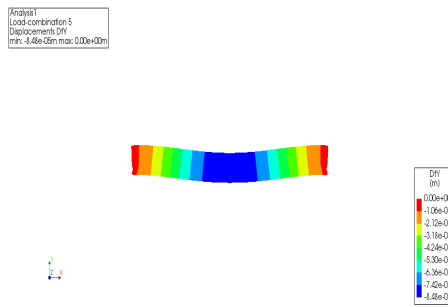


Figure A.78: Element deflection DtY - LC5

$\delta$ [m]	F.E.M. <sub>20</sub>	F.E.M. <sub>13</sub>	$\frac{FEM_{20}}{FEM_{13}}$ (%)
$\delta_{SW}$	+2.61E-04	+2.61E-04	100
$\delta_{UDL}$	+4.43E-05	+4.43E-05	100
$\delta_{Point}$	+1.42E-05	+1.42E-05	100
$\delta_P$	-2.36E-04	-2.36E-04	100
$\delta_{tot}$	+8.49E-05	+8.49E-05	100

Table A.39: Midspan element deflection per load - LC5

### Cauchy stresses SXX

The total stresses of the beam (LC5) are shown in figure [A.79](#). In table [A.40](#), the values of concrete midspan stresses according to the respective load are shown. As expected the stresses found in Case 20 have the values with the ones found in Case 13 (single element).

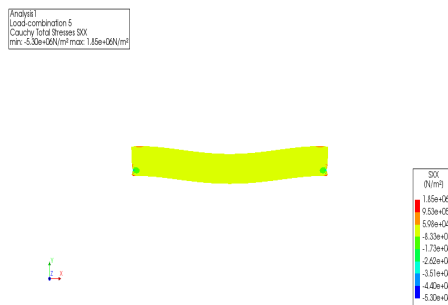


Figure A.79: Element stresses SXX - LC5

Top	SXX [N/m <sup>2</sup> ]	F.E.M. <sub>20</sub>	F.E.M. <sub>13</sub>	$\frac{FEM_{20}}{FEM_{13}}$ (%)
	SXX <sub>SW</sub>	-8.72E+05	-8.72E+05	100
	SXX <sub>UDL</sub>	-1.48E+05	-1.48E+05	100
	SXX <sub>Point</sub>	-9.33E+04	-9.33E+04	100
	SXX <sub>P</sub>	3.02E+05	3.02E+05	100
	SXX <sub>tot</sub>	-8.12E+05	-8.12E+05	100
Bottom	SXX [N/m <sup>2</sup> ]	F.E.M. <sub>20</sub>	F.E.M. <sub>13</sub>	$\frac{FEM_{20}}{FEM_{13}}$ (%)
	SXX <sub>SW</sub>	+8.58E+05	+8.58E+05	100
	SXX <sub>UDL</sub>	+1.46E+05	+1.46E+05	100
	SXX <sub>Point</sub>	+5.71E+04	+5.71E+04	100
	SXX <sub>P</sub>	-1.07E+06	-1.07E+06	100
	SXX <sub>tot</sub>	-1.25E+04	-1.25E+04	100

Table A.40: Midspan element stresses SXX

**Case 21 - Prestressed concrete beam - straight linear tendon at c.a - joint 0.05[m]**

An alternative to cases 3 (single) and 15 (equally split elements) will be the inclusion of a 0.05[m] joint at midspan assumed to be rigidly connected to the two beam elements, see figure (A.80).

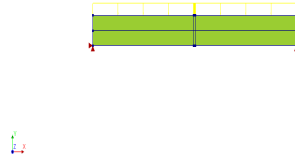


Figure A.80: Boundary and loading conditions - Case 21

**Outputs:** The deflection (DtY) and the Cauchy stresses (SXX) will be the investigated results of this analysis.

**Deflection (DtY)** The total deflection at midspan (LC5) is found to be the same with Case 3 (single beam) and Case 15 (two equal beams - no joint), see figure (A.82) and table (A.41). The vertical deflection of the element due to central prestressing should be negligible (figure (A.81)).

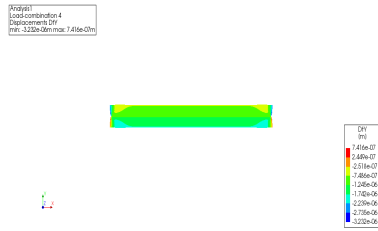


Figure A.81: Element deflection DtY - LC4

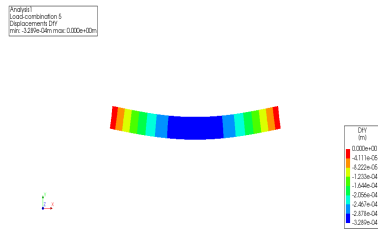


Figure A.82: Element deflection DtY - LC5

$\delta$ [m]	F.E.M. <sub>21</sub>	F.E.M. <sub>15</sub>	$\frac{FEM_{21}}{FEM_{15}}$ (%)
$\delta_{SW}$	+2.68E-04	+2.68E-04	100
$\delta_{UDL}$	+4.54E-05	+4.54E-05	100
$\delta_{Point}$	+1.46E-05	+1.46E-05	100
$\delta_P$	-7.02E-07	-7.02E-07	100
$\delta_{tot}$	+3.29E-04	+3.29E-04	100

Table A.41: Midspan element deflection per load - LC5

**Cauchy stresses SXX** The prestressing stresses of the beam (LC4) are shown in figure [A.83](#) while the total stresses (LC5) are depicted in figure [A.84](#). The midspan concrete stress values according to the respective load are presented in table [A.42](#). Comparing the concrete stresses due to the total load combination (LC5) between Cases 21 and 15, it is found that they have the same values at bottom fiber level, while they are larger by 1.62% at top fiber in Case 21. Note that there is a 20.9% increase in midspan stresses due to the point load (LC3) in the Case 21 relative to Case 15. This may be the result of irregular meshing when pre-processing the FEM.

Project: load-concentration 4  
 Cauchy (Sxx) Stress (N/m<sup>2</sup>)  
 min = -3.22e+06 max = 1.87e+06 (N/m<sup>2</sup>)



Figure A.83: Prestressing steel stresses SXX - LC4

Project: load-concentration 5  
 Cauchy (Sxx) Stress (N/m<sup>2</sup>)  
 min = -3.15e+06 max = 1.83e+06 (N/m<sup>2</sup>)



Figure A.84: Element stresses SXX - LC5

Top	SXX [N/m <sup>2</sup> ]	F.E.M. <sub>.21</sub>	F.E.M. <sub>.15</sub>	$\frac{FEM_{.21}}{FEM_{.15}}$ (%)
	SXX <sub>SW</sub>	-8.85E+05	-8.85E+05	100
	SXX <sub>UDL</sub>	-1.50E+05	-1.50E+05	100
	SXX <sub>Point</sub>	-1.19E+05	-9.41E+04	127
	SXX <sub>P</sub>	-3.91E+05	-3.91E+05	100
	SXX <sub>tot</sub>	-1.55E+06	-1.52E+06	102
Bottom	SXX [N/m <sup>2</sup> ]	F.E.M. <sub>.21</sub>	F.E.M. <sub>.15</sub>	$\frac{FEM_{.21}}{FEM_{.15}}$ (%)
	SXX <sub>SW</sub>	+8.85E+05	+8.85E+05	100
	SXX <sub>UDL</sub>	+1.50E+05	+1.50E+05	100
	SXX <sub>Point</sub>	+5.89E+04	+5.89E+04	100
	SXX <sub>P</sub>	-3.91E+05	-3.91E+05	100
	SXX <sub>tot</sub>	+7.03E+05	+7.03E+05	100

Table A.42: Midspan element stresses SXX

**Case 22 - Prestressed concrete beam - eccentric tendon at  $e_p = 0.15[m]$  below c.a - joint 0.05[m]**

The geometry used in Case 5 is used in this model, having split the initial beam in two equal in length smaller beams and including a joint of 0.05[m], assumed to be rigidly connected to the left and right elements, see figure [A.85](#).

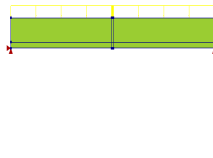


Figure A.85: Boundary and loading conditions

**Outputs:** Deflection (DtY) and Cauchy stresses (SXX) will be the investigated results of this analysis.

**Deflection (DtY)** The deflected shape of the concrete element due to the prestressing (LC4) and the total load combination (LC5) is presented in figures A.86 and A.87. The total midspan deflection of the beam (LC5) is found to be equal to the one found in Case 16. The maximum deflection values per load are shown in the following table A.43.

Analysis  
Load combination 4  
Displacement DtY  
min: -2.433e-05m; max: 2.375e-04m

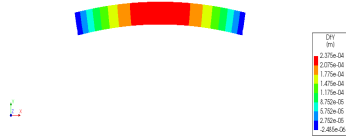


Figure A.86: Element deflection DtY - LC4

Analysis  
Load combination 5  
Displacement DtY  
min: -2.433e-05m; max: 2.375e-04m

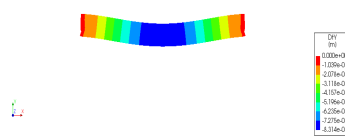


Figure A.87: Element deflection DtY - LC5

$\delta$ [m]	F.E.M. <sub>22</sub>	F.E.M. <sub>16</sub>	$\frac{FEM_{22}}{FEM_{16}}$ (%)
$\delta_{SW}$	+2.62E-04	+2.62E-04	100
$\delta_{UDL}$	+4.44E-05	+4.44E-05	100
$\delta_{Point}$	+1.43E-05	+1.42E-05	100
$\delta_P$	-2.38E-04	-2.38E-04	100
$\delta_{tot}$	+8.31E-05	+8.31E-05	100

Table A.43: Midspan element deflection per load

**Cauchy stresses SXX** The total stresses of the concrete and the reinforcement under the load combination are shown in figures A.88, A.89. Comparing the midspan stresses due to the total load combination (LC5) between Cases 22 and 16, it is found that at they are increased by 3.01% at top and by 1.09% at bottom fiber level relative to Case 16.

Analysis  
Load combination 5  
Reinforcement Cauchy total Stress SXX  
min: 7.102e-08N/m<sup>2</sup>; max: 9.923e-07N/m<sup>2</sup>

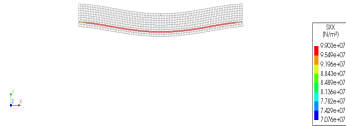


Figure A.88: Prestressing steel stresses SXX - LC5

Analysis  
Load combination 5  
Concrete total Stress SXX  
min: -4.133e-08N/m<sup>2</sup>; max: 1.912e-06N/m<sup>2</sup>



Figure A.89: Element stresses SXX - LC5

Top	SXX [N/m <sup>2</sup> ]	F.E.M. <sub>22</sub>	F.E.M. <sub>16</sub>	$\frac{FEM_{22}}{FEM_{16}}$ (%)
	SXX <sub>SW</sub>	-8.76E+05	-8.76E+05	100
	SXX <sub>UDL</sub>	-1.49E+05	-1.49E+05	100
	SXX <sub>Point</sub>	-1.19E+05	-9.35E+04	127
	SXX <sub>P</sub>	+3.06E+05	+3.06E+05	100
	SXX <sub>tot</sub>	-8.38E+05	-8.13E+05	103
Bottom	SXX [N/m <sup>2</sup> ]	F.E.M. <sub>22</sub>	F.E.M. <sub>16</sub>	$\frac{FEM_{22}}{FEM_{16}}$ (%)
	SXX <sub>SW</sub>	+8.53E+05	+8.53E+05	100
	SXX <sub>UDL</sub>	+1.45E+05	+1.45E+05	100
	SXX <sub>Point</sub>	+5.68E+04	+5.68E+04	100
	SXX <sub>P</sub>	-1.07E+06	-1.07E+06	100
	SXX <sub>tot</sub>	-1.47E+04	-1.45E+04	101

Table A.44: Midspan element stresses SXX

### Case 23 - Prestressed concrete beam - curved tendon at centroidal axis - joint 0.05[m]

An alternative to Case 6 (single beam), will be splitting the initial beam in two equal in length elements and a smaller one of 0.05[m] in length, simulating a joint in the middle. It is assumed to be rigidly connected to the beam elements, see figure (A.90).



Figure A.90: Boundary and loading conditions

**Outputs:** The deflection (DtY) and the Cauchy stresses (SXX) will be the investigated results of this analysis.

**Deflection (DtY)** The deflected shape of the concrete element due to the prestressing (LC4) and the total load combination (LC5) is presented in figures A.91 and A.92. The total deflection at midspan (LC5) is equal in value with Case 17, see table A.45.

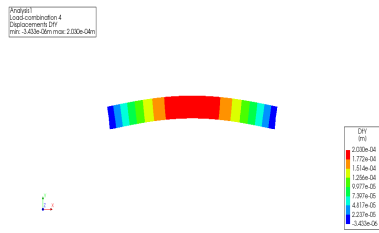


Figure A.91: Element deflection DtY - LC4

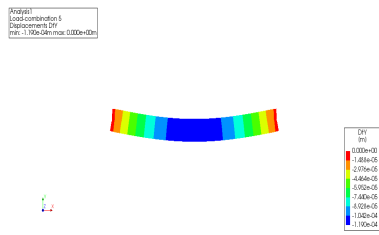


Figure A.92: Element deflection DtY - LC5

$\delta$ [m]	F.E.M. <sub>23</sub>	F.E.M. <sub>17</sub>	$\frac{FEM_{23}}{FEM_{17}}$ (%)
$\delta_{SW}$	+2.63E-04	+2.63E-04	100
$\delta_{UDL}$	+4.46E-05	+4.46E-05	100
$\delta_{Point}$	+1.43E-05	+1.43E-05	100
$\delta_P$	-2.03E-04	-2.03E-04	100
$\delta_{tot}$	+1.19E-04	+1.19E-04	100

Table A.45: Midspan element deflection per load

**Cauchy stresses SXX** The prestressing steel stresses of the beam due to the total load combination (LC5) are shown in figure [A.93](#), while in figure [\(A.94\)](#) the total concrete stresses are depicted. The midspan values of stresses according per load are presented in table [A.46](#). Comparing the stresses between Cases 23 and 17, it is found that the stresses of Case 23 are larger by 3.02% and by 0.57% at top and bottom fiber level respectively in comparison with Case 17.

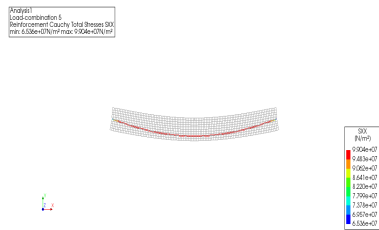


Figure A.93: Prestressing steel stresses SXX - LC5

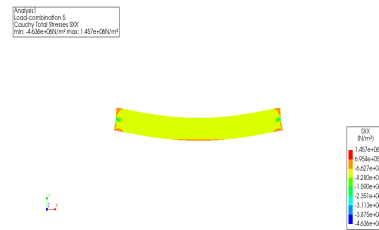


Figure A.94: Element stresses SXX - LC5

Top	SXX [N/m <sup>2</sup> ]	F.E.M. <sub>23</sub>	F.E.M. <sub>17</sub>	$\frac{FEM_{23}}{FEM_{17}}$ (%)
	SXX <sub>SW</sub>	-8.76E+05	-8.76E+05	100
	SXX <sub>UDL</sub>	-1.49E+05	-1.49E+05	100
	SXX <sub>Point</sub>	-1.19E+05	-9.35E+04	127
	SXX <sub>P</sub>	+3.08E+05	+3.08E+05	100
	SXX <sub>tot</sub>	-8.36E+05	-8.11E+05	103
Bottom	SXX [N/m <sup>2</sup> ]	F.E.M. <sub>23</sub>	F.E.M. <sub>17</sub>	$\frac{FEM_{23}}{FEM_{17}}$ (%)
	SXX <sub>SW</sub>	+8.53E+05	+8.53E+05	100
	SXX <sub>UDL</sub>	+1.45E+05	+1.45E+05	100
	SXX <sub>Point</sub>	+5.68E+04	+5.68E+04	100
	SXX <sub>P</sub>	-1.07E+06	-1.07E+06	100
	SXX <sub>tot</sub>	-1.59E+04	-1.58E+04	101

Table A.46: Midspan element stresses SXX

**Case 24 - Prestressed concrete beam - curved tendon at eccentricity  $e_p = 0.15[m]$  from c.a - curved top and bottom sides - joint  $0.05[m]$**

Case 10 geometry will be used in this model having split the initial beam length in three elements. The left and right element will simulate the beam elements, while the middle element will model a joint having a length of  $0.05[m]$ , see figure [A.95](#).

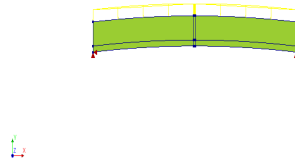


Figure A.95: Boundary and loading conditions

**Outputs:** Deflection (DtY) and Cauchy stresses (SXX) will be the investigated results of this analysis.

**Deflection (DtY)** The deflected shape of the concrete element due to the total load combination (LC5) is presented in figure [A.96](#). The total deflection (LC5) at midspan of the beam is found to be equal to the deflection found in Case 19, see table [A.47](#).

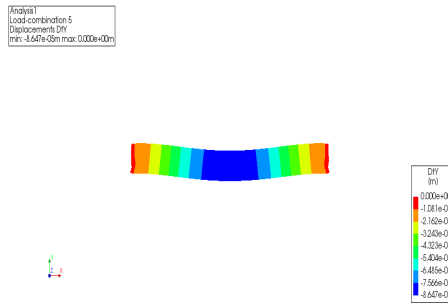


Figure A.96: Element deflection DtY - LC5

$\delta$ [m]	F.E.M. <sub>30</sub>	F.E.M. <sub>24</sub>	$\frac{FEM_{30}}{FEM_{24}}$ (%)
$\delta_{SW}$	+2.63E-04	+2.63E-04	100
$\delta_{UDL}$	+4.46E-05	+4.46E-05	100
$\delta_{Point}$	+1.43E-05	+1.43E-05	100
$\delta_P$	-2.36E-04	-2.36E-04	100
$\delta_{tot}$	+8.65E-05	+8.65E-05	100

Table A.47: Midspan element deflection per load - LC5

**Cauchy stresses SXX** The stresses of the beam under the total load combination (LC5) are shown in figure [A.97](#). In table [A.48](#), the values of midspan concrete stresses per load are shown. The stresses in this case are found to be larger by 2.98% at top fiber level and by 1.24% at bottom fiber level, than in Case 19. A reason for this result may be that creating three elements, two of which have considerably bigger length than the joint-middle element, could result in an increase of compression stresses at the smaller in length element.

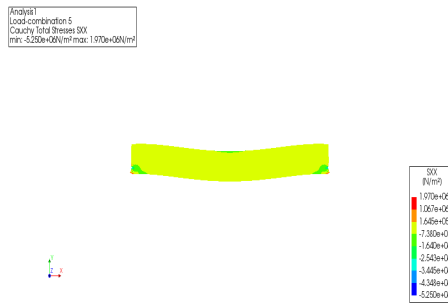


Figure A.97: Element stresses SXX - LC5

Top	SXX [N/m <sup>2</sup> ]	F.E.M. <sub>24</sub>	F.E.M. <sub>19</sub>	$\frac{FEM_{24}}{FEM_{19}}$ (%)
	SXX <sub>SW</sub>	-8.71E+05	-8.72E+05	100
	SXX <sub>UDL</sub>	-1.48E+05	-1.48E+05	100
	SXX <sub>Point</sub>	-1.18E+05	-9.32E+04	127
	SXX <sub>P</sub>	+3.02E+05	+3.02E+05	100
	SXX <sub>tot</sub>	-8.36E+05	-8.11E+05	103
Bottom	SXX [N/m <sup>2</sup> ]	F.E.M. <sub>24</sub>	F.E.M. <sub>19</sub>	$\frac{FEM_{24}}{FEM_{19}}$ (%)
	SXX <sub>SW</sub>	+8.58E+05	+8.58E+05	100
	SXX <sub>UDL</sub>	+1.46E+05	+1.46E+05	100
	SXX <sub>Point</sub>	+5.71E+04	+5.71E+04	100
	SXX <sub>P</sub>	-1.07E+06	-1.07E+06	100
	SXX <sub>tot</sub>	-1.29E+04	-1.27E+04	101

Table A.48: Midspan element stresses SXX

**Case 25 - Prestressed concrete beams - curved tendon at centroidal axis - curved top and bottom sides - right angles - joint 0.05[m]**

Case's 12 geometry will be used in this model having split the initial beam length in three elements. The left and right element will simulate the beam elements, while the middle element will simulate a joint having a length of 0.05[m], see figure [A.98](#).

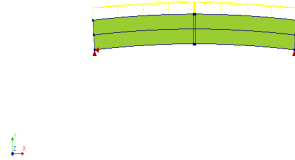


Figure A.98: Boundary and loading conditions

**Outputs:** Deflection (DtY) and Cauchy stresses (SXX) will be the investigated results of this analysis.

**Deflection (DtY)** The total displacement at mid-span of the beam (LC5) has the same value with the deflection found in Case 12, see figure [A.99](#) and table [A.49](#).

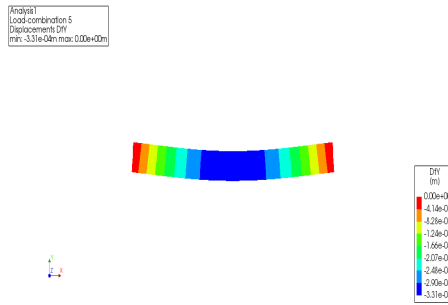


Figure A.99: Element deflection DtY - LC5

$\delta$ [m]	F.E.M. <sub>25</sub>	F.E.M. <sub>12</sub>	$\frac{FEM_{25}}{FEM_{12}}$ (%)
$\delta_{SW}$	+2.67E-04	+2.67e-4	100
$\delta_{UDL}$	+4.54E-05	+4.54e-5	100
$\delta_{Point}$	+1.46E-05	+1.45e-5	100
$\delta_P$	-3.27E-06	-3.18e-6	103
$\delta_{tot}$	+3.31E-04	+3.31e-4	100

Table A.49: Midspan element deflection per load - LC5

**Cauchy stresses SXX** The maximum midspan stresses of the beam under the total load combination (LC5) are shown in figure [A.100](#). In table [A.50](#), the values of concrete stresses according to the respective load are shown. Comparing this case with Case 12 (single beam), it is found that the stresses are similar. However, in this case, at top fiber level there is a 2.19% increase of total stresses at midspan, while at bottom fiber level, the stresses are decreased by 0.74%. Note that an unexpected stress concentration (red color in the contour plot) occurs at a concentrated location at midspan where the tendon profile coincides with the element mesh.

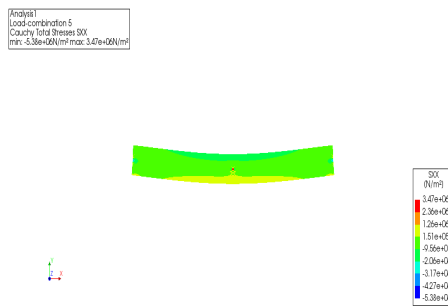


Figure A.100: Element stresses SXX - LC5

Top	SXX [N/m <sup>2</sup> ]	F.E.M. <sub>25</sub>	F.E.M. <sub>12</sub>	$\frac{FEM_{25}}{FEM_{12}}$ (%)
	SXX <sub>SW</sub>	-8.81E+05	-8.81E+05	100
	SXX <sub>UDL</sub>	-1.50E+05	-1.50E+05	100
	SXX <sub>Point</sub>	-1.19E+05	-9.39E+04	127
	SXX <sub>P</sub>	-4.01E+05	-3.91E+05	102
	SXX <sub>tot</sub>	-1.55E+06	-1.52E+06	102
Bottom	SXX [N/m <sup>2</sup> ]	F.E.M. <sub>25</sub>	F.E.M. <sub>12</sub>	$\frac{FEM_{25}}{FEM_{12}}$ (%)
	SXX <sub>SW</sub>	+8.90E+05	+8.90E+05	100
	SXX <sub>UDL</sub>	+1.51E+05	+1.51E+05	100
	SXX <sub>Point</sub>	+5.92E+04	+5.92E+04	100
	SXX <sub>P</sub>	-4.01E+05	-3.91E+05	103
	SXX <sub>tot</sub>	+7.05E+05	+7.10E+05	99

Table A.50: Midspan element stress values SXX

**Case 26 - Prestressed concrete beam - curved tendon at eccentricity  $e_p=0.15$ [m] below c.a. - curved top and bottom sides - right angles - joint 0.05[m]**

Case 's13 geometry will be used in this model, having split the initial beam length in three elements. The left and right element will simulate the beam elements, while the middle element will model a joint having a length of 0.05[m], see figure [A.101](#).

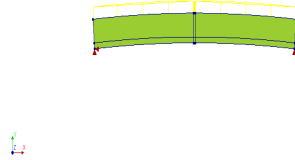


Figure A.101: Boundary and loading conditions

**Outputs:** Deflection (DtY) and Cauchy stresses (SXX) will be the investigated results of this analysis.

**Deflection (DtXYZ)** The total deflection (LC5) at midspan of the beam is found to be increased by 6.34% in comparison with the deflection found in Case 20, see figure [A.102](#) and table [A.51](#).

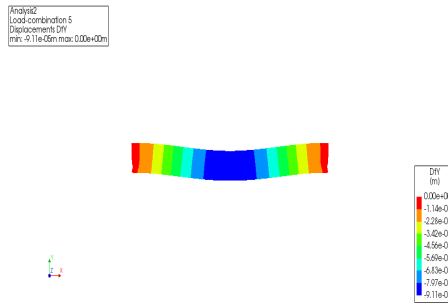


Figure A.102: Element deflection DtXYZ - LC5

$\delta$ [m]	F.E.M. <sub>26</sub>	F.E.M. <sub>20</sub>	$\frac{FEM_{26}}{FEM_{20}}$ (%)
$\delta_{SW}$	+2.61E-04	+2.67e-4	100
$\delta_{UDL}$	+4.44E-05	+4.43E-05	100
$\delta_{Point}$	+1.43E-05	+1.42E-05	100
$\delta_P$	-2.30E-04	-2.36E-04	98
$\delta_{tot}$	+9.06E-05	+8.49E-05	107

Table A.51: Midspan element deflection per load

**Cauchy stresses SXX** The midspan stresses of the beam under the total load combination (LC5) are shown in figure [A.103](#). In table [A.52](#), the values of stresses per applied load are shown. The stresses in this case are found to be larger by 8.7% at top fiber level, while they change sign at bottom fiber level and become tensile in comparison with Case 20. Note that an unexpected stress concentration (red color in the element contour plot) occurs at a concentrated location at midspan where the tendon profile coincides with the element mesh.

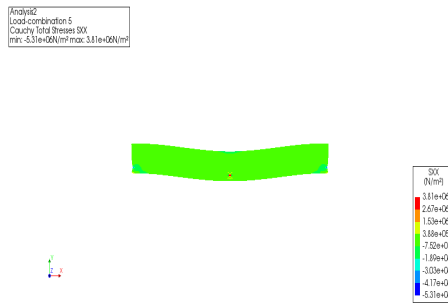


Figure A.103: Element stresses SXX - LC5

Top	SXX [N/m <sup>2</sup> ]	F.E.M. <sub>26</sub>	F.E.M. <sub>20</sub>	$\frac{FEM_{26}}{FEM_{20}}$ (%)
	SXX <sub>SW</sub>	-8.73E+05	-8.72E+05	100
	SXX <sub>UDL</sub>	-1.48E+05	-1.48E+05	100
	SXX <sub>Point</sub>	-1.18E+05	-9.33E+04	127
	SXX <sub>P</sub>	+2.52E+05	+3.02E+05	84
	SXX <sub>tot</sub>	-8.89E+05	-8.12E+05	110
Bottom	SXX [N/m <sup>2</sup> ]	F.E.M. <sub>26</sub>	F.E.M. <sub>20</sub>	$\frac{FEM_{26}}{FEM_{20}}$ (%)
	SXX <sub>SW</sub>	+8.59E+05	+8.58E+05	100
	SXX <sub>UDL</sub>	+1.46E+05	+1.46E+05	100
	SXX <sub>Point</sub>	+5.71E+04	+5.71E+04	100
	SXX <sub>P</sub>	-1.05E+06	-1.07E+06	98
	SXX <sub>tot</sub>	+1.41E+05	-1.25E+04	change of sign

Table A.52: Midspan element stresses SXX

### Case 27 - Prestressed concrete beams - tendon at centroidal axis - interface at joint

In order to simulate a 5cm joint with a different stiffness than its surrounding concrete elements, an addition of a structural interface at midspan will be included in this model. According to DIANA 10.1 manual, “the structural interface elements describe the interface behavior in terms of a relation between the normal and shear tractions and the normal and shear relative displacements across the interface. One of the typical applications for structural interface elements are joints”. The geometry of Case 1 split in two parts, including a 0.05[m] joint in between them, will be used in this case, see figure [A.104](#). The joint was set to be a structural 2D line interface with linear elastic material properties and the following rules were applied for the interface stiffnesses of this model:

1. elastic stiffness modulus:  $k_n = \frac{E}{l_{fr}} = \frac{E}{t} = \frac{36 \times 10^9}{0.01} = 36 \times 10^{11} [\frac{N}{m}]$
2. shear stiffness modulus:  $k_s = k_t = \frac{E}{2 \times l_{fr}} = \frac{E}{2 \times t} = \frac{36 \times 10^9}{2 \times 0.01} = 18 \times 10^{11} [\frac{N}{m^2}]$



Figure A.104: Boundary and loading conditions

**Outputs:** The deflection (DtY) and the Cauchy stresses (SXX) will be the investigated results of this analysis.

**Deflection (DtXYZ)** The total deflection (LC5) at midspan, is increased by 0.90% in comparison with Case 21 (rigid connection), see figure A.106 and table A.53. The vertical deflection (DtY) of the element due to central prestressing (LC4) should be negligible, see figure A.105.

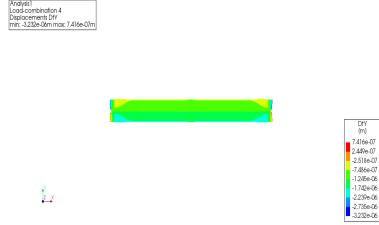


Figure A.105: Element deflection DtY - LC4

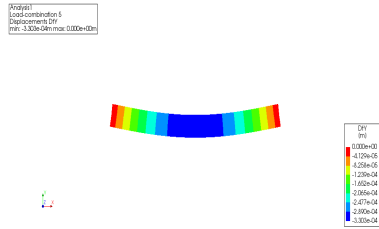


Figure A.106: Element deflection DtY - LC5

$\delta$ [m]	F.E.M. <sub>27</sub>	F.E.M. <sub>21</sub>	$\frac{FEM_{27}}{FEM_{21}}$ (%)
$\delta_{SW}$	+2.70E-04	+2.68E-04	101
$\delta_{UDL}$	+4.58E-05	+4.54E-05	101
$\delta_{Point}$	+1.48E-05	+1.46E-05	101
$\delta_P$	-7.87E-07	-7.02E-07	112
$\delta_{tot}$	+3.32E-04	+3.29E-04	101

Table A.53: Midspan element deflection per load

**Cauchy stresses SXX** The prestressing steel stresses (SXX - LC4) of the beam are shown in figure A.107, while the total midspan concrete stresses (SXX - LC5) are depicted in figure A.108. Note that there is a reduction of prestressing steel stresses at midspan, a result that was not anticipated, see discontinuity in the tendon contour. The midspan values of stresses according to the respective load are presented in table A.58. Comparing the stresses between Cases 27 and 21 (rigid joint), it is found that the stresses in the first case, are approximately the same at top (decreased by 0.26%) and at bottom (increased by 0.73%) fiber level.

Project: Load-conductor 4  
 Analysis: Cauchy (SXX) Stress (SXX)  
 min: 7.733e+07; max: 9.773e+07(N/m²)

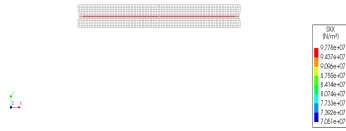


Figure A.107: Prestressing steel stresses SXX - LC4

Project: Load-conductor 5  
 Analysis: Cauchy (SXX) Stress (SXX)  
 min: -4.704e+06; max: 1.802e+08(N/m²)



Figure A.108: Element stresses SXX - LC5

Top	SXX [N/m <sup>2</sup> ]	F.E.M. <sub>.27</sub>	F.E.M. <sub>.21</sub>	$\frac{FEM_{.27}}{FEM_{.21}}$ (%)
	SXX <sub>SW</sub>	-8.85E+05	-8.85E+05	100
	SXX <sub>UDL</sub>	-1.50E+05	-1.50E+05	100
	SXX <sub>Point</sub>	-1.19E+05	-1.19E+05	100
	SXX <sub>P</sub>	-3.87E+05	-3.91E+05	99
	SXX <sub>tot</sub>	-1.54E+06	-1.55E+06	100
Bottom	SXX [N/m <sup>2</sup> ]	F.E.M. <sub>.27</sub>	F.E.M. <sub>.21</sub>	$\frac{FEM_{.27}}{FEM_{.21}}$ (%)
	SXX <sub>SW</sub>	8.85E+05	8.85E+05	100
	SXX <sub>UDL</sub>	1.50E+05	1.50E+05	100
	SXX <sub>Point</sub>	5.89E+04	5.89E+04	100
	SXX <sub>P</sub>	-3.85E+05	-3.91E+05	98
	SXX <sub>tot</sub>	7.09E+05	7.03E+05	101

Table A.54: Midspan element stresses SXX

**Case 28 - Prestressed concrete beams - eccentric tendon at distance  $e_p = 0.15[m]$  below the centroidal axis - interface at joint**

The geometry used in Case 22 is used in this model, including the 0.05[m] joint at midspan and a structural interface at both edges of the joint, see figure [A.109](#). The stiffness moduli of the joint are defined the same with case 27.

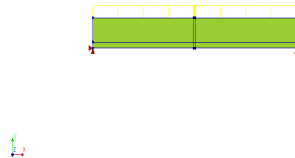
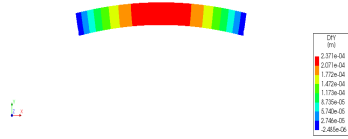


Figure A.109: Boundary and loading conditions

**Outputs:** Deflection (DtY) and Cauchy stresses (SXX) will be the investigated results of this analysis.

**Deflection (DtY)** Likewise in cases of eccentric prestressing, a downward curvature of the beam is present near the midspan, while an upward curvature is present near the supports of the beam, considered as an unexpected result, see figure [A.111](#). The deflection due to the prestressing load (DtY - LC4) becomes maximum at midspan position, see figure [A.110](#). The midspan total deflection (DtY - LC5) is increased by 2.23% in comparison with Case 22. The maximum deflection values are shown in table [A.55](#).

Model1  
Load combination 4  
Displacements (m)  
min: 2.458e-06 max: 2.371e-04m



Model1  
Load combination 5  
Displacements (m)  
min: -4.386e-05m max: 1.033e-04m

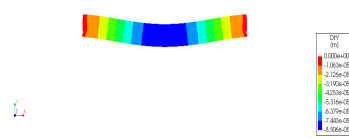


Figure A.110: Element deflection DtY - LC4

Figure A.111: Element deflection DtY - LC5

$\delta$ [m]	F.E.M. <sub>28</sub>	F.E.M. <sub>22</sub>	$\frac{FEM_{28}}{FEM_{22}}$ (%)
$\delta_{SW}$	2.63E-04	2.62E-04	100
$\delta_{UDL}$	4.46E-05	4.44E-05	100
$\delta_{Point}$	1.43E-05	1.43E-05	101
$\delta_P$	-2.37E-04	-2.38E-04	100
$\delta_{tot}$	8.50E-05	8.31E-05	102

Table A.55: Midspan element deflection per load

**Cauchy stresses SXX** The total stresses of the prestressing steel reinforcement and the concrete under the total load combination (LC5) are shown in figures [A.112](#), [A.113](#) respectively. In table [A.60](#) the values of concrete stresses according to the respective load are shown. At top fiber level, due to the eccentric tendon input, tensile stresses occur. Comparing the midspan stresses due to the load combination between Cases 28 and 22 (rigid joint), it is found that in the first case they increase by 42.53% and by 63.33% at bottom fiber level.

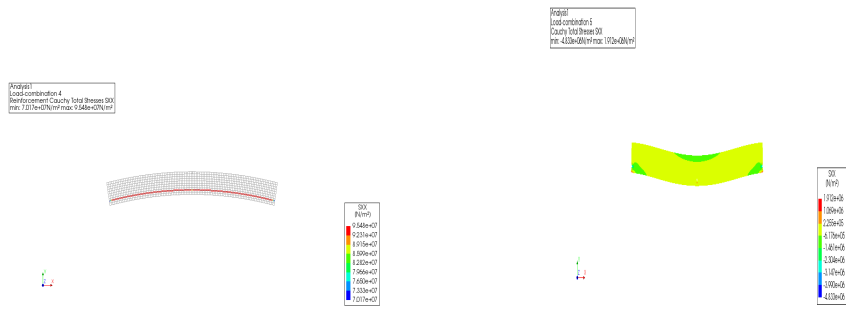


Figure A.112: Prestressing steel stresses SXX - LC4

Figure A.113: Element stresses SXX - LC5

Top	SXX [N/m <sup>2</sup> ]	F.E.M. <sub>.28</sub>	F.E.M. <sub>.22</sub>	$\frac{FEM_{.28}}{FEM_{.22}}$ (%)
	SXX <sub>SW</sub>	-8.76E+05	-8.76E+05	100
	SXX <sub>UDL</sub>	-1.49E+05	-1.49E+05	100
	SXX <sub>Point</sub>	-1.19E+05	-1.19E+05	100
	SXX <sub>P</sub>	+2.94E+05	+3.06E+05	96
	SXX <sub>tot</sub>	-8.50E+05	-8.38E+05	101
Bottom	SXX [N/m <sup>2</sup> ]	F.E.M. <sub>.28</sub>	F.E.M. <sub>.22</sub>	$\frac{FEM_{.28}}{FEM_{.22}}$ (%)
	SXX <sub>SW</sub>	+8.55E+05	+8.53E+05	100
	SXX <sub>UDL</sub>	+1.45E+05	+1.45E+05	100
	SXX <sub>Point</sub>	+5.69E+04	+5.68E+04	100
	SXX <sub>P</sub>	-1.02E+06	-1.07E+06	95
	SXX <sub>tot</sub>	+3.87E+04	-1.47E+04	change of sign

Table A.56: Midspan element stresses SXX

### Case 29 - Prestressed concrete beams - curved tendon at centroidal axis - interface at joint

As an alternative to Case 23 (rigid joint), an interface at joint's connection with the surrounding concrete elements will be included in this case, see figure (A.114). The stiffness moduli of the joint are defined the same with case 27.

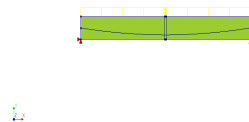


Figure A.114: Boundary and loading conditions

**Outputs:** The deflection (DtY) and the Cauchy stresses (SXX) will be the investigated results of this analysis.

**Deflection (DtXYZ)** The total deflection (LC5) at midspan is increased by 3.09% in comparison with case Case 23. An upward curvature is determining the deflected shape of the concrete element due to the total load combination (LC5).

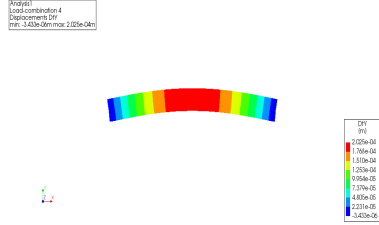


Figure A.115: Element deflection DtY - LC4

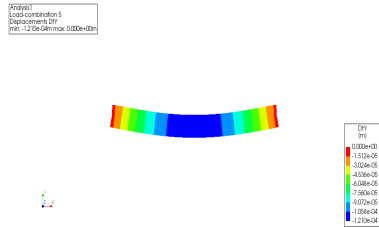


Figure A.116: Element deflection DtY - LC5

$\delta$ [m]	F.E.M. <sub>29</sub>	F.E.M. <sub>23</sub>	$\frac{FEM_{29}}{FEM_{23}}$ (%)
$\delta_{SW}$	+2.65E-04	+2.63E-04	101
$\delta_{UDL}$	+4.50E-05	+4.46E-05	101
$\delta_{Point}$	+1.45E-05	+1.43E-05	101
$\delta_P$	-2.02E-04	-2.03E-04	100
$\delta_{tot}$	+1.23E-04	+1.19E-04	103

Table A.57: Midspan element deflection per load

**Cauchy stresses SXX** The prestressing steel stresses due to the total load combination (LC5) are shown in figure [A.117](#) while the midspan concrete stresses are depicted in figure [A.118](#). The concrete stresses SXX at midspan per applied load are presented in table [A.58](#). It is found that the stresses are increased by 2.63% at top, while they change sign and turn into tensile ones at bottom fiber level bottom in comparison with the stresses found in Case 23.

Project: Load-Combination 5  
 Analysis: Concrete Cracks, Total Strain SXX  
 min: -8.58e+05, max: 2.86e+05 [N/m²]

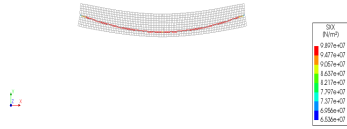


Figure A.117: Prestressing steel stresses SXX - LC5

Project: Load-Combination 5  
 Analysis: Concrete Cracks, Total Strain SXX  
 min: -8.58e+05, max: 1.45e+05 [N/m²]



Figure A.118: Element stresses SXX - LC5

Top	SXX [N/m <sup>2</sup> ]	F.E.M. <sub>29</sub>	F.E.M. <sub>23</sub>	$\frac{FEM_{29}}{FEM_{23}}$ (%)
	SXX <sub>SW</sub>	-8.77E+05	-8.76E+05	100
	SXX <sub>UDL</sub>	-1.49E+05	-1.49E+05	100
	SXX <sub>Point</sub>	-1.19E+05	-1.19E+05	100
	SXX <sub>P</sub>	2.86E+05	3.08E+05	93
	SXX <sub>tot</sub>	-8.58E+05	-8.36E+05	103
Bottom	SXX [N/m <sup>2</sup> ]	F.E.M. <sub>29</sub>	F.E.M. <sub>23</sub>	$\frac{FEM_{29}}{FEM_{23}}$ (%)
	SXX <sub>SW</sub>	8.56E+05	8.53E+05	100
	SXX <sub>UDL</sub>	1.45E+05	1.45E+05	100
	SXX <sub>Point</sub>	5.70E+04	5.68E+04	100
	SXX <sub>P</sub>	-9.69E+05	-1.07E+06	90
	SXX <sub>tot</sub>	8.92E+04	-1.59E+04	change of sign

Table A.58: Midspan element stresses SXX

**Case 30 - Prestressed concrete beams - curved tendon at a distance  $e_p = 0.15[m]$  - curved top and bottom sides - right angles - interface at joint**

The geometry used in Case 24 is used in this model, including a 0.05[m] joint at midspan and a structural interface at both edges of the joint, see figure [A.119](#). The stiffness moduli of the joint are defined the same with case 27.

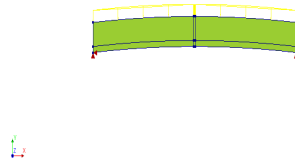


Figure A.119: Boundary and loading conditions

**Outputs:** Deflection (DtY) and Cauchy stresses (SXX) will be the investigated results of this analysis.

**Deflection (DtY)** The total displacement at mid-span (LC5) of the beam is increased by 4.17% in comparison with the deflection found in Case 24, see figure [A.120](#) and table [A.59](#).

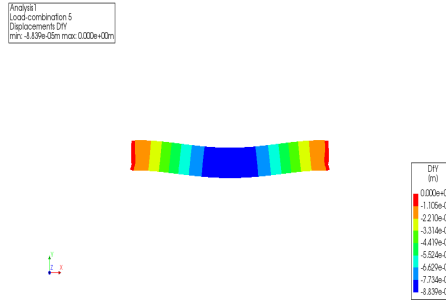


Figure A.120: Element deflection DtY - LC5

$\delta$ [m]	F.E.M. <sub>30</sub>	F.E.M. <sub>24</sub>	$\frac{FEM_{30}}{FEM_{24}}$ (%)
$\delta_{SW}$	+2.65E-04	+2.63E-04	101
$\delta_{UDL}$	+4.50E-05	+4.46E-05	101
$\delta_{Point}$	+1.45E-05	+1.43E-05	101
$\delta_P$	-2.35E-04	-2.36E-04	100
$\delta_{tot}$	+9.02E-05	+8.65E-05	104

Table A.59: Midspan element deflection per load

**Cauchy stresses SXX** The concrete stresses under the total load combination (LC5) are shown in figure [A.121](#). The midspan concrete stresses per load are presented in table [A.60](#). Comparing this case with Case 24, it is found that the midspan stresses are increased by 2.65% at top fiber level in this case, while they change sign and turn into tensile ones at bottom fiber level.

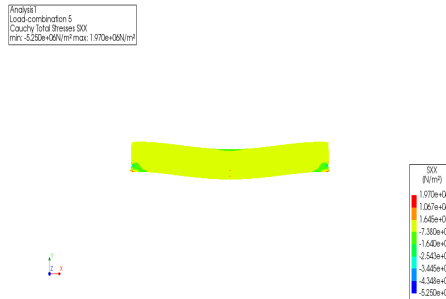


Figure A.121: Element total SXX - LC5

Top	SXX [N/m <sup>2</sup> ]	F.E.M. <sub>30</sub>	F.E.M. <sub>24</sub>	$\frac{FEM_{30}}{FEM_{24}}$ (%)
	SXX <sub>SW</sub>	-8.72E+05	-8.71E+05	100
	SXX <sub>UDL</sub>	-1.48E+05	-1.48E+05	100
	SXX <sub>Point</sub>	-1.18E+05	-1.18E+05	100
	SXX <sub>P</sub>	+2.81E+05	+3.02E+05	93
	SXX <sub>tot</sub>	-8.59E+05	-8.36E+05	103
Bottom	SXX [N/m <sup>2</sup> ]	F.E.M. <sub>30</sub>	F.E.M. <sub>24</sub>	$\frac{FEM_{30}}{FEM_{24}}$ (%)
	SXX <sub>SW</sub>	+8.60E+05	+8.58E+05	100
	SXX <sub>UDL</sub>	+1.46E+05	+1.46E+05	100
	SXX <sub>Point</sub>	+5.73E+04	+5.71E+04	100
	SXX <sub>P</sub>	-9.72E+05	-1.07E+06	91
	SXX <sub>tot</sub>	+9.19E+04	-1.29E+04	change of sign

Table A.60: Midspan element stresses SXX

**Case 31 - Prestressed concrete beams - curved tendon at centroidal axis - curved top and bottom sides - right angles - interface at joint**

The geometry used in Case 25 is used in this model, including the 0.05[m] joint at midspan and adding a structural interface at both edges of the joint, see figure [A.122](#). The stiffness moduli of the joint are defined the same with case 27.

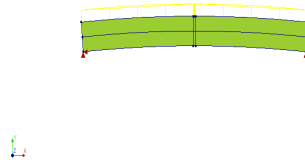


Figure A.122: Boundary and loading conditions

**Outputs:** Deflection (DtY) and Cauchy stresses (SXX) will be the investigated results of this analysis.

**Deflection (DtY)** The total displacement at mid-span of the beam (LC5) is increased by 0.24% in comparison with the deflection in Case 25, hence considered as similar result, see figure [A.123](#) and table [A.61](#)

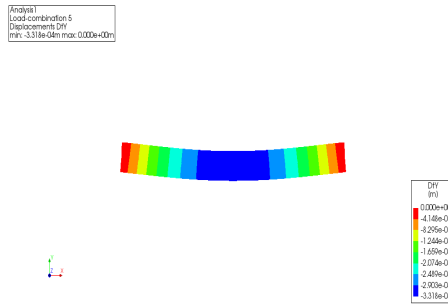


Figure A.123: Element deflection DtY - LC5

$\delta$ [m]	F.E.M. <sub>.31</sub>	F.E.M. <sub>.25</sub>	$\frac{FEM_{.31}}{FEM_{.25}}$ (%)
$\delta_{SW}$	+2.69E-04	+2.67E-04	100
$\delta_{UDL}$	+4.56E-05	+4.54E-05	100
$\delta_{Point}$	+1.47E-05	+1.46E-05	101
$\delta_P$	-3.24E-06	-3.27E-06	99
$\delta_{tot}$	+3.32E-04	+3.31E-04	100

Table A.61: Midspan element deflection per load

**Cauchy stresses SXX** The concrete stresses of the beam under the total load combination (LC5) are shown in figure [A.124](#). The values of concrete stresses at midspan according to the respective load are presented in table [A.62](#). Comparing this case with Case 25, it is found that the stresses are similar. In particular, there is a 0.19% decrease and a 0.52% increase of total midspan stresses at top and bottom fiber level respectively. Note that an unexpected stress concentration (red color in the contour plot) occurs at a concentrated location at midspan where the tendon profile coincides with the element mesh.

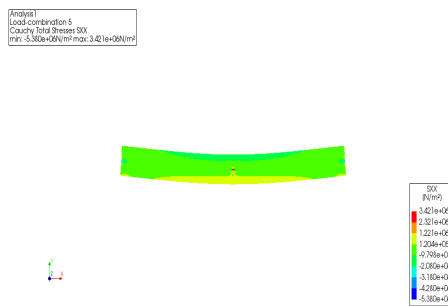


Figure A.124: Element stresses SXX - LC5

Top	SXX [N/m <sup>2</sup> ]	F.E.M. <sub>31</sub>	F.E.M. <sub>25</sub>	$\frac{FEM_{31}}{FEM_{25}}$ (%)
	SXX <sub>SW</sub>	-8.81E+05	-8.81E+05	100
	SXX <sub>UDL</sub>	-1.50E+05	-1.50E+05	100
	SXX <sub>Point</sub>	-1.19E+05	-1.19E+05	100
	SXX <sub>P</sub>	-3.98E+05	-4.01E+05	99
	SXX <sub>tot</sub>	-1.55E+06	-1.55E+06	100
Bottom	SXX [N/m <sup>2</sup> ]	F.E.M. <sub>31</sub>	F.E.M. <sub>25</sub>	$\frac{FEM_{31}}{FEM_{25}}$ (%)
	SXX <sub>SW</sub>	+8.90E+05	+8.90E+05	100
	SXX <sub>UDL</sub>	+1.51E+05	+1.51E+05	100
	SXX <sub>Point</sub>	+5.92E+04	+5.92E+04	100
	SXX <sub>P</sub>	-3.85E+05	-4.01E+05	96
	SXX <sub>tot</sub>	+7.09E+05	+7.05E+05	101

Table A.62: Midspan element stresses SXX

**Case 32 - Prestressed concrete beams - curved tendon at eccentricity  $e_p = 0.15[m]$  - curved top and bottom sides - right angles - interface at joint**

The geometry used in Case 26 is used in this model, including the 0.05[m] joint at midspan and a structural interface at both edges of the joint, see figure [A.125](#). The stiffness moduli of the joint are defined the same with case 27.

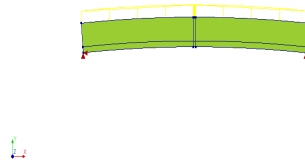


Figure A.125: Boundary and loading conditions

**Outputs:** Deflection (DtY) and Cauchy stresses (SXX) will be the investigated results of this analysis.

**Deflection (DtY)** The total deflection (LC5) at midspan of the beam is found to be increased by 3.4% compared with Case 26, see figure [A.126](#) and table [A.63](#). Note that this deflection line of the concrete element due to the total load combination was not expected and instead a constant upward curvature would be the anticipated result.

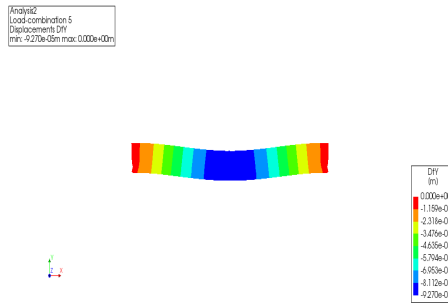


Figure A.126: Element deflection DtY - LC5

$\delta$ [m]	F.E.M. <sub>.32</sub>	F.E.M. <sub>.26</sub>	$\frac{FEM_{.32}}{FEM_{.26}}$ (%)
$\delta_{SW}$	+2.64E-04	+2.61E-04	101
$\delta_{UDL}$	+4.48E-05	+4.44E-05	101
$\delta_{Point}$	+1.44E-05	+1.43E-05	101
$\delta_P$	-2.30E-04	-2.30E-04	100
$\delta_{tot}$	+9.38E-05	+9.06E-05	104

Table A.63: Midspan element deflection per load

**Cauchy stresses SXX** The stresses of the beam under the total load combination (LC5) are shown in figure [A.127](#). The values of stresses according to the respective load are shown in table [A.64](#). The midspan concrete stresses in this case are found to be larger by 1.75% at top fiber level, while they are considerably decreased by 70% at bottom fiber level, comparing with Case 26.

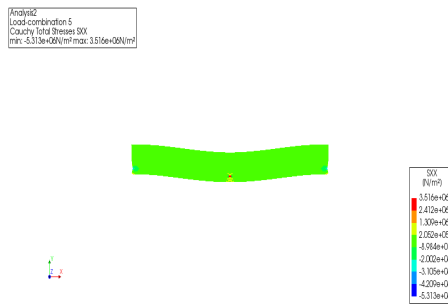


Figure A.127: Element stresses SXX - LC5

Top	SXX [N/m <sup>2</sup> ]	F.E.M. <sub>32</sub>	F.E.M. <sub>26</sub>	$\frac{FEM_{32}}{FEM_{26}}$ (%)
	SXX <sub>SW</sub>	-8.74E+05	-8.73E+05	100
	SXX <sub>UDL</sub>	-1.48E+05	-1.48E+05	100
	SXX <sub>Point</sub>	-1.18E+05	-1.18E+05	100
	SXX <sub>P</sub>	+2.38E+05	+2.52E+05	95
	SXX <sub>tot</sub>	-9.05E+05	-8.89E+05	102
Bottom	SXX [N/m <sup>2</sup> ]	F.E.M. <sub>32</sub>	F.E.M. <sub>26</sub>	$\frac{FEM_{32}}{FEM_{26}}$ (%)
	SXX <sub>SW</sub>	+8.61E+05	+8.59E+05	100
	SXX <sub>UDL</sub>	+1.46E+05	+1.46E+05	100
	SXX <sub>Point</sub>	+5.73E+04	+5.71E+04	100
	SXX <sub>P</sub>	-9.65E+05	-1.05E+06	92
	SXX <sub>tot</sub>	+9.88E+04	+1.41E+05	70

Table A.64: Midspan element stresses SXX

### Case 33 - Prestressed concrete beam - tendon at centroidal axis - increased stiffness interface at joint

Likewise in Cases 21 and 27, in order to simulate a 5[cm] joint in-between the two connected concrete element, an addition of a structural 2D line interface with linear elastic material properties will be included in this model at midspan. As aforementioned the geometry of Case 27 and will be used in this case, see figure [A.128](#). However an increased stiffness in both normal and shear direction will be used for the interface applied at midspan for this case. The following rules will apply for the interface stiffnesses in this model:

1. elastic stiffness modulus:  $k_n = \frac{E_c \times 1000}{l_{cont.element}} = \frac{36 \times 10^9 \times 10^3}{0.05} = 7.2 \times 10^{14} [\frac{N}{m}]$
2. shear stiffness modulus:  $k_s = k_t \approx k_n = 7.2 \times 10^{14} [\frac{N}{m}]$



Figure A.128: Boundary and loading conditions

**Outputs:** The deflection (DtY) and the Cauchy stresses (SXX) will be the investigated results of this analysis.

**Deflection (DtY)** The total deflection (LC5) at midspan, is decreased by 0.91% in comparison with Case 27 (smaller interface stiffness), see figure [A.130](#) and table [\(A.65\)](#). Comparing the total deflection found between Cases 36 and

21 (rigid connection), it is found that the midspan deflection has the same value for both cases. The vertical deflection of the element due to central prestressing (LC4) should be negligible, see figure [A.129](#)

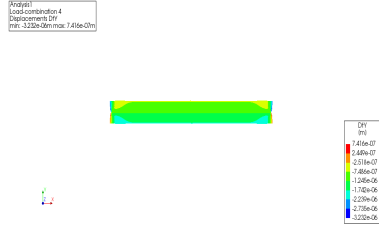


Figure A.129: Element deflection DtY - LC4

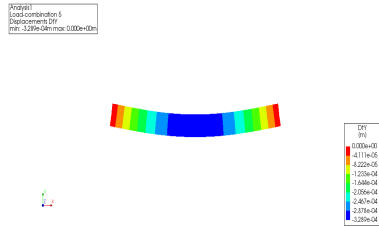


Figure A.130: Element deflection DtY - LC5

$\delta$ [m]	F.E.M. <sub>33</sub>	F.E.M. <sub>27</sub>	$\frac{FEM_{33}}{FEM_{27}}$ (%)
$\delta_{SW}$	+2.68E-04	+2.70E-04	99
$\delta_{UDL}$	+4.54E-05	+4.58E-05	99
$\delta_{Point}$	+1.46E-05	+1.48E-05	99
$\delta_P$	-7.02E-07	-7.87E-07	89
$\delta_{tot}$	+3.29E-04	+3.32E-04	99

Table A.65: Midspan element deflection per load

**Cauchy stresses SXX** The prestressing steel stresses due to the prestressing load are shown in figure [A.131](#), while the total stresses are depicted in figure [A.132](#). The midspan concrete stresses per load are presented in table [A.66](#). Comparing the stresses between Cases 33 and 27 (lower interface stiffness), it is found that the stresses in the first case, are increased by 3.4% at top fiber level, and they are decreased by 0.91% at bottom fiber level.

Program: Load-combinator 4  
 Displacement: max. 1.61E+03 [mm]  
 min.: -0.00E+00 [mm] max.: 0.77E+03 [mm]



Figure A.131: Prestressing steel stresses SXX - LC4

Program: Load-combinator 5  
 Displacement: max. 0.00E+00 [mm]  
 min.: -0.00E+00 [mm] max.: 0.00E+00 [mm]

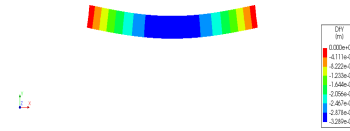


Figure A.132: Element stresses SXX - LC5

Top	SXX [N/m <sup>2</sup> ]	F.E.M. <sub>.33</sub>	F.E.M. <sub>.27</sub>	$\frac{FEM_{.33}}{FEM_{.27}}$ (%)
	SXX <sub>SW</sub>	-8.85E+05	-8.85E+05	100
	SXX <sub>UDL</sub>	-1.50E+05	-1.50E+05	100
	SXX <sub>Point</sub>	-1.19E+05	-1.19E+05	100
	SXX <sub>P</sub>	-3.91E+05	-3.87E+05	101
	SXX <sub>tot</sub>	-1.55E+06	-1.54E+06	100
Bottom	SXX [N/m <sup>2</sup> ]	F.E.M. <sub>.33</sub>	F.E.M. <sub>.27</sub>	$\frac{FEM_{.33}}{FEM_{.27}}$ (%)
	SXX <sub>SW</sub>	+8.85E+05	+8.85E+05	100
	SXX <sub>UDL</sub>	+1.50E+05	+1.50E+05	100
	SXX <sub>Point</sub>	+5.89E+04	+5.89E+04	100
	SXX <sub>P</sub>	-3.91E+05	-3.85E+05	102
	SXX <sub>tot</sub>	+7.03E+05	+7.09E+05	99

Table A.66: Midspan element stresses SXX

### Case 34 - Prestressed concrete beam - curved tendon at centroidal axis - increased stiffness interface at joint

As an alternative to Case 29 (lower shear stiffness interface), an increased normal and shear stiffness 2D line structural interface with linear elastic material properties will be included in this case, see figure (A.133). The stiffness moduli of the joint are defined the same with case 33.

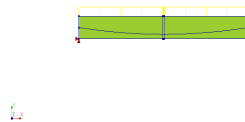


Figure A.133: Boundary and loading conditions

**Outputs:** The deflection (DtY) and the Cauchy stresses (SXX) will be the investigated results of this analysis.

**Deflection (DtXYZ)** The total deflection (LC5) at midspan is reduced by 3.11% compared with Case 29 (lower stiffness interface), see figure [A.135](#) and table [A.67](#). The deflection of the concrete elements due to the prestressing load (LC4) is depicted in figure [A.134](#).

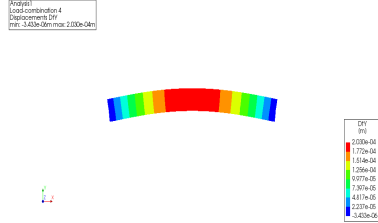


Figure A.134: Element deflection DtY - LC4

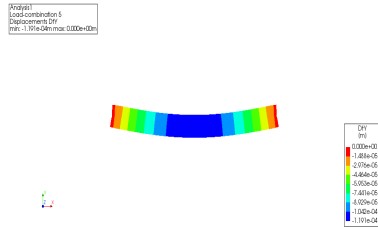


Figure A.135: Element deflection DtY - LC5

$\delta$ [m]	F.E.M. <sub>34</sub>	F.E.M. <sub>29</sub>	$\frac{FEM_{33}}{FEM_{27}}$ (%)
$\delta_{SW}$	+2.63E-04	+2.65E-04	99
$\delta_{UDL}$	+4.46E-05	+4.50E-05	99
$\delta_{Point}$	+1.43E-05	+1.45E-05	99
$\delta_P$	-2.03E-04	-2.02E-04	100
$\delta_{tot}$	+1.19E-04	+1.23E-04	97

Table A.67: Midspan element deflection per load

**Cauchy stresses SXX** The prestressing steel stresses due to the total load combination (LC5) are shown in figure [A.136](#). The concrete element stresses (LC5) are depicted in figure [A.137](#). The midspan values of concrete stresses according to the respective load are presented in table [A.68](#). The total stresses (LC5) are found to be decreased by 2.7% at the top while they change sign and turn into compressive in comparison with Case 29 (lower stiffness interface). It can be seen that the magnitude of element prestressing stresses differs in both cases, since it shows an increase when the stiffness moduli are increased compared to Case 29.

Project: load-combination 5  
 Analysis: Concrete Analysis, Mid-Beam, SXX  
 min: -8.36E+05, max: 9.23E+05, unit

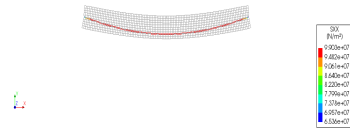


Figure A.136: Prestressing steel stresses SXX - LC4

Project: load-combination 5  
 Analysis: Concrete Analysis, Mid-Beam, SXX  
 min: -8.58E+05, max: 1.45E+06, unit



Figure A.137: Element stresses SXX - LC5

Top	SXX [N/m <sup>2</sup> ]	F.E.M. <sub>.34</sub>	F.E.M. <sub>.29</sub>	$\frac{FEM_{.34}}{FEM_{.29}}$ (%)
	SXX <sub>SW</sub>	-8.76E+05	-8.77E+05	100
	SXX <sub>UDL</sub>	-1.49E+05	-1.49E+05	100
	SXX <sub>Point</sub>	-1.19E+05	-1.19E+05	100
	SXX <sub>P</sub>	+3.08E+05	+2.86E+05	108
	SXX <sub>tot</sub>	-8.36E+05	-8.58E+05	97
Bottom	SXX [N/m <sup>2</sup> ]	F.E.M. <sub>.34</sub>	F.E.M. <sub>.29</sub>	$\frac{FEM_{.34}}{FEM_{.29}}$ (%)
	SXX <sub>SW</sub>	+8.53E+05	+8.56E+05	100
	SXX <sub>UDL</sub>	+1.45E+05	+1.45E+05	100
	SXX <sub>Point</sub>	+5.68E+04	+5.70E+04	100
	SXX <sub>P</sub>	-1.07E+06	-9.69E+05	110
	SXX <sub>tot</sub>	-1.57E+04	+8.92E+04	change of sign

Table A.68: Midspan element stresses SXX

**Case 35 - Prestressed concrete beam - anchorages at a distance of  $e_p = 0.15[m]$  from the centroidal axis - increased stiffness interface at joint**

The geometry used of Case 28 is used in this model, including an increased normal and shear stiffness structural interface at both edges of the joint, see figure [A.138](#). The stiffness moduli of the joint are defined the same with case 33.



Figure A.138: Boundary and loading conditions

**Outputs:** Deflection (DtY) and Cauchy stresses (SXX) will be the investigated results of this analysis.

**Deflection (DtY)** An upward curvature of the beam is present near the midspan, while a downward curvature is present near the supports of the beam, hence a result not to be expected. The deflection due to the prestressing load (LC4) becomes maximum at midspan position, see figure (A.139). The midspan total deflection (LC5) is decreased by 2.27% in comparison with Case 28 (smaller interface stiffness). The maximum deflection values are shown in table (A.69).

Analysis1  
Load combination 4  
Displacement: Dy  
min: -2.445E-04m; max: 2.375E-04m

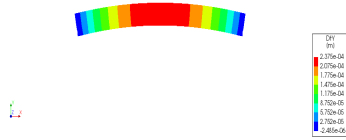


Figure A.139: Element deflection DtY - LC4

Analysis1  
Load combination 5  
Displacement: Dy  
min: -4.315E-04m; max: 4.035E-04m

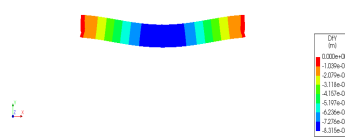


Figure A.140: Element deflection DtY - LC5

$\delta$ [m]	F.E.M. <sub>35</sub>	F.E.M. <sub>28</sub>	$\frac{FEM_{35}}{FEM_{28}}$ (%)
$\delta_{SW}$	+2.62E-04	+2.63E-04	100
$\delta_{UDL}$	+4.44E-05	+4.46E-05	100
$\delta_{Point}$	+1.43E-05	+1.43E-05	99
$\delta_P$	-2.38E-04	-2.37E-04	100
$\delta_{tot}$	+8.32E-05	+8.50E-05	98

Table A.69: Midspan element deflection per load

**Cauchy stresses SXX** The reinforcement and concrete stresses under the prestressing load (LC4) and the total load combination (LC5) respectively are shown in figures (A.141) and (A.142). The values of midspan concrete stresses per applied load are shown in table (A.70). Due to the eccentric tendon input, tensile stresses occur at top fiber level under the prestressing load (LC4). Comparing the midspan concrete stresses due to the load combination (LC5) between Cases 35 and 28 (smaller stiffness), it is found that in the first case they are decreased by 1.43% at top fiber level, while they change sign and turn into compressive ones at bottom fiber level.

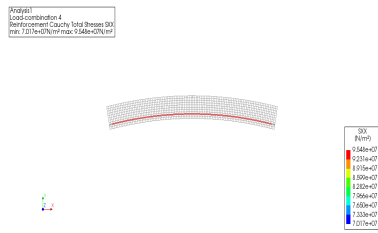


Figure A.141: Prestressing steel stresses SXX - LC4

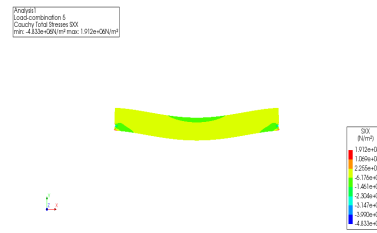


Figure A.142: Element stresses SXX - LC5

Top	SXX [N/m <sup>2</sup> ]	F.E.M. <sub>.35</sub>	F.E.M. <sub>.28</sub>	$\frac{FEM_{.35}}{FEM_{.28}}$ (%)
	SXX <sub>SW</sub>	-8.76E+05	-8.76E+05	100
	SXX <sub>UDL</sub>	-1.49E+05	-1.49E+05	100
	SXX <sub>Point</sub>	-1.19E+05	-1.19E+05	100
	SXX <sub>P</sub>	+3.06E+05	+2.94E+05	104
	SXX <sub>tot</sub>	-8.38E+05	-8.50E+05	99
Bottom	SXX [N/m <sup>2</sup> ]	F.E.M. <sub>.35</sub>	F.E.M. <sub>.28</sub>	$\frac{FEM_{.35}}{FEM_{.28}}$ (%)
	SXX <sub>SW</sub>	+8.53E+05	+8.55E+05	100
	SXX <sub>UDL</sub>	+1.45E+05	+1.45E+05	100
	SXX <sub>Point</sub>	+5.68E+04	+5.69E+04	100
	SXX <sub>P</sub>	-1.07E+06	-1.02E+06	105
	SXX <sub>tot</sub>	-1.44E+04	+3.87E+04	change of sign

Table A.70: Midspan element stresses SXX

**Case 36 - Prestressed concrete beams - curved tendon at centroidal axis - curved top and bottom edges - right angles - increased stiffness interface at joint**

The geometry of Case 31 is used in this model, including a 0.05[m] joint at midspan and an increased stiffness structural 2D line interface at both edges of the joint, see figure [A.143](#). The stiffness moduli of the joint are defined the same with case 33.

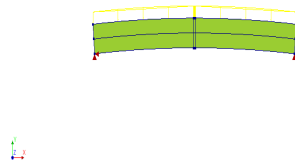


Figure A.143: Boundary and loading conditions

**Outputs:** Deflection (DtY) and Cauchy stresses (SXX) will be the investigated results of this analysis.

**Deflection (DtY)** The total displacement at mid-span of the beam is decreased by 4.04% in comparison with the deflection in Case 31 (smaller shear interface stiffness), see figure [A.144](#) and table [A.71](#).

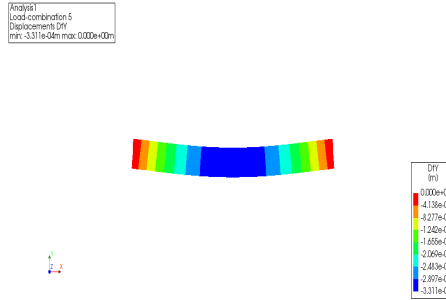


Figure A.144: Element deflection DtY - LC5

$\delta$ [m]	F.E.M. <sub>36</sub>	F.E.M. <sub>31</sub>	$\frac{FEM_{36}}{FEM_{31}}$ (%)
$\delta_{SW}$	+2.67E-04	+2.69E-04	100
$\delta_{UDL}$	+4.54E-05	+4.56E-05	100
$\delta_{Point}$	+1.46E-05	+1.47E-05	99
$\delta_P$	-3.27E-06	-3.24E-06	101
$\delta_{tot}$	+3.31E-04	+3.32E-04	100

Table A.71: Midspan element deflection per load

**Cauchy stresses SXX** The maximum midspan stresses of the beam under the total load combination (LC5) are shown in figure [A.145](#). In table [A.72](#), the values of concrete stresses according to the respective load are shown. Comparing this case with Case 31 (smaller interface stiffness), it is found that the stresses are similar. However, in this case, at top fiber level there is a 1.51% increase of total stresses at midspan, while at bottom fiber level, the stresses are decreased by 0.26%. Note that an unexpected stress concentration (red color in the contour plot) occurs at a concentrated location at midspan where the tendon profile coincides with the element mesh.

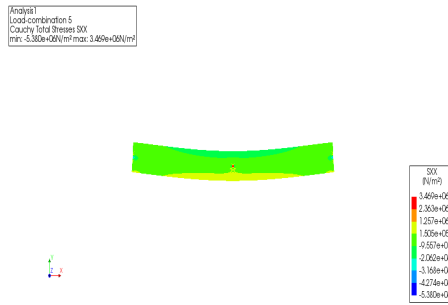


Figure A.145: Element stresses SXX - LC5

Top		SXX [N/m <sup>2</sup> ]	F.E.M. <sub>.36</sub>	F.E.M. <sub>.31</sub>	$\frac{FEM_{.36}}{FEM_{.31}}$ (%)
	SXX <sub>SW</sub>		-8.81E+05	-8.81E+05	100
	SXX <sub>UDL</sub>		-1.50E+05	-1.50E+05	100
	SXX <sub>Point</sub>		-1.19E+05	-1.19E+05	100
	SXX <sub>P</sub>		-4.01E+05	-3.98E+05	101
	SXX <sub>tot</sub>		-1.55E+06	-1.55E+06	100
Bottom		SXX [N/m <sup>2</sup> ]	F.E.M. <sub>.36</sub>	F.E.M. <sub>.31</sub>	$\frac{FEM_{.36}}{FEM_{.31}}$ (%)
	SXX <sub>SW</sub>		+8.90E+05	+8.90E+05	100
	SXX <sub>UDL</sub>		+1.51E+05	+1.51E+05	100
	SXX <sub>Point</sub>		+5.92E+04	+5.92E+04	100
	SXX <sub>P</sub>		-4.01E+05	-3.85E+05	104
	SXX <sub>tot</sub>		+7.05E+05	+7.09E+05	99

Table A.72: Midspan element stresses SXX

**Case 37 - Prestressed concrete beams - curved tendon at eccentricity  $e_p = 0.15$ [m] - curved top and bottom edges - right angles - increased stiffness interface at joint**

The geometry used in Case 32 (lower shear stiffness interface) is used in this model, including a structural interface with increased stiffness at both edges of the joint, see figure A.146. The stiffness moduli of the joint are defined the same with case 33.

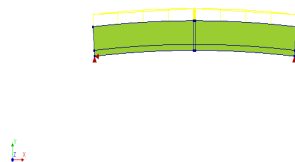


Figure A.146: Boundary and loading conditions

**Outputs:** Deflection (DtY) and Cauchy stresses (SXX) will be the investigated results of this analysis.

**Deflection (DtY)** The total deflection (LC5) at midspan of the beam is decreased by 3.51% in comparison with the deflection found in Case 32 (lower interface stiffness), see figure A.147 and table A.73. As aforementioned the deflected shape of the concrete element due to the total load combination (LC5) would be expected for a fully clamped beam and not a simply supported as in this case.

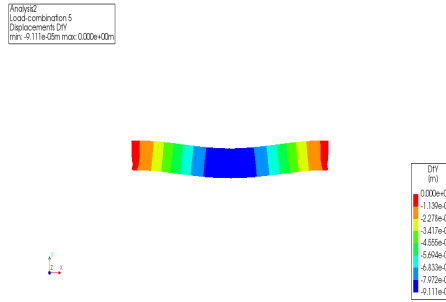


Figure A.147: Element deflection DtY - LC5

$\delta$ [m]	F.E.M. <sub>37</sub>	F.E.M. <sub>32</sub>	$\frac{FEM_{37}}{FEM_{32}}$ (%)
$\delta_{SW}$	+2.61E-04	+2.64E-04	99
$\delta_{UDL}$	+4.44E-05	+4.48E-05	99
$\delta_{Point}$	+1.43E-05	+1.44E-05	99
$\delta_P$	-2.30E-04	-2.30E-04	100
$\delta_{tot}$	+9.06E-05	+9.38E-05	97

Table A.73: Midspan element deflection per load

**Cauchy stresses SXX** The stresses of the beam under the total load combination (LC5) are shown in figure A.148. In table A.74, the values of stresses according to the respective load are shown. The stresses in this case are found to be reduced by 1.70% at top fiber level, while they are increased by 30.11% at bottom fiber level relative to Case 35 (smaller interface stiffness). Note that an unexpected stress concentration (red color in the contour plot) occurs at a concentrated location at midspan where the tendon profile coincides with the element mesh.

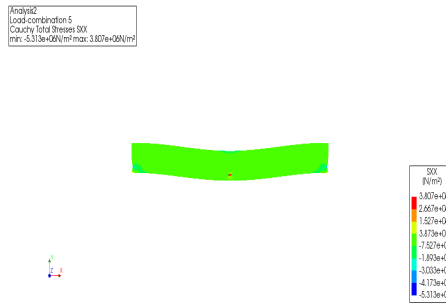


Figure A.148: Element stresses SXX - LC5

Top	SXX [N/m <sup>2</sup> ]	F.E.M. <sub>.37</sub>	F.E.M. <sub>.32</sub>	$\frac{FEM_{.37}}{FEM_{.32}}$ (%)
	SXX <sub>SW</sub>	-8.73E+05	-8.74E+05	100
	SXX <sub>UDL</sub>	-1.48E+05	-1.48E+05	100
	SXX <sub>Point</sub>	-1.18E+05	-1.18E+05	100
	SXX <sub>P</sub>	+2.52E+05	+2.38E+05	106
	SXX <sub>tot</sub>	-8.90E+05	-9.05E+05	98
Bottom	SXX [N/m <sup>2</sup> ]	F.E.M. <sub>.37</sub>	F.E.M. <sub>.32</sub>	$\frac{FEM_{.37}}{FEM_{.32}}$ (%)
	SXX <sub>SW</sub>	+8.59E+05	+8.61E+05	100
	SXX <sub>UDL</sub>	+1.46E+05	+1.46E+05	100
	SXX <sub>Point</sub>	+5.71E+04	+5.73E+04	100
	SXX <sub>P</sub>	-1.05E+06	-9.65E+05	109
	SXX <sub>tot</sub>	+1.41E+05	+9.88E+04	143

Table A.74: Midspan element stresses SXX

## RHINO models

In the following cases, the geometry of the models is defined in Rhinoceros 5, whereas in the previous cases, it was set in DIANA 10.1. The aim of this investigation is to verify whether an imported geometry from a CAD software such as Rhinoceros 5 will produce the same results in the structural analysis as found in the previous cases. First, two dimensional models will be examined. Hereafter, 3D geometry will be included. In order to avoid repetitive pictures, except from showing the model's geometry pictures corresponding to deflections and stresses will not be included in this section.

### Case 38 - Prestressed concrete beam - anchorages at a distance of 0.15m from the centroidal axis - rigid connection

The geometry used in Case 5 and Case 16 (DIANA10.1 pre-processing) is the basis for this model, now designed in Rhinoceros 5, see figure [A.149](#).

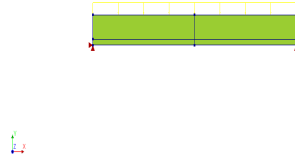


Figure A.149: Boundary and loading conditions

**Outputs:** Deflection (DtY) and Cauchy stresses (SXX) will be the investigated results of this analysis.

**Deflection (DtXYZ)** The deflection values are found identical with Case 5 (DIANA 10.1 pre-processing) as shown in table [A.75](#)

$\delta$ [m]	F.E.M. <sub>38</sub>	F.E.M. <sub>5</sub>	$\frac{F.E.M._{38}}{F.E.M._{5}}$ (%)
$\delta_{SW}$	+2.62E-04	+2.62E-04	100
$\delta_{UDL}$	+4.44E-05	+4.44E-05	100
$\delta_{Point}$	+1.42E-05	+1.42E-05	100
$\delta_P$	-2.38E-04	-2.38E-04	100
$\delta_{tot}$	+8.31E-05	+8.31E-05	100

Table A.75: Midspan element deflection per load

**Cauchy stresses SXX** The element stresses are found identical with Case 5 (2D geometry) as shown in table [A.76](#).

Top	SXX [N/m <sup>2</sup> ]	F.E.M. <sub>38</sub>	F.E.M. <sub>5</sub>	$\frac{F.E.M._{38}}{F.E.M._{5}}$ (%)
	SXX <sub>SW</sub>	-8.76E+05	-8.76E+05	100
	SXX <sub>UDL</sub>	-1.49E+05	-1.49E+05	99
	SXX <sub>Point</sub>	-9.35E+04	-9.35E+04	100
	SXX <sub>P</sub>	+3.06E+05	+3.06E+05	100
	SXX <sub>tot</sub>	-8.13E+05	-8.13E+05	100
Bottom	SXX [N/m <sup>2</sup> ]	F.E.M. <sub>38</sub>	F.E.M. <sub>5</sub>	$\frac{F.E.M._{38}}{F.E.M._{5}}$ (%)
	SXX <sub>SW</sub>	+8.53e5	+8.53e5	100
	SXX <sub>UDL</sub>	+1.45e5	+1.45e5	100
	SXX <sub>Point</sub>	+5.68e4	+5.68e4	100
	SXX <sub>P</sub>	-1.07e6	-1.07e6	100
	SXX <sub>tot</sub>	-1.45e4	-1.45e4	100

Table A.76: Midspan element stresses SXX

**Case 39 - Prestressed concrete beam - anchorages at the centroidal axis, curved tendon**

The geometry used in Case 6 (DIANA10.1 pre-processing) will be the basis for the design in Rhinoceros5 for this model.

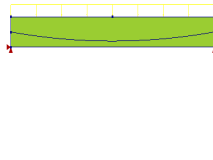


Figure A.150: Boundary and loading conditions

**Outputs:** Deflection (DtY) and Cauchy stresses (SXX) will be the investigated results of this analysis.

**Deflection (DtXYZ)** The deflections found in this case are identical with the ones in Case 6 (DIANA10.1 pre-processing), see table [A.77](#).

$\delta$ [m]	F.E.M. <sub>39</sub>	F.E.M. <sub>6</sub>	$\frac{F.E.M._{39}}{F.E.M._6}$ (%)
$\delta_{SW}$	+2.63E-04	2.63E-04	100
$\delta_{UDL}$	+4.46E-05	+4.46E-05	100
$\delta_{Point}$	+1.43E-05	+1.43E-05	100
$\delta_P$	-2.03E-04	-2.03E-04	100
$\delta_{tot}$	+1.19E-04	+1.19E-04	100

Table A.77: Midspan element deflection per load

**Cauchy stresses SXX** The element stresses are identical with the ones found in Case 6 (DIANA10.1 pre-processing), see table [A.78](#)

Top	SXX [N/m <sup>2</sup> ]	F.E.M. <sub>39</sub>	F.E.M. <sub>6</sub>	$\frac{FEM_{39}}{FEM_6}$ (%)
	SXX <sub>SW</sub>	-8.7E+05	-8.76E+05	100
	SXX <sub>UDL</sub>	-1.49+05	-1.49+05	100
	SXX <sub>Point</sub>	-9.35E+04	-9.35E+04	100
	SXX <sub>P</sub>	+3.08E+05	+3.08E+05	101
	SXX <sub>tot</sub>	-8.11E+05	-8.11E+05	100
Bottom	SXX [N/m <sup>2</sup> ]	F.E.M. <sub>39</sub>	F.E.M. <sub>6</sub>	$\frac{FEM_{39}}{FEM_6}$ (%)
	SXX <sub>SW</sub>	+8.53E+05	+8.53E+05	100
	SXX <sub>UDL</sub>	+1.45E+05	+1.45E+05	100
	SXX <sub>Point</sub>	5.68E+04	5.68E+04	100
	SXX <sub>P</sub>	-1.07E+06	-1.07E+06	100
	SXX <sub>tot</sub>	-1.58E+04	-1.58E+04	100

Table A.78: Midspan element stresses SXX

**Case 40 - Prestressed concrete beam - curved tendon at eccentricity  $e_p = 0.15$ [m] - curved top and bottom sides**

The model of Case 10 (DIANA10.1 pre-processing), will be used in this case, for the design in Rhinoceros5, see figure [A.151](#)

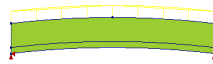


Figure A.151: Boundary and loading conditions

**Outputs:** Deflection (DtY) and Cauchy stresses (SXX) will be the investigated results of this analysis.

**Deflection (DtY)** The element deflections per load are found to be the same with the ones found in Case 10 (DIANA10.1 pre-processing). The total element deflection is almost the same as with Case 10, with a difference of 0.011%, see table

$\delta$ [m]	F.E.M. <sub>.40</sub>	F.E.M. <sub>.10</sub>	$\frac{FEM_{.40}}{FEM_{.10}}$ (%)
$\delta_{SW}$	+2.63E-04	+2.63E-04	100
$\delta_{UDL}$	+4.46E-05	+4.46E-05	100
$\delta_{Point}$	+1.43E-05	+1.43E-05	100
$\delta_P$	-2.37E-04	-2.37E-04	100
$\delta_{tot}$	+8.55E-05	+8.54E-05	100

Table A.79: Midspan element deflection per load

**Cauchy stresses SXX** The total element stresses are found to be almost the same with the ones found in Case 10 (DIANA10.1 pre-processing), see table [A.80](#).

Top	SXX [N/m <sup>2</sup> ]	F.E.M. <sub>.40</sub>	F.E.M. <sub>.10</sub>	$\frac{FEM_{.40}}{FEM_{.10}}$ (%)
	SXX <sub>SW</sub>	-8.72E+05	-8.72E+05	100
	SXX <sub>UDL</sub>	-1.48E+05	-1.48E+05	100
	SXX <sub>Point</sub>	-9.32E+04	-9.32E+04	100
	SXX <sub>P</sub>	+3.02E+05	+3.02E+05	100
	SXX <sub>tot</sub>	-8.11E+05	-8.11E+05	100
Bottom	SXX [N/m <sup>2</sup> ]	F.E.M. <sub>.40</sub>	F.E.M. <sub>.10</sub>	$\frac{FEM_{.40}}{FEM_{.10}}$ (%)
	SXX <sub>SW</sub>	+8.58E+05	+8.58E+05	100
	SXX <sub>UDL</sub>	+1.46E+05	+1.46E+05	100
	SXX <sub>Point</sub>	+5.71E+04	+5.71E+04	100
	SXX <sub>P</sub>	-1.07E+06	-1.07E+06	100
	SXX <sub>tot</sub>	-1.27E+04	-1.27E+04	100

Table A.80: Midspan element stresses SXX

### 3D models

The geometry of the 3D models was created in RHINOCEROS5 and subsequently imported in DIANA10.1.

#### Case 41 - Unreinforced concrete beam - 3D

**Loads:** The beam will be subjected to its self-weight (SW), a uniformly distributed load  $q_{UDL} = 2000[N/m]$  and a line load  $P_{line} = 2000[N]$ , both acting on its top face. The middle of the top face will be the position of the line point load. A load combination of all the loads will also be investigated in this case ( $SW + q_{UDL} + P_{line}$ ), see figure [A.152](#).

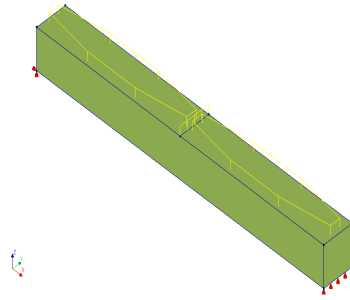


Figure A.152: Boundary and loading conditions

**Outputs:** The deflection (DtXYZ) and the element Cauchy stresses (SXX) will be the investigated results of this analysis.

**Deflection (DtXYZ)** The deflection of the beam under the loads is shown in figure A.153. The values of element deflections at midspan per load are shown in table A.81. It is proved that the total beam deflections (DtZ) are approximately the same with those in Case 1 (difference by 0.03%).

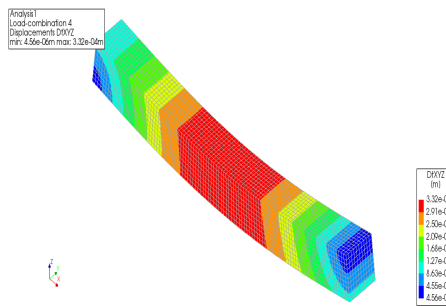


Figure A.153: Element deflection DtXYZ - LC4

$\delta$ [m]	F.E.M. <sub>41</sub>	F.E.M. <sub>1</sub>	$\frac{F.E.M._{41}}{F.E.M._{1}}$ (%)
$\delta_{SW}$	+2.71E-04	+2.71E-04	100
$\delta_{UDL}$	+4.60E-05	+4.60E-05	100
$\delta_{Point}$	+1.47E-05	+1.47E-05	100
$\delta_{tot}$	+3.32E-04	+3.32E-04	100

Table A.81: Midspan element deflection per load

**Cauchy stresses SXX** The total stresses of the beam under the total load combination (LC5) are shown in figure A.154. The midspan concrete stresses (SXX) per load are shown in table A.82. It is found that they are almost the same at midspan top and bottom fiber level.

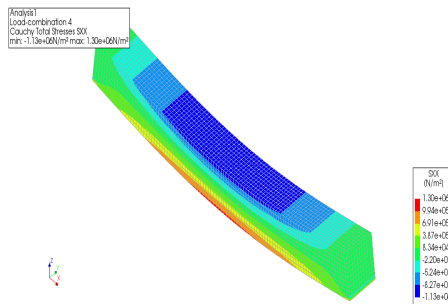


Figure A.154: Element stresses SXX - LC5

Top	SXX [N/m <sup>2</sup> ]	F.E.M. <sub>.41</sub>	F.E.M. <sub>.1</sub>	$\frac{F.E.M._{.41}}{F.E.M._{.1}}$ (%)
	SXX <sub>SW</sub>	-8.86E+05	-8.85E+05	100
	SXX <sub>UDL</sub>	-1.50E+05	-1.50E+05	100
	SXX <sub>Ppoint</sub>	-9.38E+04	-9.41E+04	100
	SXX <sub>tot</sub>	-1.13E+06	-1.13E+06	100
Bottom	SXX [N/m <sup>2</sup> ]	F.E.M. <sub>.41</sub>	F.E.M. <sub>.1</sub>	$\frac{F.E.M._{.41}}{F.E.M._{.1}}$ (%)
	SXX <sub>SW</sub>	+8.86E+05	+8.85E+05	100
	SXX <sub>UDL</sub>	+1.50E+05	+1.50E+05	100
	SXX <sub>Ppoint</sub>	+5.90E+04	+5.90E+04	100
	SXX <sub>tot</sub>	+1.09E+06	+1.10E+06	99

Table A.82: Midspan element stresses SXX

### Case 42 - Prestressed concrete beam - anchorages at the centroidal axis - straight tendon - 3D

**Loads:** Central prestressing will be applied at both ends of a simply supported beam as in Case 3 (2D geometry). A straight linear tendon will be anchored at the supports at the position of centroidal axis and the third dimension of width will be included in this model. (figure [A.155](#)).

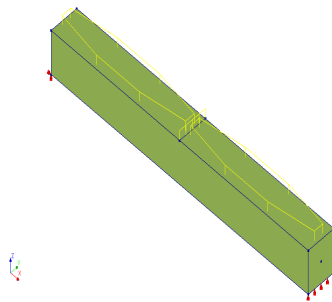


Figure A.155: Boundary and loading conditions

**Outputs:** Deflection (DtXYZ) and Cauchy stresses (SXX) will be the investigated results of this analysis.

**Deflection (DtXYZ)** The total displacement (LC5) at midspan of the beam is approximately the same with the resulted displacement value of Case 3 (figure A.157 and table A.83). As expected, almost negligible vertical deflection due to central prestressing (LC4) occurred in this case (figure A.156).

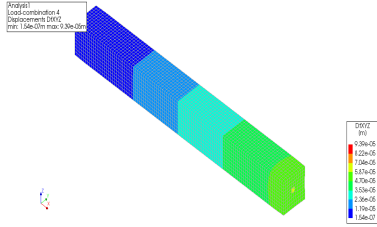


Figure A.156: Element deflection DtXYZ - LC4

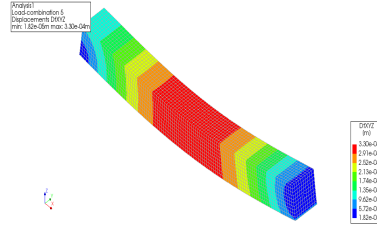


Figure A.157: Element deflection DtXYZ - LC5

$\delta$ [m]	F.E.M. <sub>42</sub>	F.E.M. <sub>3</sub>	$\frac{F.E.M.42}{F.E.M.3}$ (%)
$\delta_{SW}$	+2.71E-04	+2.68E-04	101
$\delta_{UDL}$	+4.60E-05	+4.54E-05	101
$\delta_{Point}$	+1.47E-05	+1.46E-05	101
$\delta_P$	+2.36E-07	+7.02E-07	33
$\delta_{tot}$	+3.30E-04	+3.29E-04	100

Table A.83: Midspan element deflection per load

**Cauchy stresses SXX** The midspan stresses of the beam under the total load combination (LC5) are shown in figure A.158. The maximum values of concrete stresses per load are shown in table A.84. Comparing the cases of 2D and 3D geometry (case 3 - case 42), it appears that they have approximately the same values.

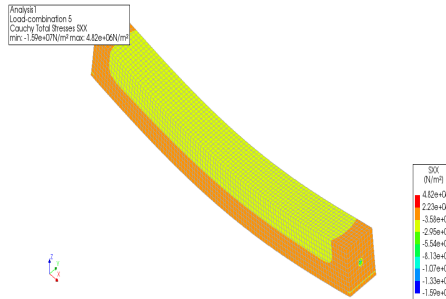


Figure A.158: Element stresses SXX - LC5

Top	SXX [N/m <sup>2</sup> ]	F.E.M. <sub>42</sub>	F.E.M. <sub>3</sub>	$\frac{FEM_{42}}{FEM_{3}} (\%)$
	SXX <sub>SW</sub>	-8.86E+05	-8.85E+05	100
	SXX <sub>UDL</sub>	-1.50E+05	-1.50E+05	100
	SXX <sub>Point</sub>	-9.38E+04	-9.41E+04	100
	SXX <sub>P</sub>	-3.91E+05	-3.91E+05	100
	SXX <sub>tot</sub>	-1.52E+06	-1.52E+06	100
Bottom	SXX [N/m <sup>2</sup> ]	F.E.M. <sub>42</sub>	F.E.M. <sub>3</sub>	$\frac{FEM_{42}}{FEM_{3}} (\%)$
	SXX <sub>SW</sub>	+8.86E+05	+8.85E+05	100
	SXX <sub>UDL</sub>	+1.50E+05	+1.50E+05	100
	SXX <sub>Point</sub>	+5.90E+04	+5.89E+04	100
	SXX <sub>P</sub>	-3.91E+05	-3.91E+05	100
	SXX <sub>tot</sub>	+7.04E+05	+7.03E+05	100

Table A.84: Midspan element stresses SXX

**Case 43 - Prestressed concrete beam - anchorages at a distance of  $e_p = 0.15$ [m] below the centroidal axis - straight tendon - 3D**

Eccentric prestressing will be applied at both ends of a simply supported beam, at a distance of 0.15[m] below the centroidal axis. The tendon is of linear straight profile likewise with Case 5, while the third dimension is also included in this model, see figure [A.159](#)

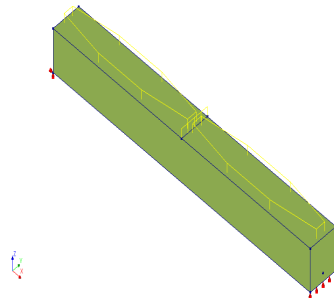


Figure A.159: Boundary and loading conditions

**Outputs:** Deflection (DtXYZ) and Cauchy stresses (SXX) will be the investigated results of this analysis.

**Deflection (DtXYZ)** The total deflection (DtZ - LC5) in this case is larger by 2.8% compared with the deflection from Case 5 (2D), see figure [A.161](#) and table [A.85](#). The prestressing load (LC4) causes a larger upward displacement in the 3D model compared with Case 5. The influence of eccentric prestressing on beam's deflection is shown in figure [A.160](#). The introduction of eccentric prestressing results in an upward curvature at midspan and a downward curvature near the supports, likewise with the two dimensional model.

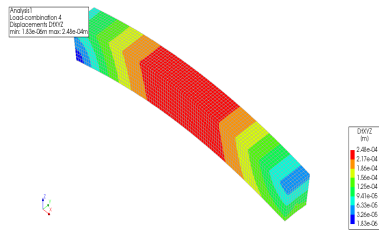


Figure A.160: Element deflection DtXYZ - LC4

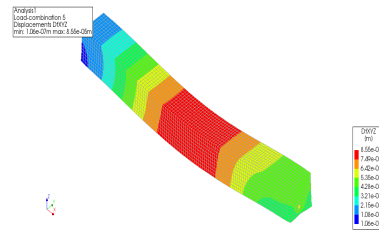


Figure A.161: Element deflection DtXYZ - LC5

$\delta$ [m]	F.E.M. <sub>43</sub>	F.E.M. <sub>5</sub>	$\frac{F.E.M._{43}}{F.E.M._{5}}$ (%)
$\delta_{SW}$	+2.64E-05	+2.62E-04	101
$\delta_{UDL}$	+4.48E-05	+4.44E-05	101
$\delta_{Point}$	+1.44E-05	+1.42E-05	101
$\delta_P$	-2.47E-04	-2.38E-04	104
$\delta_{tot}$	+8.55E-05	+8.31E-05	103

Table A.85: Midspan element deflection per load

**Cauchy stresses SXX** The total stresses SXX of concrete and prestressing reinforcement under the total load combination, are shown in figures [A.162](#) and [A.163](#). The maximum values of concrete stresses at midspan per load are shown in table [A.86](#). It appears that the stresses increase by 2.7% at bottom fiber level, while they keep constant at top fiber level, compared with the case 5 (2D), see figure [A.163](#).

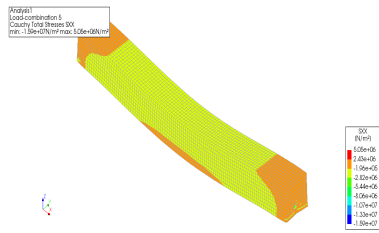


Figure A.162: Element stresses SXX - LC5

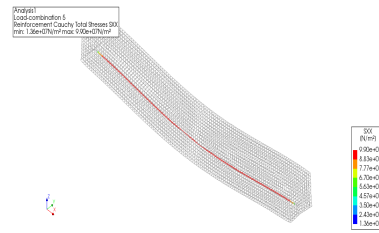


Figure A.163: Prestressing steel stresses SXX - LC4

Top	SXX [N/m <sup>2</sup> ]	F.E.M. <sub>43</sub>	F.E.M. <sub>5</sub>	$\frac{F.E.M.43}{F.E.M.5}$ (%)
	SXX <sub>SW</sub>	-8.76E+05	-8.76E+05	100
	SXX <sub>UDL</sub>	-1.49E+05	-1.49E+05	100
	SXX <sub>Point</sub>	-9.32E+04	-9.35E+04	100
	SXX <sub>P</sub>	+3.06E+05	+3.06E+05	100
	SXX <sub>tot</sub>	-8.13E+05	-8.13E+05	100
Bottom	SXX [N/m <sup>2</sup> ]	F.E.M. <sub>43</sub>	F.E.M. <sub>5</sub>	$\frac{F.E.M.43}{F.E.M.5}$ (%)
	SXX <sub>SW</sub>	+8.53E+05	+8.53E+05	100
	SXX <sub>UDL</sub>	+1.45E+05	+1.45E+05	100
	SXX <sub>Point</sub>	+5.67E+04	+5.68E+04	100
	SXX <sub>P</sub>	-1.07E+06	-1.07E+06	100
	SXX <sub>tot</sub>	-1.49E+04	-1.45E+04	103

Table A.86: Midspan element stresses SXX

#### Case 44 - Prestressed concrete beam - anchorages at the centroidal axis - curved tendon - 3D

A curved tendon profile will be modeled in this case. A curved tendon will have a drupe equal to 0.15[m] at mid-span and will be anchored at the centroidal axis at the supports as in Case 6 (2D geometry). The third dimension is also included in this model, see fig [A.164](#)

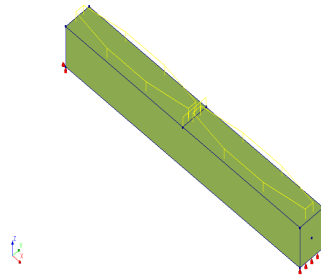


Figure A.164: Boundary and loading conditions

**Outputs:** Deflection (DtXYZ) and Cauchy stresses (SXX) will be the investigated results of this analysis.

**Deflection (DtXYZ)** The total midspan deflection DtZ (LC5) appears to be similar to (difference by 4.2%) the midspan deflection in Case 6 (2D geometry), see (figure [A.165](#) and table [A.87](#)).

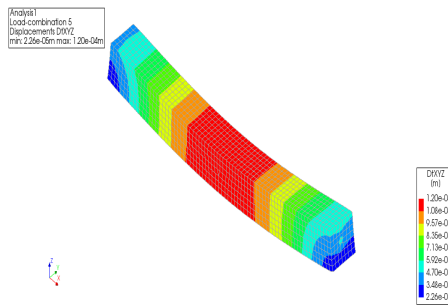


Figure A.165: Element deflection DtXYZ - LC5

$\delta$ [m]	F.E.M. <sub>44</sub>	F.E.M. <sub>6</sub>	$\frac{F.E.M.44}}{F.E.M.6}}$ (%)
$\delta_{SW}$	+3.12E-04	+2.63E-04	119
$\delta_{UDL}$	+5.0E-05	+4.46E-05	112
$\delta_{Point}$	+1.80E-05	+1.43E-05	126
$\delta_P$	-2.14E-04	-2.03E-04	105
$\delta_{tot}$	+1.24E-04	+1.19E-04	104

Table A.87: Midspan element deflection per load

**Cauchy stresses SXX** The concrete stresses SXX under the total load combination (LC5) are shown in figure [A.166](#). The prestressing steel stresses (LC4) are shown in figure [A.167](#). The concrete element stresses at midspan top and bottom fiber level per load are shown in table [A.88](#). Comparing cases 6 (2D geometry) and 46 (3D geometry), it appears that the stresses due to the total load combination (LC5) have similar values at top fiber level for both 2D and 3D geometry (difference by 1.23%), while in the last case they increase by 7.08% at the bottom.

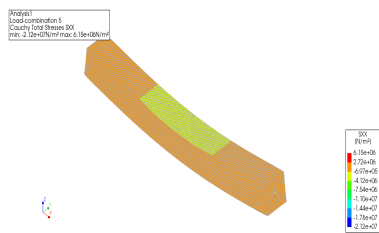


Figure A.166: Element total stresses SXX - LC5

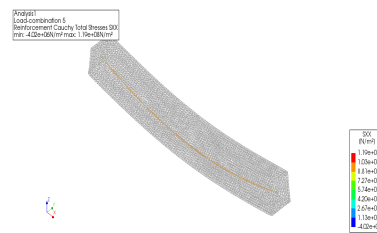


Figure A.167: Prestressing steel stresses SXX - LC 4

Top	SXX [N/m <sup>2</sup> ]	F.E.M. <sub>.44</sub>	F.E.M. <sub>.6</sub>	$\frac{FEM_{.44}}{FEM_{.6}}$ (%)
	SXX <sub>SW</sub>	-8.76E+05	-8.76E+05	100
	SXX <sub>UDL</sub>	-1.49E+05	-1.49E+05	100
	SXX <sub>Point</sub>	-1.04E+05	-9.35E+04	111
	SXX <sub>P</sub>	+3.08E+05	+3.08E+05	100
	SXX <sub>tot</sub>	-8.21E+05	-8.11E+05	101
Bottom	SXX [N/m <sup>2</sup> ]	F.E.M. <sub>.44</sub>	F.E.M. <sub>.6</sub>	$\frac{FEM_{.44}}{FEM_{.6}}$ (%)
	SXX <sub>SW</sub>	+8.53E+05	+8.53E+05	100
	SXX <sub>UDL</sub>	+1.45E+05	+1.45E+05	100
	SXX <sub>Point</sub>	+5.68E+04	5.68E+04	100
	SXX <sub>P</sub>	-1.07E+06	-1.07E+06	100
	SXX <sub>tot</sub>	-1.70e4	-1.58e4	108

Table A.88: Midspan element stresses SXX

### Case 45 - Unreinforced concrete beam - curved top and bottom edges - 3D

In this case, the geometry of the model in Case 8 is used, including the third dimension in it.

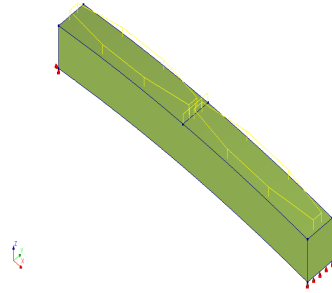


Figure A.168: Boundary and loading conditions

**Outputs:** Deflection (DtXYZ) and Cauchy stresses (SXX) will be the investigated results of this analysis.

**Deflection (DtXYZ)** The deflection of the beam under the loads is shown in figure [A.169](#). The values of midspan deflections (DtZ) according to the respective load are shown in table [A.89](#). It is found that the midspan deflection due to the total load combination (LC4) are increased by 5.7% in the 3D model.

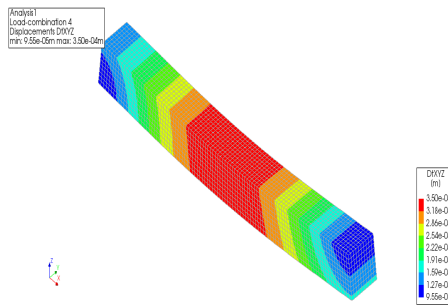


Figure A.169: Element deflection DtXYZ - LC5

$\delta$ [m]	F.E.M. <sub>.45</sub>	F.E.M. <sub>.8</sub>	$\frac{F.E.M._{.45}}{F.E.M._{.8}}$ (%)
$\delta_{SW}$	+2.84E-04	+2.68E-04	106
$\delta_{UDL}$	+4.95E-05	+4.55E-05	109
$\delta_{Point}$	+1.58E-05	+1.46E-05	108
$\delta_{tot}$	+3.48E-04	+3.28E-04	106

Table A.89: Midspan element deflection per load

**Cauchy stresses SXX** The total stresses of the beam under the total load combination (LC4) are shown in figure [A.170](#). The maximum values of concrete stresses at midspan top and bottom fiber level per applied load are shown in table [A.90](#). It is found that the stresses have almost the same values in both 2D and 3D geometry.

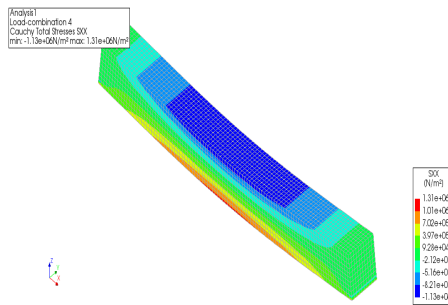


Figure A.170: Element stresses SXX - LC5

<b>Top</b>	<b>SXX [N/m<sup>2</sup>]</b>	<b>F.E.M.<sub>.45</sub></b>	<b>F.E.M.<sub>.8</sub></b>	$\frac{FEM_{.45}}{FEM_{.8}}$ (%)
	SXX <sub>SW</sub>	-8.81E+05	-8.81E+05	100
	SXX <sub>UDL</sub>	-1.50E+05	-1.50E+05	100
	SXX <sub>Point</sub>	-9.34E+04	-9.38E+04	100
	SXX <sub>tot</sub>	-1.12E+06	-1.12E+06	100
<b>Bottom</b>	<b>SXX [N/m<sup>2</sup>]</b>	<b>F.E.M.<sub>.45</sub></b>	<b>F.E.M.<sub>.8</sub></b>	$\frac{FEM_{.45}}{FEM_{.8}}$ (%)
	SXX <sub>SW</sub>	+8.90E+05	+8.90E+05	100
	SXX <sub>UDL</sub>	+1.51E+05	+1.51E+05	100
	SXX <sub>Point</sub>	+5.93E+04	+5.92E+04	100
	SXX <sub>tot</sub>	+1.10E+06	+1.10E+06	100

Table A.90: Midspan element stresses SXX

**Case 46 - Prestressed concrete beam - curved tendon at eccentricity  $e_p=0.15$ [m] - curved top and bottom edges - 3D**

The same geometry used in Case 10 will also be used in this case, including the third dimension (figure [A.171](#)).

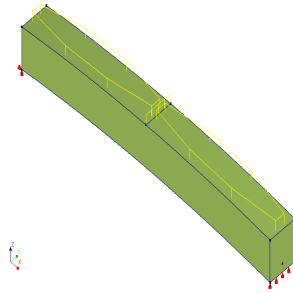


Figure A.171: Boundary and loading conditions

**Outputs:** Deflection (DtXYZ) and Cauchy stresses (SXX) will be the investigated results of this analysis.

**Deflection (DtXYZ)** Likewise in the previous models of eccentric prestressing, the deflection (DtXYZ) in this case shows an upward curvature near the supports and a downward curvature near the mid-span, see figure [A.172](#). At mid-span, the total deflection (DtZ) is increased by 2.8% in comparison with the two dimensional model of Case 10 (table [A.91](#)).

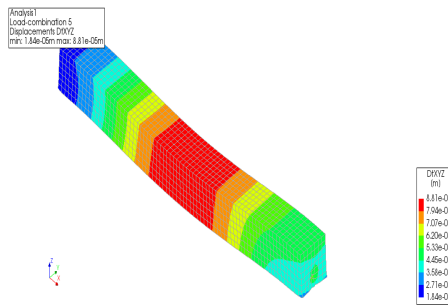


Figure A.172: Element deflection DtXYZ - LC5

$\delta$ [m]	F.E.M. <sub>.46</sub>	F.E.M. <sub>.10</sub>	$\frac{FEM_{.46}}{FEM_{.10}}$ (%)
$\delta_{SW}$	+2.74E-04	+2.63E-04	104
$\delta_{UDL}$	+4.65E-05	+4.46E-05	104
$\delta_{Point}$	+1.45E-05	+1.43E-05	101
$\delta_P$	-2.63E-04	-2.37E-04	111
$\delta_{tot}$	+8.79E-05	+8.54E-05	103

Table A.91: Midspan element deflection per load

**Cauchy stresses SXX** The midspan stresses of the beam under the total load combination (LC5) are shown in figure [A.173](#). The maximum values of stresses according to the respective load at midspan are shown in table [A.92](#). It appears that the total stresses (LC5) are decreased by 1.36% at top fiber level while they are the same at bottom fiber level compares with the 2D model of Case 10.

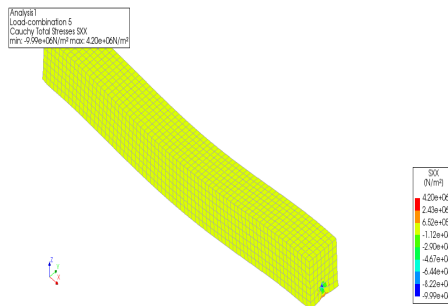


Figure A.173: Element stresses SXX - LC5

Top	SXX [N/m <sup>2</sup> ]	F.E.M. <sub>.46</sub>	F.E.M. <sub>.10</sub>	$\frac{FEM_{.46}}{FEM_{.10}}$ (%)
	SXX <sub>SW</sub>	-8.72E+05	-8.72E+05	100
	SXX <sub>UDL</sub>	-1.48E+05	-1.48E+05	100
	SXX <sub>Point</sub>	-8.16E+04	-9.32E+04	87
	SXX <sub>P</sub>	+3.01E+05	3.02E+05	100
	SXX <sub>tot</sub>	-8.00E+05	-8.11E+05	99
Bottom	SXX [N/m <sup>2</sup> ]	F.E.M. <sub>.46</sub>	F.E.M. <sub>.10</sub>	$\frac{FEM_{.46}}{FEM_{.10}}$ (%)
	SXX <sub>SW</sub>	+8.58E+05	8.58E+05	100
	SXX <sub>UDL</sub>	+1.46E+05	1.46E+05	100
	SXX <sub>Point</sub>	+5.72E+04	5.71E+04	100
	SXX <sub>P</sub>	-1.07E+06	-1.07E+06	100
	SXX <sub>tot</sub>	-1.27E+04	-1.27E+04	100

Table A.92: Midspan element stresses SXX

### Case 47 - Unreinforced concrete beam - curved top and bottom sides - right angles - 3D

The same model with case 11 will be used in this case, including the third dimension of the element, see figure [A.174](#)

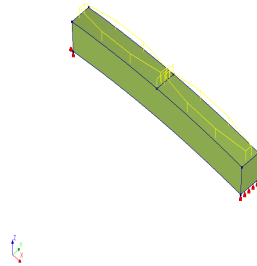


Figure A.174: Boundary and loading conditions

**Outputs:** Deflection (DtXYZ) and Cauchy stresses (SXX) will be the investigated results of this analysis.

**Deflection (DtXYZ)** The midspan deflections (DtZ) due to the total load combination (LC4) case are increased by 2.4% in the 3D model compared with the two dimensional model of Case 11, see figure [A.175](#) and table [A.93](#).

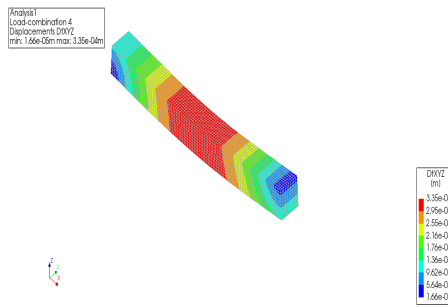


Figure A.175: Element deflection DtXYZ - LC5

$\delta$ [m]	F.E.M. <sub>.47</sub>	F.E.M. <sub>.11</sub>	$\frac{FEM_{.47}}{FEM_{.11}}$ (%)
$\delta_{SW}$	+2.72e-4	+2.67E-04	102
$\delta_{UDL}$	+4.63e-5	+4.53E-05	102
$\delta_{Point}$	+1.48e-5	+1.44E-05	103
$\delta_{tot}$	+3.34e-4	+3.26E-04	102

Table A.93: Midspan element deflection per load

**Cauchy stresses SXX** The midspan stresses of the beam under the total load combination (LC4) are shown in figure [A.176](#). The midspan values of stresses per load are shown in the table [A.94](#). The stresses found in Case 47 (3D geometry) are almost the same at top fiber level (difference by 0.88%) and are the same with the midspan stress values found in the two dimensional model of Case 11.

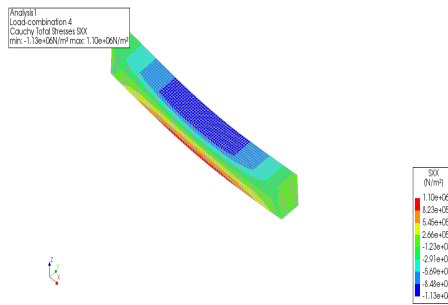


Figure A.176: Element stresses SXX - LC5

Top	SXX [N/m <sup>2</sup> ]	F.E.M. <sub>.47</sub>	F.E.M. <sub>.11</sub>	$\frac{FEM_{.47}}{FEM_{.11}}$ (%)
	SXX <sub>SW</sub>	-8.81E+05	-8.81E+05	100
	SXX <sub>UDL</sub>	-1.50E+05	-1.50E+05	100
	SXX <sub>Point</sub>	-9.36E+04	-9.39E+04	100
	SXX <sub>tot</sub>	-1.12E+06	-1.13E+06	99
Bottom	SXX [N/m <sup>2</sup> ]	F.E.M. <sub>.47</sub>	F.E.M. <sub>.11</sub>	$\frac{FEM_{.47}}{FEM_{.11}}$ (%)
	SXX <sub>SW</sub>	+8.91E+05	+8.90E+05	100
	SXX <sub>UDL</sub>	+1.51E+05	+1.51E+05	100
	SXX <sub>Point</sub>	+5.93E+04	+5.92E+04	100
	SXX <sub>tot</sub>	+1.10E+06	+1.10E+06	100

Table A.94: Midspan element stresses SXX

**Case 48 - Prestressed concrete beam - curved tendon at centroidal axis - curved top and bottom sides - right angles - 3D**

Case's 12 (2D geometry) including the third dimension, will be used to create the current three dimensional model (figure [A.177](#)).

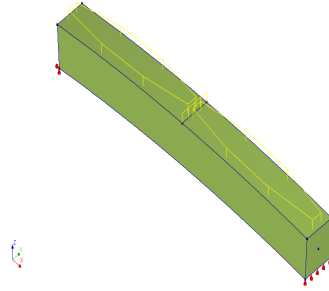


Figure A.177: Boundary and loading conditions

**Outputs:** Deflection (DtXYZ) and Cauchy stresses (SXX) will be the investigated results of this analysis.

**Deflection (DtXYZ)** The deflection shows an upward curvature along the beam's length. At midspan, the total deflection is increased by 15.6% relative to Case 12 (2D geometry), see figure [A.178](#) and table [A.95](#). Thus, no verification with regard to it can be proved between the 2D model and the 3D model.

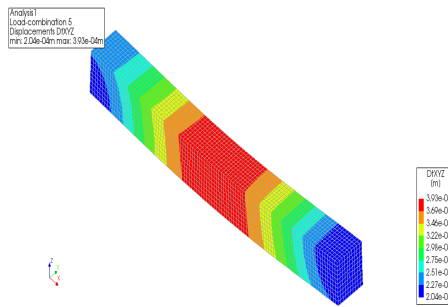


Figure A.178: Element deflection DtXYZ - LC5

$\delta$ [m]	F.E.M. <sub>48</sub>	F.E.M. <sub>12</sub>	$\frac{FEM_{48}}{FEM_{12}}$ (%)
$\delta_{SW}$	+2.73E-04	+2.67E-04	102
$\delta_{UDL}$	+5.47E-05	+4.54E-05	120
$\delta_{Point}$	+1.48E-05	+1.45E-05	102
$\delta_P$	+9.96E-05	+3.18E-06	33
$\delta_{tot}$	+3.92E-04	+3.31E-04	118

Table A.95: Midspan element deflection per load

**Cauchy stresses SXX** The stresses of the beam under the total load combination (LC5) are shown in figure [A.179](#). The maximum values of stresses per load at midspan are shown in table [A.96](#). The total stresses found in Case 48 (3D geometry) are the same with the ones found in the two dimensional model of Case 12.

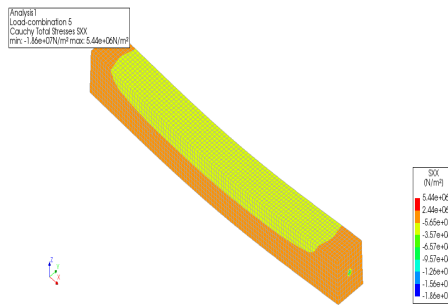


Figure A.179: Element stresses SXX - LC5

Top	SXX [N/m <sup>2</sup> ]	F.E.M. <sub>.48</sub>	F.E.M. <sub>.12</sub>	$\frac{FEM_{.48}}{FEM_{.12}}$ (%)
	SXX <sub>SW</sub>	-8.81E+05	-8.81E+05	100
	SXX <sub>UDL</sub>	-1.50E+05	-1.50E+05	100
	SXX <sub>Point</sub>	-9.36E+04	-9.39E+04	100
	SXX <sub>P</sub>	-3.92E+05	-3.91E+05	100
	SXX <sub>tot</sub>	-1.52E+06	-1.52E+06	100
Bottom	SXX [N/m <sup>2</sup> ]	F.E.M. <sub>.48</sub>	F.E.M. <sub>.12</sub>	$\frac{FEM_{.48}}{FEM_{.12}}$ (%)
	SXX <sub>SW</sub>	+8.91E+05	+8.90E+05	100
	SXX <sub>UDL</sub>	+1.51E+05	+1.51E+05	100
	SXX <sub>Point</sub>	+5.93E+04	+5.92E+04	100
	SXX <sub>P</sub>	-3.90E+05	-3.91E+05	100
	SXX <sub>tot</sub>	+7.11E+05	+7.10E+05	100

Table A.96: Midspan element stresses SXX

**Case 49 - Prestressed concrete beam - curved tendon at eccentricity  $e_p = 0.15[m]$  - curved top and bottom sides - right angles - 3D**

Case's13 geometry including the third dimension will be used for the creating of this model's geometry, see figure [A.180](#)

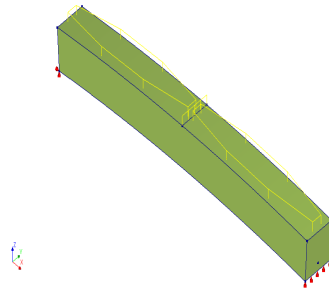


Figure A.180: Boundary and loading conditions

**Deflection (DtXYZ)** Likewise with cases 5 (linear), 10 (vertical side edges), and Case 13 (orthogonal angles) with the application of prestressing load at eccentric positions with relevance to the the beam centroidal axis, the deflection in this case, shows an upward curvature near the supports and a downward curvature near the mid-span, considered as a not expected result. Comparing the total midspan deflection (LC5) of this model with Case 13 (2D geometry), it is found that their values are increased by 0.70% in the 3D geometry, see figure [A.181](#) and table [A.97](#). Therefore, the midspan deflection between the 2D and 3D model are proved to be similar.

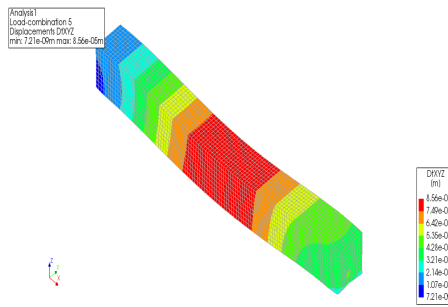


Figure A.181: Element deflection DtXYZ - LC5

$\delta$ [m]	F.E.M. <sub>49</sub>	F.E.M. <sub>13</sub>	$\frac{FEM_{49}}{FEM_{13}}$ (%)
$\delta_{SW}$	+2.67E-04	+2.61E-04	102
$\delta_{UDL}$	+4.64E-05	+4.43E-05	105
$\delta_{Point}$	+1.45E-05	+1.42E-05	102
$\delta_P$	-2.50E-05	-2.36E-04	106
$\delta_{tot}$	+8.55E-05	+8.49E-05	101

Table A.97: Midspan element deflection per load

**Cauchy stresses SXX** The midspan stresses of the beam under the load combination (LC5) are shown in figure [A.182](#). The midspan concrete stresses per load are shown in table [A.98](#). The total stresses resulted in Cases 13 and 23 (2D), as well in case 49 (3D), show that the mid-span cross section is under compression at both top and bottom fiber level. However, comparing the stresses in this case with the ones found in Case 13 (2D), they are found to be the same at top fiber level and larger by 8.1% at bottom fiber level. It must be noted that the same stresses occur for the constituent load combinations (LC1,.., LC4) at bottom fiber level for both the 2D and 3D model, hence considered to be verified with each other.

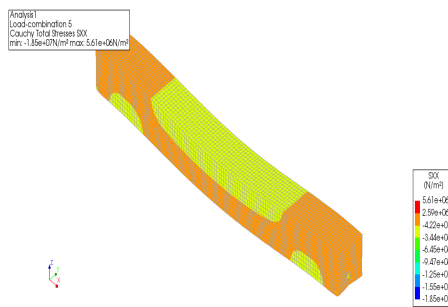


Figure A.182: Element stresses SXX - LC5

Top	SXX [N/m <sup>2</sup> ]	F.E.M. <sub>.49</sub>	F.E.M. <sub>.13</sub>	$\frac{FEM_{.49}}{FEM_{.13}}$ (%)
	SXX <sub>SW</sub>	-8.72E+05	-8.72E+05	100
	SXX <sub>UDL</sub>	-1.48E+05	-1.48E+05	100
	SXX <sub>Point</sub>	-9.30E+04	-9.33E+04	100
	SXX <sub>P</sub>	+3.01E+05	+3.02E+05	100
	SXX <sub>tot</sub>	-8.12E+05	-8.12E+05	100
Bottom	SXX [N/m <sup>2</sup> ]	F.E.M. <sub>.49</sub>	F.E.M. <sub>.13</sub>	$\frac{FEM_{.49}}{FEM_{.13}}$ (%)
	SXX <sub>SW</sub>	+8.59E+05	8.58E+05	100
	SXX <sub>UDL</sub>	+1.46E+05	+1.46E+05	100
	SXX <sub>Point</sub>	+5.72E+04	+5.71E+04	100
	SXX <sub>P</sub>	-1.07E+06	-1.07E+06	100
	SXX <sub>tot</sub>	-9.41E+03	-1.24E+04	109

Table A.98: Midspan element stresses SXX

### Case 50 - Prestressed concrete beam - anchorages at the centroidal axis - curved tendon - 3D

Case 6 geometry will be used in this model including the third dimension, see figure [A.183](#).

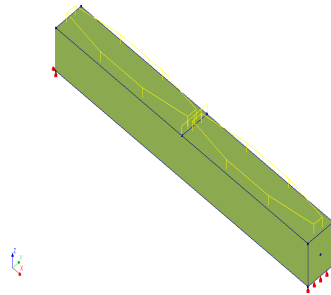


Figure A.183: Boundary and loading conditions

**Outputs:** Deflection (DtXYZ) and Cauchy stresses (SXX) will be the investigated results of this analysis.

**Deflection (DtXYZ)** The total midspan deflections (figures [A.184](#), [A.185](#), table [A.99](#)) appear to be the same in comparison with Case 6 (2D geometry).

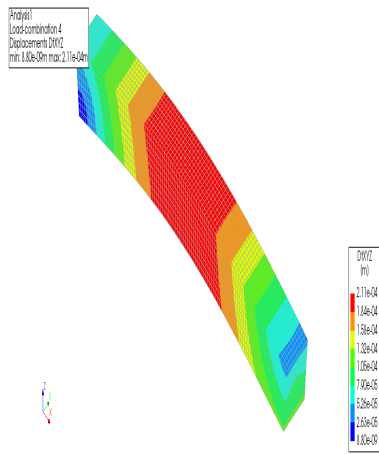


Figure A.184: Element deflection DtXYZ - LC4

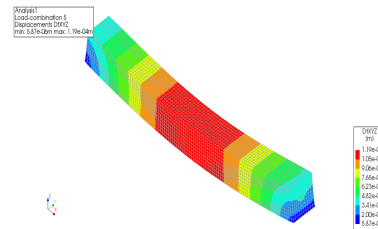


Figure A.185: Element deflection DtXYZ - LC5

$\delta$ [m]	F.E.M. <sub>50</sub>	F.E.M. <sub>6</sub>	$\frac{F.E.M.50}{F.E.M.6}$ (%)
$\delta_{SW}$	+2.66E-04	+2.63E-04	101
$\delta_{UDL}$	+4.51E-05	+4.46E-05	101
$\delta_{Point}$	+1.45E-05	+1.43E-05	101
$\delta_P$	-2.11E-04	-2.03E-04	104
$\delta_{tot}$	+1.19E-04	+1.19E-04	100

Table A.99: Midspan element deflection per load

**Cauchy stresses SXX** The values of concrete stresses according to the respective load are shown in table [A.100](#). Comparing the midspan concrete stresses due to the applied loads between the two and three dimensional model it appears that they are the same at top fiber level. However, the total stresses (LC5) in the 3D model are reduced by 8.8% in comparison with the ones found in Case 6 (2D). Since the differences between the stresses for the applied loads seem to be the same for the constituent load combinations (LC1 - LC4) it can be assumed that the stresses found in the 3D model at bottom fiber level are verified with the 2D model.

Top	SXX [N/m <sup>2</sup> ]	F.E.M. <sub>50</sub>	F.E.M. <sub>6</sub>	$\frac{FEM_{50}}{FEM_{6}}$ (%)
	SXX <sub>SW</sub>	-8.76E+05	-8.76E+05	100
	SXX <sub>UDL</sub>	-1.49E+05	-1.49E+05	100
	SXX <sub>Point</sub>	-9.32E+04	-9.35E+04	100
	SXX <sub>P</sub>	+3.08E+05	+3.08E+05	100
	SXX <sub>tot</sub>	-8.10E+05	-8.11E+05	100
Bottom	SXX [N/m <sup>2</sup> ]	F.E.M. <sub>50</sub>	F.E.M. <sub>6</sub>	$\frac{FEM_{50}}{FEM_{6}}$ (%)
	SXX <sub>SW</sub>	+8.53E+05	+8.53E+05	100
	SXX <sub>UDL</sub>	+1.45E+05	+1.45E+05	100
	SXX <sub>Point</sub>	5.66E+04	5.68E+04	100
	SXX <sub>P</sub>	-1.08E+06	-1.07E+06	101
	SXX <sub>tot</sub>	-1.44E+04	-1.58E+04	91

Table A.100: Midspan element stresses SXX

**Case 51 - Prestressed concrete beam - curved tendon at eccentricity  $e_p = 0.15[m]$  - curved top and bottom sides - two elements - 3D**

Case's 19 geometry will be used in this model including the third dimension, see figure [A.186](#)

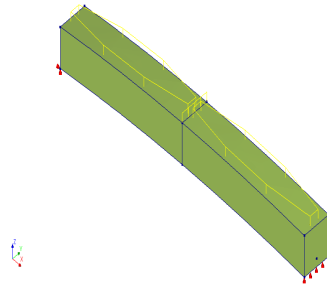


Figure A.186: Boundary and loading conditions

**Outputs:** Deflection (DtXYZ) and Cauchy stresses (SXX) will be the investigated results of this analysis.

**Deflection (DtXYZ)** The midspan total deflection (DtZ) is increased by 37% in comparison with Case 19 (2D geometry), see figure [A.187](#) and table [A.101](#)

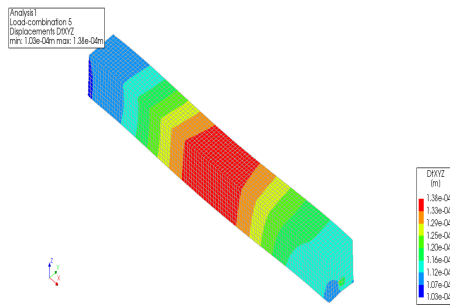


Figure A.187: Element deflection DtXYZ - LC5

$\delta$ [m]	F.E.M. <sub>.51</sub>	F.E.M. <sub>.19</sub>	$\frac{FEM_{.51}}{FEM_{.19}}$ (%)
$\delta_{SW}$	+2.74E-04	+2.63E-04	104
$\delta_{UDL}$	+4.58E-05	+4.46E-05	103
$\delta_{Point}$	+1.65E-05	+1.43E-05	115
$\delta_P$	-2.52E-04	-2.36E-04	107
$\delta_{tot}$	+1.38E-04	+8.65E-05	159

Table A.101: Midspan element deflection per load - LC5

**Cauchy stresses SXX** The total stresses of the beam are shown in figure [A.188](#). The midspan concrete stresses per load are shown in table [A.102](#). It appears that the stresses are decreased at both top and bottom fiber level by 4.4% and by 18.9% respectively, relative to Case 19 (2D geometry).

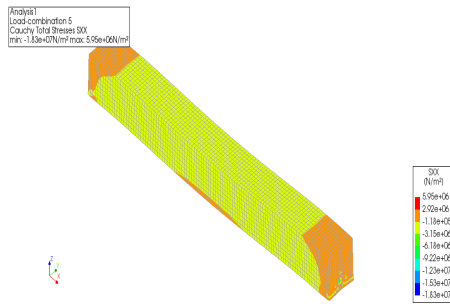


Figure A.188: Element stresses SXX - LC5

Top	SXX [N/m <sup>2</sup> ]	F.E.M. <sub>.51</sub>	F.E.M. <sub>.19</sub>	$\frac{FEM_{.51}}{FEM_{.19}}$ (%)
	SXX <sub>SW</sub>	-8.71E+05	-8.72E+05	100
	SXX <sub>UDL</sub>	-1.48E+05	-1.48E+05	100
	SXX <sub>Point</sub>	-5.73E+04	-9.32E+04	61
	SXX <sub>P</sub>	+3.01E+05	+3.02E+05	100
	SXX <sub>tot</sub>	-7.75E+05	-8.11E+05	96
Bottom	SXX [N/m <sup>2</sup> ]	F.E.M. <sub>.51</sub>	F.E.M. <sub>.19</sub>	$\frac{FEM_{.51}}{FEM_{.19}}$ (%)
	SXX <sub>SW</sub>	+8.58E+05	+8.58E+05	100
	SXX <sub>UDL</sub>	+1.46E+05	+1.46E+05	100
	SXX <sub>Point</sub>	+5.70E+04	+5.71E+04	100
	SXX <sub>P</sub>	-1.07E+06	-1.07E+06	100
	SXX <sub>tot</sub>	-1.03E+04	-1.27E+04	81

Table A.102: Midspan element stresses SXX

**Case 52 - Prestressed concrete beam - curved tendon at eccentricity  $e_p = 0.15[m]$  - curved top and bottom sides - two elements - 3D**

Case's 20 geometry will be used in this model including the third dimension, see figure [A.189](#). The curvature of the tendon follows the curvature of the beam.

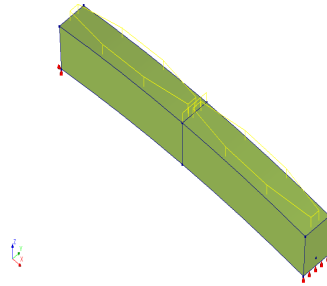


Figure A.189: Boundary and loading conditions

**Outputs:** Deflection (DtXYZ) and Cauchy stresses (SXX) will be the investigated results of this analysis.

**Deflection (DtXYZ)** The total midspan deflection (DtZ) of the connected beams in Case 52, is increased by 16% compared with Case 20 (2D), see figure [A.190](#) and table [A.103](#).

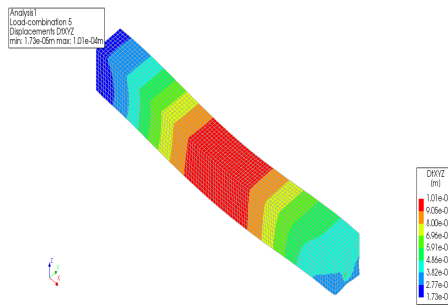


Figure A.190: Element deflection DtXYZ - LC5

$\delta$ [m]	F.E.M. <sub>.52</sub>	F.E.M. <sub>.20</sub>	$\frac{FEM_{.52}}{FEM_{.20}}$ (%)
$\delta_{SW}$	+2.79E-04	+2.61E-04	107
$\delta_{UDL}$	+5.31E-05	+4.43E-05	120
$\delta_{Point}$	+2.91E-05	+1.42E-05	204
$\delta_P$	-2.52E-04	-2.36E-04	107
$\delta_{tot}$	+1.01E-04	+8.49E-05	119

Table A.103: Midspan element deflection per load - LC5

**Cauchy stresses SXX** The total stresses of the beam are shown in figure [A.191](#). The values of midspan concrete stresses per load are shown in table [A.104](#). The total stresses (LC5) are increased by 10.27% at top fiber level while they change sign and turn in tensile ones at bottom fiber level compared with the 2D geometry in Case 20.

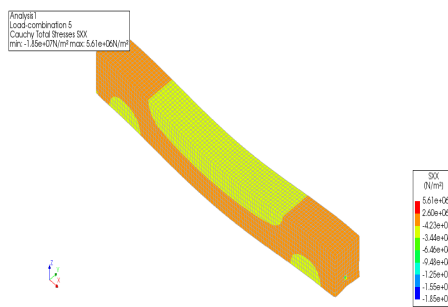


Figure A.191: Element stresses SXX - LC5

Top	SXX [N/m <sup>2</sup> ]	F.E.M. <sub>52</sub>	F.E.M. <sub>20</sub>	$\frac{FEM_{52}}{FEM_{20}}$ (%)
	SXX <sub>SW</sub>	-8.72E+05	-8.72E+05	100
	SXX <sub>UDL</sub>	-1.48E+05	-1.48E+05	100
	SXX <sub>Point</sub>	-1.86E+05	-9.33E+04	199
	SXX <sub>P</sub>	+3.01E+05	+3.02E+05	100
	SXX <sub>tot</sub>	-9.05E+05	-8.12E+05	111
Bottom	SXX [N/m <sup>2</sup> ]	F.E.M. <sub>52</sub>	F.E.M. <sub>20</sub>	$\frac{FEM_{52}}{FEM_{20}}$ (%)
	SXX <sub>SW</sub>	+8.59E+05	+8.58E+05	100
	SXX <sub>UDL</sub>	+1.46E+05	+1.46E+05	100
	SXX <sub>Point</sub>	+1.14E+05	+5.71E+04	20
	SXX <sub>P</sub>	-1.07E+06	-1.07E+06	100
	SXX <sub>tot</sub>	+5.10E+04	-1.25E+04	change of sign

Table A.104: Midspan element stresses SXX

**Case 53 - Prestressed concrete beam - curved tendon at centroidal axis - joint 0.05[m] - increased stiffness interface at joint -3D**

Case 34 geometry will be used in this model including the third dimension, see figure (A.192). The drupe of the tendon at midspan is at 0.15[m] below the centroidal axis of the beam.

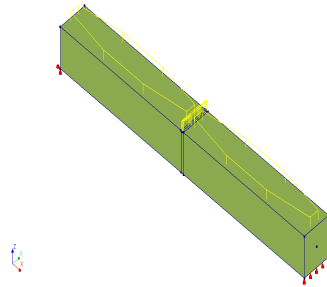


Figure A.192: Boundary and loading conditions

**Outputs:** The deflection (DtXYZ) and the Cauchy stresses (SXX) will be the investigated results of this analysis.

**Deflection (DtXYZ)** The total deflection (DtZ) at midspan has the same value with the one found in Case 34 (2D geometry).

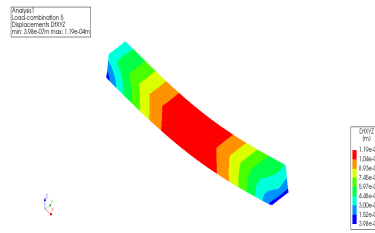


Figure A.193: Element deflection DtXYZ - LC5

$\delta$ [m]	F.E.M. <sub>53</sub>	F.E.M. <sub>34</sub>	$\frac{FEM_{53}}{FEM_{34}}$ (%)
$\delta_{SW}$	+2.62E-04	+2.63E-04	100
$\delta_{UDL}$	+4.45E-05	+4.46E-05	100
$\delta_{Point}$	+1.42E-05	+1.43E-05	100
$\delta_P$	-2.03E-04	-2.03E-04	100
$\delta_{tot}$	+1.18E-04	+1.19E-04	100

Table A.105: Midspan element deflection per load

**Cauchy stresses SXX** The prestressing stresses of the beam (LC4) are shown in figure A.194, while the total stresses (LC5) are depicted in figure (A.195). The midspan values of stresses according to the respective load are presented in table (A.106). In this case, the stresses due to the total load combinations are found to be increased by 0.8% at top fiber level and decreased by 14% at bottom fiber level in comparison with Case 34 (2D geometry).

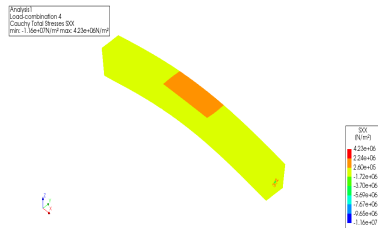


Figure A.194: Element stresses SXX - LC4

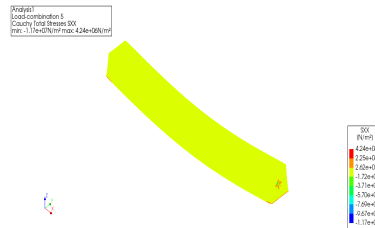


Figure A.195: Element stresses SXX - LC5

Top	SXX [N/m <sup>2</sup> ]	F.E.M. <sub>.53</sub>	F.E.M. <sub>.34</sub>	$\frac{FEM_{.53}}{FEM_{.34}}$ (%)
	SXX <sub>SW</sub>	-8.77E+05	-8.76E+05	100
	SXX <sub>UDL</sub>	-1.49E+05	-1.49E+05	100
	SXX <sub>Point</sub>	-1.25E+05	-1.19E+05	105
	SXX <sub>P</sub>	+3.08E+05	+3.08E+05	100
	SXX <sub>tot</sub>	-8.43E+05	-8.36E+05	101
Bottom	SXX [N/m <sup>2</sup> ]	F.E.M. <sub>.53</sub>	F.E.M. <sub>.34</sub>	$\frac{FEM_{.53}}{FEM_{.34}}$ (%)
	SXX <sub>SW</sub>	+8.53E+05	+8.53E+05	100
	SXX <sub>UDL</sub>	+1.45E+05	+1.45E+05	100
	SXX <sub>Point</sub>	+5.68E+04	+5.68E+04	100
	SXX <sub>P</sub>	-1.07E+06	-1.07E+06	100
	SXX <sub>tot</sub>	-9.09E+03	-1.57E+04	86

Table A.106: Midspan element stresses SXX

**Case 54 - Prestressed concrete beams - curved tendon at eccentricity  $e_p=0.15$ [m] - curved top and bottom sides - increased interface stiffness at joint - 3D**

Case 37 geometry will be used in this model including the third dimension, see figure [A.196](#).

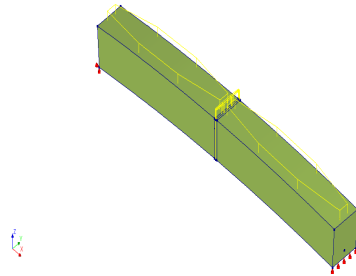


Figure A.196: Boundary and loading conditions

**Outputs:** Deflection (DtXYZ) and Cauchy stresses (SXX) will be the investigated results of this analysis.

**Deflection (DtXYZ)** The total deflection at midspan (DtZ) of the beam is decreased by 8% in comparison with the deflection found in Case 37 (2D geometry), see figure [A.197](#) and table [A.107](#).

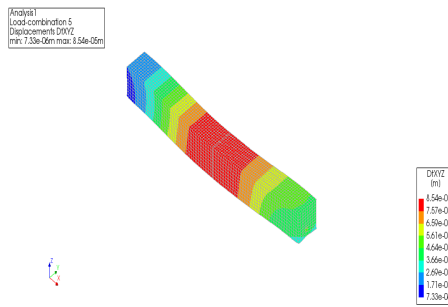


Figure A.197: Element deflection DtXYZ - LC5

$\delta$ [m]	F.E.M. <sub>.54</sub>	F.E.M. <sub>.37</sub>	$\frac{FEM_{.54}}{FEM_{.37}}$ (%)
$\delta_{SW}$	+2.60E-04	2.61E-04	100
$\delta_{UDL}$	+4.41E-05	4.44E-05	99
$\delta_{Point}$	4.23E+05	1.43E-05	296
$\delta_P$	-2.65E-04	-2.30E-04	115
$\delta_{tot}$	8.30E-05	9.06E-05	92

Table A.107: Midspan element deflection per load

**Cauchy stresses SXX** The stresses of the beam under the total load combination (LC5) are shown in figure [A.198](#). The values of stresses according to the respective load are shown in table [A.108](#). The stresses in this case are found to be increased by 6% at top fiber level, and decreased by 10% at bottom fiber level, in comparison with Case 37 (2D geometry).

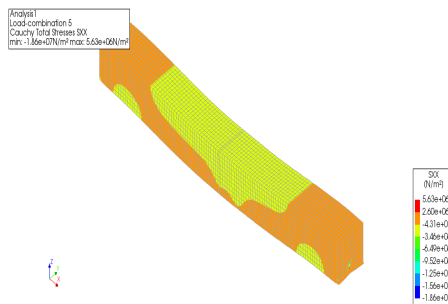


Figure A.198: Element stresses SXX - LC5

Top	SXX [N/m <sup>2</sup> ]	F.E.M. <sub>.54</sub>	F.E.M. <sub>.37</sub>	$\frac{FEM_{.54}}{FEM_{.37}}$ (%)
	SXX <sub>SW</sub>	-8.68E+05	-8.73E+05	100
	SXX <sub>UDL</sub>	-1.48E+05	-1.48E+05	100
	SXX <sub>Point</sub>	-2.17E+05	-1.18E+05	183
	SXX <sub>P</sub>	+5.42E+05	+2.52E+05	215
	SXX <sub>tot</sub>	-1.03e+06	-8.90E+05	116
Bottom	SXX [N/m <sup>2</sup> ]	F.E.M. <sub>.54</sub>	F.E.M. <sub>.37</sub>	$\frac{FEM_{.54}}{FEM_{.37}}$ (%)
	SXX <sub>SW</sub>	+8.49E+05	+8.59E+05	100
	SXX <sub>UDL</sub>	+1.44E+05	+1.46E+05	99
	SXX <sub>Point</sub>	+1.71E+05	+5.71E+04	30
	SXX <sub>P</sub>	-5.02E+06	-1.05E+06	478
	SXX <sub>tot</sub>	+1.28e+06	+1.41E+05	90

Table A.108: Midspan element stresses SXX

## B Four point bending test

### B.1 Linear static analysis

#### B.1.1 Supports distance included

The applied loads from self-weight SW, concentrated loads F or displacements  $u_{i,x=1/4}$  applied at quarter lengths  $x = \frac{l}{4}$  and prestressing steel forces  $P_i$  to be applied on the test-specimens with regard to the requirement of zero concrete tensile stresses at bottom fiber, are presented in table [B.1](#).

Table B.1: Loads applied per cable diameter - Supports distance not included

Y1860S3					
$\Phi_p$ (mm)	$S_n$ (mm <sup>2</sup> )	SW (N/mm)	$P_i$ (N)	$F_i$ (N)	$u_{i,x=1/4}$ (mm)
5.2	13.6		18972	1051	0.043
6.5	21.1	0.275	29434	1676	0.069
6.8	23.4		32643	1868	0.077
7.5	29		40455	2336	0.096
Y1860S7					
6.85	28.2		39339	2269	0.093
7.0	30		41850	2419	0.100
9.0	50		69750	4088	0.168
11.0	75		104625	6174	0.254
12.5	93	0.275	129735	7676	0.316
13.0	100		139500	8260	0.340
15.2	140		195300	11598	0.478
16.0	150		209250	12432	0.512
18.0	200		279000	16604	0.684
Y1860S7G					
12.7	112		156240	9261	0.382
15.2	165	0.275	230175	13684	0.564
18.0	223		311085	18523	0.763

The concrete stress due to prestressing load P is calculated as::

$$\sigma_{c,p} = -\frac{P_i}{A_c}$$

The concrete stress due to its self-weight SW is calculated as::

$$\sigma_{c,sw} = \frac{M_{SW}}{W_c} = \pm \frac{q_c \times l^2}{8} = 0.128 \left[ \frac{N}{mm^2} \right]$$

Cracking load F based on zero tensile stresses requirement at service life  $\sigma_c^{bot} \leq 0$  at bottom fiber level, and zero concrete tensile strength  $f_{ctm} = 0$ :

$$F_i \leq \frac{4 \times W_c}{l} \times \left( -\frac{q_{sw} \times l^2}{8} + \frac{P}{A_c} \right)$$

The concrete stress due to point load F is calculated as:

$$\sigma_{c,F} = \frac{M_F}{W_c} = \pm \frac{F_i \times l}{4W_c}$$

Comparison between the predicted hand-calculated values of the midspan concrete stresses and DIANA10.2 results is shown in table [B.2](#). Note that for this part, the distance between the supports and the elements outer edges is neglected in both the FEM and the hand calculations.

Force control			
Midspan element stresses SXX (N/m <sup>2</sup> )			
Y1860S3 (Φ5.2)	Hand calculations	DIANA10.2 results	Percentage difference (%)
SXX <sub>P</sub>	-1.725e+06	-1.72e+06	0.289
SXX <sub>SW,bot</sub>	+1.281e+05	+1.26e+05	1.639
SXX <sub>SW,top</sub>	-1.281e+05	-1.26e+05	1.639
SXX <sub>F;u;bot</sub>	+1.59e+06	+1.60e+06	0.25
SXX <sub>F;u;top</sub>	-1.59e+06	-1.60e+06	0.25
SXX <sub>tot;bot</sub>	≈0	≈0	0
SXX <sub>tot;top</sub>	-3.45e+06	-3.45e+06	0

Table B.2: Midspan predicted stresses & DIANA10.2 results - Linear static analysis

A comparison of the hand-calculated midspan deflections and DIANA10.2 results is presented in the table below:

Midspan element deflections (m)			
Y1860S3 (Φ5.2)	Hand calculations	DIANA10.2 results	Percentage difference (%)
DtY <sub>P</sub>	0	-6.99e-04	≈0
DtY <sub>G</sub>	4.341e-06	4.23e-06	2.56
DtY <sub>F;u</sub>	5.95e-02	6.14e-02	3.09

Table B.3: Midspan predicted vertical displacements & DIANA10.2 results - Linear static analysis

The occurring midspan concrete stresses due to the applied loads and load combinations, are shown in table [B.4](#). Note that rounded values are used in the tables.

Table B.4: Predicted values of concrete stresses SXX (N/mm<sup>2</sup>) - Supports distance not included

Φ <sub>p</sub> (mm)	Fiber level	Y1860S3			
		σ <sub>c,P</sub> (N/mm <sup>2</sup> )	σ <sub>c,F</sub> (N/mm <sup>2</sup> )	σ <sub>c,SW</sub> (N/mm <sup>2</sup> )	σ <sub>c,tot</sub> (N/mm <sup>2</sup> )
5.2	Bottom	-1.7	1.6	0.1	0
	Top	-1.7	-1.6	-0.1	-3.4
6.5	Bottom	-2.7	2.5	0.1	0

	Top		-2.5	-0.1	-5.4
6.8	Bottom	-3.0	2.8	0.1	0
	Top		-2.8	-0.1	-5.9
7.5	Bottom	-3.7	3.5	0.1	0
	Top		-3.5	-0.1	-7.4
Y1860S7					
$\Phi_p$ (mm)	Fiber level	$\sigma_{c,P}$ (N/mm <sup>2</sup> )	$\sigma_{c,F}$ (N/mm <sup>2</sup> )	$\sigma_{c,SW}$ (N/mm <sup>2</sup> )	$\sigma_{c,tot}$ (N/mm <sup>2</sup> )
6.85	Bottom	-3.6	3.4	0.1	0
	Top		-3.4	-0.1	-7.2
7.0	Bottom	-3.8	3.7	0.1	0
	Top		-3.7	-0.1	-7.6
9.0	Bottom	-6.3	6.2	0.1	0
	Top		-6.2	-0.1	-12.7
11.0	Bottom	-9.5	9.4	0.1	0
	Top		-9.4	-0.1	-19.0
12.5	Bottom	-11.8	11.7	0.1	0
	Top		-11.7	-0.1	-23.6
13.0	Bottom	-12.7	12.6	0.1	0
	Top		-12.6	-0.1	-25.4
15.2	Bottom	-17.8	17.6	0.1	0
	Top		-17.6	-0.1	-35.5
16.0	Bottom	-19.0	18.9	0.1	0
	Top		-18.9	-0.1	-38.0
18.0	Bottom	-25.4	25.2	0.1	0
	Top		-25.2	-0.1	-50.7
Y1860S7G					
$\Phi_p$ (mm)	Fiber level	$\sigma_{c,P}$ (N/mm <sup>2</sup> )	$\sigma_{c,F}$ (N/mm <sup>2</sup> )	$\sigma_{c,SW}$ (N/mm <sup>2</sup> )	$\sigma_{c,tot}$ (N/mm <sup>2</sup> )
12.7	Bottom	-14.2	14.1	0.1	0
	Top		-14.075	-0.1	-28.4
15.2	Bottom	-20.9	20.8	0.1	0
	Top		-20.797	-0.1	-41.9
18.0	Bottom	-28.3	28.2	0.1	0
	Top		-28.152	-0.1	-56.6

Table B.5: Ratios of the applied prestressing concrete stress and the allowed concrete stress during tensioning - Supports distance not included

Y1860S3			
$\Phi_p$ (mm)	$\sigma_{c,P}$ (N/mm <sup>2</sup> )	$\sigma_{c,alwd}$ (N/mm <sup>2</sup> )	$\frac{\sigma_{c,P}}{\sigma_{c,alwd}}$ (%)
5.2	-1.7		3.6
6.5	-2.7		5.6
6.8	-3.0	-48	6.2
7.5	-3.7		7.7

Y1860S7			
$\Phi_p$ (mm)	$\sigma_{c,P}$ (N/mm <sup>2</sup> )	$\sigma_{c,alwd}$ (N/mm <sup>2</sup> )	$\frac{\sigma_{c,P}}{\sigma_{c,alwd}}$ (%)
6.85	-3.6		7.5
7.0	-3.8		7.9
9.0	-6.3		13.2
11.0	-9.5		19.8
12.5	-11.8	-48	24.6
13.0	-12.7		26.4
15.2	-17.8		37.0
16.0	-19.0		39.6
18.0	-25.4		52.8
Y1860S7G			
$\Phi_p$ (mm)	$\sigma_{c,P}$ (N/mm <sup>2</sup> )	$\sigma_{c,alwd}$ (N/mm <sup>2</sup> )	$\frac{\sigma_{c,P}}{\sigma_{c,alwd}}$ (%)
12.7	-14.2		29.6
15.2	-20.9	-48	43.6
18.0	-28.3		58.9

### B.1.2 Supports distance included

The 55[mm] distance between the supports and the elements edges is included in the geometry of the FEM and the hand calculations. Note that rounded values are used in the tables.

The concrete stress due to its self-weight SW is calculated as:

$$\sigma_{c,sw} = \frac{M_{SW}}{W_c} = \pm \frac{\frac{q_{SW} \times l^2}{8} - \frac{q_{SW} \times l}{2}}{W_c} = 0.082 \left[ \frac{N}{mm^2} \right] \quad (B.1)$$

The concrete stress due to concentrated loads F is calculated as:

$$\sigma_{c,F} = \frac{M_F}{W_c} = \pm \frac{F_i \times \left( \frac{l}{4} - a \right)}{W_c} \quad (B.2)$$

a: distance between supports and element outer edges

The following checks were performed with regard to crushing of the concrete and yielding of reinforcement:

The concrete strain at top fiber level due to the load combination is calculated as:

$$\varepsilon_{c,tot} = \frac{\sigma_{c,tot}}{E_c} \quad (B.3)$$

The ultimate strain to be resisted by the concrete is:

$$\varepsilon_{c,u3} = 2.6\% \quad (B.4)$$

The prestressing steel strain at yield load is:

$$\varepsilon_{p,d} = \frac{f_{pd}}{E_p} = 7.81\% \quad (B.5)$$

Table B.6: Loads applied per cable diameter - Supports distance included

Y1860S3				
$\Phi_p$ (mm)	$S_n$ (mm <sup>2</sup> )	SW (N/mm)	$P_i$ (N)	$F_i$ (N)
5.2	13.6		18972	1686
6.5	21.1		29434	2662
6.8	23.4	0.275	32643	2961
7.5	29		40455	3690
Y1860S7				
6.85	28.2		39339	3586
7.0	30		41850	3820
9.0	50		69750	6423
11.0	75		104625	9677
12.5	93	0.275	129735	12020
13.0	100		139500	12931
15.2	140		195300	18137
16.0	150		209250	19439
18.0	200		279000	25946
Y1860S7G				
12.7	112		156240	14493
15.2	165	0.275	230175	21391
18.0	223		311085	28940

Table B.7: Predicted values of concrete stresses SXX (N/mm<sup>2</sup>) - Supports distance included

Y1860S3					
$\Phi_p$ (mm)	Fiber level	$\sigma_{c,P}$ (N/mm <sup>2</sup> )	$\sigma_{c,F}$ (N/mm <sup>2</sup> )	$\sigma_{c,SW}$ (N/mm <sup>2</sup> )	$\sigma_{c,tot}$ (N/mm <sup>2</sup> )
5.2	Bottom		1.6	0.1	0
	Top	-1.7	-1.6	-0.1	-3.4
6.5	Bottom		2.6	0.1	0
	Top	-2.7	-2.6	-0.1	-5.4
6.8	Bottom		2.9	0.1	0
	Top	-3.0	-2.9	-0.1	-5.9
7.5	Bottom		3.6	0.1	0
	Top	-3.7	-3.6	-0.1	-7.4
Y1860S7					
$\Phi_p$ (mm)	Fiber level	$\sigma_{c,P}$ (N/mm <sup>2</sup> )	$\sigma_{c,F}$ (N/mm <sup>2</sup> )	$\sigma_{c,SW}$ (N/mm <sup>2</sup> )	$\sigma_{c,tot}$ (N/mm <sup>2</sup> )
6.85	Bottom		3.5	0.1	0
	Top	-3.6	-3.5	-0.1	-7.2
7.0	Bottom		3.7	0.1	0
	Top	-3.8	-3.7	-0.1	-7.6
9.0	Bottom		6.3	0.1	0

	Top		-6.3	-0.1	-12.7
11.0	Bottom	-9.5	9.4	0.1	0
	Top		-9.4	-0.1	-19.0
12.5	Bottom	-11.8	11.7	0.1	0
	Top		-11.7	-0.1	-23.6
13.0	Bottom	-12.7	12.600	0.1	0
	Top		-12.600	-0.1	-25.4
15.2	Bottom	-17.8	17.7	0.1	0
	Top		-17.7	-0.1	-35.5
16.0	Bottom	-19.0	18.9	0.1	0
	Top		-18.9	-0.1	-38.0
18.0	Bottom	-25.4	25.3	0.1	0
	Top		-25.3	-0.1	-50.7
Y1860S7G					
$\Phi_p$ (mm)	Fiber level	$\sigma_{c,P}$ (N/mm <sup>2</sup> )	$\sigma_{c,F}$ (N/mm <sup>2</sup> )	$\sigma_{c,SW}$ (N/mm <sup>2</sup> )	$\sigma_{c,tot}$ (N/mm <sup>2</sup> )
12.7	Bottom	-14.204	14.1	0.1	0
	Top		-14.1	-0.1	-28.4
15.2	Bottom	-20.925	20.8	0.1	0
	Top		-20.8	-0.1	-41.9
18.0	Bottom	-28.280	28.2	0.1	0
	Top		-28.2	-0.1	-56.6

Table B.8: Total concrete strains at top fiber level  $\epsilon_c$ - Supports distance included

Y1860S3				
$\Phi_p$ (mm)	Fiber level	$\epsilon_{c,tot}$	$\epsilon_{c,u3}$	$\frac{\epsilon_{c,tot}}{\epsilon_{c,u}}$ (%)
5.2	Top	-8.21E-05		3
6.5	Top	-1.27E-04	-2.60E-03	5
6.8	Top	-1.41E-04		5
7.5	Top	-1.75E-04		7
Y1860S7				
$\Phi_p$ (mm)	Fiber level	$\epsilon_{c,tot}$	$\epsilon_{c,u3}$	$\frac{\epsilon_{c,tot}}{\epsilon_{c,u}}$ (%)
6.85	Top	-1.70.E-04		7
7.0	Top	-1.81.E-04		7
9.0	Top	-3.02.E-04		12
11.0	Top	-4.53.E-04		17
12.5	Top	-5.62.E-04	-2.60E-03	22
13.0	Top	-6.04.E-04		23
15.2	Top	-8.45.E-04		33
16.0	Top	-9.06.E-04		35
18.0	Top	-1.21.E-03		46
Y1860S7G				
$\Phi_p$ (mm)	Fiber level	$\epsilon_{c,tot}$	$\epsilon_{c,u3}$	$\frac{\epsilon_{c,tot}}{\epsilon_{c,u}}$ (%)

12.7	Top	-6.76E-04		26
15.2	Top	-9.96E-04	-2.60E-03	38
18.0	Top	-1.35E-03		52

No concrete crushing failure is expected to occur according to [B.8](#)

Table B.9: Prestressing steel strains - Supports distance included

Y1860S3				
$\Phi_p$ (mm)	Prestressing steel strain $\epsilon_{p,m\infty}$	Prestressing steel strain at yield $\epsilon_{p,d}$		$\frac{\epsilon_{p,m\infty}}{\epsilon_{pd}}$ (%)
5.2				
6.5	7.15E-03		7.81E-03	91.5
6.8				
7.5				
Y1860S7				
$\Phi_p$ (mm)	Prestressing steel strain $\epsilon_{p,m\infty}$		$\epsilon_{c,tot}$	$\frac{\epsilon_{p,m\infty}}{\epsilon_{pd}}$ (%)
6.85				
7.0				
9.0				
11.0				
12.5	7.15E-03		7.81E-03	91.5
13.0				
15.2				
16.0				
18.0				
Y1860S7G				
$\Phi_p$ (mm)	Prestressing steel strain $\epsilon_{p,m\infty}$		$\epsilon_{c,tot}$	$\frac{\epsilon_{p,m\infty}}{\epsilon_{pd}}$ (%)
12.7				
15.2	7.15E-03		7.81E-03	91.5
18.0				

No yielding of the prestressing steel is expected according to [B.9](#)

## B.2 Cracking loads

The supports distance from the elements outer edges is included in this part.

### B.2.1 Calculations with regard to the maximum displacements $u_{max}$

Assuming that the the applied downward displacements  $u$  at  $\frac{l}{4} - a = 98.25[mm]$  from the supports will cause an increase of the prestressing steel stress from the applied prestressing steel stress  $\sigma_{p,m\infty} = 1395[MPa]$  to  $\sigma_{p,max} = 1691[MPa]$ , so that the prestressing steel reaches its maximum value, the prestressing steel

strain increase for the applied loading is calculated as:

$$\Delta\varepsilon_p = \frac{\Delta\sigma_p}{E_p} = \frac{\sigma_{p,max} - \sigma_{p,m0}}{E_p} = 1.517 \times 10^{-3} \quad (\text{B.6})$$

The increase of the prestressing steel length due to the rigid body rotation results in an increase of the prestressing steel strain, which is calculated as:

$$\Delta\varepsilon_p = \frac{\Delta l_p}{l_p} = \frac{2 \times \theta \times z}{l_p} = \frac{2 \times \frac{u}{98.25} \times \frac{h}{2}}{l_p} = 9.132 \times 10^{-4} \times u \quad (\text{B.7})$$

Combining equations [B.6](#) and [6.18](#), the applied downward vertical displacements  $u$  that would lead to maximum prestressing steel stresses after cracking, are calculated to be:

$$u_{max} = 1.66[\text{mm}] \quad (\text{B.8})$$

The increase in the prestressing steel stress per cable diameter, is calculated according to the following equation:

$$\Delta\sigma_p = \Delta\varepsilon_p \times E_p = 296[\text{MPa}] \quad (\text{B.9})$$

The maximum increase of the prestressing steel force  $\Delta P_{max}$  for the 5.2[mm] cable diameter, can then be formulated as:

$$\Delta P_{5.2,max} = \Delta\sigma_{p,max} \times S_{n5.2} = 4024[\text{N}] \quad (\text{B.10})$$

The corresponding total maximum prestressing steel force  $P_{u,max}$  after cracking is calculated as:

$$P_{u,5.2,max} = P_{5.2} + \Delta P_{5.2,max} = 22996[\text{N}] \quad (\text{B.11})$$

The concrete compressive force  $N_c$  at maximum prestressing load, acting at hinge location is calculated as:

$$N_{c,max} = 0.5 \times b \times x_{u,5.2} \times f_{cd} \quad (\text{B.12})$$

Taking the horizontal equilibrium of left-hand side rigid body, it follows that:

$$N_c = P_{u,5.2,max} \quad (\text{B.13})$$

The compression zone height  $x_{u,5.2}$  required to resist the maximum prestressing force applied is calculated as:

$$x_{u,5.2,max} = \frac{P_{u,5.2,max}}{0.5 \times b \times f_{cd}} = \frac{22992}{0.5 \times 200 \times 53.33} = 4.31[\text{mm}] \quad (\text{B.14})$$

The corresponding values of the point loads  $F_{i,max}$  under displacements  $u_{max}$ , are found via the following formula:

$$F_{5.2,max} = \frac{1}{\left(\frac{l}{4} - a\right)} \times \left\{ P_{u,5.2,max} \times \frac{h}{2} - \left( \frac{q_{SW} \times l^2}{8} - \frac{q_{SW} \times a \times l}{2} \right) \right\} = \frac{1}{98.25} \times \{ 22996 \times 27.5 - 8281 \} = 6352[\text{N}] \quad (\text{B.15})$$

### B.2.2 Calculations with regard to the displacements at start of horizontal plateau - $u = 0.6[mm]$

The increase of the prestressing steel strain under displacements  $u = 0.6[mm]$  is calculated as:

$$\Delta\varepsilon_{p,5.2} = \frac{\Delta l_p}{l_p} = \frac{2 \times \theta \times z}{l_p} = 9.132 \times 10^{-4} \times u = 5.479 \times 10^{-4} \quad (B.16)$$

The corresponding total prestressing steel strain  $\varepsilon_{p,u}$  is calculated as:

$$\varepsilon_{p,u,5.2} = \varepsilon_{p,m\infty} + \Delta\varepsilon_p = 7.154 \times 10^{-4} + 5.479 \times 10^{-4} = 7.702 \times 10^{-3} \quad (B.17)$$

It is proved that the prestressing steel does not yield under displacements  $u = 0.6[mm]$  according to the following equation:

$$\varepsilon_{p,u,5.2} = 7.702 \times 10^{-3} < \varepsilon_{p,d} = 7.81 \times 10^{-3} \quad (B.18)$$

The corresponding increase of the prestressing steel stress  $\Delta\sigma_p$ , is calculated according to the following equation:

$$\Delta\sigma_{p,5.2} = \Delta\varepsilon_p \times E_p = 107[MPa] \quad (B.19)$$

The increase of the prestressing steel force  $\Delta P$  for the  $5.2[mm]$  cable diameter, is calculated as:

$$\Delta P_{5.2} = \Delta\sigma_p \times S_{n5.2} = 1454[N] \quad (B.20)$$

The total prestressing steel force  $P_u$  after cracking is calculated as:

$$P_{u,5.2} = P_{5.2} + \Delta P_{5.2} = 20425[N] \quad (B.21)$$

The compression zone height  $x_{u,5.2}$  required to resist the maximum prestressing force applied is calculated as:

$$x_{u,5.2} = \frac{P_{u,5.2}}{0.5 \times b \times f_{cd}} = \frac{20425}{0.5 \times 200 \times 53.33} = 3.83[mm] \quad (B.22)$$

The corresponding values of the point loads  $F_i$  under displacements  $u$ , are found via the following formula:

$$F_{u,5.2} = \frac{1}{\left(\frac{l}{4} - a\right)} \times \left\{ P_{u,5.2} \times \frac{h}{2} - \left( \frac{q_{SW} \times l^2}{8} - \frac{q_{SW} \times a \times l}{2} \right) \right\} = \frac{1}{98.25} \times \{ 20425 \times 27.5 - 8281 \} = 5633[N] \quad (B.23)$$

The concrete stress due to the total prestressing steel load at  $u = 0.6[mm]$  is calculated as:

$$\sigma_{c,p,u,5.2} = -\frac{P_{u,5.2}}{A_c} = -\frac{20425}{200 \times 55} = -1.86[MPa] \quad (B.24)$$

The concrete stress due to its self-weight SW is calculated as:

$$\sigma_{c,sw} = \frac{M_{SW}}{W_c} = \pm \frac{\frac{q_{SW} \times l^2}{8} - \frac{q_{SW} \times l}{2}}{W_c} = 0.082[MPa] \quad (B.25)$$

L.S.0	Midspan concrete stresses ( $N/mm^2$ )				
Fiber	$\sigma_{c,p}$	$\sigma_{c,sw}$	$\sigma_{c,FBY}$	$\sigma_{c,tot}$	SXX
Top	-1.72	-0.08	0	-1.8	-1.805
Bottom	1.72	+0.08	0	-1.64	-1.644

Table B.10: Concrete stresses - L.S.0

The concrete stress due to concentrated loads  $F_i$  under  $u = 0.6[mm]$  displacements is calculated as:

$$\sigma_{c,F,5.2} = \frac{M_{F_{u,5.2}}}{W_c} = \pm \frac{F_{u,5.2} \times (\frac{l}{4} - a)}{W_c} = \pm 5.49[MPa] \quad (B.26)$$

The total concrete stress at top fiber level  $\sigma_{c,tot}$  under  $u = 0.6[mm]$  displacements is calculated as:

$$\sigma_{c,tot,u,5.2} = \sigma_{c,p,u,5.2} + \sigma_{c,sw} + \sigma_{c,F,5.2} = 7.43[MPa] \quad (B.27)$$

The concrete strain at top fiber level due to the load combination under  $u = 0.6[mm]$  displacements is calculated as:

$$\varepsilon_{c,tot,u,5.2} = \frac{\sigma_{c,tot,u,5.2}}{E_c} = \frac{7.43}{42000} = 1.768 \times 10^{-4} \quad (B.28)$$

It is proved that the concrete does fail due to compression under at top fiber level  $u = 0.6[mm]$  displacements, according to the equation:

$$\varepsilon_{c,tot,u,5.2} = 1.768 \times 10^{-4} < \varepsilon_{c,u3} = 2.60 \times 10^{-3} \quad (B.29)$$

### B.2.3 Point 0

Prestressing loads (P) and concrete self-weight (SW) are applied at this step. Since the displacements  $u$  are not acting yet, the reaction forces (FBY) under the applied  $u$  loads are zero:

$$FBY = 0[N] \quad (B.30)$$

The bending moment due to the concrete self-weight and the reaction force FBY is calculated as:

$$M_{ext} = M_{SW} + M_{FBY} = 8.281[Nm] \quad (B.31)$$

A comparison between the hand-calculated values of midspan concrete stresses and the DIANA10.2 results is shown in table [B.10](#). The calculated concrete stresses at midspan cross-section (SXX) are depicted in figure [B.1](#). It is proved that the results are verified.

L.S.7 Midspan concrete stresses ( $N/mm^2$ )					
Fiber	$\sigma_{c,p}$	$\sigma_{c,SW}$	$\sigma_{c,FBY}$	$\sigma_{c,tot}$	SXX
Top	-1.72	-0.08	-0.43	-2.23	-2.231
Bottom	-1.72	+0.08	+0.43	-1.21	-1.218

Table B.11: Concrete stresses - L.S.7

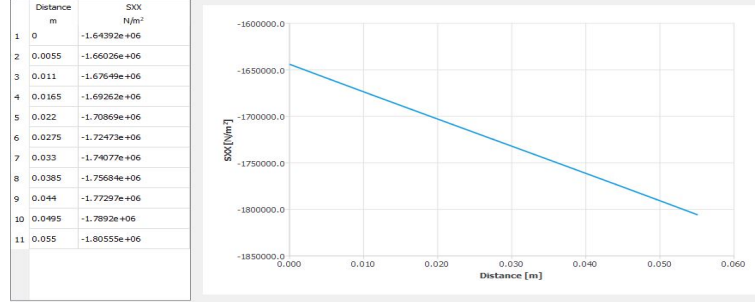


Figure B.1: Midspan concrete stresses (SXX) - L.S.0 - DIANA10.2

#### B.2.4 Load step 7

Displacements  $u = 7.82E - 6[m]$  are added to the previously applied loads of prestressing and concrete self-weight. The reaction forces at the locations of the applied displacements are calculated with DIANA10.2:

$$FBY = 436[N] \quad (B.32)$$

The resulting concrete stress due to the reactions FBY, can be calculated as:

$$\sigma_{c,FBY} = \frac{FBY \times (\frac{l}{4} - a)}{W_c} = \pm 0.43[MPa] \quad (B.33)$$

The bending moment due to the concrete self-weight and the reaction force FBY is calculated as:

$$M_{ext} = M_{SW} + M_{FBY} = (8.281 + 42.837) = 51.20[Nm] \quad (B.34)$$

A comparison between the hand-calculated values of midspan concrete stresses and the DIANA10.2 results is shown in table [B.11](#). The calculated concrete stresses at midspan cross-section (SXX) are depicted in figure [B.2](#). It is proved that the results are verified.

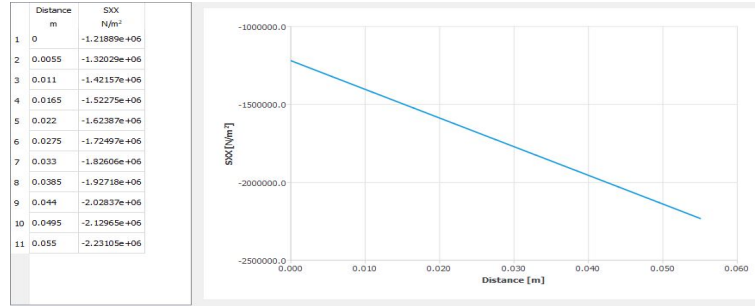


Figure B.2: Midspan concrete stresses (SXX) - L.S.7 - DIANA10.2

### B.2.5 Load step 24

It is the step before concrete cracking. Displacements  $u = 2.82E - 5[m]$  are added to the previously applied loads of prestressing and concrete self-weight. The calculated concrete stresses at midspan cross-section (SXX) are depicted in figure B.3. It is proved that the results are verified.

The reaction forces at the locations of the applied displacements are calculated with DIANA10.2:

$$FBY = 1673[N] \quad (B.35)$$

The resulting concrete stress due to the reactions FBY, can be calculated as:

$$\sigma_{c,FBY} = \frac{FBY \times (\frac{l}{4} - a)}{W_c} = \pm 1.63[MPa] \quad (B.36)$$

The bending moment due to concrete the self-weight and the reaction force FBY is calculated as:

$$M_{ext} = M_{SW} + M_{FBY} = 172[Nm] \quad (B.37)$$

A comparison between the hand-calculated values of midspan concrete stresses and the DIANA10.2 results is shown in table B.12. The whole cross section is under compression:

$$x_u = 55[mm] \quad (B.38)$$

The increase of strain  $\Delta\varepsilon$  over the compression zone height is:

$$\Delta\varepsilon = \frac{SXX_{top}}{E_c} = \frac{-3.43}{42000} = 8.167 \times 10^{-5} \quad (B.39)$$

Combining equations B.38 and B.39, the curvature at midspan cross-section is calculated as:

$$k = \frac{\Delta\varepsilon}{x_u} = \frac{8.167 \times 10^{-5}}{55 \times 10^{-3}} = 0.001485[m^{-1}] \quad (B.40)$$

L.S.7 Midspan concrete stresses ( $N/mm^2$ )					
Fiber	$\sigma_{c,p}$	$\sigma_{c,SW}$	$\sigma_{c,FBY}$	$\sigma_{c,tot}$	SXX
Top	-1.72	-0.08	-1.63	-3.43	-3.436
Bottom	-1.72	+0.08	+1.63	-0.01	-0.016

Table B.12: Concrete stresses - L.S.24

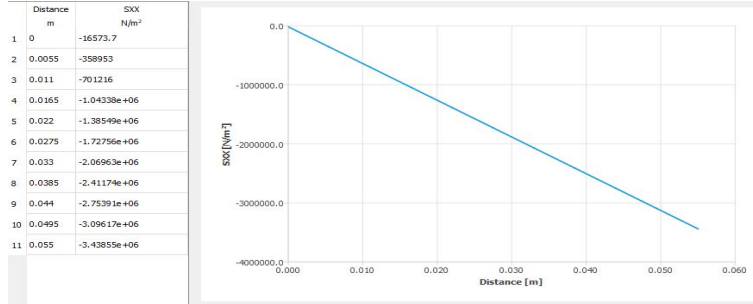


Figure B.3: Midspan concrete stresses (SXX) - L.S.24 - DIANA10.2

### B.2.6 Load step 25

It is the step after concrete cracking. Displacements  $u = 2.94E - 5[m]$  are added to the previously applied loads of prestressing and concrete self-weight. The reaction forces at the locations of the applied displacements are calculated with DIANA10.2:

$$FBY = 1746[N] \quad (B.41)$$

The hand-calculated value of the load that would lead to concrete cracking can be found in [B.6](#)

$$F_{cr} = 1686[N] \quad (B.42)$$

It is proved that it is in between the reaction forces FBY of load steps 24 and 25:

$$1673 < F_{cr} = 1686[N] < 1746 \quad (B.43)$$

Almost the whole cross section is under compression, see figure [B.4](#). Tensile stresses occur at bottom fiber level.

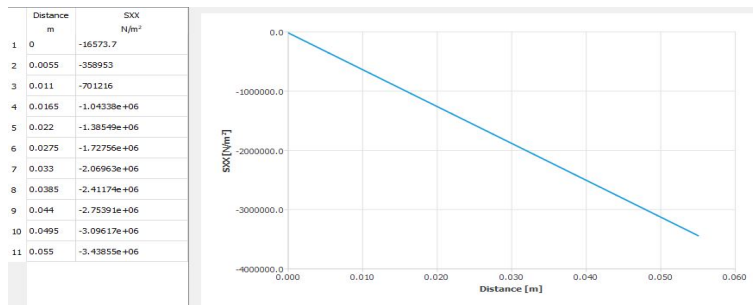


Figure B.4: Midspan concrete stresses (SXX) - L.S.25 - DIANA10.2

### B.2.7 Load step 29

Displacements  $u = 3.42E - 5[m]$  are added to the previously applied loads of prestressing and concrete self-weight. The reaction forces at the locations of the applied displacements are calculated with DIANA10.2:

$$FBY = 2032[N] \quad (B.44)$$

The bending moment due to concrete self-weight (SW) is:

$$M_{SW} = 8.281[Nm]$$

The bending moment due to the reaction forces (FBY) at loads location is:

$$M_{FBY} = FBY \times \left(\frac{l}{4} - a\right) = 199.644[Nm] \quad (B.45)$$

The external bending moment due to the concrete self-weight (SW) and the reaction forces (FBY) is:

$$M_{ext} = M_{SW} + M_{FBY} = 207[Nm] \quad (B.46)$$

As it can be seen from figure [B.5](#), the compression zone height is reduced to:

$$x_u = 50[mm] \quad (B.47)$$

The resulted DIANA10.2 stress SXX value at top fiber level is:

$$SXX_{top} = -3.8[MPa] \quad (B.48)$$

The concrete compressive force  $N_c$  is calculated as:

$$N_c = \frac{1}{2} \times b \times x_u \times SXX_{top} = \frac{1}{2} \times 200 \times 50 \times 3.8 = 19000[N] \quad (B.49)$$

The lever arm between the prestressing steel force P at the centroidal axis and the concrete compressive force is:

$$z = \frac{h}{2} - \frac{x_u}{3} = 27.5 - 16.67 = 10.83[mm] \quad (B.50)$$

The internal bending moment due to the concrete compressive force is:

$$M_{int} = N_c \times z = 19000 \times 10.83 \times 10^{-3} = 206[Nm] \quad (B.51)$$

From equations [B.46](#) and [B.51](#) is proved that:

$$M_{ext} \simeq M_{int} \quad (B.52)$$

The increase of strain  $\Delta\varepsilon$  over the compression zone height is:

$$\Delta\varepsilon = \frac{SXX_{top}}{E_c} = \frac{-3.8}{42000} = 9.047 \times 10^{-5} \quad (B.53)$$

Combining equations [B.38](#) and [B.39](#), the curvature at midspan cross-section is calculated as:

$$k = \frac{\Delta\varepsilon}{x_u} = \frac{9.047 \times 10^{-5}}{50 \times 10^{-3}} = 0.00181[m^{-1}] \quad (B.54)$$

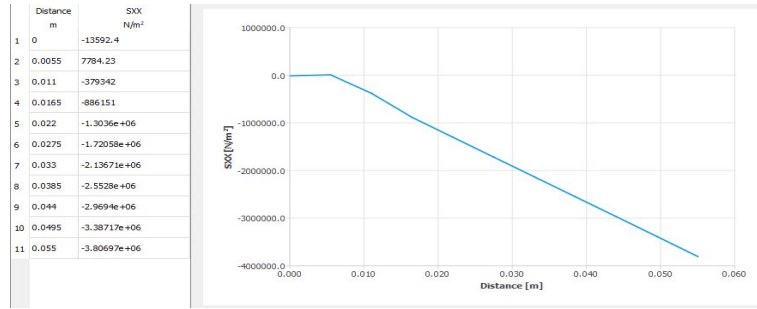


Figure B.5: Midspan concrete stresses (SXX) - L.S.29 - DIANA10.2

### B.2.8 Load step 45

Displacements  $u = 5.34E - 5[m]$  are added to the previously applied loads of prestressing and concrete self-weight. The reaction forces at the locations of the applied displacements are calculated with DIANA10.2:

$$FBY = 3038[N] \quad (B.55)$$

The bending moment due to concrete self-weight (SW) is:

$$M_{SW} = 8.281[Nm]$$

The bending moment due to the reaction forces (FBY) at loads location is:

$$M_{FBY} = FBY \times \left(\frac{l}{4} - a\right) = 298[Nm] \quad (B.56)$$

The external bending moment due to the concrete self-weight (SW) and the reaction forces (FBY) is:

$$M_{ext} = M_{SW} + M_{FBY} = 306[Nm] \quad (B.57)$$

As it can be seen from figure [B.6](#), the compression zone height is getting further reduced to approximately:

$$x_u = 33[mm] \quad (B.58)$$

The resulted DIANA10.2 stress SXX value at top fiber level is:

$$SXX_{top} = -5.5[MPa] \quad (B.59)$$

The concrete compressive force  $N_c$  is calculated as:

$$N_c = \frac{1}{2} \times b \times x_u \times SXX_{top} = \frac{1}{2} \times 200 \times 33 \times 5.5 = 18150[N] \quad (B.60)$$

The lever arm between the prestressing steel force P at the centroidal axis and the concrete compressive force is:

$$z = \frac{h}{2} - \frac{x_u}{3} = 27.5 - 11 = 16.5[mm] \quad (B.61)$$

The internal bending moment due to the concrete compressive force is:

$$M_{int} = N_c \times z = 18150 \times 16.5 \times 10^{-3} = 299[Nm] \quad (B.62)$$

From equations [B.57](#) and [B.62](#) is proved that:

$$\frac{M_{ext}}{M_{int}} (\%) = 102\% \quad (B.63)$$

The increase of strain  $\Delta\varepsilon$  over the compression zone height is:

$$\Delta\varepsilon = \frac{SXX_{top}}{E_c} = \frac{-5.5}{42000} = 1.309 \times 10^{-4} \quad (B.64)$$

Combining equations [B.38](#) and [B.39](#), the curvature at midspan cross-section is calculated as:

$$k = \frac{\Delta\varepsilon}{x_u} = \frac{1.309 \times 10^{-4}}{33 \times 10^{-3}} = 0.0039[m^{-1}] \quad (B.65)$$

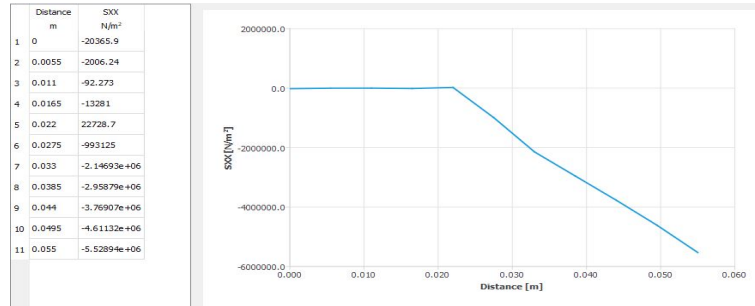


Figure B.6: Midspan concrete stresses (SXX) - L.S.45 - DIANA10.2

### B.2.9 Load step 70

Displacements  $u = 1.18E - 4[m]$  are added to the previously applied loads of prestressing and concrete self-weight. The reaction forces at the locations of the applied displacements are calculated with DIANA10.2:

$$FBY = 4508[N] \quad (B.66)$$

The bending moment due to concrete self-weight (SW) is:

$$M_{SW} = 8.281[Nm]$$

The bending moment due to the reaction forces (FBY) at loads location is:

$$M_{FBY} = FBY \times \left(\frac{l}{4} - a\right) = 443[Nm] \quad (B.67)$$

The external bending moment due to the concrete self-weight (SW) and the reaction forces (FBY) is:

$$M_{ext} = M_{SW} + M_{FBY} = 450[Nm] \quad (B.68)$$

As it can be seen from figure [B.7](#), the compression zone height is getting further reduced to approximately:

$$x_u = 12[mm] \quad (B.69)$$

The resulted DIANA10.2 stress SXX value at top fiber level is:

$$SXX_{top} = -17.3[MPa] \quad (B.70)$$

The concrete compressive force  $N_c$  is calculated as:

$$N_c = \frac{1}{2} \times b \times x_u \times SXX_{top} = \frac{1}{2} \times 200 \times 12 \times 17.3 = 20760[N] \quad (B.71)$$

The lever arm between the prestressing steel force  $P$  at the centroidal axis and the concrete compressive force is:

$$z = \frac{h}{2} - \frac{x_u}{3} = 27.5 - 4 = 23.5[mm] \quad (B.72)$$

The internal bending moment due to the concrete compressive force is:

$$M_{int} = N_c \times z = 20760 \times 23.5 \times 10^{-3} = 488[Nm] \quad (B.73)$$

From equations [B.68](#) and [B.73](#) is proved that:

$$\frac{M_{ext}}{M_{int}} (\%) = 92\% \quad (B.74)$$

The increase of strain  $\Delta\varepsilon$  over the compression zone height is:

$$\Delta\varepsilon = \frac{SXX_{top}}{E_c} = \frac{-17.3}{42000} = 4.119 \times 10^{-4} \quad (B.75)$$

Combining equations [B.38](#) and [B.39](#), the curvature at midspan cross-section is calculated as:

$$k = \frac{\Delta\varepsilon}{x_u} = \frac{4.119 \times 10^{-4}}{12 \times 10^{-3}} = 0.034[m^{-1}] \quad (B.76)$$

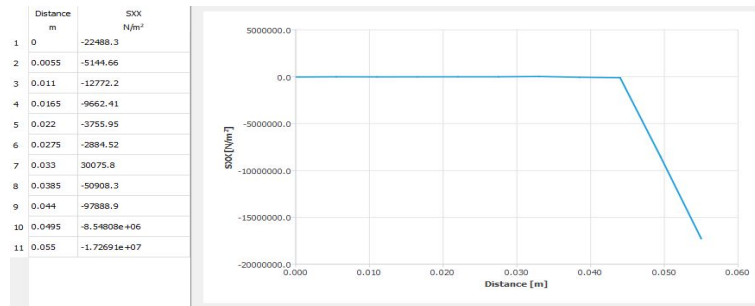


Figure B.7: Midspan concrete stresses (SXX) - L.S.70 - DIANA10.2

### B.2.10 Load step 116

Displacements  $u = 3.31E - 4[m]$  are added to the previously applied loads of prestressing and concrete self-weight. The reaction forces at the locations of the applied displacements are calculated with DIANA10.2:

$$FBY = 5000[N] \quad (B.77)$$

The bending moment due to concrete self-weight (SW) is:

$$M_{SW} = 8.281[Nm]$$

The bending moment due to the reaction forces (FBY) at loads location is:

$$M_{FBY} = FBY \times \left(\frac{l}{4} - a\right) = 491[Nm] \quad (B.78)$$

The external bending moment due to the concrete self-weight (SW) and the reaction forces (FBY) is:

$$M_{ext} = M_{SW} + M_{FBY} = 500[Nm] \quad (B.79)$$

As it can be seen from figure [B.8](#), the compression zone height is getting further reduced to approximately:

$$x_u = 5[mm] \quad (B.80)$$

The resulted DIANA10.2 stress SXX value at top fiber level is:

$$SXX_{top} = -48.7[MPa] \quad (B.81)$$

The concrete compressive force  $N_c$  is calculated as:

$$N_c = \frac{1}{2} \times b \times x_u \times SXX_{top} = \frac{1}{2} \times 200 \times 5 \times 48.7 = 24350[N] \quad (B.82)$$

The lever arm between the prestressing steel force P at the centroidal axis and the concrete compressive force is:

$$z = \frac{h}{2} - \frac{x_u}{3} = 27.5 - 1.67 = 25.83[mm] \quad (B.83)$$

The internal bending moment due to the concrete compressive force is:

$$M_{int} = N_c \times z = 24350 \times 25.83 \times 10^{-3} = 629[Nm] \quad (B.84)$$

From equations [B.79](#) and [B.84](#) is proved that:

$$\frac{M_{ext}}{M_{int}} (\%) = 79\% \quad (B.85)$$

The increase of strain  $\Delta\varepsilon$  over the compression zone height is:

$$\Delta\varepsilon = \frac{SXX_{top}}{E_c} = \frac{-48.7}{42000} = 1.15 \times 10^{-3} \quad (B.86)$$

Combining equations [B.38](#) and [B.39](#), the curvature at midspan cross-section is calculated as:

$$k = \frac{\Delta\varepsilon}{x_u} = \frac{1.15 \times 10^{-3}}{5 \times 10^{-3}} = 0.232[m^{-1}] \quad (\text{B.87})$$

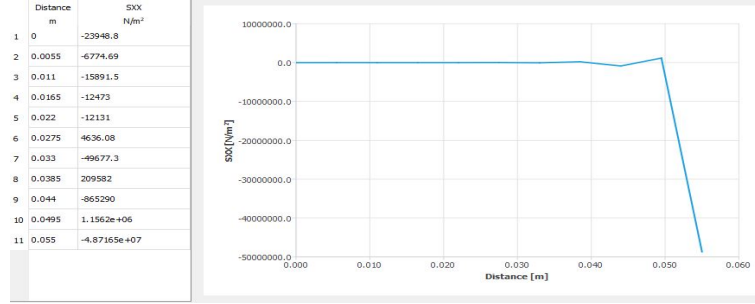


Figure B.8: Midspan concrete stresses (SXX) - L.S.70 - DIANA10.2

### B.2.11 Load step 154

Displacements  $u = 5.59E - 4[m]$  are added to the previously applied loads of prestressing and concrete self-weight. The reaction forces at the locations of the applied displacements are calculated with DIANA10.2:

$$FBY = 5223[N] \quad (\text{B.88})$$

The bending moment due to concrete self-weight (SW) is:

$$M_{SW} = 8.281[Nm]$$

The bending moment due to the reaction forces (FBY) at loads location is:

$$M_{FBY} = FBY \times \left(\frac{l}{4} - a\right) = 513[Nm] \quad (\text{B.89})$$

The external bending moment due to the concrete self-weight (SW) and the reaction forces (FBY) is:

$$M_{ext} = M_{SW} + M_{FBY} = 521[Nm] \quad (\text{B.90})$$

As it can be seen from figure [B.9](#), the compression zone height has reached a value of approximately:

$$x_u = 4[mm] \quad (\text{B.91})$$

The resulted DIANA10.2 stress SXX value at top fiber level is:

$$SXX_{top} = -72.4[MPa] \quad (\text{B.92})$$

The concrete compressive force  $N_c$  is calculated as:

$$N_c = \frac{1}{2} \times b \times x_u \times SXX_{top} = \frac{1}{2} \times 200 \times 4 \times 72.4 = 28960[N] \quad (\text{B.93})$$

The lever arm between the prestressing steel force P at the centroidal axis and the concrete compressive force is:

$$z = \frac{h}{2} - \frac{x_u}{3} = 27.5 - 1.33 = 26.17[mm] \quad (B.94)$$

The internal bending moment due to the concrete compressive force is:

$$M_{int} = N_c \times z = 28960 \times 26.17 \times 10^{-3} = 758[Nm] \quad (B.95)$$

From equations [B.90](#) and [B.95](#) is proved that:

$$\frac{M_{ext}}{M_{int}} (\%) = 68.7\% \quad (B.96)$$

The increase of strain  $\Delta\varepsilon$  over the compression zone height is:

$$\Delta\varepsilon = \frac{SXX_{top}}{E_c} = \frac{-72.4}{42000} = 1.724 \times 10^{-3} \quad (B.97)$$

Combining equations [B.38](#) and [B.39](#), the curvature at midspan cross-section is calculated as:

$$k = \frac{\Delta\varepsilon}{x_u} = \frac{1.724 \times 10^{-3}}{4 \times 10^{-3}} = 0.431[m^{-1}] \quad (B.98)$$

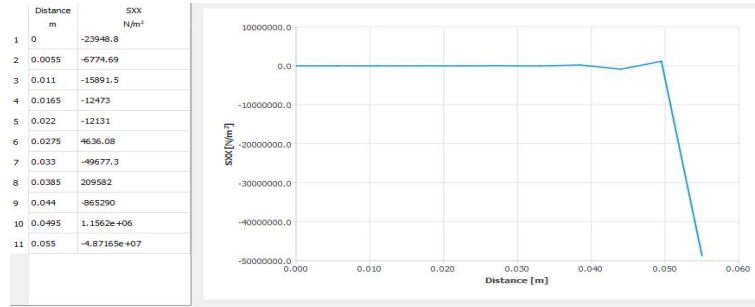


Figure B.9: Midspan concrete stresses (SXX) - L.S. 70 - DIANA10.2

### B.2.12 Relation between curvature and load

The curvature calculated for load steps 24, 29, 45, 70, 116, 154 is shown in table [B.13](#)

Load step	24	29	45	70	116	154
FBY (N)	1673	2032	3038	4508	5000	5223
$x_u$ (mm)	55	50	33	12	5	4
$\Delta\varepsilon$	8.167E-05	9.048E-05	1.310E-04	4.119E-04	1.160E-03	1.724E-03
k (m <sup>-1</sup> )	1.485E-03	1.810E-03	3.968E-03	3.433E-02	2.319E-01	4.310E-01

Table B.13: Compression zone height curvature and strains per load step

where,

FBY: reaction force at displacements location

$x_u$ : compression zone height

$\Delta\varepsilon$ : increase of concrete strain of compression zone height

k: curvature

## C Post-tensioned concrete arch structure

A hingeless arch is considered in this research, implying that two supports that are clamped with an assumed stiff soil, form the boundary conditions. Although the segmented arch is consisting of 11 elements and 10 joints, the hand calculations were performed based on a continuous arch approach. The degree of static indeterminacy is three. Thus, the extra 3 unknowns required to calculate the arc's internal loads due to its self weight can be calculated with the method of strain energy. Prestressing steel forces are not considered in the hand calculations. Half of the arc is considered due to symmetry in loading and boundary conditions, and therefore the angle  $\vartheta$  varies between  $0^\circ$  and  $90^\circ$ , see figure 7.9

The two post-tensioning steel cables are set at  $\frac{b}{6} = 166.67[mm]$  from the element edges following the center-line ( $\frac{t}{2} = 27.5[mm]$ ) of the arch. The type of prestressing steel cables (Y1860S3) as well as the magnitude of the applied prestressing steel forces at the four anchorages ( $10[KN]$ ) is not based on a structural requirement like with the case of the four-point bending test and it was randomly chosen. All elements and joints have the same concrete material properties and are of type C80/95. The eleven elements are monolithically connected to the joints in between them. The joints are assumed to have the same material properties with the surrounding concrete elements. A linear static analysis was performed in combination with hand-calculations based on the strain energy method of a hingeless arch.

The distance between the two prestressing steel cables is 467mm, see figure 7.6. Two locations of the arch are taken into consideration, i.e. at the crown (element 1090) and at right hand-side of the arch structure (element 482), see figures C.5, C.6. These are the locations where the maximum tensile stresses SXX due to the combined loading of concrete self-weight and prestressing steel forces, occur. The values of the maximum stresses for the selected elements are presented in tables C.1 and C.2. Reinforcement stresses SXX and SZZ due to the prestressing steel loads are shown in figures C.7, C.8. The reinforcement cross-section forces are presented in figure C.9.

### C.1 Hand calculations:

The moment of inertia  $I_C$  and the cross-section area  $A_C$  of the arch, were calculated based on the approximation of a radial half arch, although it must be noted that this is not exactly the case for the current structure since drap  $f$  is 14% larger than the radius of the arc  $R_C$ .

$$A_c = \frac{\pi \times (R_{out}^2 - R_{in}^2)}{2} \quad \text{and} \quad I_C = \frac{\pi \times (R_{out}^4 - R_{in}^4)}{8} \quad (C.1)$$

The total strain energy of a linear elastic solid contains bending, axial, shear and torsion components according to the following formula:

$$U = \int_0^s \frac{M^2 ds}{2EI} + \int_0^s \frac{N^2 ds}{2EA} + \int_0^s \frac{V^2 ds}{2G \frac{A}{a}} + \int_0^s \frac{T^2 ds}{2GJ} \quad (C.2)$$

where, M, N, V, T are the bending moment, the axial, shear and torsion developed in the arch. The arc length is denoted as  $s$  ( $= R_C \times d\theta$ ). Young's modulus of elasticity is E, and shear modulus is G.  $\frac{A}{a}$  is the effective shear area and I and J are the bending and torsional moment of inertia.

Neglecting the shear and torsion components, equation [C.2](#) results in:

$$U = \int_0^s \frac{M^2 ds}{2EI} + \int_0^s \frac{N^2 ds}{2EA} \quad (C.3)$$

Support locations are denoted with letters “A” and “B” respectively and are both clamped, restraining horizontal thrust  $H_{A,B}$ , bending moment  $M_{A,B}$  and vertical forces  $V_{A,B}$ . Therefore, at support “A” or “B” it holds:

$$\frac{\partial U}{\partial M_{A,B}} = 0, \quad \frac{\partial U}{\partial V_{A,B}} = 0, \quad \frac{\partial U}{\partial H_{A,B}} = 0 \quad (C.4)$$

Crown location is denoted as “C”. The shear force at the crown is zero due to the symmetry of the arc and of the applied loading. Therefore at the crown also holds:

$$\frac{\partial U}{\partial M_C} = 0, \quad \frac{\partial U}{\partial N_C} = 0 \quad (C.5)$$

Based on equations (31), equation (29) can be re-written in the form of [C.6](#) and [C.7](#) as:

$$U = \int_0^s \frac{M}{EI} \frac{\partial M}{\partial M_C} ds + \int_0^s \frac{N}{EA} \frac{\partial N}{\partial M_C} ds \quad (C.6)$$

and ,

$$U = \int_0^s \frac{M}{EI} \frac{\partial M}{\partial N_C} ds + \int_0^s \frac{N}{EA} \frac{\partial N}{\partial N_C} ds \quad (C.7)$$

Taking into account equation [C.8](#),

$$\frac{\partial M}{\partial M_C} = 1, \quad \frac{\partial N}{\partial M_C} = 0, \quad \frac{\partial M}{\partial N_C} = y, \quad \frac{\partial N}{\partial N_C} = \cos\theta \quad (C.8)$$

equations [C.6](#) and [C.7](#) result in [C.9](#) and [C.10](#):

$$U = \int_0^s \frac{M}{EI} \times 1 ds + \int_0^s \frac{N}{EA} \times 0 ds \quad (C.9)$$

$$U = \int_0^s \frac{M}{EI} \times y ds + \int_0^s \frac{N}{EA} \times \cos\theta ds \quad (C.10)$$

Denoting the bending moment at the crown as  $M_C$  and the bending moment caused by a load in this case the self-weight as  $M_G$ , the internal loads of axial force and bending moment at any cross-section of the arch are calculated via equations [C.11](#) and [C.12](#):

$$M = M_C + N_C \times y + M_G \quad (C.11)$$

$$N = N_C \times \cos\theta + N_G \quad (C.12)$$

Combining [C.9](#), [C.10](#), [C.11](#), [C.12](#) the following two equations are obtained:

$$\int_0^s \frac{M_C}{EI} ds + \int_0^s \frac{N_C \times y}{EI} ds = - \int_0^s \frac{M_G}{EI} ds \quad (C.13)$$

$$\int_0^s \frac{M_C \times y}{EI} ds + \int_0^s \frac{N_C \times y^2}{EI} ds + \int_0^s \frac{N_C \times \cos^2 \theta}{EA} ds = - \int_0^s \frac{M_G \times y}{EI} ds - \int_0^s \frac{N_G \times \cos \theta}{EA} ds \quad (C.14)$$

The horizontal reaction forces and bending moments at the supports are calculated as:

$$H_A = H_B \quad \text{and} \quad M_A = M_B \quad (C.15)$$

Where A and B are the left and right support respectively. Note that A is not shown in figure 7.9

Using the elastic center method (figure 7.9), the internal loads of compression  $N_C$  and bending moment  $M_C$  at the arch crown, are calculated by finding the corresponding internal loads  $N_0$  and bending  $M_0$  at the elastic center of the arch. The distance “d” of the elastic center of the arch (denoted as “O”) to the crown “C”, is found, by fulfilling the following requirement (C.16):

$$y_1 + d = y \quad \text{to satisfy} \quad \int_0^s \frac{y_1}{EI} ds = 0 \quad (C.16)$$

Where, y is the vertical distance from the crown to the investigated location and  $R_C$  is the radius of the arch at its center-line:

$$y = R_C \times (1 - \cos \theta) \quad (C.17)$$

Thus, the distance “d” is calculated as:

$$d = \frac{\int_0^s y ds}{\int_0^s 1 ds} \quad (C.18)$$

Rewriting equation C.13 results in:

$$\int_0^s \frac{M_C}{EI} ds + \int_0^s \frac{N_C \times (y_1 + d)}{EI} ds = - \int_0^s \frac{M_G}{EI} ds \quad (C.19)$$

Combining equations C.18 and C.19 and taking into account of a constant bending stiffness EI, results in the bending moment  $M_0$  at the elastic arch center:

$$M_0 = M_C + N_C \times d = - \frac{\int_0^s \frac{M_G}{EI} ds}{\int_0^s \frac{1}{EI} ds} = - \frac{\int_0^s M_G ds}{\int_0^s 1 ds} \quad (C.20)$$

The bending moment caused by the self-weight  $M_G$  is calculated:

$$M_G = q_G \times R_C - q_G \times \frac{x^2}{2} \quad (C.21)$$

,where x is the horizontal distance from the crown “C” to the investigated location:

$$x = R_C \times \sin \theta \quad (C.22)$$

The axial force from self-weight  $N_G$ , at a distance “x” from the arch crown “C” is calculated as”

$$N_G = q_G \times (R_c - x) \times \cos\theta \quad (C.23)$$

Combining equations C.14 and C.16, results in the horizontal reaction force at the elastic center  $H_0$  which is also equal to the axial force at the crown  $N_C$ :

$$H_0 = N_C = -\frac{\int_0^s \frac{M_G \times y_1}{EI} ds + \int_0^s \frac{N_G \times \cos\theta}{EA} ds}{\int_0^s \frac{y_1^2}{EI} ds + \int_0^s \frac{\cos^2\theta}{EA} ds} \quad (C.24)$$

Equations C.16 to C.24, are solved for  $\vartheta$  varying between  $[0, \frac{\pi}{2}]$ .

$$A_c = \frac{\pi \times (R_{out}^2 - R_{in}^2)}{2} = 348263.767[mm^2]$$

$$I_C = \frac{\pi \times (R_{out}^4 - R_{in}^4)}{8} = 7.07539E + 11[mm^4]$$

The vertical distance  $y$  of the investigated point from the arch crown is calculated as:

$$y = R_C \times (1 - \cos\theta) = 2015.56 \times (1 - \cos\theta)$$

The horizontal distance  $x$  of the investigated point from the arch crown is calculated as:

$$x = R \times \sin\theta = 2015.56 \times \sin\theta$$

where  $\vartheta$  varies between  $[0, \pi/2]$  rad.

The arc length  $s$  measured at center line is calculated as:

$$ds = R \times d\theta = 2015.56 \times d\theta$$

The vertical distance  $d$  between the elastic center and the arch crown is calculated as:

$$d = \frac{\int_0^s y ds}{\int_0^s 1 ds} = \frac{\int_0^{\frac{\pi}{2}} y ds}{\int_0^{\frac{\pi}{2}} 1 ds} = 1150.47[mm]$$

The vertical distance  $y_1$  from the supports to the arch elastic center is calculated as:

$$y_1 = R_C \times (1 - \cos\theta) - d = 865.09 - 2015.56 \times \cos\theta$$

The concrete self-weight  $q_G$  is calculated as:

$$q_G = A_c \times \gamma_c = 8.706[\frac{N}{mm}]$$

The bending moment caused by the self-weight  $M_G$  is calculated:

$$M_G = q_G \times R_C - q_G \times \frac{x^2}{2} = 17548.66 - 17685191.55 \times \sin^2\theta[Nmm]$$

The bending moment  $M_0$  at the elastic center is calculated as:

$$M_0 = M_C + N_C \times d = -\frac{\int_0^s \frac{M_G}{EI} ds}{\int_0^s \frac{1}{EI} ds} = -\frac{\int_0^s M_G ds}{\int_0^s 1 ds} = +8829.55[Nmm]$$

The axial compressive force  $N_G$  at a distance  $x$  from the elastic center is calculated as:

The horizontal reaction force at the elastic center  $H_0$  which is also equal to the axial force at the crown  $N_C$ :

$$N_G = q_G \times (R_c - x) \times \cos\theta = 8.706 \times (2015.56 - 2015.56 \times \sin\theta) \times \cos\theta$$

$$H_0 = N_C = -\frac{\int_0^s \frac{M_G \times y_1}{EI} ds + \int_0^s \frac{N_G \times \cos\theta}{EA} ds}{\int_0^s \frac{y_1^2}{EI} ds + \int_0^s \frac{\cos^2\theta}{EA} ds} = -\frac{-\frac{2.93661 \times 10^{11}}{EI} + \frac{1.7684 \times 10^7}{EA}}{\frac{1.77155 \times 10^9}{EI} + \frac{1583.02}{EA}} = -7144.354[N]$$

The bending moment at the crown is calculated as:

$$M_C = M_0 - N_C \times d = 8829.55 + 7144.354 \times 1150.47 = 8228194.496[Nmm] = 8228.194[Nm]$$

## C.2 Linear static analysis

### C.2.1 DIANA10.2 results

The internal loads of concrete and reinforcement under the loads of concrete self-weight and the applied post-tensioning steel forces are presented in figures C.1 to C.9. The concrete stresses due to the considered loads are presented in tables C.1 and C.2.

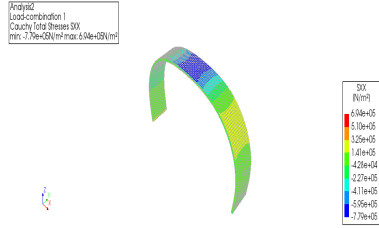


Figure C.1: Concrete elements stress distribution SXX due to self-weight SW - DIANA10.2

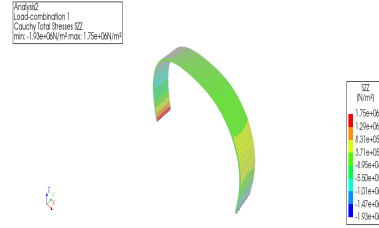


Figure C.2: Concrete element stress distribution SZZ due to self-weight SW - DIANA10.2

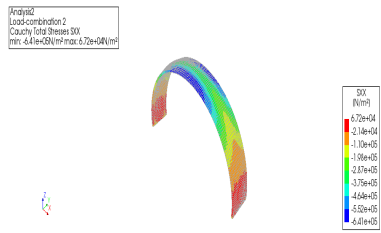


Figure C.3: Concrete elements stress distribution SXX due to prestressing loads P - DIANA10.2

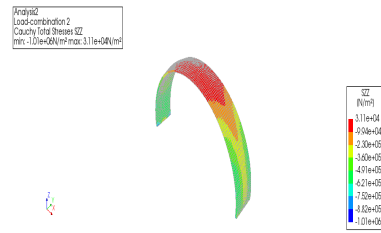


Figure C.4: Concrete element stress distribution SW due to prestressing loads P - DIANA10.2



Figure C.5: Concrete elements stress distribution SXX due to combined loading - DIANA10.2



Figure C.6: Concrete element stress distribution SZZ due to combined loading - DIANA10.2



Figure C.7: Reinforcement stress distribution SXX due to prestressing steel loads - DIANA10.2



Figure C.8: Reinforcement stress distribution SZZ due to prestressing steel loads - DIANA10.2

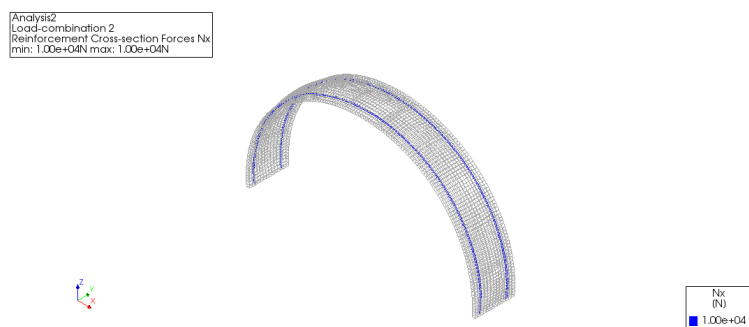


Figure C.9: Reinforcement cross section forces  $N_x$  - DIANA10.2

Element 1090 stresses (N/m <sup>2</sup> ) - DIANA10.2									
	Self weight (SW)			Prestressing steel forces (P)			Combined loading (P+SW)		
	SXX	SYX	SZZ	SXX	SYX	SZZ	SXX	SYX	SZZ
top	-695000	-58600	2437.64	-348000	404000	-114.29	-1060000	346000	2709.16
bot	694000	62300	3213.79	-505000	-410000	-675.78	192000	-348000	2476.46

Table C.1: Element 1090 stresses - DIANA10.2

Element 482 stresses (N/m <sup>2</sup> ) - DIANA10.2									
	Self weight (SW)			Prestressing steel forces (P)			Combined loading (P+SW)		
	SXX	SYX	SZZ	SXX	SYX	SZZ	SXX	SYX	SZZ
top	152000	68700	522000	-70500	413000	-254000	74700	482000	261000
bot	-196000	-74600	-665000	-120000	-419000	-405000	-315000	-493000	-1070000

Table C.2: Element 482 stresses - DIANA10.2

### C.2.2 Comparison of DIANA10.2 results with hand-calculations

1. The predicted values of the internal loads and reaction forces do not verify the DIANA10.2 results. In particular, the horizontal reaction force due to SW at the arch supports, was calculated at a value of 7144.354[N] being larger than the DIANA10.2 value of 982[N]. Hand calculations may be reconsidered in case the FEA results are correct or vice versa.
2. Although expected that the concrete arch structure under its self-weight would be governed by compression stresses, there is still tension in this structure not only at the disturbed zones of the clamped supports. In particular, at the bottom fiber of the arch crown (element 1090) and at the top fiber of the sides of the arc structure.
3. Based on the the assumption of zero instantaneous and time dependent losses in the prestressing steel, the reinforcement cross-sectional forces  $N_x$ , remain constant along the arc length. However, the reinforcement stresses SXX are increased from a value of  $9.85e + 03[\frac{N}{m^2}]$  at the anchors, to a value of  $4.27e + 08[\frac{N}{m^2}]$  at the crown, while the reinforcement stresses SZZ are decreased from a value of  $4.27e + 08[\frac{N}{m^2}]$  at the anchors to a value of  $5.20e + 04[\frac{N}{m^2}]$  at midspan of the arch.

## References

- Eurocode 2 - nen-en 1992.
- P. Eigenraam. Flexible mould for production of double-curved concrete elements. Master's thesis, TU Delft, 2013.
- Eline Hartog. Prefabrication of concrete shells. Master's thesis, TU Delft, 2008.
- B. Belletti Hendriks, A. de Boer. Guidelines for nonlinear finite element analysis of concrete structures. Technical report, Rijkswaterstaat Ministry of Infrastructure and the Environment, 2016.
- Johan Blaauwendraad Jeroen H. Hoefakker. *Solid Mechanics and Its Applications Structural Shell Analysis Understanding and Application*, volume 200. Springer, 2014.
- K. Hughe and Schoofs. Precast double curved concrete panels. Master's thesis, TU Delft, 2009.
- B. Janssen. Double curved precast load bearing concrete elements. Master's thesis, TU Delft, 2011.
- C.R. Braam J.C. Walraven. *Prestressed concrete*. Delft University of Technology, 2015.
- Marijn Kok. Textile reinforced double curved concrete elements, manufacturing free form architecture with a flexible mould. Master's thesis, TU Delft, 2013.
- Simon Jan Johannes Luitse. Deconstruction: A new construction method for prefab shell structures. Master's thesis, TU Delft, 2016.
- R.N. Ter Maten. Ultra high performance concrete in large span shell structures. Master's thesis, TU Delft, 2011.
- M. Rippman and P. Block, editors. *Rethinking structural masonry: unreinforced, stone-cut shells*. In *Proceedings of the ICE-Construction Materials 166(6):378-389*, 2013.
- M.K.H.M. Van Roesbroeck. The construction of prefab concrete shells. morphology - segmentation - material - production method. Master's thesis, TU Delft, 2006.
- H.R. Schipper. *Double-curved precast concrete elements. Research into technical viability of the flexible mould method*. PhD thesis, TU Delft, 2015.
- S. Troian. Crack evaluation in double-curved precast concrete elements. research into technical viability of the flexible mould method. Master's thesis, TU Delft, 2014.
- S. Witterholt. The application of double-curved precast concrete elements for the project green planet. Master's thesis, TU Delft, 2016.